OPTICAL SCIENCES

A. D. Yablon

Optical Fiber Fusion Splicing

Springer

Springer Series in

OPTICAL SCIENCES 103

founded by H.K.V. Lotsch

Springer Series in

OPTICAL SCIENCES

The Springer Series in Optical Sciences, under the leadership of Editor-in-Chief *William T. Rhodes*, Georgia Institute of Technology, USA, provides an expanding selection of research monographs in all major areas of optics: lasers and quantum optics, ultrafast phenomena, optical spectroscopy techniques, optoelectronics, quantum information, information optics, applied laser technology, industrial applications, and other topics of contemporary interest.
With this broad coverage of topics, the series is of use to all research scientists and engineers who need up-to-date reference books.

The editors encourage prospective authors to correspond with them in advance of submitting a manuscript. Submission of manuscripts should be made to the Editor-in-Chief or one of the Editors.

Andrew D. Yablon

Optical Fiber Fusion Splicing

With 137 Figures

Springer

Dr. Andrew D. Yablon
OFS Laboratories
19 Schoolhouse Road
Somerset, NJ 08873
USA
E-mail: ayablon@ofsoptics.com

ISSN 0342-4111

ISBN 3-540-23104-8 Springer Berlin Heidelberg New York

Library of Congress Control Number: 2004114851

Springer is a part of Springer Science+Business Media

springeronline.com

Printed in Germany

Camera-ready by the author using a Springer TEX macropackage
Cover concept by eStudio Calamar Steinen using a background picture from The Optics Project. Courtesy of John T. Foley, Professor, Department of Physics and Astronomy, Mississippi State University, USA.
Cover production: *design & production* GmbH, Heidelberg
Production: LE-TEX Jelonek, Schmidt, Vöckler GbR, Leipzig
Printed on acid-free paper 57/3141/YL 5 4 3 2 1 0

To Dalia

Preface

Significant advances in optical fiber technology have created a need for an up-to-date book about optical fiber fusion splicing. Over the past 15 years, a variety of new optical fibers including rare-earth-doped fiber, dispersion-compensating fiber, dispersion-matched fiber pairs, and microstructured fiber have been introduced. These fibers are currently used extensively in both research and commercial applications. Fusion splicing of these fibers has a significant impact on their performance but the relevant technical information has hitherto only been accessible by sifting through numerous technical articles published over a span of several decades. This book consolidates this scattered knowledge base into one coherent reference source.

This text is intended to serve as a reference for an audience that is both diverse and rapidly growing. This audience includes academic researchers investigating the latest optical fiber technology, designers of commercial optical fiber, fiber splicing equipment engineers, and product development engineers designing optical fiber devices from commercially available components. Manufacturers of optical fiber, optical fiber components, optical fiber devices, and optical fiber splicers all require a sophisticated understanding of optical fiber fusion splicing.

Optical fiber fusion splicing is a multi-disciplinary topic that combines concepts from diverse fields including optical waveguide theory, heat transfer, materials science, mechanical engineering, reliability theory, fluid mechanics, and even image processing. This book is unique in that it includes rigorous analyses from all of these very diverse fields. Scientists and engineers interested in optical fiber splicing who have a background in one or two of these fields will benefit from relevant knowledge in an unfamiliar field.

In order to appeal to the broadest possible audience while permitting a thorough treatment of the subject matter, the reader is assumed to be comfortable with higher mathematics including calculus and undergraduate physics. An abundance of citations from the technical literature enables interested readers to readily locate primary sources. Finally, this book contains a discussion of the future of optical fiber fusion splicing as well as the trend toward increasing automation.

This book is intended to serve as a complete reference for optical fiber fusion splicing, ranging from fiber preparation to the packaging and long-term reliability of the completed splice. The material is organized into ten chapters, including an initial introductory chapter.

Chapters 2 discusses fiber preparation including stripping, cleaving, and alignment. Chapter 3 introduces mechanical concepts relevant to fusion splicing. Chapter 4 is a theoretical discussion of the optical characteristics of fusion splices. Chapter 5 discusses loss estimation and fiber imaging. Chapter 6 provides an overview of splice strength, reliability, and packaging. Chapter 7 introduces techniques for splice measurement and characterization. Chapter 8 is a toolbox of general strategies and specific techniques for optimizing fusion splice quality. Chapter 9 specifically considers fusion splicing of contemporary specialty fibers including dispersion-compensating fiber, erbium-doped gain fiber, and polarization-maintaining fiber. This chapter also contains an up-to-date and detailed discussion of the latest and most exciting recent development in optical fiber technology: microstructured fibers, also known as photonic crystal fibers or holey fibers. The final chapter is an overview of contemporary hardware for fusion splicing.

The first portion of the book (Chaps. 3–6) is more theoretical in nature while the latter portion (Chaps. 7–10) is more practical, demonstrating the practical implications of the fundamental concepts presented earlier. A reader wrestling with a challenging fusion splice can go directly to the specific strategies presented in Chapters 8 and 9, but will better understand the physics underlying those strategies by reading the relevant sections in Chapters 3 through 6.

This project could never have been completed without extensive support and assistance from my colleagues and my management at *OFS Laboratories* (formerly the Optical Fiber Research Department of *Bell Laboratories, Lucent Technologies*). I thank Baishi Wang, Harish Chandan, Susan Flesher, and Rodney Casteel for their close reading and constructive criticism of various parts of the manuscript. I am indebted to Stephen Mettler, one of the pioneers of optical fiber fusion splicing, for his stimulating discussions and important advice. Angela Lahee and Claus Ascheron at Springer-Verlag were tremendously helpful in composing and editing the manuscript. I am also indebted to David J. DiGiovanni for encouraging me to pursue this effort from its earliest stages to its completion. Man F. Yan was been exceedingly generous with his time and provided much valuable advice. Special thanks to Latha Venkataraman, Ken Nelson, Michael Harju, Bob Swain, and Bjorn DeBear of *Vytran Corporation* and Tom Liang at *Furukawa America, Inc.* for their helpful discussions and excellent digital images of splicer hardware. John Krause, another important pioneer of optical fiber fusion splicing, provided me with a wealth of information and knowledge. Justin Ging was a great resource for compiling and preparing digital images. I owe a debt of gratitude to Eric W. Mies for first introducing me to the field of optical fiber fusion splicing during my time at *Vytran Corp.* Finally, I would like to express my gratitude to my wife Dalia whose generous support has enabled me to complete this book.

Murray Hill, New Jersey, August, 2004 *Andrew D. Yablon*

Contents

1. Introduction

1.1 An Overview of Fusion Splicing and Its Applications

Optical fiber fusion splicing is the process by which a permanent, low-loss, high-strength, welded joint is formed between two optical fibers. If an optical communication network can be thought of as a roadway system for transporting information, then optical fiber fusion splices can considered the joints that connect pavement sections together. Just like joints in a roadway, ideal optical fiber fusion splices are imperceptible to the traffic passing across them and are reliable for decades or more at a time. Optical fiber fusion splices may not play a glamorous role in the optical network, but they play a crucial one nonetheless.

The ultimate goal of optical fiber fusion splicing is to create a joint with no optical loss yet with mechanical strength and long-term reliability that matches the fiber itself. Ideally the splicing process should be fast, inexpensive, and should not require excessive skill or expensive equipment to execute. Achieving all these ideals is generally impossible so the details of the fusion splicing process involve trade-offs among the various requirements. For some applications, such as laboratory "hero" experiments, the quality of the splice is determined exclusively by the optical loss, regardless of the splice's mechanical strength or reliability. For other applications, such as undersea telecommunications, optical loss may actually be less important than long-term reliability.

There are many important advantages of optical fiber fusion splicing over competing approaches for interconnecting optical fibers, which include connectorization, mechanical splicing, or free-space optical coupling. Fusion splice joints are very compact, and when recoated they exhibit a cross-sectional area no larger than the original optical fiber. The optical loss and reflectance of a fusion splice are typically much lower than alternative optical fiber connecting technologies. Fusion splices are permanent, and can exhibit mechanical strength and long-term reliability that approaches the original fiber itself. Optical fiber fusion splices are very stable so their alignment, and hence their optical transmission, does not change over time or with temperature. Optical fiber fusion splices can withstand extremely high temperatures or extremely high optical power densities. Additionally, fusion splices do not allow dust or contaminants to enter the optical path.

Nearly all contemporary optical fibers are fabricated from high-purity fused silica glass. The silica glass comprising the fiber is deliberately doped with small amounts of other substances to provide desirable optical or mechanical characteristics. The physics of optical fiber fusion splicing depends in large part on the nature of these materials.

Optical fiber fusion splicing is practiced in a variety of environments by a diverse group of professionals using a wide variety of equipment. This diversity is described by three general categories of fusion splicing: (1) *field* splicing, (2) *factory* splicing (also termed *original equipment manufacturing (OEM)* splicing), and (3) *laboratory* splicing. An example of field splicing is a fiber installer fusion splicing multi-fiber ribbon cable with a commercial ribbon splicer high on a telephone pole. Another important example of field splicing is the assembly of undersea fiber optic cables aboard fiber deployment ships. An example of production or OEM splicing is the assembly of fiber devices such as erbium-doped optical fiber amplifiers (EDFA) in a production environment. Laboratory splicing is performed by researchers using the latest technology optical fibers, frequently with the aid of specially designed or modified fusion splicing equipment. Although the setting as well as the fibers themselves are very different in these three categories, the basic underlying scientific principles are the same. This book instructs the reader in those basic principles so that they may be effectively applied to all varieties of optical fiber fusion splicing.

Optical fiber fusion splicing is a multi-disciplinary topic that combines concepts from many subjects including optical waveguide theory, heat transfer, materials science, mechanical engineering, fluid mechanics, and even image processing. This book serves as a reference for those readers who lack a background in some of these diverse fields. Those readers who desire an even more in-depth treatment from primary sources will be pleased to find copious references throughout this monograph.

The advent of optical fiber devices such as optical amplifiers and dispersion-compensating modules has elevated the significance of optical fiber fusion splicing. The design and performance of these optical fiber devices depends on, among other things, the quality of the splices within the device. Achieving low-loss fusion splices between the different fiber types comprising such fiber devices poses daunting technical challenges. Splicing difficulties are increasingly influencing the design of the fibers themselves. This book provides a detailed understanding of the physics of optical fiber fusion splicing so that the reader can apply this knowledge to the optical fibers of the future.

We begin this chapter with a detailed discussion of the fusion splicing process. Subsequent sections describe relevant optical, materials, and mechanical characteristics of optical fibers. Fusion splices are compared and contrasted with fiber connectors and mechanical splices. The role of fusion splices in the optical network is also presented and a brief history of optical fiber fusion splicing is included. We conclude with a discussion of the frontiers of optical fiber fusion splicing technology.

1.2 The Fusion Splicing Process

Optical fiber fusion splicing can be broken down into a series of basic tasks summarized in Fig 1.1. First, the polymer coating protecting the fiber must be completely *stripped*. Next flat fiber end faces must be achieved, typically by *cleaving* the fibers. The fibers must then be laterally *aligned* to each other including, in some cases, rotational alignment about their axes. The fiber tips must be *heated* to their softening point and then must be *pressed* together to form a joint. This press stroke is termed a *hot push*. Some sort of quality check such as *loss estimation* is typically performed. The splice may be *proof tested* to help ensure its long term mechanical reliability. Finally, the completed splice must then be *protected* from the environment by packaging it. In some cases, the splice is packaged before proof testing. Depending on the particular application, one or more of these tasks can be omitted. For example, in the laboratory, the long term reliability of a splice may not be important so the splice may be neither protected nor proof tested.

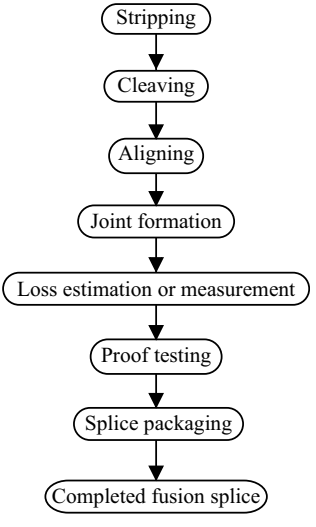

Fig. 1.1. Flowchart for the generalized fusion splice process. Note that some steps, such as loss estimation or proof testing, may be omitted and that sometimes splice packaging precedes proof testing

There is a wide variety of commercial hardware on the market designed to accomplish the various tasks comprising the fusion splice process. Contemporary fusion splicing hardware is discussed in detail in Chap. 10. Figure 1.2 is a simplified depiction of a fusion splicer. At a minimum, a fusion splicer requires a heat source and fiber chucks for gripping and aligning the fiber tips. Modern fusion splicers incorporate microscope objectives, CCD cameras, and

a microprocessor for performing tasks such as fiber alignment and loss estimation. The cost of commercial fusion splicing hardware can range from less than $10,000 (USD) for a basic, portable fusion splicer with a minimum of features to over $100,000 (USD) for the latest technology fully automated production fusion splicing equipment. Some commercial splicing equipment, termed *ribbon splicing* or *mass fusion splicing* equipment, can simultaneously splice all the fibers comprising a 24-fiber ribbon cable [1.1]. Different manufacturers have developed different solutions for the various tasks comprising the fusion splice process. For example, some splicing equipment heats the fiber with an electric arc discharge while other equipment uses a resistively heated metal filament.

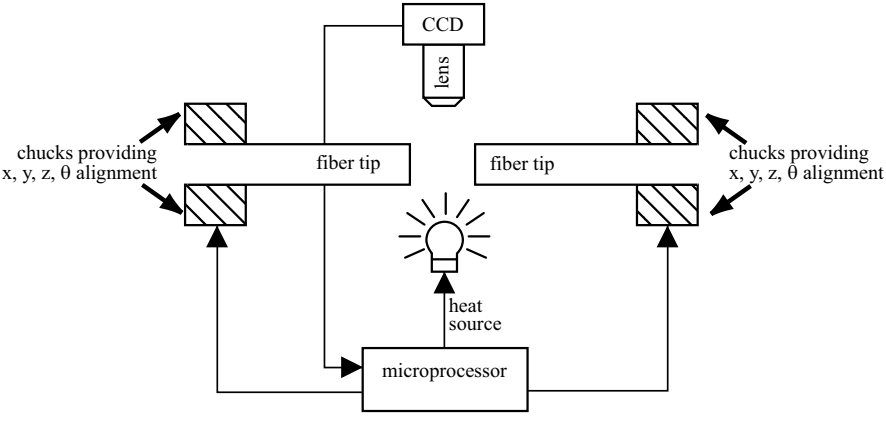

Fig. 1.2. Components of a simplified fusion splicer including heat source, imaging lens, CCD, microprocessor, and chucks for positioning and aligning fiber tips. The thin arrows denote the flow of control to or from the microprocessor

The first step in the fusion splice process, stripping the optical fiber's polymer coating, is important since it can introduce flaws to the surface of the exposed glass thus weakening the strength and long-term reliability of the fibers. In a laboratory or factory environment, aggressive solvents such as methylene chloride or hot acids can be used to ensure a clean, defect-free glass surface. In a field environment, thermo-mechanical or mechanical stripping equipment is safer and more convenient, but is also more likely to reduce the fiber strength than the aforementioned solvent stripping.

The second step of the fusion splice process, cleaving, is important because very flat fiber end faces are required to minimize deformation of the fibers when they are pressed together during the hot push. Fiber stripping and fiber cleaving are both discussed in greater detail in Chap. 2.

Once the fiber tips are prepared, they must be aligned to each other. Three types of fiber alignment are in common practice: passive alignment, active alignment, and light injection and detection (LID). Older fusion splic-

ing equipment and many ribbon fusion splicers use a fixed v-groove system to passively align the fiber tips. More modern fusion splicers perform active alignment based on a magnified image of the fiber tips. Specific features in the fiber, such as the fiber's core, may be used for alignment purposes. In addition, light may be injected into one of the fibers and detected at the other to provide a direct measurement of the alignment quality. If the fibers are polarization-maintaining (PM), their rotational angles must be aligned as well.

The heart of the fusion splicing process is the actual heating of the fiber tips and the formation of the joint. Although different fusion splicers may employ different heat sources and different terminology is used for the various stages of the actual joint formation, the basic principles are the same. Figure 1.3 is a representative timeline of the splice process depicting all the major steps that may occur during the heating portion of the fusion splice process.

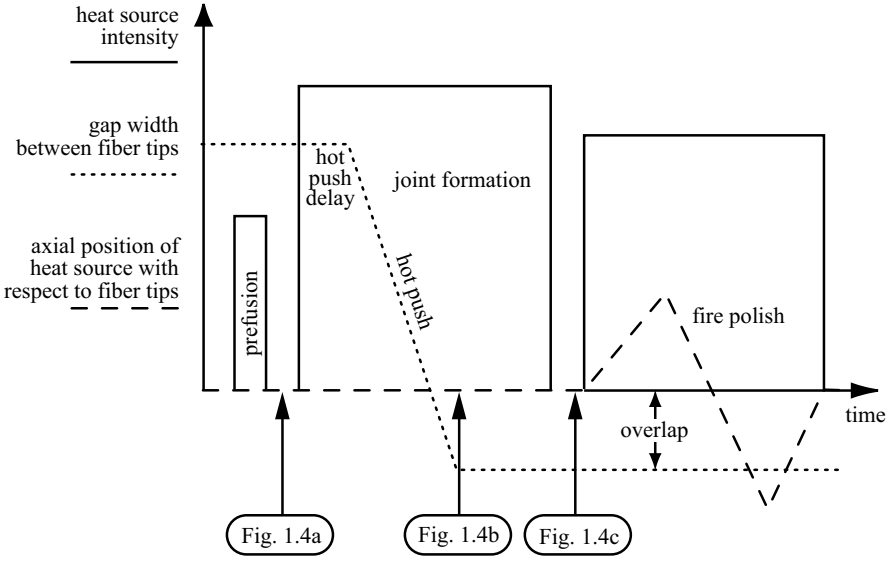

Fig. 1.3. Schematic illustration of splice process depicting heat source intensity (*solid line*), gap width between fiber tips (*dotted line*), and axial position of heat source with respect to splice (*dashed line*). The heat source intensity is depicted here as a sequence of step functions whose magnitude approximately corresponds to the temperature at the splice. The hot push reduces the gap width between the fibers from its initial value of about 10 μm at the start of the splice to a negative value. Negative gap width represents overlap of the fiber tips. Joint formation commences when the fiber tips make contact. In this depiction, the heat source position is held constant until joint formation is completed at which time the final heating is applied while the heat source is scanned back and forth along the splice to perform a fire-polish. The timing of the fusion splice images depicted in Fig. 1.4 are indicated on the horizontal axis

A brief flash of heat at the start of the process, termed *prefusion cleaning*, serves to clean the fiber tips by decomposing and vaporizing any debris. This prefusion heating is important since any particulate contamination present on the fiber tips during splicing can release volatile gases which produce bubbles at the splice joint. After alignment and prefusion are completed, the fiber tips are subject to an intense burst of heat to raise their temperature to the softening point. Following a brief delay, termed a *hot push delay*, the fibers are fed together during the *hot push*. Unfortunately, some splicer manufacturers have referred to the hot push delay as the *prefusion time*, which confuses the hot push with the prefusion cleaning mentioned already. Some manufacturers refer to the hot push as the press stroke or the fiber feed. Usually the hot push exceeds the original gap between the fiber tips by an amount termed the *overlap*, which is typically anywhere from 2 to 20 μm. While the fiber tips are pressed together at high temperature, phenomena such as surface tension, viscosity, and dopant diffusion influence the development of the splice joint. After a prescribed time, termed the *splice duration*, the heat is removed and the completed splice rapidly cools down to room temperature.

Figure 1.4 contains images of a fusion splice between two pieces of standard single-mode fiber (SMF) during different stages of the splice process. A detailed discussion of the features visible in the images of the fiber, such as the fiber's core and cladding region, is presented in Sect. 5.1.2. Prior to the splice, the fiber tips are aligned to each other as in Fig. 1.4a. Figure 1.4b shows the fibers in the midst of a fusion splice, after the fibers have been pressed together by the hot push. The vertical line in Fig. 1.4b is the incompletely formed joint between the fibers. Surface tension has begun to round the tips of the fibers and form the joint. Note how difficult it is to resolve the splice location in the image of the completed splice, Fig. 1.4c. The associated splice loss here is below 0.01 dB (>99.7% optical power transmission), which is essentially unmeasurable. Techniques for splice characterization and measurement are discussed in Chap. 7.

Sometimes, a post splice heat treatment is applied to improve the quality of the splice. Depending on the situation, quality can refer to optical loss or mechanical strength or both. For example, Fig. 1.3 shows a *fire polish* which takes place after the splice is completed. A fire polish is a heat treatment in which the heat source is scanned back and forth relative to the completed splice joint as depicted by the dashed line in Fig. 1.3. This heat treatment can clean the surface of the completed splice by burning off contaminants and melting away surface cracks [1.2]. The fire polish increases the mechanical strength of the splice and hence its long-term reliability. The fire polish can also modify the refractive index profile of the fiber tips so as to reduce splice loss between dissimilar fibers [1.3]. Fire polishing is discussed in more detail in Sect. 8.2.1.

As is apparent from the preceding description of the splice process, there are many different *splicing parameters* which control the quality of the splice

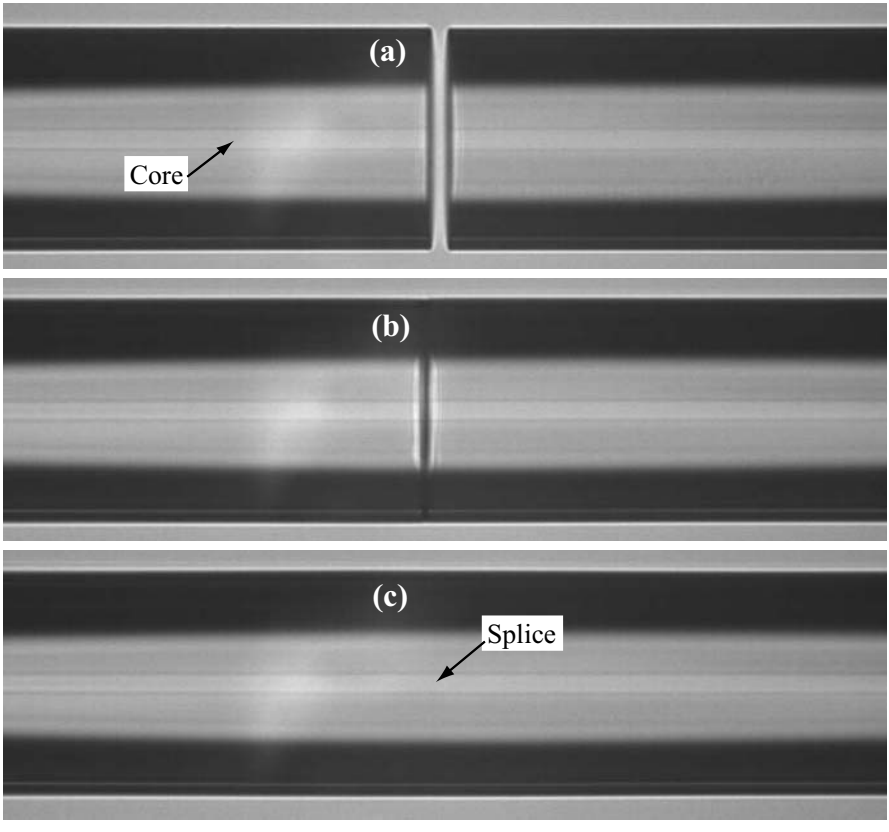

Fig. 1.4. Various stages during a fusion splice of ordinary single-mode fiber. Core and cladding regions of the fiber are visible and labeled. The timing of these images during a typical fusion splice is depicted in Fig. 1.3. (**a**) Fiber tips aligned prior to splicing. (**b**) Fiber tips following hot push during joint formation. (**c**) Completed splice with a loss less than 0.01 dB

including the amount of overlap, the hot push delay, the intensity of the heat, the duration of the splice, etc. Finding the best choice of splice parameters is called *splice optimization* and is discussed in Chap. 8. The optimum splicing parameters sensitively depend on the fibers' characteristics. Certain basic physical relationships can provide insights as to how to optimize a splice. However, finding the best splice parameters usually requires resorting to design of experiments (DOE) methods.

Following completion of the fusion splice, commercial fusion splicing equipment usually provides an estimate of the optical loss. Loss estimation is not always accurate and so it cannot substitute for accurate splice loss measurement. However, loss estimation can be essential when it is inconvenient or impossible to directly measure the splice loss. Loss estimation is discussed in Chap. 5.

A completed splice must be protected from the environment to ensure its long-term reliability. Splice protection comes in many forms including heat shrinkable tubing with integrated splints or hard plastic cases. For many applications, *recoating* is an attractive option since it preserves the dimensions and mechanical flexibility of the original fiber. Recoated splices rely on the mechanical strength of the spliced fibers themselves, rather than on a splint. The recoat material is an ultraviolet light curable acrylate similar to the original fiber coating and is applied to the bare splice in a special mold. Splice strength, reliability, and packaging is discussed in Chap. 6.

The emergence of many novel fiber types such as erbium-doped amplifier fiber (EDF), dispersion-compensating fiber (DCF), and microstructured fiber (also termed "holey fibers") have necessitated important innovations in the fusion splicing process. As new *specialty fibers* are introduced and new fusion splicing challenges are encountered, special fusion splicing strategies are developed. Some important special fusion splicing strategies discussed in Chap. 8 include

- bridge fibers between dissimilar fibers
- thermal diffusion of dopants
- low-temperature splices
- tapered splices
- fattened splices
- fire polishing
- offset heating

A detailed analysis of the specific issues and optimum strategies for fusion splicing specific specialty fiber types is provided in Chap. 9.

1.3 Essential Optical Fiber Concepts

1.3.1 Optical Characteristics

Optical fibers are waveguides designed to confine light beams so that they may propagate long distances. The refractive index of an optical fiber is designed to maximize the available bandwidth for signal transmission as well as to maximize the signal propagation distance. In depth treatments of the optical characteristics of fibers are available in monographs by Snyder and Love [1.4], Neumann [1.5], Jeunhomme [1.6], Ghatak and Thyagarajan [1.7]. In this section, we will survey the optical characteristics of optical fibers that are relevant to fusion splicing.

With a few notable exceptions discussed in Sect. 9.5, an optical fiber guides light because the refractive index is higher in the interior, or *core*, region than it is in the exterior, or *cladding region*. Contemporary optical fibers have a cladding diameter of about 125 μm while the core diameter can

be as little as 1 μm or more than 100 μm depending on the fiber design. The refractive index difference between the core and cladding may be expressed in absolute units as Δn where

$$\Delta n = n_{\text{core}} - n_{\text{clad}} \tag{1.1}$$

and n_{core} represents the core index and n_{clad} represents the cladding index. The refractive index difference between the core and cladding of an optical fiber may also be specified on a relative scale as Δ where

$$\Delta = \frac{n_{\text{core}} - n_{\text{clad}}}{n_{\text{clad}}} \, . \tag{1.2}$$

Most optical fibers have a relatively small difference, Δ, between core and cladding, which ranges from as little as .1% (or 0.001) to as much as 3% (or 0.03).

Creating a low-loss fusion splice requires that the cores of the two fiber tips be aligned to each other with micron-scale precision. The fiber cladding is typically surrounded by a polymer coating with a refractive index higher than the cladding in order to strip out light that is not confined by the core structure. The cladding is usually undoped silica glass but some specialty multimode fibers actually have a polymer cladding which must be stripped off prior to fusion splicing.

In certain cases, the wave-guiding characteristics of an optical fiber can be explained by *total internal reflection*. This interpretation is most accurate when analyzing multimode fibers which have relatively large core diameters. Total internal reflection occurs as a consequence of Snell's Law for refraction at an interface:

$$n_1 \sin\theta_1 = n_2 \sin\theta_2 \, , \tag{1.3}$$

where n_1 is the refractive index of the original medium, θ_1 is the angle of incidence in that medium, n_2 is the refractive index of the second medium, and θ_2 is the refracted angle in that second medium. This geometry is illustrated in Fig. 1.5. It is not hard to show that when $n_1 > n_2$ there is a set of incident angles for which $\theta_2 > 90°$. In this case, there is no physical solution for a light ray to propagate from medium 1 into medium 2. The critical angle, θ_{crit}, is the angle at which $\theta_2 = 90°$. In an optical fiber, the core can be thought of as medium 1 while the cladding can be thought of as medium 2 such that light rays with $\theta > \theta_{\text{crit}}$ are trapped in the core region and cannot escape. Given the range of Δ listed previously, the critical angle for a ray propagating inside an optical fiber ranges from about 79° to 86°. Thus, the angle between the critical ray inside the fiber and the fiber axis ranges from about 4° to 14° in a typical optical fiber.

Due to refraction, the critical angle of a light ray incident on a fiber's end face is different from the critical angle for light rays propagating inside the fiber's core. The *numerical aperture* or NA is commonly used to characterize the critical acceptance angle for a cone of light incident on the fiber's end

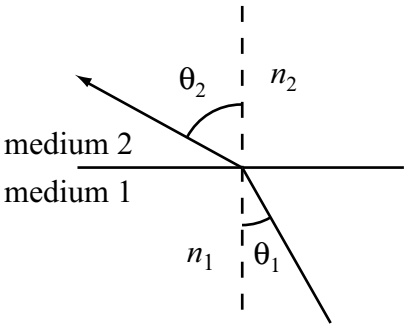

Fig. 1.5. Illustration of Snell's law

face. The NA is the sine of the angle between the fiber's axis and the critical ray impinging on the end of the fiber and may be expressed as

$$\mathrm{NA} = \sqrt{n_{\mathrm{core}}^2 - n_{\mathrm{clad}}^2}\ , \tag{1.4}$$

so the NA of an optical fiber is typically 0.1 to 0.3. When Δ is much smaller than unity, as is the case for most optical fibers, the NA may be equivalently expressed as

$$\mathrm{NA} = n_{\mathrm{clad}}\sqrt{2\Delta}\,. \tag{1.5}$$

This ray analysis of optical fiber is overly simplistic, especially for the case of single mode fibers. The actual propagation of an optical signal in a fiber is most completely described by Maxwell's equations, which govern the behavior of electromagnetic waves. Maxwell's equations, and the central role they play in describing the optical characteristics of fusion splices, will be presented in Chap. 4.

A *mode* is a spatial distribution of optical energy that propagates unchanged through a waveguide. Depending on the precise nature of the refractive index structure of the fiber, the fiber may guide a single mode or simultaneously guide multiple modes. The single, guided, mode of a single-mode fiber usually resembles a Gaussian function in that its amplitude is a maximum at the center of the fiber core and drops off rapidly in the cladding region. The various guided modes of a multimode fiber have more complex structures, often with many maxima and minima, but the amplitudes of these modes also approach zero in the cladding region of the fiber. The core diameter of a single mode fiber designed for 1550 nm propagation is usually less than 12 μm while the core diameters of multimode fibers are usually larger than 20 μm. Generally, it is more difficult to achieve a low-loss splice with single-mode fibers compared with multimode fibers since their smaller core diameters make fiber alignment more critical.

The refractive index profile of an optical fiber is a representation of how the refractive index varies as a function of radial position in the fiber. Fig-

ure 1.6 depicts index profiles for two common types of multimode fiber. Step index multimode fiber typically has a core radius anywhere from 50 μm to 100 μm depending on the application. In a graded-index multimode fiber (GIF), the refractive index profile of the core is approximately parabolic in shape. In a multimode fiber, different modes travel at different speeds and this can reduce the fiber's available bandwidth. GIF has the advantage that the velocity difference between its various modes is relatively small, so GIF can be used for relatively high bandwidth communications applications.

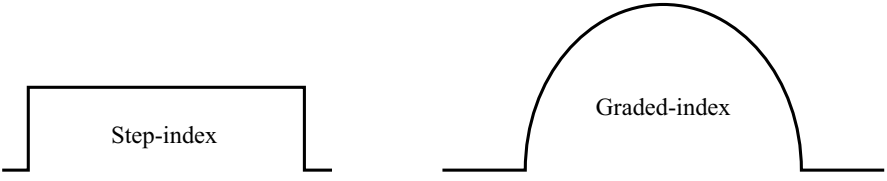

Fig. 1.6. Index profiles representing main multimode fiber designs. Horizontal scale represents radial position in fiber. Vertical scale represents refractive index

Figure 1.7 depicts index profiles for several contemporary single-mode fiber types. Standard matched clad single-mode fiber (SMF) has a core index about 0.005 higher than the surrounding cladding index and a core diameter of about 8 μm. Non-zero dispersion-shifted fiber (NZ-DSF) is a single mode fiber designed to have much lower dispersion than SMF in the 1550 nm communications window lying between 1530 and 1580 nm. Dispersion-compensating fiber (DCF) is a single-mode fiber designed to have a dispersion that is opposite to that of a transmission fiber so that it can "undo" the deleterious effects of dispersion. The central core diameter of DCF can be as small as 2 μm. Figure 1.7 shows how small the central core of DCF is relative to SMF which partly accounts for the difficulty of splicing DCF fibers. Specific information relevant to fusion splicing these and other fibers is presented in Chap. 9.

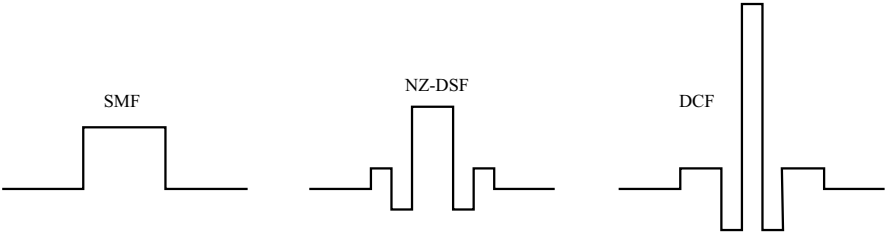

Fig. 1.7. Index profiles representative of several single mode fiber designs. Vertical scale represents refractive index. Horizontal scale represents radial position in fiber. SMF = matched clad single mode fiber, NZ-DSF = non-zero dispersion-shifted fiber, DCF = dispersion-compensating fiber

The normalized frequency of an optical fiber, V, determines the number of modes guided by an optical fiber:

$$V = \frac{2\pi R_{\text{core}}\text{NA}}{\lambda} = \frac{2\sqrt{2}\,\pi\sqrt{\Delta}\,R_{\text{core}}\,n_{\text{clad}}}{\lambda}, \tag{1.6}$$

where R_{core} is the core radius and λ is the wavelength. For $V < 2.405$ an optical fiber is single-mode, otherwise it is multimode. The wavelength at which $V = 2.405$ is termed the cutoff wavelength, λ_{c}, since that is the wavelength at which the first higher order mode is cutoff from propagation. As V increases, the number of guided modes increases as well. A single-mode fiber with a large normalized frequency can be thought of as a *strongly guiding* fiber while a fiber with a small V can be thought of as a *weakly guiding* fiber. From (1.6) we see that the light is guided more strongly by fibers with a larger core radius, larger Δ, larger NA, or smaller λ_{c}.

The *mode field diameter* (MFD) is a measure of the diameter of the optical beam propagating in a single-mode fiber. The MFD of a single-mode fiber typically scales with the core diameter. Standard SMF has an MFD of about 10.5 μm at 1550 nm. NZ-DSF typically has a smaller MFD while the MFD of EDF is smaller still. A fiber with a smaller MFD is more vulnerable to core misalignments than a fiber with a larger MFD. The MFD of some fibers, such as DCF, is wavelength dependent in order to achieve desirable wave guiding characteristics.

Polarization-maintaining optical fibers are similar to standard SMF except that their refractive index profile is birefringent. In other words, light with one particular linear polarization state propagates at a higher speed than light with the orthogonal polarization state. Some fibers have an elliptical rather than circular core to achieve this birefringence. More often, the cladding contains regions of glass, termed stress-applying members (SAM), with very different mechanical properties from the rest of the cladding. The stress-applying members create a stress field in the fiber which in turn causes birefringence. There is an added burden of aligning the SAM when fusion splicing these fibers to ensure that there is no energy exchanged, or crosstalk, between the orthogonal polarization states traveling through the fiber. Fusion splicing of PM fibers is detailed in Sect. 9.2.

Microstructured fibers are recently developed fibers containing air holes or voids running along the length of the fiber. Air- or vacuum-filled voids provide a very large contrast in refractive index compared to silica glass ($\Delta \sim 33\%$). The voids can even be filled with a polymer or a metal to produce waveguides with unique characteristics. Some microstructured fibers also contain dopants as in a conventional fiber. Fusion splicing these fibers can be particularly challenging since the heat from splicing can locally collapse the voids which can have a significant impact on the splice loss. Fusion splicing these revolutionary new types of optical fibers are detailed in Sect. 9.5.

1.3.2 Material and Mechanical Characteristics of Silica Fibers

The material properties of optical fibers are central to the physics of fusion splicing and result from their molecular structure. With a few notable exceptions, all contemporary optical fibers are fabricated from high-silica glasses also termed *vitreous silica*. Glass is an *amorphous material* meaning that it is a material that does not exhibit any long-range structural order in the manner of a crystalline material [1.8]. Silica glass is comprised of tetrahedral molecular structures linked at their vertices to form a three-dimensional network [1.9]. This ordered arrangement of tetrahedra extends for only a few molecules: over long distances the material appears randomly ordered.

Some physical characteristics of high-silica glasses that are particularly important to optical fiber fusion splicing include viscosity, surface tension, dopant diffusion, thermal expansion/contraction, and brittleness. Unlike a crystalline substance, glasses do not exhibit a well-defined transition between their solid and liquid states. Instead, the surface tension, viscosity, density, and other physical properties of a glass vary smoothly over a large temperature range. Moreover, the physical properties of a glass depend, in part, on its thermal history.

The viscosity of high-silica glass decreases exponentially with increasing temperature. In order to form a fusion splice, the fiber must be softened, meaning that its viscosity must be reduced to a certain value (typically about 10^5 Poise) by heating it above 2000° C. Very few heat sources can raise a silica fiber to such high temperatures while confining the heat to the very tips of the fibers. The so-called "electric arc discharge" is the most prevalent heat source used in commercial fusion splicers. Alternative heat sources include a resistively heated tungsten filament, a CO_2 laser, or an oxy-hydrogen flame. Some discussion of these various heat sources appears in Chap. 10.

At splicing temperatures, surface tension is the dominant force driving the flow of glass, and it is resisted primarily by the viscosity of the glass. Surface tension can act as either friend or foe during the splice process. It tends to align the cladding of the two fibers to each other, which in many cases improves the alignment of the fiber cores and thus reduces splice loss. However, in some cases the fiber tips may be deliberately offset to compensate for eccentricity between the core and cladding in which case surface tension will attempt to suppress the offset, thus misaligning the fiber cores and increasing splice loss. The role of surface tension during fusion splicing is discussed in Sect. 3.2.

The refractive index of an optical fiber is primarily determined by the concentration of chemical dopants. The most common optical fiber dopants are germanium (Ge), which raises the refractive index of the silica glass and fluorine (F), which lowers it. Other common dopants include phosphorus (P), erbium (Er), aluminum (Al), and boron (B). Dopants not only alter the refractive index of the silica glass, but also alter its thermal and mechanical properties. At splicing temperatures dopants can diffuse through the silica

glass host. Different dopant species diffuse at different rates: for example fluorine diffuses more rapidly than germanium. Dopant diffusion can radically alter the refractive index profile of the fibers in the vicinity of the completed splice. As with surface tension driven flow, this effect may be beneficial or deleterious. In some cases, such as when splicing erbium-doped amplifier fiber to standard SMF, the dopant diffusion can make the transition between dissimilar fiber types more gradual, and thus reduce the splice loss. In other cases, especially when splicing fibers heavily doped with fluorine, diffusion can increase splice loss. This issue is explored in detail in Sect. 3.3.

Stresses and strains can arise in the vicinity of a fusion splice because the viscosity and thermal expansion coefficient of the glass depends upon the dopant concentration. These stresses and strains can affect the fiber's refractive index profile as well as its mechanical strength. If the thermal expansion coefficients of two fibers are sufficiently different, a fusion splice between them will fall apart as the fiber cools down from splicing temperatures. These issues are discussed in detail in Sect. 3.4.

Glasses are brittle materials, meaning their primary failure mode is fracture rather than plastic deformation as is the case for ductile metals or plastics. The theoretical ultimate tensile strength of vitreous silica can be estimated from the amount of energy required to break the molecular bonds holding the material together. Using this method, the theoretical maximum strength of a vitreous silica sample with no cracks or surface flaws is about 20 GPa [1.8, 1.9]. The practical fracture strength of silica fibers is primarily controlled by the surface condition of the fiber [1.9]. Small imperfections on the surface of optical fibers serve as nucleation site for crack growth. Hydroxyl ions (OH) are known to accelerate crack growth in silica so humidity is thought to contribute to a reduction in the mechanical strength of optical fibers and fusion splices [1.10]. Short lengths of most practical optical fibers exhibit a failure stress of about 5.5 GPa, which is equivalent to about 800 kpsi (kpsi=kilopounds force per square inch, a common unit in the optical fiber industry). For a 125 μm diameter fiber, this failure strength corresponds to an axial load corresponding to almost 7 kg force, or a theoretical minimum bend diameter of less than two millimeters!

Proper handling of optical fibers is an important and often overlooked aspect of optical fiber fusion splicing because even the tiniest surface scratches can prevent a fusion splice from meeting strength requirements. The splicing process itself can introduce new imperfections to the surface of an optical fiber also reducing its failure strength. Moreover, failure strength can sometimes serve as an indicator of a fusion splice's long term reliability [1.11]. For terrestrial applications, fusion splices are proof tested to ensure they can survive a 100 kpsi proof test. Undersea applications demand more stringent splice reliability requirements so a higher threshold, such as 200 or 235 kpsi, is mandated. Splice strength and reliability is discussed in great detail in Chap. 6. The brittle nature of optical fibers also has a significant impact on how fibers are cleaved to obtain planar end faces for splicing. The details

of optical fiber cleaving are discussed in the next chapter. Optical fibers are coated with a polymer to protect their surfaces from scratches that would reduce their strength and reliability. The removal and restoration of these protective coatings are discussed in Chaps. 2 and 6 respectively.

In high power applications, such as in fiber lasers, small particles or dirt and/or losses at a joint between fibers can initiate a peculiar phenomenon termed *fiber fuse* [1.12]. During fiber fuse, the core of an optical fiber is damaged in a spectacular vaporization phenomenon that propagates back through the fiber towards the source at velocities on the order of 1 m/s. High quality optical fiber fusion splices are critical to high power applications to help suppress the likelihood of fiber fuse initiation.

The polymer coating protecting the glass fiber has certain mechanical characteristics that can also affect fusion splicing. The polymer coating typically exhibits a phenomenon termed *curl* meaning that in the absence of any applied forces, the coated optical fiber takes on a curved shape. This happens because the polymer coating has a certain amount of shape-memory and coiling the fiber around a spool imparts curl to the coating. The radius of fiber curvature is a measure of the amount of curl. A curl radius larger than a few meters has little impact on fusion splicing. However, when the curl radius is on the order of a meter or less, fixturing and aligning the fibers will be very difficult. Some manufacturers market equipment for straightening coating curl with a heat treatment. A typical minimum specification for fiber curl radius is 4 meters. Such stringent curl specifications are critical to achieving low-loss fusion splices between the fibers comprising a multiple fiber ribbon.

The glass fiber itself can exhibit a certain amount of curl which has the same negative impact on fiber fixturing and alignment as coating curl. This curl does not stem from wrapping the fiber around a spool but rather from asymmetries in the fiber fabrication process. Encountering curl in the glass is rare but can occur in prototype or research-grade optical fibers. Unfortunately, curl in the glass cannot be repaired in the manner of coating curl.

1.4 Alternatives to Fusion Splicing

Fusion splicing is not the only way to join together two optical fibers: *free-space coupling*, *mechanical splices*, and *connectors* are important alternatives. Free-space coupling refers to using conventional bulk glass lenses and mirrors to focus light down to a small spot and couple it into or out of optical fibers. Free-space coupling is obviously not practical for telecommunications systems in the field, but is extensively used in research laboratory environments. Free-space coupling is very flexible and can readily interconnect dissimilar optical fibers. However, free-space coupling can exhibit relatively high reflectance and requires tedious alignment. Moreover, dust or other contamination can find its way into the optical path and can lead to damage, especially during high-power operation.

A mechanical splices is a permanent connection between two optical fibers that does not have thermally welded joint as in a fusion splice [1.13–1.16]. The lack of a thermally welded joint can be an advantage, for example when splicing together fibers fabricated from two materials that are thermally incompatible, such as silica glass and fluoride glass fibers (Sect. 3.4.1).

In a mechanical splice, two cleaved fiber tips are mechanically aligned to each other by a special housing. Usually, index matching gel is positioned between the fiber tips to maximize coupling and minimize reflectance. Unfortunately, the refractive index of most index matching compounds varies with temperature so the optical performance of a mechanical splice can be sensitive to ambient temperature. Mechanical splices can be constructed relatively quickly without the need for expensive specialized equipment such as a fusion splicer. However, mechanical splices are not thought to be as reliable as fusion splices over long periods of time and exhibit higher loss than fusion splices. Partly for these reasons, mechanical splices are no longer widely used in the industry [1.17]. Mechanical splices are generally used only in relatively benign environments such as inside an office building.

Connectors are special devices attached to the end of optical fibers that can easily be coupled or uncoupled to other connectors or devices. Connectors are required when a fiber must be periodically disconnected, for example for testing or switching purposes. Connectors are typically used at the termination points of optical fiber cables, such as at the transmitter or receiver. They are also employed on test and measurement equipment, at the interfaces between networks, on patch panels where signals may be routed through different pathways, and inside office buildings.

Many different connector designs tailored to the characteristics of specific fiber types and their applications have been introduced over the years. Most connectors require the fiber tip to be epoxied inside a ceramic ferrule and then polished. Many connectors require the polished ferrule to have a special geometry, such as an angle or a radius, in order to minimize reflectance and maximize coupling efficiency. Installing a connector to the end of an optical fiber is typically more time-consuming than either a fusion splice or a mechanical splice [1.18]. Some connectors, such as polarization-maintaining (PM) fiber connectors, are keyed to ensure that the rotational orientation of the fiber is correctly aligned at the joint. There are even connectors for twelve fiber ribbon cable.

Although they can be easily coupled and uncoupled, connectors typically exhibit higher loss and reflectance than either fusion splices or mechanical splices. Connectors can induce modal noise or multipath interference (MPI) because of their higher reflectance and loss. Connector losses range from about 0.05 dB to 0.5 dB between similar fibers and even higher if the fibers exhibit different guiding properties. Connector loss can change with temperature fluctuations or mechanical shock and they are less stable over time than fusion splices. Finally, connectors are more vulnerable to damage during high-power operation than fusion splices.

In summary, fusion splices are generally more compact, exhibit lower loss, lower reflectance, and are more reliable than free-space coupling, mechanical splices or connectors. However, fusion splicing equipment is relatively expensive and consequently is only cost-effective when amortized over a large number of fusion splices. In contrast to fusion splices which are permanent, to some extent mechanical splices, and especially free-space coupled fibers and connectors, can be readily disconnected and reconnected.

1.5 Fusion Splices in the Optical Network

The contemporary optical network is an engineering marvel. Recent research has suggested that the ultimate carrying capacity of an individual optical fiber is on the order of 100 Tb/s [1.19] which is about 30 times higher than the actual carrying capacity of the most advanced optical fiber systems at the time of writing. There are many different types of optical networks, categorized as single-mode or multimode, and as analog or digital. Optical pathways can span thousands of kilometers as in an undersea optical network or just meters as in a local area network. Although optical fiber fusion splices are just one building block of these optical communication networks, they are a ubiquitous one. Fusion splices are present throughout the installed base of transmission fiber as well as inside devices and components such as dispersion-compensating modules and optical amplifiers.

The location of fusion splices in a contemporary dense wavelength-division-multiplexing (DWDM) long-haul optical fiber link is depicted in Fig. 1.8a. A typical erbium fiber amplifier contains dozens of fusion splices (Fig. 1.8b) connecting many different fiber types.

The large number of fusion splices in worldwide optical communication networks is apparent from the large market for optical fiber fusion splices. The total commercial market for fusion splicers was US$233 million in 2002 [1.20] and is expected to grow robustly over the next decade. In 1999, about half of the world's fusion splicers were sold in North America while about one quarter were sold in the European and Asian markets respectively. By 2007 this market is expected to grow to nearly half a billion US$. Much of this growth is expected to occur in Japan and the Pacific Rim regions [1.20].

In high-bandwidth optical fiber transmission systems, multiple fibers are packaged in protective cables, sometimes as many as several hundred in a single cable. Fusion splices may be already included in the cabled fiber by the cable manufacturer. Other fusion splices link cables together at intervals that can range up to 10 km. The constituent fibers of a cable must be exposed in order to be spliced and the spliced fibers are fixtured in splice trays. Up to several splice trays are protected in a splice housing which is often designed to be weatherproof and waterproof [1.21] (Fig. 1.9). This enclosure system organizes the fibers, facilitates identification, and provides convenient

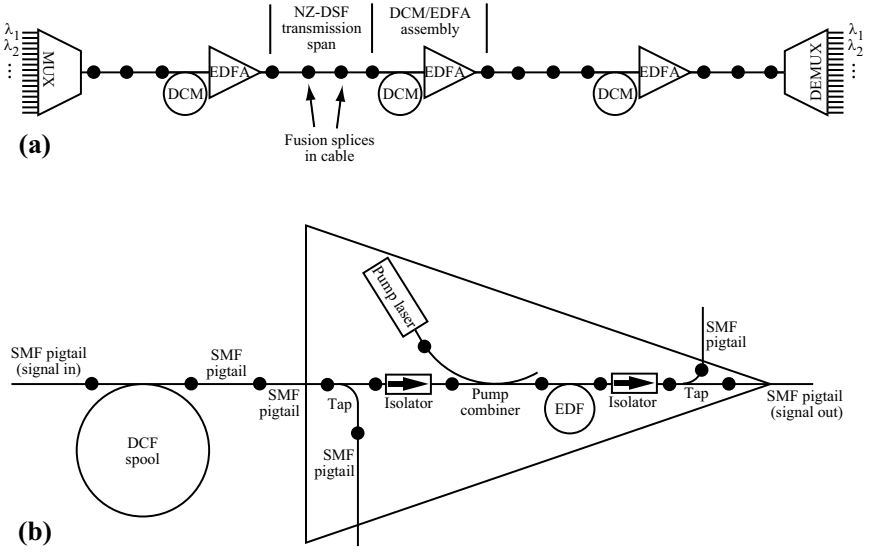

Fig. 1.8. Simplified illustration of the ubiquitous nature of fusion splices in a long-haul DWDM optical network. Dark filled circles indicate fusion splice locations. **(a)** Simplified view of entire system. MUX = wavelength multiplexer, DEMUX = wavelength demultiplexer. **(b)** Close-up of simplified dispersion-compensating module (DCM) and simplified erbium-doped fiber amplifier (EDFA) assembly. The *pump laser* is the power source for optical amplification. A *pump combiner* mixes the pump laser output with the optical signal. An *isolator* prevents optical signals from propagating in the backward direction (to the left). *Taps* siphon off small amounts of optical signal for monitoring and control. High quality fusion splices involving erbium-doped fiber (EDF) can be particularly challenging to fabricate

access [1.17]. During an optical fiber installation, fusion splices may need to be made in harsh environments under adverse conditions.

The emergence of ribbon fiber has significantly increased the efficiency and lowered the cost of field fusion splicing. Modern ribbons consist of up to 24 individual fiber strands, which can all be simultaneously fusion spliced by a ribbon fiber fusion splicer. Fusion splicing can comprise much of the cost associated with optical fiber deployment so the ability to fusion splice so many fibers in a single operation with a single instrument is a particular advantage.

The performance of an optical fiber communications system depends on the signal-to-noise ratio (SNR) that in turn depends on the optical losses in the system. Splice losses reduce the SNR and thus increase the bit-error-rate (BER) in digital communication systems. The optical fiber network is designed with a *loss budget* that takes into account losses stemming from fiber attenuation and splices, as well as gain provided by optical amplifiers [1.22].

The contribution of splices to the loss budget largely depends on the nature of the network design. In traditional long-distance fiber networks em-

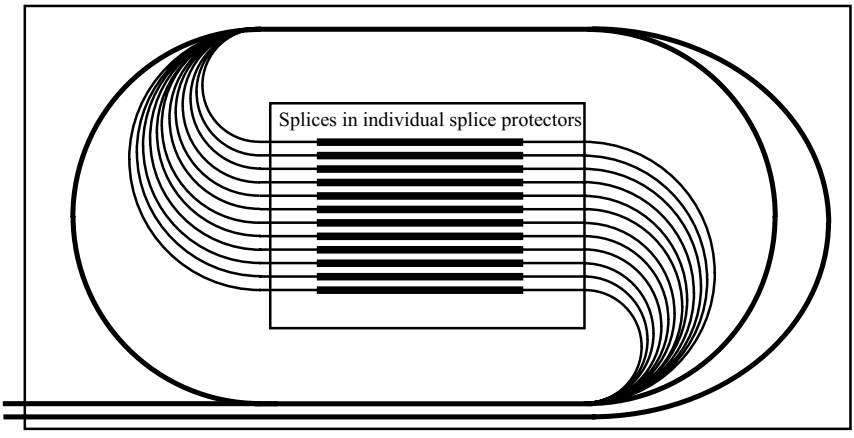

(a)

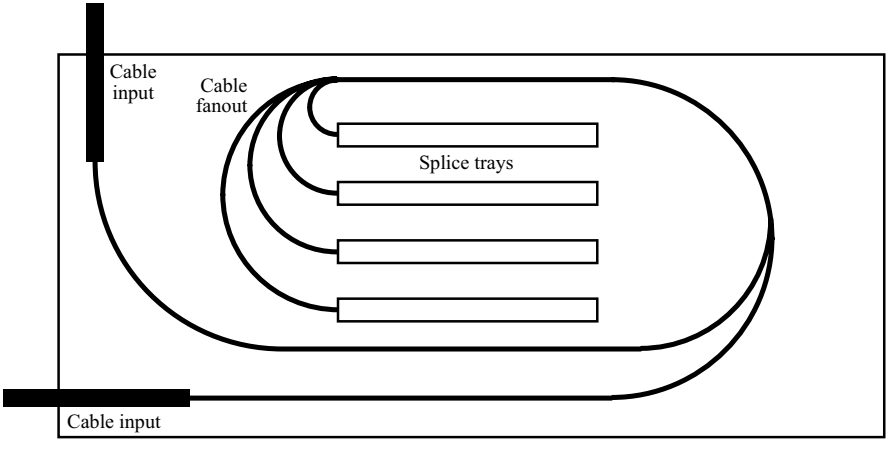

(b)

Fig. 1.9. Schematic illustration of enclosure system for protecting field splices [1.21]. **(a)** Splice tray showing arrangement of splices linking multiple fibers. Fibers are routed in and out of the splice tray at the bottom left. **(b)** Splice housing containing multiple splice trays. After [1.21]

ploying standard single-mode fiber (SMF), splices are spaced several kilometers apart. Under controlled laboratory conditions, SMF can be consistently spliced with less than 0.01 dB of loss. However, a variety of extrinsic factors including weather, operator skill, and the condition of the splicing equipment can increase average field splice loss to as much as 0.1 dB. Assuming a spacing of 4 km between splices, and a fiber attenuation of 0.2 dB/km at 1550 nm, the splice losses contribute about 10% percent to the total loss budget. In a

long-distance standard SMF system, the vast majority of span loss originates in the fiber attenuation.

More modern long-distance optical fiber networks utilize non-zero dispersion shifted fiber (NZ-DSF) which also has attenuation around 0.2 dB/km at 1550 nm but average field splice losses as high as 0.15 dB. Splice loss accounts for a larger fraction of the loss budget, perhaps as much as 15%, for such NZ-DSF systems. Future long-distance optical fiber networks may employ dispersion-engineered spans in which a span is constructed from alternating sections of two distinct fiber designs in order to achieve a low path-averaged dispersion. Splice losses between these distinct fiber designs can exceed 0.25 dB so splice losses will play an even greater role in the loss budget.

In shorter reach systems, such as metropolitan-area networks, shorter cable lengths result in more frequent fusion splices and so contribute a larger fraction to the loss budget and also a larger fraction to the installation cost than in long-distance systems.

Attenuation of the optical signal isn't the only potential problem associated with fusion splicing. The portion of the optical signal "lossed" at a single-mode fusion splice can be scattered into a higher order mode that can propagate for a short distance. If a second lossy splice is located in close proximity, the optical signal guided in the higher order mode can be recoupled back into the fundamental mode where it interferes with the original optical signal. This phenomenon is termed *modal noise* and it can be minimized with high quality fusion splices. Interference can also result when multiple reflections occur between two highly reflective splices in close proximity. This phenomenon is termed *multipath interference (MPI)*. MPI can be a particularly difficult problem in systems employing connectors since they typically exhibit higher reflectance and loss. Fortunately, fusion splices exhibit extremely low back reflection and very low optical losses so MPI is usually not a serious problem. Interference noise phenomena such as MPI and modal noise reduce the SNR and thus increase the BER. These deleterious effects can also be expressed as *power penalties*, or extra loss in the loss budget, since increasing the signal strength, and hence the SNR, is one way of coping with interference noise [1.22].

The effect of fusion splices on multimode optical fiber communication systems can be particularly confusing. In contrast to the behavior of single-mode fiber splice, the loss of a multimode fiber splice can depend on its proximity to other splices. This is because a splice can scramble the distribution of optical power amongst the various modes, and splice loss partly depends on this power distribution. Even stranger, fusion splices between multimode fibers can, in rare cases, increase the bandwidth of the overall multimode fiber span if the fusion splice induces a more favorable distribution of power amongst the modes [1.17,1.23]. Multimode and single-mode fusion splice loss, as well as modal noise and MPI, are discussed in more detail in Chap. 4.

Field installers rely on both loss estimation provided by their splicing equipment during installation, and measurements acquired with optical time-

domain reflectometers (OTDRs) after installation to ensure that their splices meet the system specifications determined in the loss budget. Loss estimation is based on images of the completed splice and can give the installer an estimate of the actual splice loss. Not only must the loss estimation process be reasonably accurate, but the acceptance criteria for individual fusion splices must be appropriately set to maximize yield during network installation while minimizing the need to replace occasional high-loss fusion splices [1.24–1.27].

OTDR loss measurements are used since they can locate splices and accurately measure splice loss in installed fiber from many kilometers away. The completed splice is often strength tested to ensure it meets mechanical reliability requirements. Loss estimation, OTDR measurements, and strength testing are beneficial since replacing a defective splice requires service interruption and is expensive. Loss estimation is discussed in detail in Chap. 5 while splice loss measurement and OTDRs is discussed in Chap. 7.

Splices are not only present in the transmission cables of an optical network, but also inside various optical fiber devices that are situated at the terminus of transmission spans. For example, modern optical fiber networks rely heavily on dispersion compensating fiber (DCF). Multiple kilometer lengths of DCF are wound onto a spool that is terminated at both ends with "pigtails" of SMF. Since the DCF fiber design is very different from the SMF design, splice losses between DCF and SMF are usually several tenths of a dB. Needless to say, these splice losses make an impact on the overall system loss budget and minimizing them is important.

Over the years, various standards bodies have issued a plethora of standards and requirements for optical fiber fusion splices. Some of the major standards bodies concerned with fusion splicing include Telcordia (formally Bellcore), the Telecommuncations Industry Association (TIA), International Electrotechnical Commission (IEC, also known as CEI), the International Telecommunications Union (ITU), and the European Telecommunications Standards Institute (ETSI). These standards and requirements pertain to fiber preparation equipment (cleavers and coating strippers), fusion splicing equipment, splice protectors as well as fusion splices themselves. Specifications detailed in these standards include temperature and humidity tolerance, maximum permissible splice loss, proof test strength requirements, loss estimation accuracy requirements, and equipment safety requirements. Appendix C lists several published standards for the benefit of the interested reader.

1.6 A Brief History of Fusion Splicing

The first optical fiber fusion splices were performed soon after the development of optical fibers themselves. Much of the fundamental research concerning fusion splicing was conducted in the 1970's on early silica and non-silica single- and multimode fibers. Simple loss prediction models, basic fiber prepa-

ration techniques, various heat source options, and certain packaging issues were investigated during that time period.

The first documented optical fiber fusion splices were performed by Bisbee at Bell Laboratories [1.28] only one year after researchers at Corning achieved a milestone by fabricating an optical fiber with less than 20 dB/km attenuation [1.29]. Bisbee's initial fusion splicing study was tremendously influential and it detailed all the major issues relevant to fusion splicing. Bisbee proposed numerous techniques that are now standard practice in optical fiber fusion splicing. He recognized that proper preparation of the fiber tips is critical to fabricating a low-loss splice. He proposed controlled fracture of the fiber, now termed cleaving, as a convenient way of obtaining suitably planar end faces. He also proposed using a system of mirrors to permit orthogonal views of the fiber tips for fiber alignment, and this strategy is now standard on all fusion splicing equipment. Bisbee's splices were heated with resistive nichrome wire, which was able to generate enough heat to splice his relatively low-temperature glass fibers. The optical losses of these pioneering multimode fusion splices were measured to be as low as 0.5 dB [1.28].

Two years later, researchers in the UK performed the first fusion splice of single-mode fibers fabricated from low-temperature glasses [1.30]. This group recognized the extreme importance of fiber alignment for achieving low-loss single mode fibers. Following Bisbee, resistively heated nichrome wire served as the heat source. The best case splice losses were on the order of 0.5 dB as was the case for the earlier multimode fiber fusion splices.

In 1973, Bell Labs researchers documented the first optical fiber cleaver designed to take advantage of brittle fracture to obtain extremely flat fiber end faces [1.31]. The utility of this cleaving device was apparent when butt-coupling losses as low as 0.04 dB were achieved with multimode fibers.

When it became apparent that high-purity silica glass was the preferred material for optical fibers on account of its low attenuation, higher temperature heat sources were sought out. Inspired by laser fiber drawing of silica-based optical fibers done at Western Electric Co. [1.32], researchers at Hitachi in Japan turned to a CO_2 laser in 1976 [1.33]. This heat source provided sufficiently high temperatures for fusion splicing the highest temperature fibers, but the bulky and expensive CO_2 laser systems available at that time were only appropriate for laboratory splicing.

During the same period, researchers at Corning Inc. suggested the use of an electric arc discharge to splice silica fibers [1.34]. Researchers at Corning, Bell Labs, and NTT immediately reported on the new arc fusion splicing technique [1.34–1.36]. Bisbee documented multimode fiber splice losses as low as 0.03 dB with this technique which nearly matches contemporary multimode splice losses [1.34]. Meanwhile, Jocteur and Tarday documented the first flame-heated fusion splicing [1.37]. Bisbee introduced the idea of recoating a splice with polymer to safeguard its surface from scratches [1.34]. Kohanzadeh recognized the possibility of simultaneously splicing multiple fibers with a single electric arc [1.35].

In 1977, Marcuse published a seminal paper describing how the splice loss of a single mode fiber depends on geometric misalignments [1.38]. This description of splice loss was simplistic but laid the foundation for future splice loss estimation research. In 1983, White and Puhl applied coupled mode theory to optical fiber splice loss and obtained a theoretical model that could estimate splice loss based on deformations of a single mode fiber core [1.39]. This result served as the basis for many future commercial loss estimation routines.

The first mass fusion splices of optical fiber ribbon cable was performed with a CO_2 laser by Kinoshita and Kobayashi in 1979 [1.40]. However, the fibers could only be spliced one at a time. Tachikura followed the lead of Kohanzadeh by simultaneously splicing five multimode fibers with an electric arc in 1981 [1.41].

In the early days of optical fiber fusion splicing, most researchers assumed that it was impossible to achieve a fusion splice whose failure strength matched that of the original fiber. However in 1985, Krause and Kurkjian of Bell Labs reported fabricating single-mode fiber splices whose failure strengths were just as good as the unspliced fiber [1.10]. This result was achieved using an oxy-hydrogen flame as the heat source in conjunction with chlorine gas to suppress the deleterious effects of water vapor on fiber strength. Although their approach was not practical outside the laboratory, it demonstrated the amazing possibility of fabricating fusion splices that were both mechanically and optically indistinguishable from the original fiber. In the mid-1990s, Berg and Johansen achieved similar results using a more practical electric arc fusion splicer [1.42].

During the 1980's a variety of commercial fusion splicing equipment was introduced. Most of these fusion splicers used an electric heat source but others employed metal filaments. Significant efforts were made to understand splice strength and reliability as the first optical fiber communication links were introduced into service.

In the 1990's a wide variety of specialty fibers such as erbium-doped gain fiber, dispersion-compensating fiber, and microstructured fiber were introduced. Each of these specialty fibers came with their own unique challenges and a variety of specialty fiber fusion splicing strategies were developed. It seems assured that future developments in optical fiber technology will continue to push the frontiers of optical fiber fusion splicing as they have for the past 30 years.

1.7 The Frontiers of Fusion Splicing

Optical fiber fusion splicing is an area of active research and development because it is so critical to modern communications networks. Important developments are underway in research laboratories, factory fusion splicing, and even field installation fusion splicing. A search of the United States Patent

Office database (available at http:\\www.uspto.gov) reveals that hundreds of patents related to optical fiber fusion splicing have been issued over the past several years.

Field splicing evolves along with the optical fiber cables themselves. Fiber cable manufacturers are increasing the fiber content of their cables and splicer manufacturers are responding by designing mass fusion splicers that can splice more fibers at a time. State of the art mass fusion splicers can simultaneously splice fiber ribbon cable containing 24 individual fibers. Improving splicing quality and consistency while reducing the cost of splicing equipment and the time required to complete a splice is an important focus of research.

The driving force for change in the factory environment is the need to reduce costs while improving quality and consistency. One way to satisfy this need is to increase the level of automation thus reducing human involvement in the fusion splice process. Much of the variation in the quality of fusion splices stems from human handling of the fibers before and after the actual splice itself. For example, an operator can easily reduce the ultimate strength, and hence the reliability, of a fusion splice by inadvertently touching the bare fiber. Poor cleave quality resulting from human operation of the cleaving equipment contributes to fusion splice loss. Automation can avoid these sources of inconsistency. Furthermore, automation can reduce costs by performing the tasks comprising the fusion splice process faster than a human operator.

Most contemporary splicing hardware automatically aligns the fiber tips, splices them together, and evaluates the quality of the resulting fusion splice but it does not automatically prepare the fiber tips. Several fusion splice manufacturers have recently marketed fully automatic fusion splicers which prepare the fiber tips, fusion splice them, and package them. The general approach has been to integrate several fiber processing stations, each of which performs a single task from fusion splice process (Fig. 1.1). In some systems, the stations are automatically transported to the fibers, in others, the fibers are transported from station to station. Some fully automatic fusion splicing systems can simultaneously process several fibers and can fusion splice as many as two fibers every minute. A human operator is still required to lace fibers on a pallet which is then fed into the fully automatic fusion splicer. A representative fully automatic fusion splicing system is discussed in Chap. 10.

Nearly all businesses are connected by broadband data links, and highly aggregated data streams are all transmitted over optical fiber. However, the "last-mile" in modern communications networks, the link between central offices and private homes, is typically not a broadband connection. Part of the reason is the high cost associated with installing fiber-to-the-home (FTTH also known as fiber-to-the-premises, FTTP). At the time of writing, various solutions for providing FTTH are under consideration. The potential of the FTTH market is driving the development of low-end low-cost optical fiber fusion splicing technologies [1.43].

The frontiers of fusion splicing are shaped by the evolution of fiber designs. Multimode and standard single-mode are older fiber designs and contemporary splicing hardware is quite capable of obtaining high quality results with these fiber types. Dispersion shifted fiber, erbium-doped gain fiber, dispersion-compensating fiber, and polarization-maintaining fiber represent the current state-of-the-art in fiber design and can be effectively fusion spliced with contemporary equipment in most cases. However, some of these specialized fiber designs are extremely difficult to splice. Achieving low-loss splices with such fibers is an area of active, and often very proprietary, research.

Great progress has been made in the development of plastic optical fibers [1.44,1.45]. In contrast to silica glasses, polymer optical fibers can be cut with a sharp blade, simplifying fiber tip preparation. Certain polymer fibers can be fusion spliced in a manner similar to silica based fibers, although at much lower temperatures [1.46,1.47]. In one instance, plastic fibers were fused by a metal filament in a quartz mold at temperatures of about 180° C [1.46] with losses on the order of 0.5 dB. However these splices were relatively weak. Higher splice strengths and lower splice losses were achieved by fusing plastic fibers inside a tube of poly-ether-ether-ketone (PEEK) [1.47]. Another option for fusion splicing of polymer optical fibers is "chemical splicing." Polymethylmethacrylate (PMMA) plastic optical fibers can be chemically fused at room temperature with solvents that dissolve the plastic and produce a fused joint with losses as low as 0.2 dB [1.48].

Microstructured fibers may very well fill important new roles in fiber devices and might even serve as long-haul transmission fiber. These fibers pose particularly unique and difficult problems for fusion splicing. Commercialization of these fibers will no doubt have a profound impact on the future evolution of fusion splicing technology. The future of optical fiber may very well lie with microstructured fiber or perhaps even non-silica based optical fiber, which pose even greater challenges.

1.8 Summary

An optical fiber fusion splice is a permanent welded joint between two optical fibers that exhibits minimal optical loss and reflectance with long-term reliability rivaling the fibers themselves. Such fusion splices are ubiquitous in the optical communications network, connecting together transmission fibers as well as specialty fibers inside optical fiber devices. Fusion splicing technology has been around almost as long as the optical fibers themselves. Fusion splicing is becoming increasingly important as novel high-performance optical fibers and optical fiber devices are developed. Future developments in fusion splicing technology will likely involve increased levels of automation, the emergence of the metro and fiber-to-the-home (FTTH) markets, and novel fiber designs and materials.

2. Fiber Preparation and Alignment

As we learned in Chap. 1, optical fiber fusion splicing is comprised of many steps aside from heating the fiber tips to form a welded joint. Prior to actually forming a joint, the fiber tips must be specially prepared. Nearly all silica optical fibers are coated with a protective polymer material that must be removed, or *stripped*, prior to fusion splicing. Following stripping, the fiber tips must be *cleaved* in order to obtain planar end faces suitable for fusion splicing. These preparatory steps are usually performed by instruments separate from the fusion splicer that actually forms the splice joint. Once the tips are prepared, they must be *aligned* to each other in preparation for joint formation. Over the past three decades, both fiber preparation and fiber alignment have evolved along with optical fibers themselves.

One might assume that fiber preparation for fusion splicing is relatively unimportant compared to the actual joint formation, loss estimation, or splice packaging. Previous treatments of optical fiber fusion splicing have indeed overlooked fiber preparation. However, certain aspects of fiber preparation are of critical importance since they significantly impact both the optical quality and the long-term reliability of the resulting fusion splice. For example, the cleave quality is a major contributor to geometric deformation in a fusion splice, and this geometric deformation is often a dominant factor controlling the splice loss (see Chaps. 4 and 5). The stripping process is often the dominant factor controlling the ultimate tensile strength of the resulting splice, which in turn determines the long-term reliability of the splice (see Chap. 6).

In this chapter we present a general introduction to optical fiber stripping, cleaving, and alignment technology applied to fusion splicing. More specific information is available in the numerous references cited throughout the chapter.

2.1 Stripping

The fundamental motivation for stripping the coating from a fiber prior to fusion splicing is that the high temperatures experienced during joint formation will damage polymer coatings and possibly damage the heated portion of glass contacting the coating. Furthermore, alignment of the fiber is more

accurate when gripping on the bare glass surface because the dimensional tolerances of the glass are usually far superior to that of the polymer coating. Finally, optical fiber coatings often exhibit shape memory, known as *curl*, which can complicate fiber alignment (see Sect. 3.2.1).

However, the stripping process can reduce the fiber's mechanical strength and long-term reliability by degrading the pristine glass surface [2.1, 2.2]. Furthermore, bare silica fiber can easily incur new strength-reducing surface flaws. Finally, any splice package or protector must be at least as long as the length of stripped fiber. For these reasons, fusion splicers are designed to work with a minimum length of stripped fiber, which typically ranges from about 5 mm to about 20 mm when measured from the cleaved tip.

The ultimate tensile strength of a fusion splice is closely correlated with its long term mechanical reliability (see Chap. 6), and this tensile strength is often directly determined by the details of the stripping process. The ultimate tensile strength of as-drawn, coated, 125 µm diameter fiber is about 57 N, which is equivalent to about 5.5 GPa or 800 kpsi (kpsi stands for kilopounds force per square inch, a common industry unit) of tensile stress. Stripping can reduce this tensile strength by as much as, and sometimes even more than, an order of magnitude. Furthermore, any coating residue left on the glass fiber's surface can interact with the heated fiber during joint formation leading to significantly lower tensile strength and reduced long term reliability.

Coating removal technologies can be broadly organized into three categories: (1) mechanical and thermo-mechanical stripping, (2) chemical stripping, and (3) vaporization techniques (which include laser- and flame-based techniques). Generally speaking, chemical and vaporization techniques are essential for high-strength fusion splices. However, they also require more expensive and more complicated hardware, and may pose serious safety hazards. Thus, most field splicing, and a good deal of laboratory and factory splicing, is performed with the aid of mechanical and thermo-mechanical stripping. As more production fusion splicing is automated, chemical, and especially vaporization techniques are becoming more common.

In this section we will provide an introduction to optical fiber stripping for fusion splicing. We begin our treatment with a discussion of common optical fiber coating designs. We then discuss each of the three major categories of stripping. For the interested reader, a comprehensive and up-to-date review of optical fiber cable construction and coating removal is available in [2.3].

2.1.1 Fiber Coatings

An analysis of the stripping process requires an understanding of the optical fiber coating itself. An optical fiber's coating design obviously depends on the fiber's application. For example, connectorized optical fiber cable jumpers and patchcords are typically endowed with several robust polymer layers, as well as a Kevlar yarn layer, to endure frequent handling. In contrast, a specialty fiber, such as erbium-doped fiber (EDF), is usually not designed to withstand

much handling or environmental stress, so it is typically available as a single strand with only a soft 250 micron diameter acrylate coating. Ribbon fiber consists of several individual coated fiber strands held together in a linear arrangement by a soft polymer binder. Some specialty multimode fibers have pure silica cores directly coated with a low refractive index polymer that also serves as the optical cladding.

Despite this wide variety, coatings of fibers designed for fusion splicing share some common features. The innermost polymer coating is nearly always a relatively soft, UV-cured, urethane acrylate, which exhibits a refractive index higher than that of silica in order to strip out and attenuate unwanted light. This acrylate coating consists of one or two distinct layers (Fig. 2.1). If there are two layers, the inner acrylate layer, known as the *primary* coating, is very soft in order to minimize microbend losses [2.3, 2.4], and has an outer diameter of about 180 μm. The outer layer, known as the *secondary* coating, is a harder acrylate, thus providing better abrasion resistance. The outer diameter of the entire acrylate coated fiber is usually 250 μm, although specialty fiber coatings can be as large as 400 μm. When the glass fiber itself is only 80 μm in diameter, the outer diameter of the acrylate coated fiber is also smaller, often on the order of only 150 μm.

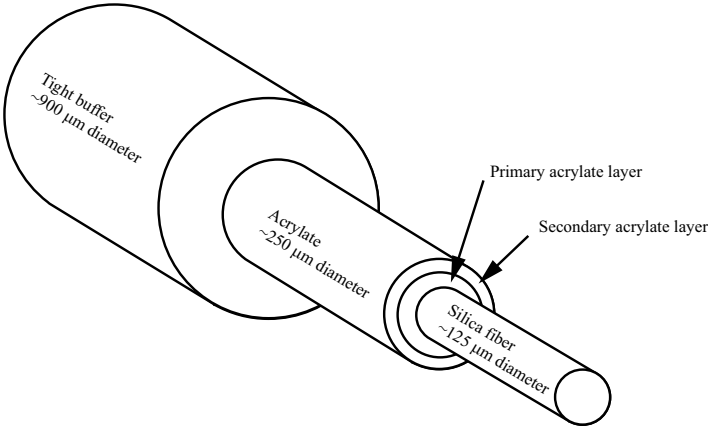

Fig. 2.1. Schematic illustration of typical polymer coating architecture for single stranded fiber. Figure not to scale

The individual strands comprising a ribbon fiber are also usually coated with a dual acrylate layer, and the strands are bonded together by an acrylate polymer matrix (Fig. 2.2). These relatively soft polymer materials facilitate the stripping process.

In addition to the innermost coating layers, some fibers have additional layers of polymer, termed *buffer* layers. One common additional layer is the *tight buffer*, which can exhibit an outer diameter ranging from 500 to 1000 μm

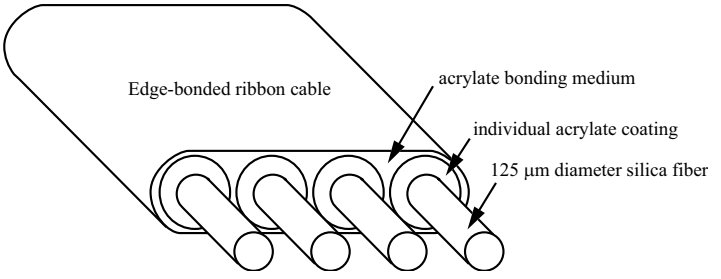

Fig. 2.2. Schematic illustration of an edge-bonded ribbon fiber. After [2.3]

but is usually 900 μm. Tight buffer coating is a hard plastic (much harder than acrylate) that tightly grips the underlying acrylate and usually must be removed in conjunction with the acrylate underneath. As its name suggests, *loose buffer* differs from tight buffer in that it does not tightly grip the underlying acrylate layers, so it can be removed without damaging the underlying acrylate.

Optical fiber coatings are often color coded to facilitate identification. This is especially true in ribbon fiber cables. The coloring agent in the coating usually does not affect the stripping process, but in some cases, such as when TiO_2 is used as a coloring agent and chemical stripping is performed, stripping conditions must be modified to maintain high tensile strength [2.5].

One alternative to the usual acrylate coatings is a single layer of only 10 μm of polyimide coating. Polyimide is attractive for some extreme applications because of its stability at high temperature. Some polyimide coated fibers can withstand temperatures as high as 300° C for long periods of time and 400° C for short durations. However, polyimide coatings are much more difficult to remove, and are generally only found on certain specialty fibers.

Some large diameter (200 μm or more) multimode silica fibers are coated with a hard, low refractive index polymer, which can serve as both a coating and an optical cladding. The coatings of these *hard clad silica* fibers, commercially known as HCS^{TM} or $TECS^{TM}$, improves fiber strength and abrasion resistance so these fibers can often be cabled without Kevlar yarn. Moreover, connectors can usually be mechanically attached directly to the hard coating, facilitating connectorization. Like polyimide coatings, hard plastic coatings are difficult to remove so these fibers are usually intended to be connectorized, rather than fusion spliced.

Individual coated transmission fibers are often packaged into cables, which often exhibit a complex architecture and can include hundreds of individual fiber strands. The interested reader is referred to [2.3, 2.6, 2.7] for a detailed treatment of such transmission cables, and how they are prepared for splicing.

Some specialty silica fibers are fabricated with a thin layer of amorphous or crystalline carbon on the outer surface of the glass cladding just underneath the innermost polymer coating [2.3, 2.8]. This carbon layer is called a

hermetic coating since it is designed to prevent hydrogen or water molecules from diffusing into the fiber from the ambient environment. These hermetic coatings have been shown to improve the mechanical fatigue characteristics of optical fibers. Hermetic carbon coatings cannot be removed by mechanical means. However, heating the fiber to a high temperature can remove the carbon coating and the very high temperatures experienced during fusion splicing will naturally remove the carbon coating in the vicinity of the fusion splice and therefore also permit visualization of the fiber core and loss estimation [2.8].

2.1.2 Mechanical and Thermo-Mechanical Stripping Techniques

Mechanical and thermo-mechanical techniques are by far the most commonly employed methods to strip the coating from optical fiber in preparation for fusion splicing. These techniques are inexpensive, fast, and applicable to a fairly wide variety of coating designs (with the notable exception of polyimide and hard clad silica). Both mechanical and thermo-mechanical stripping can be performed with relatively inexpensive hand-held tools. Nearly all field splicing utilizes mechanical or thermo-mechanical stripping. A large segment of factory or laboratory fusion splices are also prepared with these techniques.

As their names suggest, mechanical and thermo-mechanical stripping involve cutting into the coating with a hard tool to fracture the coating, and then translating the tool along the fiber to peel the coating from the fiber and push it off the surface [2.4]. When the coating is relatively rigid, the coating will delaminate from the glass fiber's surface. When the coating is made from a softer polymer, such as the primary coating of a dual acrylate coating, it may leave a residue of coating adhering to the glass fiber's surface. Generally speaking, dual acrylate coatings require less force to mechanically or thermo-mechanically strip the fiber than single acrylate coatings [2.4].

Many mechanical fiber stripping tools closely resemble wire stripping tools, and share the same principle of operation (Fig. 2.3). The initially coated fiber is usually pulled through a tiny aperture, which contains sharp surfaces that cut through the coating. Unlike in a conventional wire stripping tool, the aperture in a optical fiber stripping tool is carefully designed to minimize the possibility that it will contact the vulnerable glass surface and damage it. Conventional wire stripping tools *cannot* be used to strip optical fiber as they will scratch the glass surface making the fiber fragile.

Thermo-mechanical stripping is a variant of mechanical stripping in which an electric heater softens the polymer coating to facilitate removal. The heat from a thermo-mechanical stripping tool can also help to straighten a fiber exhibiting a large amount of coating curl. Thermo-mechanical stripping is particularly attractive when the coating consists of a single acrylate layer. When the fiber has a dual acrylate coating, the softer inner layer is more easily separated from the glass surface, so mechanical stripping usually suffices.

Fig. 2.3. Common optical fiber mechanical stripping tool applied to standard single-mode fiber with a standard 250 μm diameter dual layer acrylate coating

Thermo-mechanical stripping is commonly used to strip ribbon fiber, which is usually designed with a soft, easily stripped acrylate coatings. Even ribbons containing as many as 12 or 24 individual fibers can be stripped down to the bare glass with relatively little force with the aid of a suitable thermo-mechanical stripping tool. However, the tensile force applied to the ribbon cable during thermo-mechanical stripping is proportional to the number of fiber strands in the cable so large forces are required to thermo-mechanically strip 24-fiber ribbon cable [2.9].

In another variant of mechanical stripping that is very similar to chemical stripping, the fiber coating can be briefly soaked in a solvent, such as methylene chloride (also known as dichloromethane or methylene dichloride), which causes the coating to soften and to swell, thus facilitating mechanical stripping [2.10]. However, the need for such a solvent, which may be toxic, makes this variant less convenient and less common than other forms of mechanical stripping.

When the fiber is coated with a tight buffer as well as an acrylate coating, a thermo-mechanical stripper can be used to simultaneously remove the tight buffer and the acrylate coating. The fiber chucks of many commercial fusion splicers are designed to accommodate tight-buffered fiber. Alternatively, special tools employing sharp razor blades can sometimes remove the tight buffer without damaging the underlying acrylate coating.

Mechanical stripping usually leaves some amount of coating residue on the glass surface of the fibers. This results from the fact that the stripping aperture cannot physically contact the glass surface or it would significantly reduce the fiber's mechanical strength. Any coating residue remaining on the fiber can interfere with the fiber chucks, the splicer's image-processing based

fiber alignment process, or can be baked into the fiber surface during joint formation, thus weakening the mechanical strength and long term reliability of the resulting splice. Coating residue on the fiber surface should be removed with some kind of cleaning solvent. Organic solvents such as alcohol, acetone, or even methylene chloride are used to wash away coating residue. Ultrasonic agitation of a solvent bath is a common strategy to accelerate residue removal. Alternatively, wiping the fiber with a solvent soaked swab or tissue can effectively remove coating residue, at the expense of introducing surface defects which will significantly reduce the mechanical strength of the resulting splice.

Another significant disadvantage of mechanical or thermo-mechanical stripping is that it will always induce some degradation of the fiber surface thus weakening the fiber's mechanical strength and also its long term reliability. Mechanical and thermo-mechanical strippers are designed to minimize the severity of this effect. When operated properly, a high quality mechanical stripping tool, such as the one depicted in Fig. 2.3, can yield tensile strengths of about 3.5 GPa (500 kpsi) when applied to a standard 250 μm outer diameter dual-acrylate coating on a 125 μm diameter silica fiber. However, this requires skill and careful attenuation to the process.

2.1.3 Chemical Stripping Techniques

Chemical stripping involves the use of an aggressive solvent to remove the polymer coating of the fiber. Chemical stripping is attractive since, unlike mechanical stripping, it does not require mechanical forces that cause defects on the fiber surface leading to strength and reliability degradation. Moreover, chemical stripping is effective for nearly all optical fibers, including polyimide coated and hard clad silica. However, most of the chemicals are toxic, and some are even flammable. Thus chemical stripping does not lend itself to field splicing, but has been frequently employed in the laboratory or factory environments, especially when extremely high tensile strength and mechanical reliability is required. Chemical stripping requires on the order of one minute of processing time, which is longer than mechanical or vaporization stripping techniques.

Sulfuric acid, or a mixture of sulfuric and nitric acid (for example 95% H_2SO_4 and 5% HNO_3 by weight), heated to about 200° C is the most common solvent for chemical stripping [2.5,2.10,2.11]. Hot acid is particularly effective for stripping hard clad silica or polyimide fiber coatings, which are otherwise very difficult to strip. Typical acid baths require about 30 seconds of soaking to completely remove a 250 micron outer diameter acrylate coating from a 125 μm fiber. At lower temperature or at higher pH, the processing time is significantly lengthened. To achieve the best possible stripping performance, the acid must be changed when it becomes heavily contaminated by dissolved coating material [2.1]. Acid stripping poses many serious safety hazards and

the working environment must be well ventilated (for example by fume hood) to ensure the safety of the operator.

Some papers have claimed that hot-acid stripping actually degrades the strength of the fiber, but recent work has refuted that claim [2.10]. Soaking a fiber in a clean hot acid bath for long amounts of time (multiple minutes) does not appear to degrade the fiber's mechanical strength [2.10]. In fact, Krause and Kurkjian showed that fusion splices exhibiting no measurable reduction in tensile strength compared to the original as-drawn fiber could be fabricated with acid stripping [2.12].

Methylene chloride (also known as dichloromethane or methylene dichloride) is an alternative to acid for removing acrylate coatings. Several minutes soaking in methylene chloride can soften acrylate coatings to the point that they may be readily peeled off the fiber intact. However, like hot acid, methylene chloride poses serious safety risks as it is a suspected carcinogen and is also flammable. Some solvents, especially methylene chloride, can wick up long lengths of fiber causing the primary coating to separate from the glass.

Although chemical stripping usually leaves no coating residue, a final rinse step is necessary to ensure no solvent remains on the fiber. Depending on the stripping solvent, water, acetone, or alcohol are commonly employed as rinse agents.

2.1.4 Vaporization Stripping Techniques

A number of vaporization stripping techniques have recently been developed and commercialized so they are viable alternatives to chemical and mechanical stripping. In these techniques, the coating material is removed from the fiber by high temperatures. Vaporization techniques are very fast, avoid dangerous solvents, minimize the amount of force applied to the fiber, minimize the amount of coating residue, and often maximize the surface quality of the resulting stripped fiber. However, the hardware required for vaporization-based fiber stripping is substantial, which precludes field splicing applications. Vaporization stripping techniques are well suited to automated splicing applications in a factory setting.

Most fiber coatings are flammable and can actually be removed through combustion in an oxygen atmosphere (including ambient) in a process sometimes termed *flame stripping*. However, burning off the coating significantly reduces the tensile strength of the stripped fiber, to an even greater extent than mechanical stripping. When hot acid is unavailable, a flame or some other high temperature heat source, is the only effective way to remove polyimide or hard clad silica fiber coatings.

Scanning a hot jet of gas over a coated fiber is one of the most common vaporization techniques [2.11, 2.13–2.16]. The temperature of the gas jet is on the order of several hundred degrees Celsius, which is much higher than the maximum temperature the coating can withstand, but still much lower than the softening point of the optical fiber itself. Hot gas jet coating

removal has been attributed to explosive thermal stresses in the coating material by one source [2.16] and rapid dehydration by another [2.11]. After the gas jet stripping process (but prior to fusion splicing) the tensile strength of a standard 125 μm diameter fiber has been cited to be on the order of 5 GPa (700 kpsi) [2.11, 2.14, 2.16], which is nearly as strong as the virgin fiber (5.5 GPa or 800 kpsi).

In another technique, termed *thermo-vacuum vaporization* (TVV) [2.17, 2.18] the coating blows off after being heated for a few seconds while held under vacuum. The fiber strengths following TVV are also quite impressive, on the order of 4 GPa (600 kpsi) [2.17] for a standard 125 μm diameter fiber.

Tightly focused laser beams have also been used to remove coating from optical fibers. This type of coating removal process is also termed *laser ablation*. The laser wavelength must be strongly absorbed by the coating to be effective. Frequency doubled copper vapor lasers as well as UV-emitting excimer or far-IR emitting CO_2 lasers have been used to strip coating from optical fiber [2.19–2.21].

2.2 Cleaving

Optical fiber fusion splicing nearly always requires that the fiber tips exhibit a smooth end face that is perpendicular to the fiber axis. A sufficiently perpendicular and planar fiber end face can be achieved via a process termed *cleaving*, in which the brittle glass fiber is fractured in a controlled manner. As we shall see, cleave quality is an important factor controlling fusion splice loss. High quality cleaves are essential when fusion splicing challenging specialty fibers such as erbium-doped fiber (EDF) or dispersion-compensating fiber (DCF).

Polishing a fiber tip can result in even higher quality fiber end faces, but polishing requires more expensive equipment and more processing time, so it is very rarely employed for fusion splicing. However, polishing is commonly used for fabricating optical fiber connectors.

A wide variety of cleaving instruments are now commercially available. Some cleavers are intended for field splicing applications while others are geared for laboratory or factory environments. Some ribbon fiber cleavers can simultaneously cleave all 24 individual optical fibers comprising a high fiber count ribbon [2.9]. Automated fiber preparation systems, including automated fiber cleavers, are now commercially available as well. Cleavers are available for non-standard optical fiber diameters, which can range up to and beyond 1 mm.

Excellent treatments of optical fiber cleaving are available in [2.22–2.24]. The physics of fiber fracture, with an emphasis on mechanical reliability, are discussed in Chap. 6, and especially in Sect. 6.2. In this section we will provide a practical introduction to fiber cleaving for fusion splicing.

2.2.1 Cleaving Techniques and Hardware

An optical fiber is cleaved by applying a sufficiently high tensile stress in the vicinity of a sufficiently large surface crack, which then rapidly expands across the fiber cross section at the sonic velocity. (Fig. 2.4). This idea has many different practical implementations in a variety of commercial cleaving equipment. Some cleavers apply a tensile stress to the fiber while scratching the fiber's surface with a very hard scribing tool, usually a diamond edge. Other designs scratch the fiber surface first, and then apply tensile stress. Some cleavers apply a tensile stress that is uniform across the fiber cross section while others bend the fiber through a tight radius, producing high tensile stresses on the outside of the bend. Cleave tension is commonly specified in grams of force rather than Newtons. A typical high performance cleaver is shown in Fig. 2.5.

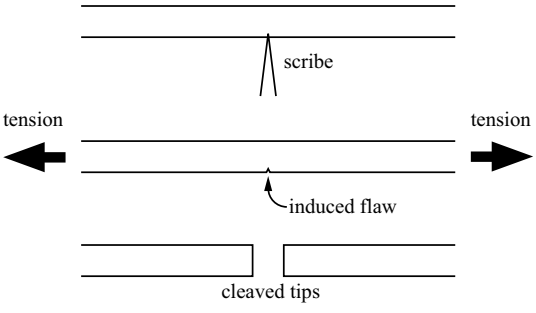

Fig. 2.4. Schematic illustration of scribe-and-tension strategy for cleaving optical fibers

Commercial instruments for simultaneously cleaving all the fibers in a ribbon fiber are also widely available. These ribbon fiber cleavers operate on the same principles as single fiber cleavers. The average cleave quality of a ribbon cleaver is somewhat inferior to that of a single fiber cleaver.

2.2.2 Basic Cleaving Principles

Despite the variation in cleaver design, some basic principles apply to all. The fracture face resulting from a cleave consists of three regions, termed *mirror*, *mist*, and *hackle* [2.22]. These regions are schematically depicted in Fig. 2.6 and photographed in Fig. 2.7a. The mirror zone, which is optically smooth, is produced first as the crack propagates across the fiber. As the crack propagates further away from the initiation site, it forks into multiple crack fronts and hackle results. The hackle is a rough surface that is undesirable for fusion splicing. Mist is the transition region between the mirror zone and the hackle zone.

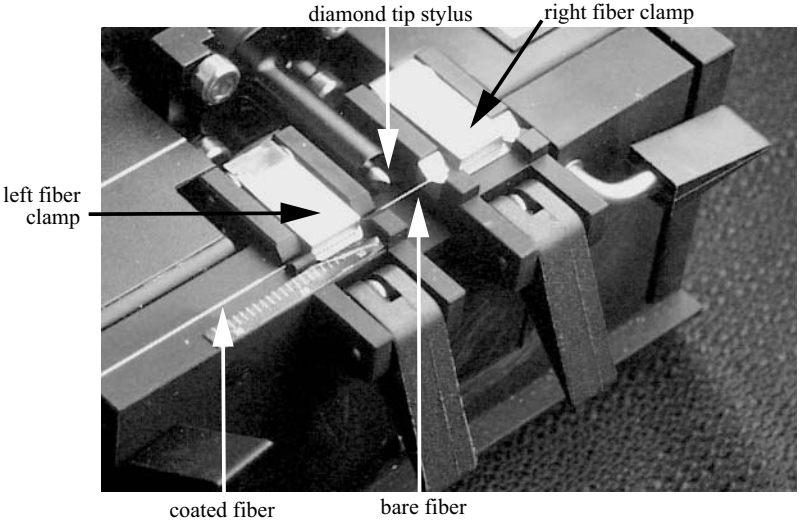

Fig. 2.5. Close-up of the *York FK-11* cleaver which is a typical high performance factory or laboratory optical fiber cleaver. Note the diamond tip stylus which is touched against the tensioned fiber to produce an initial crack which leads to a cleave. Typical cleave angles for this type of cleaver are less than 0.5°

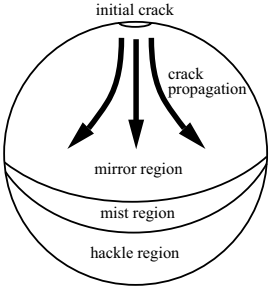

Fig. 2.6. Illustration of different zones associated with cleaving

A high quality optical fiber cleave requires that there be no hackle and minimum mist. The boundary of the mist region is governed by [2.22]

$$\sigma_{\mathrm{a}}^2 D_{\mathrm{mist}} = K_{\mathrm{fract}}^2 \ , \tag{2.1}$$

where σ_{a} is the locally applied tensile stress, D_{mist} is the distance from the crack initiation site to the mist boundary, and K_{fract} is a constant determined by the material. The applied tensile stress, σ_{a}, can be approximated as the cleave tension divided by the fiber's cross sectional area.

The cleave tension must be low enough to ensure that the entire cross sectional area of the fiber falls within the mirror region. When a cleave exhibits hackle, excessive cleave tension may be to blame. However, insufficient

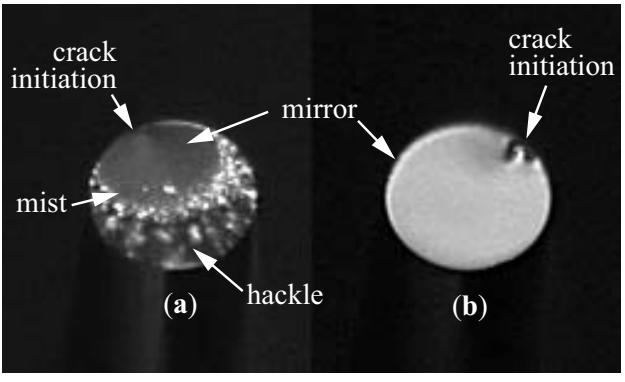

Fig. 2.7. Comparison of two 125 μm diameter cleaved fiber tips viewed with a 0.1 NA 5× microscope objective illuminated obliquely: (**a**) 300 g cleave tension and (**b**) 200 g cleave tension. Note the significant amount of hackle and mist apparent in (**a**) and the nearly complete mirror surface in (**b**)

cleave tension can lead to an angled fiber end face, as discussed in the next Subsection. Furthermore, insufficient cleave tension requires that the initial crack be very large, and this large initial crack may itself comprise a defect in the end face of the final cleaved fiber. The relationship between the stress required to fracture a fiber and the initial crack size is described by crack growth theory and is discussed in Sect. 6.2. Crack growth theory suggests that when a 125 μm diameter fiber is cleaved at a conventional cleave tension of about 200 g force, the initial crack length is on the order of several microns. This is consistent with published studies of initial crack geometry [2.24].

If the distance between the initial crack and mist initiation, D_{mist}, is set equal to the fiber diameter, then (2.1) can be manipulated to show that proper cleave tension approximately scales with the fiber diameter raised to the 3/2 power. If the optimal cleave tension for conventional 125 μm diameter silica fibers is taken to be about 200 g, this scaling law can be used to predict the cleave tension appropriate for other fiber diameters, such 80 μm diameter fibers which require a cleave tension of about 100 g. Figure 2.8 shows how optimal cleave tension varies with silica fiber diameter.

Optical fibers designed to exhibit abrasion resistance are much harder to cleave than regular fibers. The formation of the initial crack during cleaving can be thought of as a form of abrasion. An example of an abrasion resistant fiber is *Corning Titan*^{TM} fiber whose outer cladding is comprised of a TiO_2/SiO_2 glass mixture. One explanation for the difficulty of cleaving this fiber is that the low thermal expansion coefficient of the TiO_2/SiO_2 glass induces residual thermal compressive stresses on the outer surface of the fiber [2.25, 2.26]. Residual compressive stresses on the surface of an optical fiber reduce the amount of tensile stress available for crack growth, thereby inhibiting fracture.

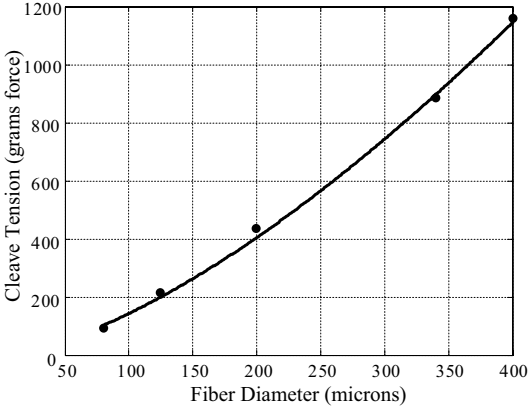

Fig. 2.8. Optimal cleave tension for silica fibers scales with the fiber diameter raised to the 3/2 power. The experimentally observed optimal cleave tensions (*solid circles*) agree with a theoretical prediction based on (2.1). (*solid line*)

Optical fibers with significant amounts of draw-induced residual compressive stress (see Sect. 3.4) on the outer surface of the cladding are also difficult to cleave. For example, fibers drawn at high tension with a low-viscosity glass, such as a heavily fluorine-doped layer, are very difficult to cleave [2.27]. In this case, there will be draw-induced residual compressive stress (see Sect. 3.4) on the outer surface of the fiber that will make it very abrasion resistant and hence difficult to cleave.

2.2.3 Cleave Defects

Since fracture is such a violent and difficult to control process, even the best commercial cleaver will periodically yield defective cleaves. Some common types of cleave defects are depicted in Fig. 2.9. A *lip* (Fig. 2.9a) is a projecting spike of glass at the periphery of the fiber tip. Lips can be a serious problem when they are more than a few microns long, which is enough to interfere with the ability to gap the fibers. Generally a fiber should be re-cleaved when it exhibits a lip that is visible in the magnified image of a fusion splicer.

A *chip* (Fig. 2.9b) is an absent section of glass on the periphery of the cleaved fiber tip. Small chips are often of no consequence. Larger chips represent a deficit of material that will induce surface tension to shear the molten glass at the fiber tip, thus distorting the splice geometry. Cleaved tips exhibiting a chip visible in the magnified image of a fusion splicer should be recleaved.

Any torsion of the fiber during the cleave will result in an *angle* (Fig. 2.9c). This is because a crack will propagate in a direction perpendicular to the local principal tensile stress [2.29, 2.30]. Torsion of the fiber causes the principal stresses of the fiber to be angled with respect to the fiber axis. Angled end

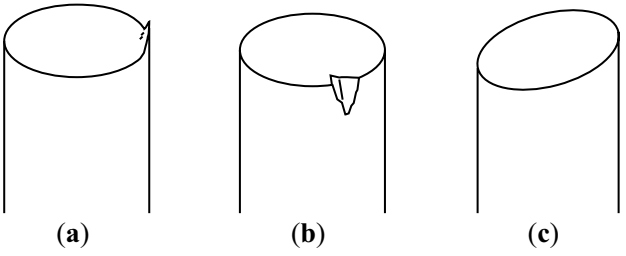

Fig. 2.9. Illustration of three common cleave problems: (**a**) lip, (**b**) chip, (**c**) angle. After [2.23, 2.28]

faces are a clue that the cleaving instrument is inadvertently applying torsion to the fiber; often the fiber clamps are the culprit. Excessively low cleave tension can result in an angled cleave since even small amounts of torsion can significantly alter the direction of the principal stresses. Angled fiber end faces are useful for suppressing reflectance in optical fiber terminations. Fusion splices exhibit such low reflectance (usually less than 60 dB) such that angled cleaves are unnecessary.

Most commercial fusion splice equipment include image processing routines which can measure the end face angle of the fiber tips in two orthogonal axes and abort the splice if the angles exceed a preset threshold. More accurate measurements of fiber end angle, and the topography of the fiber end face, can be performed with an interferometer [2.28]. Convenient, portable hand-held interferometric cleave checkers are commercially available and can be used to measure the discarded portion of the cleaved fiber thus avoiding any contamination of the cleaved fiber tip. Fig. 2.10 depicts some representative interferograms of cleaved fiber tips. When the absolute lowest loss fusion splices are required, cleaved tips can be screened with an interferometric cleave checker.

When a substantial portion of the cross sectional area of an optical fiber is comprised of regions of glass with very different mechanical properties, achieving a defect free end face can be very difficult. This is a common problem with polarization-maintaining (PM) fibers because they typically include large areas of glass with very different mechanical properties and also significant residual stresses. The sonic velocity varies in the different regions so the cleave does not propagate evenly across the end face of the fiber. These issues are discussed in more detail in Sect. 9.2.

2.2.4 The Importance of Cleave Quality

The impact of cleave quality on the quality of the resulting fusion splice should not be underestimated. Deficiencies in a fiber cleave are one of the most common causes for geometric deformation in the resulting splice, which are particularly onerous for single-mode fiber. Much of the variation in splice

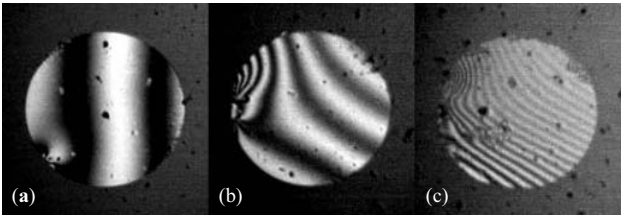

Fig. 2.10. Interferograms of 125 μm diameter optical fiber cleaves obtained using the handheld *Norland Cleave-Chek Interferometer*. (**a**) High quality cleave with an end angle of about 0.3°. The cleave initiation site is visible on the bottom left edge of the fiber. (**b**) More typical cleave with an end angle of about 0.5°. The cleave initiation cite is visible on the left edge of the fiber, as is a small chip on the fiber end face. (**c**) Poor quality cleave with an end angle greater than 2°. Dirt on the reference optical flat is visible in all three interferograms. The operating wavelength of this interferometer is about 650 nm so each degree of end face angle corresponds to about 7 fringes

loss observed between different splices fabricated using the same splice parameters is due to variation in cleave quality.

There are several ways in which a poor cleave can reduce the quality of the resulting splice. It can compromise the performance of image processing routines that perform fiber alignment. Cracks in the fiber's end face (Fig. 9.3) can lead to a bubbles at the splice joint, which usually requires the splice to be remade.

Furthermore, if the end face of the opposing fiber tips are angled with respect to each other, there will usually be a deficit of glass material when the fibers are brought together during the hot push. This deficit of material typically induces shearing of the molten glass, resulting in significant core deformation (Fig. 2.11). One way to reduce the deleterious effects of excessive cleave angles when splicing standard single-mode fiber (SMF) is to use relatively long heating times which encourages surface tension to minimize core deformation [2.31]. However, this strategy is less effective on specialty fibers such as erbium-doped fiber (EDF) or dispersion-compensating fiber (DCF).

Determining a threshold cleave quality for a given fusion splice depends on the fiber designs, the splicing equipment, and the loss requirements. For standard single strand single-mode fiber, typical cleave quality requirements are end face angles less than 1° with minimal lips or chips [2.31, 2.32]. Since cleaving ribbon fiber is more challenging, the maximum cleave angle is often specified to be on the order of 3 or 4° [2.32]. High quality low-loss fusion splices of single-mode fiber, especially fiber exhibiting a small mode field diameter (MFD), will generally require a tighter specification of 0.5°. However, if the cleave requirements are too severe, the cleave yield will be very low and an individual splice will require excessive time to fabricate.

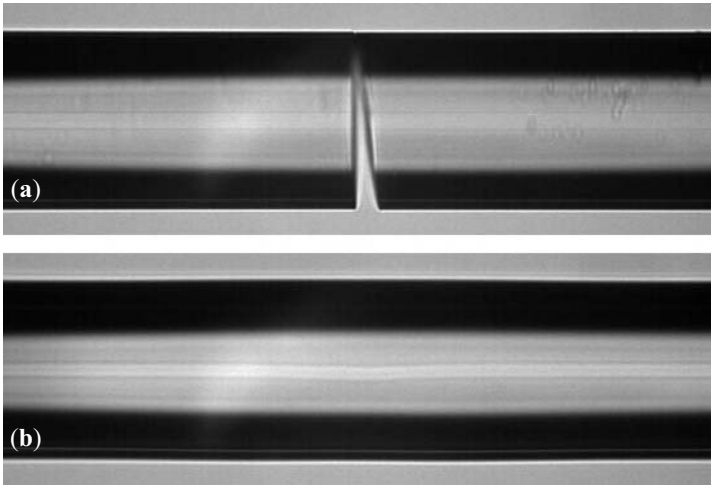

Fig. 2.11. Illustration of the effect of cleave quality on an optical fiber fusion splice showing two fiber tips (**a**) before splice during alignment and (**b**) after splice. The cleave angle of the right fiber tip was about 5°. The geometric deformation of the core evident in the figure induced about 0.25 dB loss at 1550 nm

2.3 Alignment

Once the fiber tips have been prepared, they must be accurately aligned to each other so that the resulting fusion splice exhibits optimal optical performance, which is commonly defined as low loss and minimal reflectance. As we shall see in this section, several strategies are available for aligning optical fibers.

In the earliest days of optical fiber technology, single-mode fibers were considered to be of questionable value since aligning two 10 μm diameter fiber cores to form a joint was thought to be too difficult. These concerns were quickly dispelled by the first generation of optical fiber fusion splicing equipment.

Most modern fusion splicers grip the optical fiber tips within some form of v-groove. These v-grooves may grip onto the stripped portion of glass, or onto the polymer coating. Gripping on the glass can permit a more precise alignment than gripping on the polymer coating since the glass usually exhibits less curl and is not compliant. On the other hand, gripping on the glass can induce surface defects that reduce the tensile strength and hence the long-term reliability of the fusion splice (Chap. 6). Normally the axes of the v-grooves are parallel to each other, but a high quality optical fiber fusion splice usually requires that the fiber tips be actively aligned to each other. This alignment normally occurs in the two orthogonal transverse axes. In addition, specialty fibers such as polarization-maintaining (PM) fiber and microstructured fiber require rotational alignment as well (Chap. 9). It is

important to note that surface tension effects can significantly alter fiber alignment, as discussed in Sect. 3.2.

In this section we will survey both passive and active strategies for aligning optical fibers in preparation for fusion splicing. The specific details of these alignment strategies depend on related topics, such as the optics of fusion splices, splice loss measurement, and fiber imaging, which are discussed in Chaps. 4, 5, and 7 respectively.

2.3.1 Passive Alignment

The simplest fiber alignment strategy is termed *passive alignment*, and as its name suggests, it requires no active intervention by the operator or the fusion splicer. A passively aligned fusion splice relies on the accurate pre-alignment of fiber v-grooves that grip the outer surface of the fiber tips. The advantages of passive alignment include extremely low cost, simplicity, and speed.

However, passive fiber alignment is characterized by several important disadvantages. Passive fiber alignment requires the fiber tips to exhibit extremely low core eccentricity, low curl, and a well controlled cladding diameter. Passive fiber alignment is less effective when the fiber core diameter is very small, since such fibers are more sensitive to small core misalignments. Passive alignment will not function properly when either the v-groove or the fiber surface is contaminated by dirt.

For these reasons, passive alignment is only found on earlier generation fusion splicing machines or on lower cost field fusion splicers or mass fusion splicers. Nearly all contemporary optical fiber fusion splicers employ some form of active alignment.

2.3.2 Image-Based Active Fiber Alignment

The most common strategy for performing fiber alignment is image-based active fiber alignment in which a microprocessor activates fiber positioners based on a digital image of the fiber tips obtained with the aid of an imaging system comprised of an illumination source, a microscope objective, and a digitizing camera [2.33–2.36] (see Fig. 5.2 and Sect. 5.1). Such an alignment system is obviously more expensive and complex than a passive alignment system, but it is much more powerful and flexible, capable of compensating for small amounts of fiber curl, core eccentricity, dirty fibers or v-grooves, and cladding diameter variations. Moreover, as we shall see in Chap. 5, the same imaging system used for fiber alignment can serve as the basis for loss estimation of the completed splice.

Image-based active fiber alignment systems can align the fiber tips based on the fiber cladding position. Many fusion splices can even use the image of the fiber cores to align the fiber tips. This is termed a *profile alignment system (PAS)* since it aligns the fiber tips based on their refractive index profiles.

However, as we shall learn in Sect. 3.2.3, surface tension effects during fusion splicing can corrupt fiber alignment based on the detected core position.

Contemporary mass fusion splicing systems commonly use image-based active fiber alignment. However, the alignment system does not actively align each individual fiber strand comprising the ribbon. Instead, the individual fiber strands comprising a ribbon are gripped in a substrate containing fixed v-grooves. The two opposing substrates are actively aligned with each other based on the averaged position of the detected fiber claddings (Fig. 2.12). Since this scheme depends on the fiber cladding for alignment, core concentricity and cladding diameter stability can have an important impact on the resulting fusion splice loss.

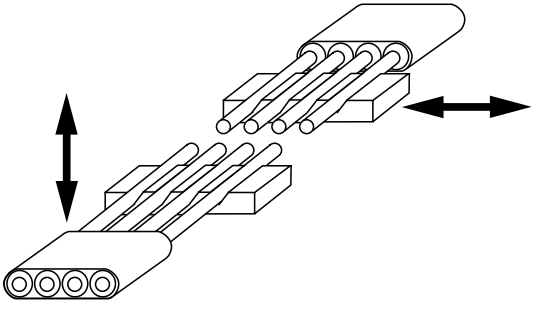

Fig. 2.12. Schematic illustration of a common mass fusion splicer alignment scheme. All the strands of a ribbon fiber tip are simultaneously gripped by fixed v-grooves in a substrate. The two opposing substrates are aligned to each other in two orthogonal axes (indicated by the heavy arrows) by micropositioners. Typically an image-based active alignment system detects the surface of each fiber's cladding and actively aligns the two substrates by minimizing the average cladding misalignment of the individual fiber strands. For the sake of clarity, the figure depicts a ribbon cable with only four fibers, but contemporary ribbon fibers consist of as many as 24 individual fiber strands

Polarization-maintaining (PM) are not rotationally symmetric so high quality fusion splices involving these fibers usually require that the two fiber tips be rotationally aligned to each other. This type of alignment is nearly always performed using image-based alignment systems. Most equipment aligns these fibers based on transverse images but some equipment can align these fiber tips based on endview images of their cleaved end faces. Issues concerning PM fiber alignment are discussed in Sect. 9.2.

2.3.3 Transmitted-Power Based Active Fiber Alignment

Instead of relying on CCD images of the fiber tips, the fiber tips can be actively aligned by monitoring the amount of optical power transmitted across

a small air gap (Fig. 2.13). Transmitted-power based active alignment inherently involves a measurement of optical loss, which is described in greater detail in Chap. 7.

Active alignment systems include an optical source, such as a laser diode (LD) or a light-emitting diode (LED), that is coupled into the free end of one fiber, and an optical power meter that detects the amount of power emitted by the free end of the other fiber. A microprocessor programmed with an appropriate algorithm moves the fiber positioners to the location of maximum transmitted power, which is assumed to be the optimal fiber alignment. Unfortunately, active alignment can lead to alignment errors resulting from imperfect cleave angles, which refract the light as it traverses the air gap between the fiber tips so that the alignment with maximum transmitted power may not correspond to alignment of the fiber cores.

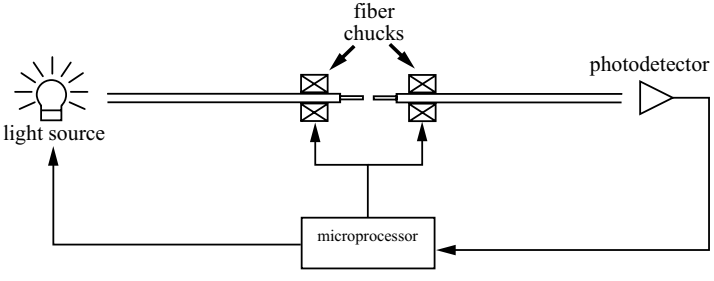

Fig. 2.13. Schematic illustration of a generalized transmitted-power based active alignment system. The arrows denote the flow of control to or from the microprocessor

Monitoring the transmitted power can also be used to determine when joint formation is completed, or when dopant diffusion has minimized the splice loss [2.37, 2.38] (dopant diffusion is discussed in Sect. 3.3). However, if the optical source used for alignment is relatively weak or if the power meter is a broadband detector, the inherent blackbody infrared emission of the heated fiber tips can affect the transmission loss measurement. Active alignment is most often used when fusion splicing erbium-doped amplifier fiber (EDF), although it is important to note that EDF strongly absorbs optical signals in its amplification band near 1550 nm so that active alignment of EDF is often performed at a wavelength of 1310 nm.

Another important disadvantage of active alignment are alignment errors associated with interference fringes that result from multiple reflections between the closely spaced end faces of the fiber tips. The refractive index difference between glass and air induces approximately 4% of reflection at a single fiber end face, which corresponds to about 0.3 dB of transmission loss. When the air gap is sufficiently small (less than about 20 microns), most optical sources, including light-emitting diodes (LEDs) and laser diodes (LDs),

will exhibit a wavelength dependent loss associated with this reflection that varies between 0 and 0.6 dB [2.40]. The wider the bandwidth of the optical source, the smaller the air gap separation required for interference fringes, but only white light sources have a sufficiently broad spectral content to avoid these fringes during final fiber alignment when the separation between the fiber tips is on the order of 20 microns or less. Figure 2.14 shows how these interference fringes vary with the air gap distance between two conventional single-mode fiber (SMF) tips at 1550 nm. The figure shows that even perfectly aligned conventional SMF fiber tips with perfectly perpendicular cleave angles can exhibit nearly 0.6 dB of loss prior to fusion splicing. Minute variations in the fiber tip separation can occur during lateral alignment of the fiber tips. Since variations as small as 100 nm can induce several tenths of a dB variation in transmission loss, these interference fringes can confuse an active alignment algorithm.

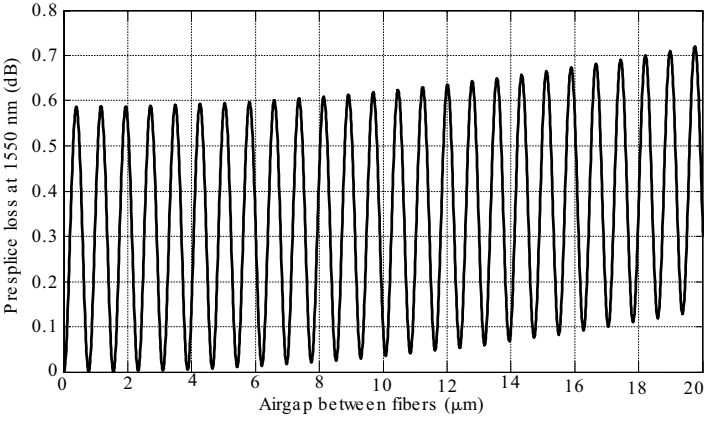

Fig. 2.14. Transmission loss across the air gap between two conventional single-mode fiber tips at 1550 nm. The sinusoidal fringes are caused by multiple reflections between the end faces of the fiber tips. The gradual loss increase at larger gap distances is caused by diffraction of the optical signal as it traverses across the air gap

2.3.4 Light-Injection and Detection (LID) Technology

Light-injection and detection (LID) is a transmitted-power based alignment system that does not require access to the free ends of the fibers to be spliced. Instead, an unstripped portion of the fiber near one of the tips is bent through a tight radius and illuminated with laser radiation [2.41–2.43] (Fig. 2.15). Bending an optical fiber, especially a single-mode fiber, induces loss because some of the light is scattered out of the fiber. Since a bent fiber can couple light out of the core into the external environment, light can also be coupled

from the external environment into the core of the fiber. Brightly illuminating a fiber with a bend diameter on the order of several millimeters can couple a substantial amount of light into the core [2.42].

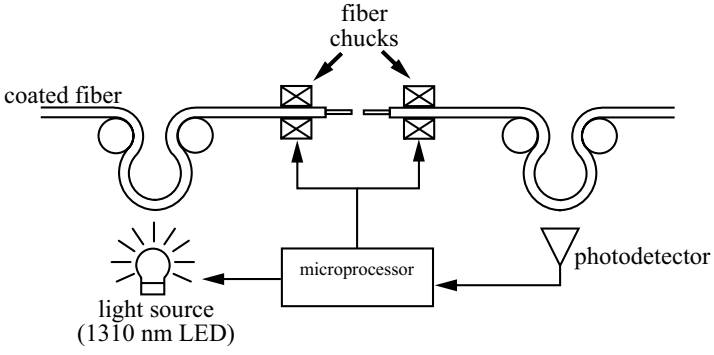

Fig. 2.15. Schematic illustration of an LID fiber alignment system. The coated fiber is bent near the fiber tips to launch light and detect light. The arrows denote the flow of control to or from the microprocessor

In order to detect the amount of light traversing the air gap between the fiber tips, a downstream tight fiber bend is situated near a photodetector. The tightly bent portion of the fiber must be coated to protect against breakage. Like other types of transmitted-power based alignment, LID is sensitive to the cleave angle. In principle, the LID system can also be used for loss measurement of a completed splice.

2.4 Summary

Optical fiber fusion splicing requires the initial fiber tips to be stripped and cleaved. These preparatory steps are important to the resulting splice loss, tensile strength, and long term mechanical reliability.

Stripping is necessary since the polymer coating cannot withstand the high temperatures of joint formation, and in many cases stripping permits superior fiber alignment since the glass geometry is much more precise than the polymer coating. Stripping can be accomplished with mechanical, thermomechanical, chemical, or vaporization techniques. Mechanical and thermomechanical techniques are well suited to all types of fusion splicing, but typically induce surface defects that reduce the tensile strength and long term mechanical reliability of the resulting fusion splice. Chemical and vaporization techniques permit much higher tensile strengths and superior mechanical reliability, but are more hazardous and more costly so they are restricted to laboratory or factory splicing. Chemical and vaporization stripping techniques are essential to high-strength fusion splicing.

Cleaving is a controlled fracture of an optical fiber intended to achieve a mirror-smooth, perfectly perpendicular fiber end face. Even the best cleaving instrument will periodically produce cleaves with defects. Cleave imperfections are a major source for splice loss variation between different splices fabricated with the same splicing parameters. Image processing built into most commercial fusion splicing equipment can detect cleave defects, especially end face angles. High quality cleaves are essential to low-loss fusion splicing of difficult-to-splice specialty fibers such as erbium-doped fiber (EDF) or dispersion-compensating fiber (DCF).

Prior to joint formation, the optical fiber tips must be aligned relative to each other. Some fusion splicing hardware employs passive alignment using fixed position v-grooves. More sophisticated alignment strategies include image-based active alignment in which the microscope images of the fiber's core or cladding are used for alignment purposes. Fibers can also be actively aligned based on the amount of optical power transmitted across the air gap between the fibers. Light-injection and detection (LID) permits active alignment based on transmitted power without requiring access to the fiber ends. Polarization-maintaining (PM) optical fiber fusion splices usually require that the fiber tips be rotationally aligned relative to each other.

3. Mechanics of Fusion Splicing

At its most basic level, fusion splicing is a mechanical process in which two optical fibers are welded together to form a joint. This welding is accomplished by heating the fiber tips until they attain a temperature at which they soften and coalesce. Mechanical forces, heat transfer, and mass transfer all interact to shape the fusion splice process. An engineering analysis of these phenomena can provide valuable insights into strategies for fabricating low-loss, high strength fusion splices.

In this chapter, we will analyze the mechanical aspects of optical fiber fusion splicing beginning with heat transfer in Sect. 3.1. The relevant mechanical forces will be discussed in Sect. 3.2 and the theory of dopant diffusion will be covered in Sect. 3.3. In the concluding section, we will discuss the impact of stress and strain on optical fiber fusion splices.

3.1 Heat Transfer During Fusion Splicing

All three fundamental heat transfer mechanisms, radiation, convection, and conduction, play an important role in the fusion splice process. A detailed review of heat transfer theory is beyond the scope of this book but is available in [3.1,3.2]. In this section we present a basic analysis of heat transfer during the fusion splice process.

Fusion splicing requires the fiber tips to be heated to a temperature high enough to weld them together, which is about 2000° C for silica fibers [3.3]. Other types of glass fibers, such as borosilicate, fluoride, phosphate, or chalcogenide require lower temperatures. Naturally, the heat source must be at a higher temperature than the fibers in order to provide a driving force for the transfer of heat. Ultimately, the heat produced during an optical fiber fusion splice is dissipated into the ambient environment, but this heat load is of little consequence since a typical fusion splice requires on the order of 10 W [3.3] for a duration of about five seconds which amounts to about 50 J.

Despite the fact that heat transfer is clearly a central issue in optical fiber fusion splicing, there have been surprisingly few published analyses of this topic. Heat transfer during optical fiber fusion splicing is inherently complex because fusion splicing is an *unsteady*, or time-dependent, process. Moreover heat transfer during fusion splicing is a non-linear process because the material properties, and hence the heat flux, depend on the temperature of

the glass. It is difficult to capture all the relevant physics with purely analytical models and therefore a precise description of heat transfer during fusion splicing requires numerical modeling techniques. Numerical modeling of optical fibers heated in a manner similar to fusion splicing compares favorably to experimental data [3.4–3.6]. In this section we avoid such numerical modeling techniques to provide a more qualitative, rather than quantitative, description of heat transfer during fusion splicing.

The heat source employed for fusion splicing may be an electric arc, a resistively heated metal filament, a chemical flame, or a laser. Nearly all commercial fusion splicers employ an arc heat source with filament heating making up most of the balance. Laser and flame heat sources are mostly of historical interest but there are instances in which a laser or a flame might be useful for laboratory fusion splicing. Chemical flames usually employ oxygen and hydrogen as fuels [3.7, 3.8]. The CO_2 laser is an appropriate laser to serve as a heat source since its 10.6 µm radiation is strongly absorbed by silica [3.9, 3.10]. In contrast to other types of heat sources that heat the fiber through a combination of convection and radiation, a laser heats the fiber exclusively through radiation. Another difference between a laser and other heat sources is that the laser can confine the heat to a small zone at the fiber tips while other heat sources tend to heat a longer length of fiber.

3.1.1 Arc-Discharge Heating

Since arc-discharge heating is by far the most common method to heat the fiber tips, it is worthwhile to analyze it in some detail. In an arc discharge, a voltage is applied across two electrodes separated by an air gap of a few millimeters. Figure 3.1 depicts the variation of current with voltage applied to electrodes separated by an air gap for a generalized discharge. The resulting current flow heats the surroundings via thermal radiation and convection. Technically, this heat source is a *glow discharge*, rather than an arc discharge, since it operates in the so-called glow regime of a few milliamps [3.11]. Despite this, we will adhere to the convention of referring to this glow discharge heating as arc discharge heating since that terminology is so prevalent in the industry.

The heating profile of the arc discharge heat source has been analyzed in the literature by measuring the optical intensity of the discharge and quantifying the current density, i, which is measured in current per unit area (A/m^2) [3.11]. The radiative intensity fits a Gaussian in the transverse direction so the current density can be assumed to be a radially symmetric Gaussian. At any axial position z between the electrodes, the total current between the electrodes is denoted by I_{tot}. Given these assumptions, the current density is given by [3.11]

$$i(r,z) = \frac{I_{\text{tot}}}{2\pi\sigma_{\text{arc}}^2(z)} \exp\left(-\frac{r^2}{2\sigma_{\text{arc}}^2(z)}\right) , \tag{3.1}$$

where r is the radial coordinate, z is the axial coordinate along the axis of the two electrodes, and $\sigma_{\text{arc}}(z)$ is the characteristic width of the Gaussian at

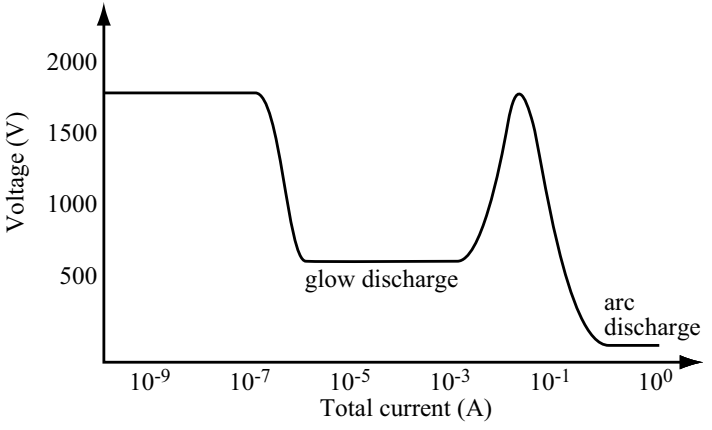

Fig. 3.1. Voltage versus current for a generalized electrical discharge. After [3.6, 3.12]

any axial position z. Integrating this current density over all radial positions yields the total current I_{tot}. Based on Tachikura's experimental data, $\sigma_{\text{arc}}(z)$ can be approximately expressed as [3.11]

$$\sigma_{\text{arc}}(z) = \sigma_0(1 + C_{\text{arc}}z^2)^{-1/3} \,, \tag{3.2}$$

where $z = 0$ at the midpoint between the electrodes, σ_0 characterizes the width of the Gaussian at $z = 0$, and C_{arc} is a constant determined from the variation of the radiative intensity in the z-direction.

Tachikura found that the radiative intensity scaled with the square of the current density and concluded that the local energy density also scaled with the square of the current density. For the purposes of a heat transfer analysis, it is reasonable to assume that the temperature of the discharge is proportional to the energy density. Thus, the arc discharge is hottest at the electrode tips and along the $r = 0$ axis the arc discharge temperature reaches a minimum at the midpoint between the electrode tips. The hottest point at any fixed z position occurs at $r = 0$, along the electrode's axis. Figure 3.2 depicts this current density and energy density distribution with the aid of contours that delineate lines of constant energy density and hence temperature. Single fiber fusion splicing typically occurs at the midpoint between the electrodes where $r = 0$ and $z = 0$. When splicing multi-fiber ribbon cable, the fibers should be positioned relative to the electrodes along a contour of constant energy density (as shown by open circles in Fig. 3.2) to ensure that all the fibers experience equal heating. Tachikura's experimental measurements of fiber temperatures support this view [3.11, 3.16].

The heating characteristics of an arc discharge depend upon environmental variables such as the temperature, barometric pressure, and relative humidity. Consequently, the splicing parameters can depend on the ambient environment, especially during field splicing [3.17–3.19]. Furthermore, the total

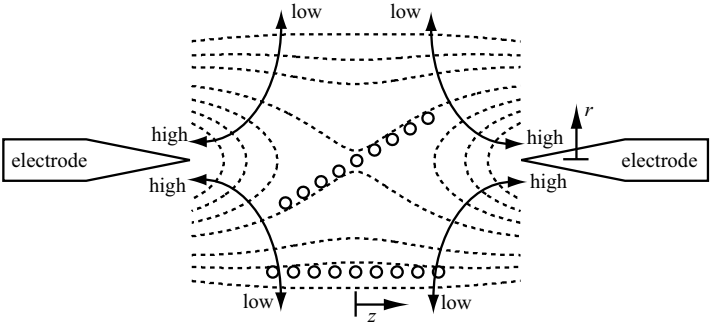

Fig. 3.2. Illustration of current and energy density distribution in an arc fusion splicer. Current and energy density is rotationally symmetric about the $r = 0$ axis. Dashed lines represent contours of constant current flux or constant energy density. Curved solid line with arrow illustrates direction of higher or lower current density. Circles depict favorable locations for ribbon fiber to ensure equal heating. After [3.11, 3.15, 3.16]

amount of heat produced by an arc is not continuously variable; below a certain current, the arc discharge is unstable and may terminate entirely. Despite the fact that this stability threshold is sensitive to the ambient environment, a low level of heating is sometimes desirable, for example when physically tapering a fusion splice (Sect. 8.2.6) or performing a low-temperature fusion splice (Sect. 8.2.4). In such cases the arc discharge may be rapidly pulsed at a higher discharge current [3.13] to achieve a lower fiber temperature while maintaining a stable arc discharge.

The heating profile of an arc also depends upon the purity of the electrode tips, which are normally fabricated from a refractory metal such as tungsten. During normal operation, the electrode tips have a tendency to accumulate a coating of contamination, which can include silica or dust particles. These particles can perturb the electrical current path and hence the arc's heating profile, which can increase fusion splice loss [3.14, 3.19]. Moreover, contamination particles have been shown to deposit onto the fiber tips during fusion splicing, thus reducing the mechanical strength and long-term reliability of the fusion splice. This issue is discussed further in Sect. 6.1. The solution to this problems is to regularly clean the arc electrodes with a special brush. Over time arc electrodes wear out and develop pits that result in an unsteady or non-uniform heating. Well maintained arc electrodes can last for 1000 splices or more before requiring replacement.

3.1.2 Heat Flow

Figure 3.3 schematically illustrates heat flow during a fusion splice. The heat transferred to the fiber tips by convection and radiation is primarily dissipated to the surroundings via radiation and conduction down the length of

the fibers. In fact, the thermal radiation emitted by the heated tips can couple into guided fiber modes and consequently an optical power meter will often measure an increase in optical intensity during a fusion splice. For this reason splice loss measurements are inaccurate while the splice is heated to a high temperature.

The gap between the fiber tips is usually very small at the beginning of a fusion splice and is reduced to zero by the hot push soon after. Furthermore, the heat source and the fiber tips are usually symmetric about the gap so there will be no heat flux across it. Consequently we will neglect the gap between the fiber in our analysis and treat the fibers as if they are a single continuous rod of glass. To further simplify the analysis we assume that the heat source and the fibers are cylindrically symmetric so that the domain reduces to two spatial coordinates, radial r, and axial z.

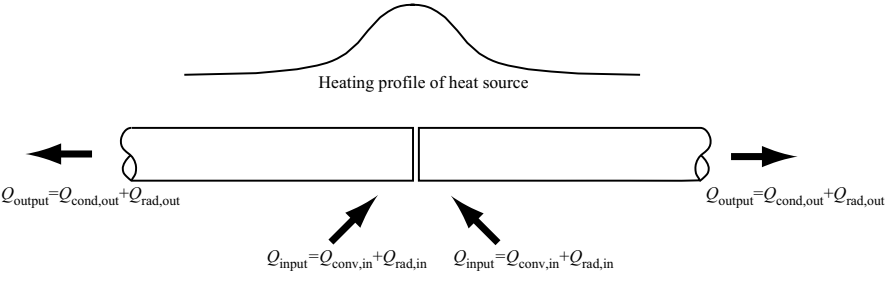

Fig. 3.3. Schematic illustration of heat flow during optical fiber fusion splice. The characteristic width of the heat source refers qualitatively to both convection and radiation at the fiber surface. After [3.6]

An energy balance relates the temperature change in the fiber, $\frac{\mathrm{d}T}{\mathrm{d}t}$, to the total heat flux across the fiber surface

$$\int \varrho\, c_\mathrm{p} \frac{\mathrm{d}T}{\mathrm{d}t}\, \mathrm{d}V_\mathrm{fiber} = Q_\mathrm{input} - Q_\mathrm{output}\ , \tag{3.3}$$

where ϱ is the fiber density ($\sim$2.2 kg/m^3 for silica glass [3.20]), c_p is the fiber heat capacity ($\sim$700 J/kg-K for silica glass at room temperature [3.20]) and the integral is computed over the entire volume of the fiber, V_fiber. As depicted in Fig. 3.3, Q_input is the total input heat flux made up of convection, Q_conv, and the input radiation, $Q_\mathrm{rad,in}$, so

$$Q_\mathrm{input} = Q_\mathrm{conv,in} + Q_\mathrm{rad,in}\ , \tag{3.4}$$

while Q_output is the total output heat flux and is made up of conduction, Q_cond, and the output radiation, $Q_\mathrm{rad,out}$, so

$$Q_\mathrm{output} = Q_\mathrm{cond,out} + Q_\mathrm{rad,out}\ . \tag{3.5}$$

The Biot number, Bi, is a non-dimensional parameter which compares the relative importance of heat transfer inside the fiber to heat transfer through

the fiber surface. When Bi>>1 most of the thermal resistance comes from conduction inside the fiber rather than convection at the fiber surface. Conversely, when Bi<<1, most of the thermal resistance occurs in convection at the surface of the fiber and the temperature gradient in the fiber itself will be small. The Biot number for a cylindrical object like an optical fiber is defined as [3.1]

$$\mathrm{Bi} = \frac{hD_{\mathrm{fiber}}}{2\kappa_{\mathrm{T}}} \,, \tag{3.6}$$

where D_{fiber} is the diameter of the fiber, h is the convective heat transfer coefficient at the fiber surface and κ_{T} is the thermal conductivity, which is about $1.38\,\mathrm{W/mK}$ [3.1] at room temperature and increases with temperature [3.1, 3.6].

The convective heat transfer coefficient, h, quantifies how efficiently heat is transferred from the surrounding medium into the fiber [3.1]

$$Q_{\mathrm{conv,in}} = \int h(T_{\mathrm{surround}} - T_{\mathrm{surface}})\mathrm{d}A \,, \tag{3.7}$$

where A is the surface area of the fiber exposed to the heat convection, T_{surround} is the temperature of the medium just outside the fiber surface, and T_{surface} is the temperature of the fiber surface. If the convective heat transfer per unit area is denoted by q_{conv} then we can write

$$q_{\mathrm{conv,in}} = h(T_{\mathrm{surround}} - T_{\mathrm{surface}}) \,. \tag{3.8}$$

It is very difficult to estimate h, as it depends on the subtleties of the heat source and the medium surrounding the fiber. Estimates for h at the surface of a $125\,\mu\mathrm{m}$ diameter fiber during arc heating range from 24 to $113\,\mathrm{W/m^2}$ [3.6, 3.21]. Other estimates for h are $158\,\mathrm{W/m^2}$ for a $125\,\mu\mathrm{m}$ diameter fiber experiencing flame heating [3.22] and $300\,\mathrm{W/m^2}$ during fiber drawing [3.23]. Based on these values for h and κ_{T}, Bi can be estimated to be somewhere between 1×10^{-4} to $1 \times 10^{-2}\,\mathrm{W/m^2}$ for a $125\,\mu\mathrm{m}$ diameter fiber. Since Bi<<1 we may safely assume most of the thermal resistance during optical fiber fusion splicing occurs at the fiber surface. This fact permits a significant simplification: the temperature of the fiber will be largely independent of radial position at any axial position along the fiber [3.4, 3.6].

Since the fiber temperature is largely constant with respect to radius during fusion splicing, most of the variation in the fiber temperature occurs in the axial, or z, direction. This axial temperature gradient gives rise to a conduction heat flux in the axial direction via Fourier's Law [3.1]

$$Q_{\mathrm{cond,out}} = \frac{\pi D_{\mathrm{fiber}}^2}{4}\kappa_{\mathrm{T}}\frac{\mathrm{d}T_{\mathrm{fiber}}}{\mathrm{d}z} \,. \tag{3.9}$$

Radiation heat transfer in hot glass is complex and a complete treatment is beyond the scope of this monograph. However, important conclusions may be drawn from simple observations. Silica glass is relatively opaque to

thermal radiation in the far-infrared (wavelengths longer than 4 μm) where most room temperature thermal radiation is found [3.24–3.26]. On the other hand, pure silica glass is relatively transparent in the visible and near-infrared (wavelengths below 2 μm) where most high temperature thermal radiation is found [3.24–3.26]. After all, optical fibers are fabricated from the purest possible glass to achieve the highest possible transmission of near-infrared optical signals! The peak emission wavelength, λ_{peak}, for a blackbody thermal emitter is given by Wien's law [3.1]

$$\lambda_{\text{peak}} = 2913/T \,, \tag{3.10}$$

where T is the blackbody temperature in Kelvins and λ_{peak} is in μms. For a heat source operating between 1750 and 3000° C, $0.9\,\mu m < \lambda_{\text{peak}} < 1.5\,\mu m$. Since optical fibers are so transparent in this wavelength range, thermal radiation in high temperature silica is really a bulk, rather than a surface phenomenon.

Since the absorption of silica fibers is strongly wavelength dependent, it is not well described by a gray body radiation model. Furthermore, experimental data suggests that the near- and mid-infrared spectral absorption coefficient of pure silica glass, as well as its spectral emissivity, increases substantially at high temperature [3.24, 3.26–3.28]. Thus, radiation heat transfer in a silica fiber is difficult to quantify without resorting to numerical modeling. Prior efforts to avoid this difficulty have approximated optical fibers as simple gray bodies and crudely assumed that the fibers' effective surface emissivity and absorptivity is on the order of 0.1 [3.4, 3.6, 3.23] at high temperature.

Heat transfer inside a high temperature optical fiber occurs through both conduction *and* radiation because high temperature thermal radiation can travel through the glass bulk. The effective absorption coefficient, μ_{a}, of high temperature thermal radiation in silica has been roughly estimated to be on the order of $4\,\text{cm}^{-1}$ [3.6]. In the radial direction, communications fibers are much thinner than $1/\mu_{\text{a}}$ so thermal radiation in the radial direction is described by the *optically thin limit*. In the direction of the fiber axis, the fibers are much thicker than $1/\mu_{\text{a}}$ so thermal radiation in the axial direction may be described by the *optically thick limit*, also known as the *Rosseland approximation* [3.29], in which thermal radiation inside the bulk material behaves diffusively and thus manifests itself as a kind of thermal conductivity. This radiation thermal conductivity, κ_{R}, can be defined for the fiber along its axis as [3.6]

$$\kappa_{\text{R}} = \frac{16 n^2 \sigma_{\text{SB}} T^3}{3\mu_{\text{a}}} \,, \tag{3.11}$$

where n is the refractive index of the material (about 1.45 for silica glass), σ_{SB} is the Stefan-Boltzmann constant ($5.67 \times 10^{-12}\text{W/m}^2\text{K}$), and T is local fiber temperature in Kelvins. The apparent thermal conductivity is the sum of the "true" conductivity and the radiative conductivity. At splicing temperatures, κ_{R} is more than 20 W/mK indicating that most of the apparent

conductivity of a fiber at high temperatures is really due to radiation. Note that κ_{R} does not change Bi very much since Bi is based on the apparent thermal conductivity in the radial direction which is not significantly affected by radiation since the fiber diameter is much less than $1/\mu_{\mathrm{a}}$. The radiation heat flow out of the fiber, $Q_{\mathrm{rad,out}}$ may be estimated by

$$Q_{\mathrm{rad,out}} \approx \frac{\pi D_{\mathrm{fiber}}^2}{4} \kappa_{\mathrm{R}} \frac{\mathrm{d}T_{\mathrm{fiber}}}{\mathrm{d}z} \ . \tag{3.12}$$

The total output heat flux, Q_{output}, may then be estimated by

$$Q_{\mathrm{output}} \approx \frac{\pi D_{\mathrm{fiber}}^2}{4} (\kappa_{\mathrm{T}} + \kappa_{\mathrm{R}}) \frac{\mathrm{d}T_{\mathrm{fiber}}}{\mathrm{d}z} \ , \tag{3.13}$$

which is proportional to the cross-sectional area of the fiber and hence the square of the fiber diameter. The total heat flux into the fiber at the splice itself, Q_{input}, results from convection and radiation from the heat source. If we crudely model the fiber as an absorbing gray body with absorptivity e_{rad} then [3.1]

$$Q_{\mathrm{rad,in}} \approx e_{\mathrm{rad}} \sigma_{\mathrm{SB}} (T_{\mathrm{surround}}^4 - T_{\mathrm{fiber}}^4) \ . \tag{3.14}$$

We can then approximate the total input heat flux as

$$Q_{\mathrm{input}} \approx \pi D_{\mathrm{fiber}} L [h(T_{\mathrm{surround}} - T_{\mathrm{fiber}}) + e_{\mathrm{rad}} \sigma_{\mathrm{SB}} (T_{\mathrm{surround}}^4 - T_{\mathrm{fiber}}^4)] \ , \tag{3.15}$$

where L is the characteristic width of the hot zone. Thus the total input heat flux, Q_{input}, is proportional to the surface area of the heated fiber region and hence the fiber diameter. The ratio of Q_{output} and Q_{input} scales with the fiber diameter

$$\frac{Q_{\mathrm{output}}}{Q_{\mathrm{input}}} \sim D_{\mathrm{fiber}} \ . \tag{3.16}$$

This relation explains the observation that when other factors are kept constant, fusion splicing a larger diameter fiber typically requires more heat than a smaller diameter fiber since the larger fiber permits a relatively larger amount of heat to escape down the length of the fiber.

Another important observation related to the axial temperature gradient along the fiber is that substantial portions of the fiber on either side of the splice are heated to intermediate temperatures, much higher than room temperature, but not as high as splicing temperatures. As long as the heat source is relatively clean, the surface of the glass in the immediate vicinity (typically within 500 μm) of the splice is melted and smoothed by surface tension so that it is nearly flaw-free. The fiber far from the splice (typically several millimeters) is unaltered since it is not heated by the splice. However, the portion of fiber between these two regions (500 μm to several mm from the splice) is heated to a temperature at which flaws can form at the fiber surface but is not heated so much as to melt and clean the surface. Surface flaws originating in this intermediate region can reduce the strength of the splice and account for the observation that spliced fibers often fracture about

one millimeter away from the splice itself, in the intermediate heated zone. A very clean splicing environment and a clean heat source, in combination with a post-splice fire polish can minimize this strength reduction. These and other issues related to splice strength and mechanical reliability are discussed at length in Chap. 6.

A simplified heat transfer analysis permits us to estimate the time dependent behavior of the temperature field in the fiber. The thermal conduction time-constant, t_{cond}, measures the time required for heat to penetrate from the outside of the fiber into its center. In a cylindrical geometry, this parameter may be expressed as [3.1]

$$t_{\text{cond}} = \frac{D_{\text{fiber}}^2}{4\alpha_{\text{T}}} , \tag{3.17}$$

where $\alpha_{\text{T}} = \frac{\kappa_{\text{T}}}{\varrho c_{\text{p}}}$ is the thermal diffusivity of the fiber which is on the order of $1 \times 10^{-6}\,\text{m}^2/\text{s}$ for silica glass at room temperature. Thus only a few milliseconds are required to transfer heat from the outside to the inside of the fiber and establish a uniform temperature field.

If we ignore Q_{output} and $Q_{\text{rad,in}}$ we can estimate the time required to heat the fiber tips up to splicing temperatures. To make the estimate we take $\varrho c_{\text{p}} \frac{\text{d}T}{\text{d}t}$ out of the integral in (3.3)

$$\pi \frac{D_{\text{fiber}}^2}{4} L \varrho c_{\text{p}} \frac{\text{d}T_{\text{fiber}}}{\text{d}t} = \pi D_{\text{fiber}} L q_{\text{conv}} , \tag{3.18}$$

where L is the characteristic width of the heated zone. We recognize that since there is no variation in temperature in the radial direction, T_{surface} in (3.8) is the same as T_{fiber} so (3.8) and (3.18) may be combined to obtain

$$\frac{\text{d}T_{\text{fiber}}}{\text{d}t} = \frac{4h}{\varrho D_{\text{fiber}} c_{\text{p}}} (T_{\text{surround}} - T_{\text{fiber}}) . \tag{3.19}$$

If T_{surround} is a constant then (3.19) is a linear first order ordinary differential equation with time constant $\frac{\varrho D_{\text{fiber}} c_{\text{p}}}{4h}$. Based on the values for h previously cited, this time constant is on the order of several hundred milliseconds which is consistent with experimental observations. Notice that this time constant is much slower than the fiber's thermal conduction time constant, t_{cond}, indicating that the fiber temperature is largely uniform with respect to radius even as it heats up or cools down. In reality, this lumped parameter model is very crude since it neglects both heat transfer down the length of the fiber and radiative heating at the splice. The former increases the time required to heat up the fiber while the latter decreases the required time.

3.2 Mechanical Forces During Fusion Splicing

The fiber tips experience a variety of mechanical forces during fusion splicing. The splicer's fiber holders (chucks), surface tension, and viscosity all shape

the fusion splice process. A variety of important phenomena such as bending, buckling, tapers, bubbles, and fiber neckdown depend on the mechanical forces occurring during fusion splicing. In this Section we will explore these phenomena and the forces which are responsible for them. A good general review of the mechanical behavior of materials is available in [3.30].

3.2.1 Compressive, Tensile, and Bending Forces

Figure 1.2 shows that the fiber tips are rigidly clamped in the fiber chucks. Depending on the fusion splicer design, the fiber tips protrude a distance of 5 to 20 μm from the rigidly clamped region. For a typical 125 mm diameter fiber, this aspect ratio of length to diameter is on the order of 100. To better understand the mechanical forces during fusion splicing, it is useful to approximate the fiber as an elastic beam. Prior to splicing, the fiber tips behave as cantilevered elastic beams that are rigidly clamped at one end and free at the other. During joint formation, the portion of glass connecting the two fibers is soft with a jelly-like consistency. It is at this stage of the process that surface tension forces become significant. As the splice joint cools and the glass solidifies, viscous forces once again dominate over surface tension forces and the fiber once again behaves as an elastic beam.

Prior to splicing, the fiber tips must be aligned to each other. Since the fiber tips are so thin, a deflection can be caused by a relatively small force. The deflection can be quantified with standard bending beam analysis. If the fiber tip is assumed to be an elastic beam rigidly clamped by the fiber chuck, the amount of deflection, δ_{bending}, may be related to the transverse force concentrated at the fiber tip, F_{bending}, by [3.30]

$$\delta_{\text{bending}} = \frac{F_{\text{bending}} L^3}{3 E_{\text{y}} I_{\text{bend}}} \,, \tag{3.20}$$

where E_{y} is Young's modulus, I_{bend} is the bending moment of inertia, and L is the length of the free fiber end (Fig. 3.4). Young's modulus for high purity fused silica glass at room temperature is about 72.9 GPa [3.20]. The bending moment of inertia characterizes the stiffness of an elastic member and for an object with a circular cross section, such as an optical fiber, is given by [3.30]

$$I_{\text{bend}} = \frac{\pi D_{\text{fiber}}^4}{64} \,, \tag{3.21}$$

where D_{fiber} is the fiber diameter. A 125 μm diameter fiber has $I_{\text{bend}} = 1.2 \times 10^{-17} \text{m}^4$.

Sometimes a force is uniformly distributed along the fiber length. If this force-per-unit-length is denoted by F'_{dist}, then the amount of deflection, δ_{dist} may be expressed as [3.30]

$$\delta_{\text{dist}} = \frac{F'_{\text{dist}} L^4}{8 E_{\text{y}} I_{\text{bend}}} \,. \tag{3.22}$$

Equations (3.20,3.22) show that short fiber tips are much more resistant to transverse bending forces than longer tips since deflection varies with the cube of the tip length times the total applied force. According to (3.20), only 26 μN concentrated at the fiber tip is required to deflect a 125 μm diameter, 10 mm long silica fiber by 10 μm. Only about 5 μN of transverse force is required to deflect a 125 μm diameter silica fiber by 2 μm, a distance sufficient to substantially increase splice loss in single-mode fibers. Consequently, relatively little force can cause a relatively large transverse shift in the fiber tip.

Static electricity is an example of a relatively weak force than can cause substantial deflection of a fiber tip. Mechanical removal of the fiber's polymer coating can sometimes leave the exposed fiber tip with an undesirable static charge that causes the tip to deflect. Gravity is an example of a distributed force acting on the fiber tip. Gravity, however, is almost always negligible in optical fiber fusion splicing. The gravitational force per unit length of a 125 μm diameter silica fiber is about 2.7×10^{-4} N/m so a 10 mm long cantilevered section of such a fiber experiences a total force of about 2.7 μN and deflects only about 0.4 μm under the force of gravity. Although static electricity can affect fiber alignment, surface tension forces will always overwhelm both gravity and static electricity in practical fusion splicing situations.

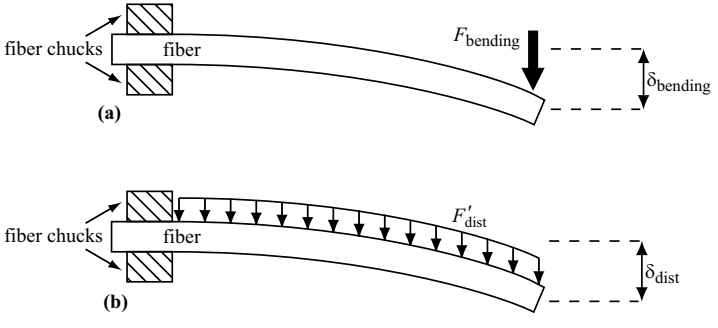

Fig. 3.4. Bending of a fiber tip modeled as an elastic beam rigidly clamped at its root. (**a**) Force concentrated at the tip. (**b**) Force uniformly distributed along fiber length

Another sideways force encountered during fusion splicing results from *fiber curl* . Fiber curl refers to the tendency of a fiber to naturally assume a curved shape in the absence of applied force. This usually occurs because the polymer coating has shape memory and it "remembers" the shape it assumes when it is wound around a fiber spool. A typical commercial optical fiber specification is that the fiber curl radius be greater than 4 m. When the curl radius is less than 2 m, the fibers can be very difficult to align for splicing. One common solution is to remove enough of the polymer coating that the splicer chucks actually grip on the glass itself, which usually exhibits

little or no curl. However, touching the bare glass surface of the fiber with the fiber chucks can introduce flaws onto the fiber surface which will significantly reduce the splice strength. Another solution is to employ a device which heats the coated fiber and "erases" the shape memory of the polymer and hence the curl. In rare cases, excessive fiber curl results from the glass fiber itself rather than from the polymer coating. This problem is not easily solved and can severely degrade ribbon fiber alignment leading to increased loss in a ribbon fiber splice.

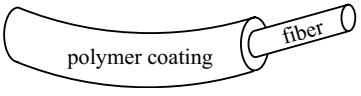

Fig. 3.5. Illustration of fiber curl resulting from shape memory in the polymer coating

During the hot push, the softened fiber tips are pressed together. The tendency of the fiber tips to buckle places an upper limit on the compressive force that can be exerted when pressing the tips together (Fig. 3.6). If the fibers buckle during the hot push, severe core misalignments are likely to result and so buckling of the fiber tips is to be avoided at all costs. To avoid buckling, the applied compressive force must be less than the critical buckling force, F_{crit}. This can be estimated by treating the two fiber tips as a single cantilevered beam that is rigidly clamped at both ends. The theory of buckling [3.30] shows that the critical buckling force is given by

$$F_{\text{crit}} = \frac{4\pi^2 E_{\text{y}} I_{\text{bend}}}{L^2} \ . \tag{3.23}$$

A higher critical buckling force is desirable since it reduces the risk of buckling during splicing. Since the critical buckling force varies inversely with the square of the tip length, shorter tip lengths permit much higher compressive forces during the splice. This can be a particular advantage when splicing fibers at low temperature where larger compressive forces are required to form a joint (see Sect. 8.2.4 for a discussion of low-temperature splicing). For a 10 mm long section of 125 μm diameter silica fiber, F_{crit} is about 0.021 N. The corresponding axial compressive stress, the critical buckling force divided by the fiber's cross sectional area, is 1.7 MPa for a 125 μm diameter fiber. The actual critical buckling force can be significantly lower than that predicted by (3.23) when the fiber tips are softened or when the cleaves are not perfectly planar. The precise nature of the fiber chucks will also affect the critical bucking forces since if the fibers are not clamped rigidly, the critical buckling force will be lower than (3.23). Unfortunately, most commercial splicers control the distance, but not the force, of the hot push. Thus, splice optimization often requires iterating through several sets of splicing parameters to find a set which minimizes the likelihood of buckling.

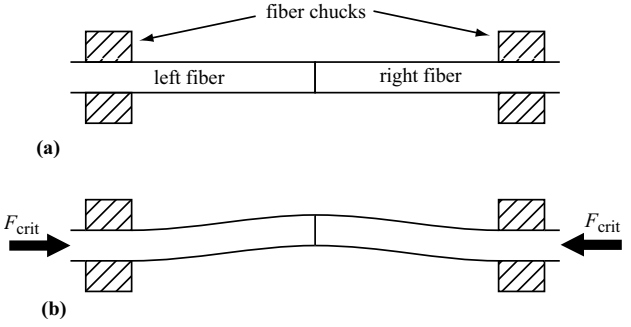

Fig. 3.6. Illustration of buckling during fusion splice hot push. (**a**) Fibers aligned to each other prior to hot push. (**b**) Buckling occurs when the fibers are pressed together with a force greater than or equal to the critical buckling load

When splicing fibers with very different refractive index profiles or very different cladding diameters the fusion splice loss can sometimes be reduced by "fattening" the splice [3.31]. If one fiber has a much smaller mode field diameter (MFD) than the other fiber, the fusion splice loss between the fibers may be high. If an unusually large hot push (100 µm or more) is applied to the splice while the joint is soft, the fiber diameter in the vicinity of the splice can be substantially increased (Fig. 3.7). If the diameter increase is biased towards the fiber with the smaller mode field diameter, splice losses can be reduced to 0.1 dB [3.31]. The hot push velocity and the temperature of the splice must be carefully controlled to suppress buckling. Fattened splices are discussed in more detail in Sect. 8.2.7.

Once the splice process is completed and a joint is formed, tension may be applied to the fibers in order to physically taper them to a smaller diameter. In contrast to the case of compressive force, large tensile forces can be applied to a fiber without buckling. Thus it is easier to produce a tensile deformation than a compressive deformation of a fiber. For this reason, tapering or drawing a fiber requires a lower temperature than fusion splicing since fusion splicing requires a certain amount of compressive fiber deformation. Conventional splicing equipment can readily apply tensile forces comparable to the fiber draw tension, on the order of 1 N. For a 125 µm diameter fiber, 1 N corresponds to a tensile stress of 81.4 MPa which is almost two orders of magnitude higher than the critical buckling compressive stress cited above.

Tapering has been shown to improve the lateral alignment of fusion splices thus reducing the splice loss [3.32, 3.33]. Tapering can also be useful when splicing dissimilar fibers. If one fiber has a much smaller mode field than the other fiber, preferentially tapering the fiber with the larger mode field diameter can sometimes reduce the splice loss [3.34, 3.35]. Another strategy to reduce the splice loss between dissimilar fibers is to taper the fibers to the point where the mode field is no longer bound by the core but rather is

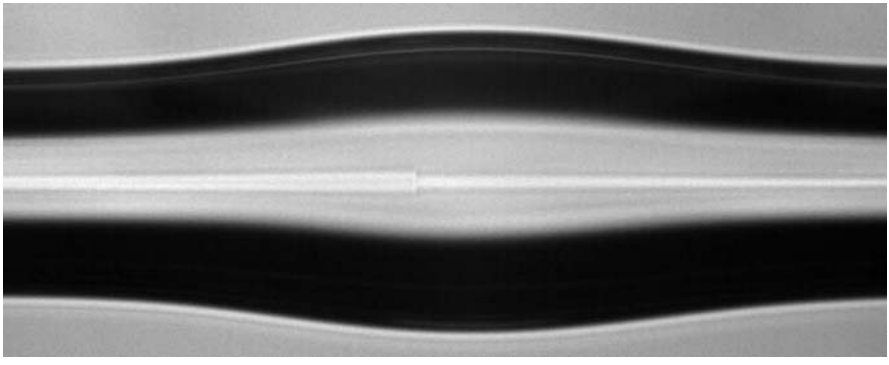

Fig. 3.7. Asymmetrically fattened splice between ordinary SMF (left) and *Corning Flexcor 1060* single-mode fiber (right). Notice that the splice is deliberately offset with respect to the bulge to maximize the core diameter of the *Flexcor 1060* relative to the SMF. The original fiber diameters are 125 μm and the maximum diameter of the bulge is 164 μm

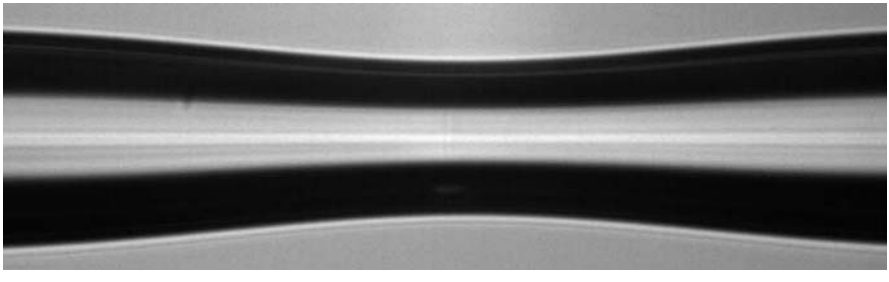

Fig. 3.8. Symmetrically tapered splice between two SMFs. The original fiber diameters are 125 μm and the diameter at the waist is 84 μm

bound by the cladding/air interface [3.36]. Low splice loss can be achieved between very different fibers with this technique. A major disadvantage of this technique is that the splice will be sensitive to both bending and also to the optical properties of the medium surrounding the fiber. Although the cross sectional area of the tapered portion of fiber is less than that of the original fiber, the ultimate strength of a tapered splice is usually not that much lower than a regular splice since splice strength is primarily determined by the surface condition of the glass. The benefits of fusion splice tapering are discussed in detail in Sect. 8.2.6.

3.2.2 Surface Tension and Viscosity

Surface tension, γ, is a force that results from the subtle differences in molecular structure between the material at a surface interface and material inside the bulk [3.37]. It has units of force/length so it is expressed in the SI units

N/m. As its name suggests, it mimics an elastic membrane stretched around the bulk material. Surface tension always acts to reduce the total surface area of the material. Equivalently, surface tension acts to smooth out fine texture and blunt sharp edges. Surface tension is present in glass even at room temperature, but it cannot deform silica glass at such low temperatures because the glass viscosity is too high. The surface tension of silica is not very temperature sensitive and is about 0.3 N/m over the range of temperatures relevant to splicing [3.20, 3.38]. Surface tension is responsible for joint formation during fusion splicing and is one of the most important and strongest mechanical forces experienced by the fiber tips. Surface tension is also the main cause for deformation of the fiber core that leads to splice loss.

When a surface has curvature, surface tension can produce a force acting normal to the surface. Consider a differential element of a surface as depicted in Fig. 3.9a. This differential element has a curvature with radius R_{x} in the x-direction and curvature R_{y} in the y-direction where x and y are a set of two orthogonal directions, each perpendicular to the surface normal vector. The resultant force per unit area, P_γ, acting normal to the surface element is given by

$$P_\gamma = \frac{\gamma}{R_{\mathrm{x}}} + \frac{\gamma}{R_{\mathrm{y}}} \,. \tag{3.24}$$

The entire surface of a long cylindrical object, such as optical fiber or a cylindrical hole running down the inside of an optical fiber, experiences a force per unit area of $P_\gamma = \gamma/2R$ where R is the radius of the cylinder. From the perspective of the cylindrical entity, this surface tension is indistinguishable from a pressure of $\gamma/2R$ uniformly applied to its surface. In other words, the surface tension exerts a *hydrostatic pressure* of $\gamma/2R$ on the object. In the case of a spherical object, such a spherical bubble in an optical fiber, the equivalent hydrostatic pressure is γ/R. These two cases are schematically illustrated in Fig. 3.9b–c respectively.

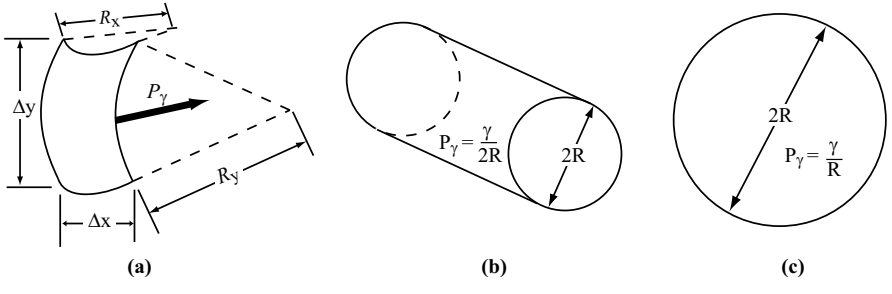

Fig. 3.9. Equivalence of surface tension to an applied hydrostatic pressure. (**a**) Geometry of a curved differential surface element. (**b**) Cylindrical surface. (**c**) Spherical surface

Viscosity, η, is dissipative force that resists relative motion or shear. This can be quantitatively expressed as

$$\tau = -\eta \frac{\mathrm{d}V_{\mathrm{flow}}}{\mathrm{d}x} \ , \tag{3.25}$$

where τ is the viscous shear stress in units of shear force/area, x is in the direction normal to the plane of the shear stress, and V_{flow} is the velocity flow of the material in a direction perpendicular to x. Viscosity inhibits fiber deformation since deformation requires relative motion and shear. The higher the viscosity, the stronger the resistance to deformation. Viscosity has units mass/length·time and is commonly expressed in the unit *Poise* ($1\,\mathrm{Poise} = 1\,\mathrm{g/cm \cdot}\,s{=}10\,\mathrm{kg/m{\cdot}s}$). In contrast to surface tension, the viscosity of silica varies sharply with temperature and thus it is primarily the viscosity which controls the temperature required for fusion splicing. Figure 3.10 depicts the viscosity of high purity vitreous silica as a function of temperature. Viscosity also depends on the concentration of dopants or impurities in the glass and its thermal history [3.39–3.41]. Generally speaking, dopants or impurities such as OH radicals reduces the viscosity of the glass. For example, graded-index multimode fiber (GIF) can be fusion spliced at a much lower temperature than standard SMF since it has a much larger core containing a much higher germania dopant concentration so its viscosity is significantly lower. Other highly doped fibers such as titania-clad fiber (such as *Corning Titan* fiber) or pure-silica core fiber (such as *Sumitomo* "*Z*" fiber) also exhibit this characteristic.

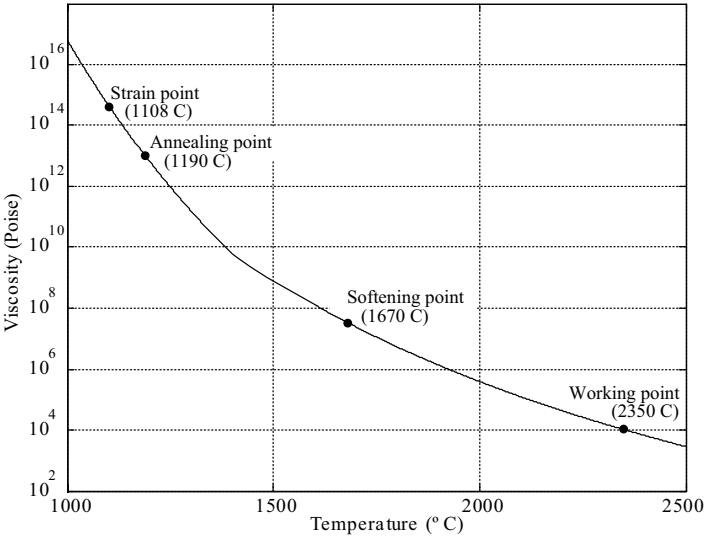

Fig. 3.10. Variation of extremely pure vitreous silica viscosity as a function of temperature based on [3.20]

The variation of viscosity with temperature can be characterized by specific temperatures at which the viscosity attains certain standardized values [3.39]. For example, at the *annealing point*, the viscosity of glass is $10^{13.4}$ Poise. At the *softening point* the viscosity is 10^7 Poise. Fusion splicing usually takes place when the viscosity is on the order of 10^5 Poise. The *working point* of the glass which occurs when the viscosity is 10^4 Poise. For the purpose of comparison, the viscosity of honey at room temperature is on the order of 10^3 Poise.

The relationship between surface tension and viscosity is commonly exploited to calibrate the heat source used during fusion splicing. As noted earlier, the heat resulting from an arc discharge can vary depending on the condition of the electrodes and the environmental conditions so calibration can be important. Typically two cleaved fibers are positioned as if to be spliced but the hot push step is omitted. The two fiber tips will "melt back" upon themselves and ball up at their tips. The extent of this meltback can be used to calibrate the magnitude and position of the heat source [3.42]. Following a melt back calibration, the fiber tips resemble those in Fig. 3.15c.

3.2.3 Implications for Core Alignment

When two softened fiber tips are touched together during splicing, surface tension will act to align the claddings of the two tips together (Fig. 3.11), even if the claddings were initially offset. Considering the geometry in Fig. 3.11 the surface tension driven restoring force F_γ may be approximated by [3.3]

$$F_\gamma \approx \frac{\pi D_{\text{fiber}} \gamma \delta_{\text{clad}}}{L} \,, \tag{3.26}$$

where δ_{clad} is the offset, L is the width of fiber section which is hot enough to flow, $\delta_{\text{clad}} << D_{\text{fiber}}$, and $\delta_{\text{clad}} << L$. The length of fiber hot enough to flow, L, is hard to estimate since the fiber temperature, and hence its viscosity, varies smoothly along its length from the heated region to the unheated region. However, empirical observations of fiber deformation indicate that for the purposes of this analysis, L is on the order of 50 µm when splicing 125 µm diameter fibers so F_γ is on the order of 20 µN when δ_{clad} is 10 µm. This calculation shows that the surface tension forces experienced at the splice are strong enough to deflect the fiber according to previous calculations using (3.20). In Sect. 3.2.1 we showed that the gravitational force acting on a 10 mm long section of 125 µm diameter silica fiber amounts to about 2.7 µN of distributed force and induces a deflection of only 0.4 µm. Thus surface tension exerts significantly more lateral force than gravity. The viscous force resisting surface tension, F_η may be approximated by [3.3]

$$F_\eta \approx \frac{\pi D^2 \eta}{4L} \frac{\mathrm{d}\delta_{\text{clad}}}{\mathrm{d}t} \,, \tag{3.27}$$

where t is time. Equations (3.26-3.27) may be set equal to obtain a linear first order differential equation for the offset, δ_{clad}, which can be solved to

yield an approximate expression for the time dependence of the cladding self-alignment

$$\delta_{\text{clad}}(t) \approx \delta_{\text{clad}}|_{t=0} \exp\left(-\frac{4\gamma}{D_{\text{fiber}}\eta}t\right) . \tag{3.28}$$

Equation (3.28) shows that the time constant for cladding self-alignment, $\frac{D_{\text{fiber}}\eta}{4\gamma}$, scales with the fiber diameter. Since the viscosity is a sensitive function of temperature and surface tension is not, the time required for self-alignment will be largely determined by the splicing temperature. A typical viscosity at splicing temperatures is about 10^5 Poise so that the time required for a 125 μm cladding to self-align is on the order of a second.

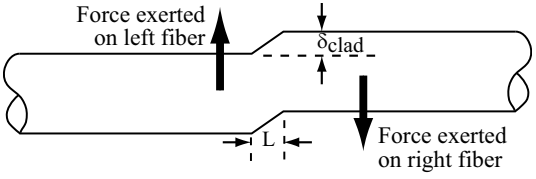

Fig. 3.11. Illustration of the geometry for (3.27) and (3.28). Softened portion of joined fiber tips has total length L while fiber tip offset is δ_{clad}. After [3.3]

When the cladding self-aligns, there will be a shearing flow of glass right at the fiber tip. This shearing flow causes a sideways displacement in the fiber core right at the fiber tips, called *sheared cores*, which can significantly increase the splice loss (Fig. 3.13a). For this reason, it is desirable to minimize δ_{clad}.

In the case that the fiber refractive index structure is concentric with the cladding, a small amount of cladding self-alignment (less than 1 μm) is beneficial as it will also naturally align the cores to each other. However, the core of an optical fiber may not be concentric with the cladding due to manufacturing problems. This phenomenon is also termed *core eccentricity* and can result in higher splice loss, which can be estimated either using the overlap integral or the Gaussian approximation that are discussed in the next Chapter. A typical fiber core eccentricity specification is 0.25 μm but occasionally fiber eccentricities can exceed 1 μm. Figure 3.12 shows two fiber tips with extreme core eccentricity. Core eccentricity can be a difficult problem but there are effective strategies for suppressing its effect. Figure 3.13b–d illustrates how core eccentricity and cladding self-alignment interact.

The simplest strategy is to align the two cores to each other so that the claddings are misaligned at the start of the splice (Fig. 3.13c). If the splicing temperature is very low and the splice duration is short, cladding self-alignment can be suppressed and the cores will be aligned to each other. However, low temperatures and short splice durations can often lead to reduced splice strength and reliability. At higher splicing temperatures and

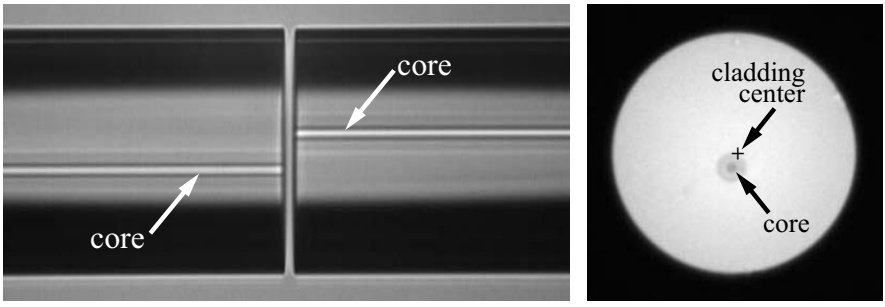

Fig. 3.12. Illustration of severe core eccentricity. Fiber diameter is 140 μm and core eccentricity is about 9 μm. (**a**) Sideview of fibers just prior to splicing. Notice how the fiber claddings are aligned to each other but the cores are offset by many μm. (**b**) Fiber viewed end on

longer splice times, the cladding self-alignment effect will cause a kink inside the narrow fiber region of width L which was heated to the highest temperatures. Unfortunately the optical signal traveling through the fiber usually cannot negotiate such a sudden bend over such a short distance so splice loss will usually be elevated in this situation.

A better approach is to over-compensate with extra lateral offset so that the surface tension will reduce the offset to a desirable level (Fig. 3.13d) [3.43]. In this case, the fiber cores can be made to align to each other at long distances but there will still be a certain amount of core deformation at the splice joint itself.

The best strategy to deal with core eccentricity is to rotate the fiber tips about their axes such that the angle of the eccentricity is the same in each fiber (Fig. 3.14). Once this rotational alignment is completed, the splice can proceed with standard cladding alignment. However, in many cases, the fibers have differing amounts of core eccentricity which limits the effectiveness of this technique. In the case that one fiber is perfectly concentric, this rotation-based strategy is completely useless. Thus, splicing with rotational core alignment is only beneficial when the cores have similar eccentricity. Fusion splicers designed for polarization-maintaining (PM) fiber (Sect. 9.2) include the capability to manipulate the rotational alignment of a fiber.

3.2.4 Fusion Splice Duration

It is interesting to note that the time required for fusion splice joint fabrication has been found to scale approximately linearly with fiber diameter. The fusion splice time for a 125 μm diameter silica fiber is usually on the order of about 5 s whereas a 250 μm diameter silica fiber will usually require on the order of 10 s. This observation is consistent with (3.28) where the time

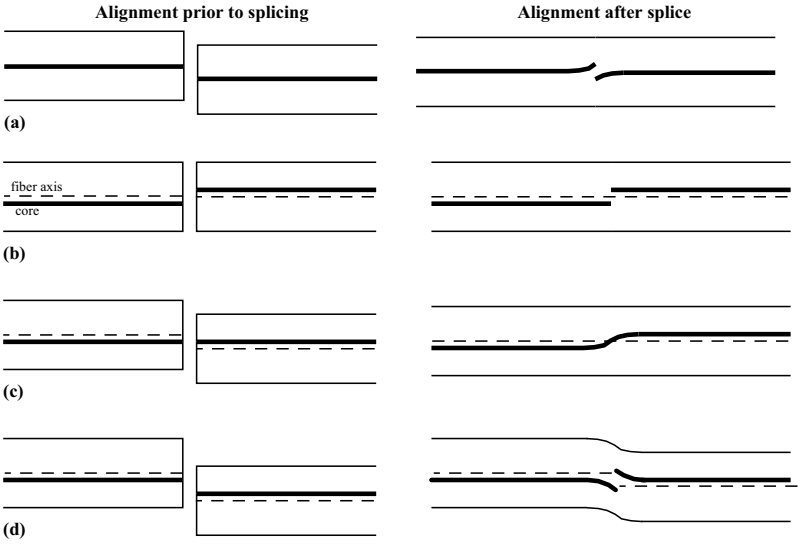

Fig. 3.13. Interaction between cladding alignment, core eccentricity, core alignment, and surface tension. Left side shows fiber following alignment but prior to splicing, corresponding right side depicts outcome of splice. Figure depicts core (*solid heavy line*) and center of cladding (*dashed line*). (**a**) Concentric fiber cores with claddings misaligned. Note the characteristic core deformation of sheared cores. The resulting deformation generally results in elevated splice loss. (**b**) Eccentric core fibers aligned to each other's claddings. Such lateral misalignment of the cores results in high splice loss. (**c**) Eccentric core fibers aligned to each other's core. Usually, the fact that the cores are laterally misaligned far from the completed splice results in high loss even though the cores are aligned locally at the finished splice. (**d**) Eccentric fibers offset an extra amount to ensure that cores are aligned far from the completed splice despite local deformation at the splice. This case often results in lower loss than case (**c**). After [3.44, 3.45]

constant for cladding self alignment was shown scale linearly with the fiber diameter. Fusion splicing of silica fibers is usually performed when the glass is heated to about 2100° C, regardless of fiber diameter, so the viscosity of the heated glass is about the same regardless of fiber diameter. Surface tension provides the main driving force for joint formation, just as it does for cladding self alignment.

3.2.5 Neckdown, Dissimilar Fiber Diameters, and Dissimilar Fiber Viscosities

When a splice is held at a very high temperature for a long period of time, for example to encourage dopant diffusion (see Sect. 3.3), surface tension can reduce the fiber diameter in the immediate vicinity of the splice by squeezing molten glass away from the splice region. Figure 3.15 depicts various stages of neckdown in a standard SMF. Neckdown increases the splice loss by creating

a very localized physical taper in the fiber. This neckdown phenomenon is closely related to a stability problem in fluid mechanics. When the ratio between the length and the diameter of a cylinder of liquid confined by surface tension is greater than π, it is unstable and the slightest perturbation to the liquid diameter encourages surface tension to squeeze down and pinch off the cylinder into two separate droplets [3.46,3.47]. The driving force for neckdown results from the internal pressure P_γ created by the surface tension squeezing on the fiber circumference as depicted in Fig. 3.9b. It is easy to appreciate the unstable nature of this process since a smaller fiber diameter results in an even stronger driving force. Ultimately, the surface tension squeezes the molten glass down to the point that the fibers pull apart and ball up at their tips (Fig. 3.15c). This instability occurs at a fusion splice when

$$\frac{L}{D_{\text{fiber}}} > \pi \,, \tag{3.29}$$

where L is the characteristic length of the softened zone of fiber. As noted earlier, the characteristic length of the molten fiber section during a fusion splice is hard to quantify since the temperature and hence the viscosity varies smoothly between the heated and unheated regions. Estimates for L depend on the viscosity threshold chosen to discriminate between softened and solid fiber. For a 125 µm diameter fiber to experience this instability and resulting neckdown, L must be on the order of 400 µm. A 400 µm long section of fiber centered on a fusion splice will indeed be heated and softened to some degree so we anticipate that this surface tension instability will cause the fiber to neckdown. At normal splicing temperatures ($\sim$2050° C) and splice times (a few seconds), the viscosity of the fiber far from the splice is high enough to ensure that neckdown occurs too slowly to have any significant effect. However when a fusion splice is heated to much higher temperatures (causing a much wider hot zone width) or held at high temperatures for a long enough amount of time, neckdown will occur.

When splicing single-mode fibers, splice loss mainly results from disturbances or changes in the core region of the fiber. Thus, fibers with different cladding diameters can be spliced to each other with low loss providing the core structures in both fibers are similar. An image of a fusion splice between fibers of dissimilar cladding diameters but similar core diameters appears in Fig. 3.16. As discussed in Sect. 3.1, less heat is required to soften smaller diameter fibers and as Fig. 3.9b shows, the driving force for neckdown is stronger. Consequently, it is usually beneficial to offset the heat source and preferentially heat the larger diameter fiber. Even if the cladding diameters are identical, a viscosity difference between the fibers can necessitate offsetting the heat source to prevent neckdown in the lower viscosity fiber. Offset heating is discussed in Sect. 8.2.5.

An interesting patent describes a technique for fabricating a fiber tip with an expanded core from a dissimilar fiber diameter splice [3.48]. Surface-tension-induced deformation at the splice joint between dissimilar fibers

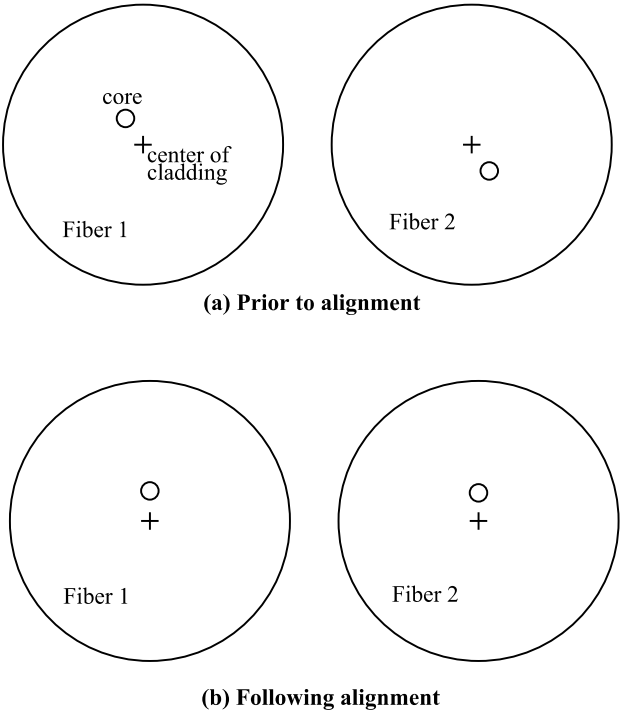

Fig. 3.14. Rotational alignment of two fibers with comparable eccentricities. Fibers are viewed end on showing core position (*small circle*) and center of cladding (*plus sign*). (**a**) Fibers initially have a random angle between their cores and the center of their claddings. (**b**) Angle of fiber cores aligned to each other

causes the core diameter of the smaller fiber to increase slightly (Fig. 3.17). The completed splice can be cleaved exactly at the joint to yield a fiber tip with an expanded core diameter and hence an expanded MFD. This expanded MFD results in a longer free-space collimation length, lower power density at the fiber tip, and greater tolerance to lateral misalignments.

3.2.6 Bubbles, Airlines, and Air Holes

For various reasons, voids may be present in the vicinity of a splice. Dirt on the fiber tips can become trapped at the splice and release gasses that form a *bubble* (Fig. 3.18). Defects in the fiber manufacturing process can lead to *airlines* in the fiber. Some fibers, specifically microstructured fibers are deliberately produced with *air holes* running down their entire length. Microstructured fibers are discussed in Sect. 9.5.

A bubble is usually formed by volatile gases emitted by contaminants when they are heated to splicing temperatures. A clean splicing environment including a clean heat source and proper use of prefusion fiber tip cleaning

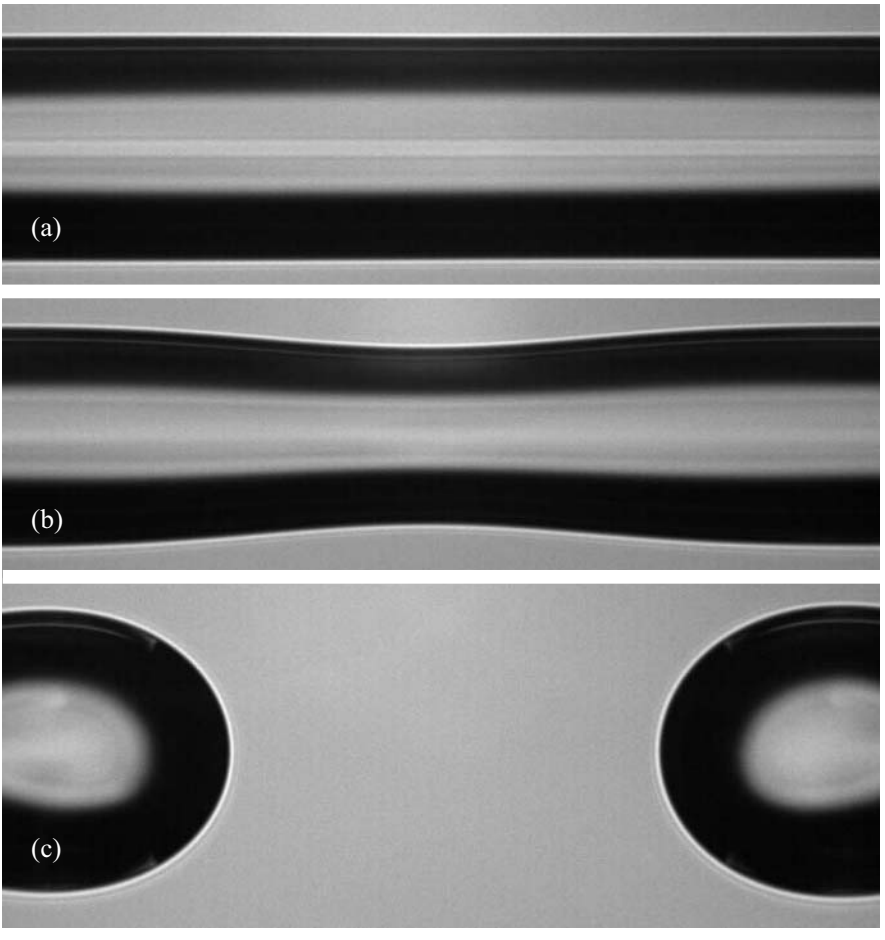

Fig. 3.15. Surface tension driven neckdown of ordinary SMF spliced at high temperature. (**a**) Fiber immediately following joint formation. (**b**) Fiber after many more seconds of high temperature heating. Note the pinching effect of surface tension and the faded appearance of the core resulting from substantial dopant diffusion. (**c**) Fiber tips fully separated and balled up by surface tension

can help to reduce the occurrence of bubbles. Bubbles usually do not reduce the ultimate strength of a fusion splice since surface tension ensures that they have smooth walls which do not serve as stress concentrators or crack nucleation sites. However, bubbles typically induce substantial splice loss unless they occur near the cladding surface, far away from the guided optical signal. Bubbles will nearly always confound loss estimation routines (Chap. 5).

An incompletely formed seam between the fiber tips can sometimes be mistaken for a bubble (Fig. 3.19). Surface tension serves to smooth the seam that forms between the two fiber tips during splicing but if the splice temper-

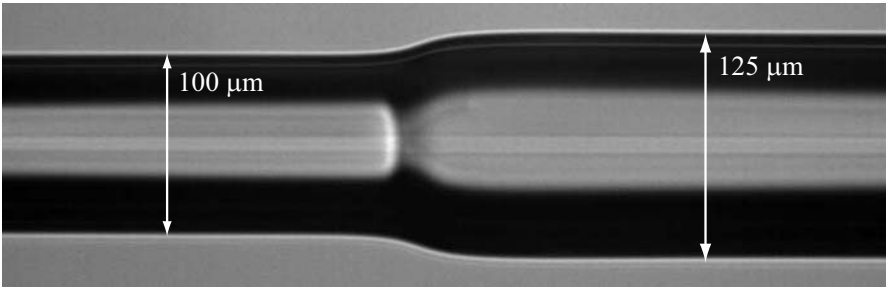

Fig. 3.16. Fusion splice between dissimilar diameter SMF. Fiber diameters are 100 μm and 125 μm for the lefthand and righthand fibers, respectively. Core diameter is about 8 μm in both fibers

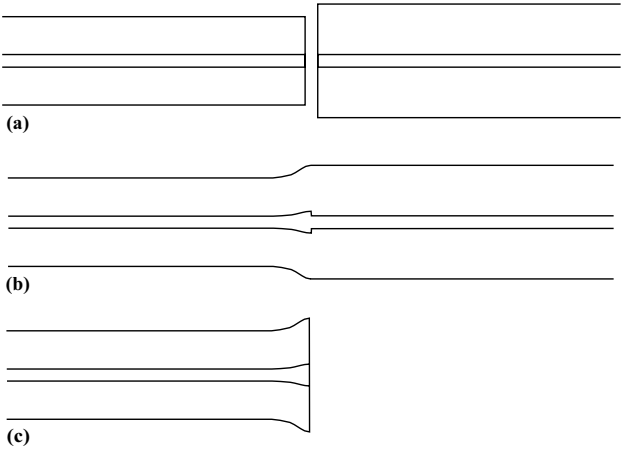

Fig. 3.17. Illustration of expanded-core fiber tip fabricated via a dissimilar diameter fiber splice. (**a**) Fibers prior to splice. (**b**) Fibers immediately following splice. Left fiber exhibits core expansion from surface tension driven deformation. (**c**) When the right fiber is cleaved away an expanded-core fiber tip results. After [3.48]

ature is sufficiently low or if the splice duration sufficiently brief, this process may not be completed. When the splice is viewed at high magnification, the resulting deformations in the fiber cladding at the splice joint can refract the light so as to give the appearance of either a bubble or a vertical line at the exact site of the splice. Sometimes a seam can indicate reduced strength and reliability or elevated reflectance. A seam is a common side-effect of low-temperature splices, which are discussed in detail in Sect. 8.2.4.

As discussed earlier, surface tension will act to shrink voids in a softened fiber but it will be opposed by the glass viscosity and possibly by the presence of gasses trapped in the voids. An analysis of the surface tension driven collapse of an empty spherical or cylindrical void in an infinite viscous medium

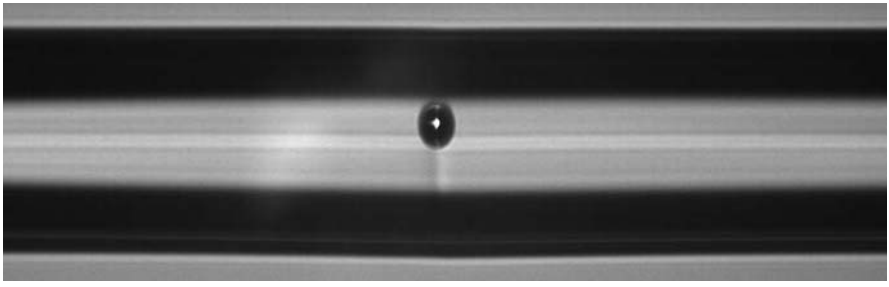

Fig. 3.18. Image of a bubble at the fusion splice between two ordinary SMF fibers. Bubbles such as this one cause extremely high splice loss but often do not significantly reduce the tensile strength of the splice. This bubble resulted from dirt on the fiber tip end face. Proper fiber handling and prefusion cleaning significantly reduces the occurrence of such bubbles

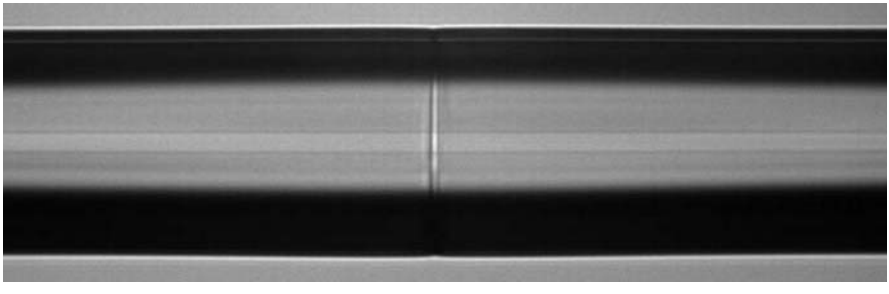

Fig. 3.19. Image of a splice with an incompletely formed seam at the joint. The vertical line results from refraction of light at the surface of the splice joint

was first performed within the context of metal powder sintering [3.49]. Curiously, the surface-tension-driven collapse velocity of a void's surface, V_{collapse}, is independent of its size and is the same whether it is a spherical bubble or a cylindrical hole

$$V_{\text{collapse}} = \frac{\gamma}{2\eta} \,, \tag{3.30}$$

where γ is the surface tension and η is the viscosity. Trapped gasses will resist this surface driven collapse and reduce the collapse velocity. In fact, trapped gasses usually cause bubbles to expand and ultimately rupture when heated to fusion splicing temperatures. Bubble rupture can have a disastrous effect on a fiber splice because it can cause substantial core deformation.

3.3 Dopant Diffusion

In an optical fiber, both the optical properties, such as refractive index, and mechanical properties, such as sonic velocity or softening point, depend on

the local dopant concentration. When an optical fiber is heated to high temperatures, such as those encountered during fusion splicing, the dopants in the fiber can diffuse through the glass host material, thus changing the optical and mechanical properties of the fiber. Local gradients in the dopant concentration provide the driving force for dopant diffusion.

Dopant diffusion is not unique to the fusion splice process; it also occurs during the fiber draw process and even to some extent during preform fabrication. However, the high temperatures encountered during fusion splicing coupled with the small dimensions and hence large concentration gradients present in the fiber can induce substantial dopant diffusion, which can be either beneficial or deleterious [3.50]. Various investigations have shown that dopant diffusion can be harnessed to reduce optical fiber splice loss between dissimilar fibers [3.51–3.53]. The use of dopant diffusion as a special splicing strategy is detailed in Sect. 8.2.3.

Introductory treatments of mass diffusion, and the more general field of mass transfer, are available in [3.1, 3.2]. In this section we present a detailed analysis of the specific topic of dopant diffusion in optical fibers. We begin with the theory of dopant diffusion and derive a general expression for the evolution of a radially symmetric dopant concentration. We then discuss published values of diffusion coefficients pertinent to optical fibers. We conclude with specific dopant diffusion examples.

3.3.1 Theory of Dopant Diffusion

We begin our analysis of dopant diffusion with Fick's law of diffusion in a one-dimensional geometry [3.1]

$$j_{\mathrm{x}} = -D\frac{\mathrm{d}C}{\mathrm{d}x}\ , \tag{3.31}$$

where j_{x} is the molecular flux of the diffusing species in units of molecules/m^2 s, D is the dopant diffusion coefficient in units of m^2/s, C is the local dopant concentration in units of molecules/m^3, and x is the relevant coordinate direction. D depends on the dopant species, the host material, and the local temperature as we shall see below. Readers familiar with heat transfer will immediately recognize that (3.31) is identical to Fourier's law of heat diffusion where temperature is analogous to dopant concentration, molecular flux is analogous to heat flux, and the dopant diffusion coefficient is analogous to thermal conductivity (compare to (3.9)). Consequently, the equations of heat conduction can be directly applied to solve dopant diffusion problems.

The basic constitutive equation for diffusion, (3.31), may be developed into the diffusion equation which is a partial differential equation relating the local dopant concentration gradients to the time-dependent dopant concentration. We define an infinitesimal control volume in Cartesian coordinates (Fig. 3.20) in which there is a molecular flux obeying (3.31) across all 6 surfaces. The rate of change of the total amount of dopant in the control volume,

$\frac{\partial}{\partial t}(\Delta x \cdot \Delta y \cdot \Delta z \cdot C)$, can be related to the dopant flux across the control volume surfaces

$$\Delta x \Delta y \Delta z \frac{\partial C}{\partial t} = \Delta y \Delta z (j_{x+\Delta x} - j_x) + \Delta x \Delta z (j_{y+\Delta y} - j_y) + \Delta x \Delta y (j_{z+\Delta z} - j_z) \ . \tag{3.32}$$

If D is constant then dividing through by $\Delta x \cdot \Delta y \cdot \Delta z$ and allowing Δx, Δy, and Δz to each approach zero yields the diffusion equation

$$\frac{\partial C}{\partial t} = \nabla \cdot (D \nabla C) \ . \tag{3.33}$$

The partial differential equation in (3.33) describes the general case of dopant diffusion for an arbitrary geometry. Even though some fibers, specifically polarization-maintaining (PM) fibers (Sect. 9.2), are *not* axisymmetric, the core of nearly all fibers, including most PM fibers, *are* axisymmetric so we can restrict our attention to axisymmetric geometries when considering dopant diffusion in the fiber's core. Moreover, Sect. 3.1 showed that the temperature of a heated fiber is nearly uniform with respect to radial position so it is reasonable to assume that the diffusion coefficient, D, is constant with respect to r. Diffusion in the axial direction can usually be neglected since axial temperature gradients occur over many hundreds of μm and the axial concentration gradients within a fiber are very small. Axial diffusion of dopants does occur across the interface of a fusion splice joint between dissimilar fibers, but this phenomenon has almost no effect upon fusion splice loss. However, we shall see in Sect. 4.1.5 that axial diffusion across the interface between dissimilar fibers can help to suppress reflections at fusion splices.

If we neglect axial and azimuthal diffusion, then (3.33) yields a simplified dopant diffusion equation in radial coordinates

$$\frac{\partial C}{\partial t} = D \frac{1}{r} \frac{\partial}{\partial r} \left(r \frac{\partial C}{\partial r} \right) \ . \tag{3.34}$$

Equation (3.34) has a closed form solution for only the simplest initial dopant concentrations. For example, if the initial dopant concentration, $C_0(r)$, is a Gaussian function

$$C_0(r) = \frac{C_{\text{total}}}{\pi r_0^2} \exp\left(-\frac{r^2}{r_0^2} \right) \ , \tag{3.35}$$

where r_0 characterizes the initial width of the Gaussian distribution and C_{total} is the total amount of dopant in the fiber, then the solution to (3.34) at any radius r and later time t is also a Gaussian

$$C(r,t) = \frac{C_{\text{total}}}{4\pi D(t + \frac{r_0^2}{4D})} \exp\left(-\frac{r^2}{4D(t + \frac{r_0^2}{4D})} \right) \ . \tag{3.36}$$

Thus we observe that an initially Gaussian distribution will diffuse into a broader Gaussian distribution while conserving the total amount of dopant.

Actually, all initial dopant concentrations asymptotically approach a Gaussian dopant distribution after a long enough time period has elapsed. However, most initial optical fiber dopant distributions are *not* Gaussian (they may be a "top-hat", a ring, or other shapes) and their evolution is of much practical interest.

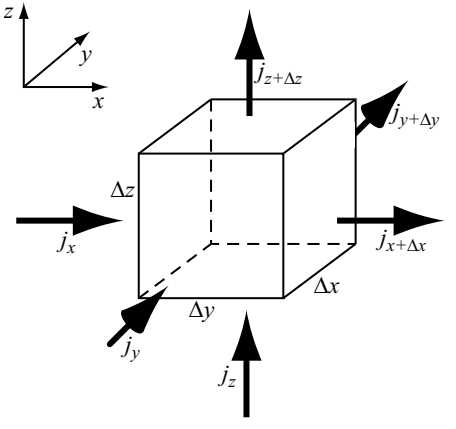

Fig. 3.20. Illustration of Cartesian control volume used for (3.32–3.33)

Arbitrary initial dopant concentrations require numerical solution techniques. Given an arbitrary initial dopant concentration $C_0(r)$ at time $t = 0$, Fourier series may be used to express the dopant distribution at any radius r and time t by [3.55]

$$C(r,t) = \frac{2}{R_{\text{fiber}}^2} \sum_{n=1}^{\infty} \exp(-D\alpha_n^2 t) \frac{\mathrm{J_0(r\alpha_n)}}{\mathrm{J_1^2(R_{fiber}\alpha_n)}} a_n \ , \tag{3.37}$$

where

$$a_n = \int_0^{R_{\text{fiber}}} r C_0(r) \mathrm{J_0}(R_{\text{fiber}}\alpha_n) \mathrm{d}r \ , \tag{3.38}$$

where J_0 is the Bessel function of the first kind, order 0, and the eigenvalues, α_n, are determined from $J_0(R_{\text{fiber}}\alpha_n) = 0$.

Equations (3.37) and (3.38) are somewhat cumbersome. Instead, Green's functions yield a particularly convenient and efficient way to numerically solve (3.34) for $C(r,t)$ given an arbitrary initial concentration distribution $C_0(r)$ [3.56]

$$C(r,t) = \frac{1}{2Dt} \int_{r'=0}^{r'=\infty} C_0(r')\, r' \, \exp\left(-\frac{r^2 + r'^2}{4Dt}\right) \mathrm{I_0}\left(\frac{rr'}{2Dt}\right) \mathrm{d}r' \ , \tag{3.39}$$

where $\mathrm{I_0}$ is the modified Bessel function of the first kind, order 0, and r' is a dummy variable of integration. Unfortunately, (3.39) cannot be solved

analytically even when the initial dopant distribution is very simple, such as in a step index fiber. A single numerical integration of (3.39) rapidly yields the dopant distribution given any initial dopant concentration. When the initial dopant distribution is a step function, (3.39) is a form of the integral "$J(x, y)$" found in [3.57] where asymptotic solutions are also provided.

In a step-index fiber whose core is comprised of a single dopant, the initial concentration distribution, $C_0(r)$, is a uniform C_0 from r=0 to $r = R_{\text{core}}$ so we can simplify (3.39) to yield

$$C_{\text{si}}(r,t) = \frac{1}{2Dt} \int_{r'=0}^{r'=R_{\text{core}}} C_0 \; r' \; \exp\left(-\frac{r^2 + r'^2}{4Dt}\right) \; \text{I}_0\left(\frac{rr'}{2Dt}\right) \; \text{d}r' \; , \tag{3.40}$$

where $C_{\text{si}}(r,t)$ is the dopant concentration for a step-index fiber.

Notice how D always appears with t in (3.39) and (3.40). From this we conclude that the heating time can be increased to compensate for a slow diffusion coefficient or the heating time can be decreased to compensate for a fast diffusion coefficient. Furthermore, a dimensional analysis of (3.33) reveals a non-dimensional parameter, τ_D, which characterizes the extent of dopant diffusion

$$\tau_{\text{D}} = \frac{Dt}{\delta_{\text{D}}^2} \; , \tag{3.41}$$

where δ_{D} is a characteristic length scale for the diffusion. If we set δ_{D} equal to the core radius of a step index fiber, R_{core}, and we let $\hat{r}$ denote the normalized radial position such that $\hat{r}$=r/R_{core}, we can express (3.40) in a non-dimensional form

$$C_{\text{si}}(\hat{r},\tau) = \frac{1}{2\tau_{\text{D}}} \int_{r'=0}^{r'=1} C_0 \; \hat{r} \; \exp\left(-\frac{\hat{r}^2 + r'^2}{4\tau_{\text{D}}}\right) \; \text{I}_0\left(\frac{\hat{r}r'}{2\tau_{\text{D}}}\right) \; \text{d}r' \; . \tag{3.42}$$

By setting τ_{D} of (3.41) equal to unity we can obtain an equation which relates the characteristic diffusion length to the diffusion coefficient and the time interval for the diffusion

$$t_{\text{diff}} = \frac{\delta_{\text{D}}^2}{D} \; . \tag{3.43}$$

Equation (3.43) is analogous to (3.17) when the fiber radius R_{fiber} replaces δ_{D} and when the thermal diffusivity, α_{T} replaces the dopant diffusivity, D, because both dopant diffusion and heat conduction are diffusion phenomena. The factor of 4 in (3.17) is only a matter of convention. Equation (3.43) shows that the time required for a dopant to diffuse a certain distance varies with the square of that distance.

Equation (3.43) provides important insights into the nature of dopant diffusion. Since the time required for diffusion scales with the square of the characteristic length, diffusion proceeds more rapidly in a small core fiber than in a larger core fiber. Thus, multimode fibers are usually not affected by dopant diffusion since their characteristic length scale (i.e. core radius) is

on the order of tens of μm. On the other hand, very small core single-mode fibers, such as erbium-doped fiber (EDF), can have core radii as small as 1 μm, so they are extremely vulnerable to dopant diffusion, even when the splice duration is short (<1 s) and the splicing temperatures are relatively low (<∼ 2000° C).

As a dopant diffuses, its characteristic length scale increases and so the rate of diffusion decreases. Thus, when held at a fixed temperature, a dopant distribution changes most rapidly at the beginning of the heating, and more slowly as time goes on. When a splice is made between two step-index single-mode fibers with identical dopant species but different core diameters, the smaller core will initially diffuse more rapidly since it has a smaller characteristic length scale. As the diffusion progresses, the smaller core will "catch up" to the larger core diameter and both dopant distributions will approach a similar Gaussian shape. In this way, dopant diffusion can help to reduce the splice loss between dissimilar waveguides by making one fiber's core structure, and hence its mode field shape, more similar to another [3.51–3.53]. However, one consequence of (3.34) is that the evolution of the fiber refrac-

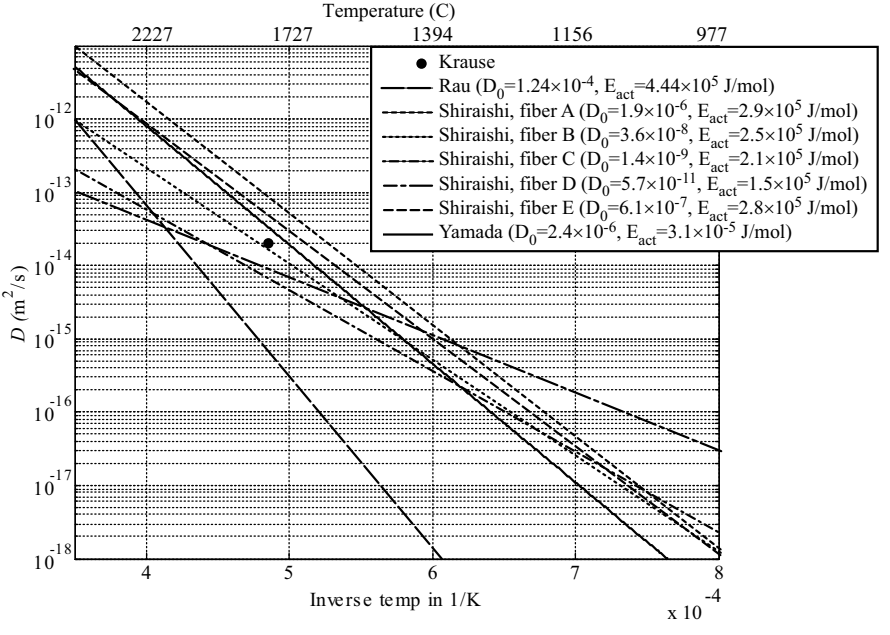

Fig. 3.21. Germania diffusion coefficient in fused silica from several sources in the literature. Krause refers to [3.50], Rau refers to [3.58], Shiraishi refers to [3.59], and Yamada refers to [3.60]. D_0 and E_{act} are parameters in (3.44). A large portion of the discrepancy between these curves is thought to stem from differences in the glass composition such as the presence or absence of co-dopants or contaminants. For example, Shiraishi fiber A contains some chlorine

tive index profile is largely predetermined by the initial dopant distribution. The diffusion of the dopants can only be controlled by controlling the fiber temperature and the time of exposure. Dopant diffusion cannot be used to produce an arbitrary index profile or an arbitrary mode field shape. Practical implementations of dopant diffusion are discussed in more detail in Sect. 8.2.3.

When dopant diffusion occurs at a fusion splice, the transition between the original and diffused regions of the fiber can have a significant impact on the splice loss. Cultivating a smooth transition between these two regions of fiber is critical to obtaining a low-loss fusion splice. In Chap. 4 we discuss such transition loss and provide general numerical tools for predicting the loss of an optical fiber whose index profile changes along its length.

3.3.2 Dopant Diffusion Coefficients

Various investigations have shown that diffusion coefficients in silica obey an Arrhenius relation meaning that the diffusion coefficient scales with the exponential of the inverse temperature. This relationship can be expressed as:

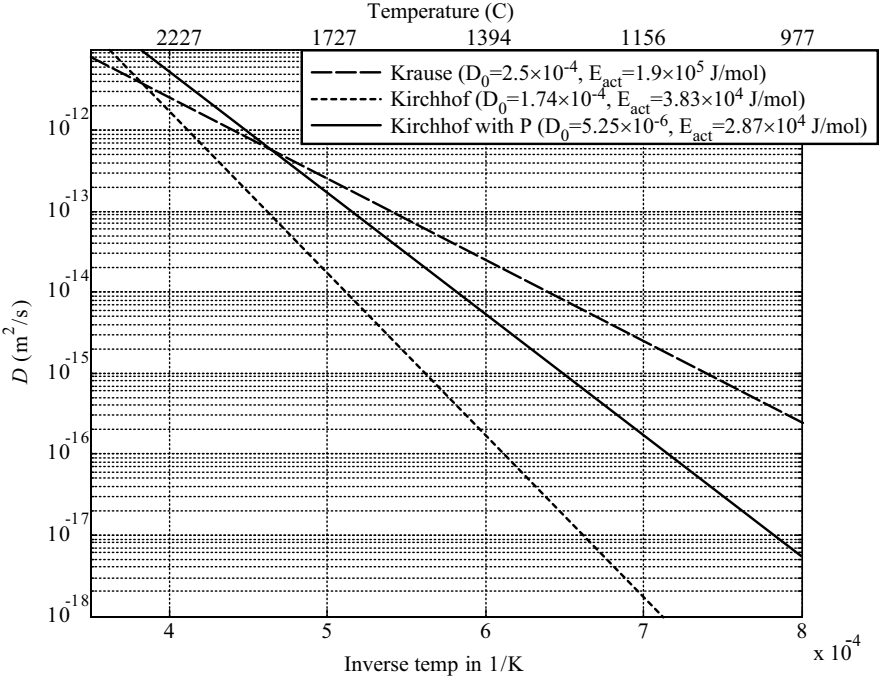

Fig. 3.22. Fluorine diffusion coefficient in fused silica from several sources in the literature. Krause refers to [3.50] and Kirchhof refers to [3.61] which incorporates data from [3.62]. D_0 and $E_{\rm act}$ are parameters in (3.44). Kirchhof with P refers to the presence of 1.6 mole-% phosphorus as a co-dopant with fluorine

$$D = D_0 \exp\left(-\frac{E_{\text{act}}}{\mathcal{R}T}\right) , \tag{3.44}$$

where D_0 is a leading coefficient in units of m^2/s, E_{act} is the activation energy in units of J/mole, T is the temperature in Kelvins, and $\mathcal{R}$ is the ideal gas constant or universal gas constant, which can be expressed as 8.3145 J/mole-K. At splicing temperatures, dopant diffusion coefficients in silica fibers are generally on the order of $10^{-13}\,\text{m}^2/\text{s}$. Figures 3.21 and 3.22 summarize diffusion coefficient measurements for germania and fluorine in fused silica respectively. These measurements show that at given temperature, fluorine diffuses more rapidly than germania [3.50].

There is significant variation in measured values for diffusion coefficients. Part of this variation has been attributed to the fact that the diffusion of one species of dopant can depend on the presence of another. For example, Kirchhof [3.61] argues that the discrepancy between his measurements of fluorine's diffusivity in fused silica (dotted line in Fig. 3.22) and Krause's measurements (dashed line in Fig. 3.22) partly stem from the presence of phosphorus in Krause's samples. In other words, the diffusion coefficient D in (3.33) is not really a constant because it depends on the local dopant concentration. Despite these non-linearities, useful order of magnitude estimates can be obtained when considering the dopant diffusion coefficient to be a constant.

3.3.3 Diffusion Examples

To illustrate the practical implications of dopant diffusion theory, we will consider two examples. In the first example, we will examine the diffusion of a single dopant in a step-index SMF. In the second example, we will consider the more complicated case of multiple dopant diffusion.

Conventional single-mode fiber is typically composed of an 8.5 μm diameter core which is doped with about 3.5 mole-% germania to make its index about 0.005 higher than the surrounding pure-silica cladding. Sometimes other dopants are added to the fiber but in our example we will assume that germania is the only dopant and that the difference between the local refractive index of the glass and the pure-silica cladding, $n - n_0$, scales linearly with the local germania concentration. Figure 3.23a depicts the initial refractive index profile of the fiber (solid line) and the refractive index profile after various amounts of diffusion (broken lines). The germania concentration, and hence the refractive index profile, was determined from (3.40) with diffused index profiles corresponding to normalized diffusion, τ_{D}, of 0.1 and 1.0.

Mode fields corresponding to the refractive index profiles of Fig. 3.23a were computed according to the methods of Chap. 4 and are depicted in Fig. 3.23b. Notice how the mode field expands in diameter as the core dopants diffuse outward. This phenomenon has been employed to create expanded

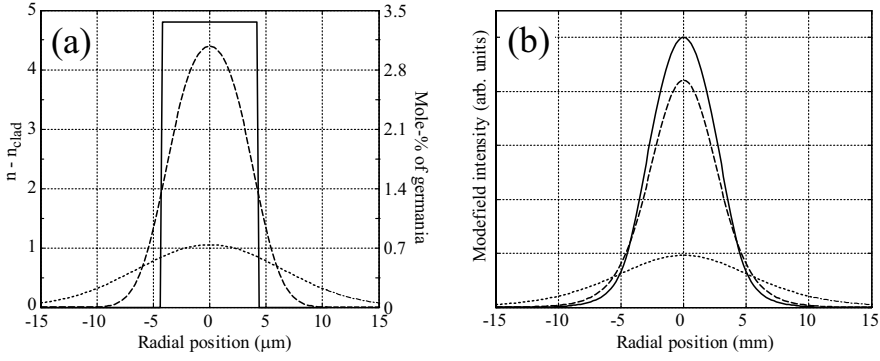

Fig. 3.23. Illustration of single dopant diffusion and its effects in an idealized step index fiber. The diffusion was computed with (3.40) and the traces depict three cases: $\tau_{\mathrm{D}} = 0$ (*solid line*), $\tau_{\mathrm{D}} = 0.1$ (*dashed line*), $\tau_{\mathrm{D}} = 1$ (*dotted line*). (**a**) Refractive index and dopant concentration profiles for an idealized germania-doped fiber. The difference between the local refractive index and the cladding refractive index, $n - n_{\mathrm{clad}}$, is assumed to be linearly proportional to the dopant concentration. The cladding refractive index, n_{clad}, is assumed to be equal to the refractive index of pure silica (about 1.444 at 1550 nm). (**b**) Corresponding mode field intensity patterns computed according to the method described in Sect. 4.4.3. The mode field diameters computed with (4.41) are 10.4 μm (*solid line*), 12.3 μm (*dashed line*), 26 μm (*dotted line*)

mode field fibers useful for fiber beam expanders and fiber collimators [3.54, 3.59, 3.63, 3.64]. Equation (1.6) shows that the normalized frequency of an optical fiber scales with the core radius R_{core} times the square root of the relative index difference between the core and cladding, $\sqrt{\Delta}$. In other words, the square of the normalized frequency, V, scales with the square of the core radius times the index difference in the core, which in turn scales with the total amount of dopant in the fiber. Based on this observation we conclude that in a fiber with a single diffusing dopant, the normalized frequency, V, of the fiber does not change. In the next Chapter we show that V determines the total number of guided modes in a fiber, therefore the number of guided modes remains constant during diffusion in fiber containing a single dopant. However, when multiple dopants are present, especially when one dopant raises the refractive index and another lowers it, this principle may not apply, so diffusion might change the normalized frequency of the fiber and hence the number of guided modes.

Contemporary fiber designs, such as DCF, utilize multiple dopants since they require depressed, as well as elevated, refractive index regions [3.52,3.53]. Fluorine is a common choice for an index lowering dopant and has been implicated as a source of elevated fusion splice loss when splicing certain fiber types [3.53]. In the next example we consider a fiber in which multiple dopants, specifically fluorine and germania, participate in the diffusion. The evolution of the refractive index profile is determined by separately computing

the diffusion of each dopant and its associated refractive index profile, and then summing them to obtain the total refractive index profile.

For the purposes of this new example, we have assumed diffusion coefficients of $1 \times 10^{-13}\,\mathrm{m}^2/\mathrm{s}$ and $1 \times 10^{-12}\,\mathrm{m}^2/\mathrm{s}$ for germanium and fluorine, respectively. These values are consistent with the data in Figs. 3.21 and 3.22 assuming a temperature on the order of 1950° C. The local refractive index of the fiber is assumed to scale linearly with the local concentration of fluorine and germania. The initial refractive index and germania concentration profile is depicted by the solid line in Fig. 3.24a. The initial refractive index and fluorine concentration is depicted by the solid line in Fig. 3.24b. The total initial refractive index profile is the sum of the two constituent index profiles which is depicted by the solid line in Fig. 3.24c.

After a heating time of 4 seconds, the germania dopant concentration, and hence the portion of the refractive index due to germania, is equal to the dotted curve in Fig. 3.24a. Likewise, after a heating time of 4 seconds, the fluorine dopant concentration, and hence the portion of the refractive index due to fluorine, is equal to the dotted curve in Fig. 3.24b. The total refractive index profile is the sum depicted by the dotted line in Fig. 3.24c. Mode fields corresponding to the index profiles of Fig. 3.24c were computed according to the methods of Chap. 4 and are depicted in Fig. 3.24d. It is apparent that the dopant diffusion substantially alters the fiber refractive index profile. The difference between the mode field shapes can be quantified by using the overlap integral presented in the next Chapter to compute the optical coupling loss, which is about 0.5 dB.

As the number of dopant species increases, the evolution of the refractive index profile becomes more complex. In these examples, we have assumed purely linear dopant diffusion (D is assumed constant). In reality D may depend on the local concentration of the dopant, or even on the local concentration of other dopants. This behavior is not well characterized in the literature and is consequently often ignored when making dopant diffusion calculation.

3.4 Stress and Strain

Optical fibers contain residual elastic stresses and strains that result from their composition and from the fiber fabrication process [3.65]. By residual, we mean that stresses and strains are present in the fiber even when there are no external forces applied to the fiber. In some cases, the residual stresses and strains are critical to the guiding properties of the fiber. For example, most polarization-maintaining (PM) fibers have a non-radially symmetric residual stress field that causes a desirable birefringence.

At room temperature, a fiber may be considered to be an elastic solid meaning that the stresses and strains are linearly related [3.30]. Residual stresses and strains influence the optical and mechanical properties of

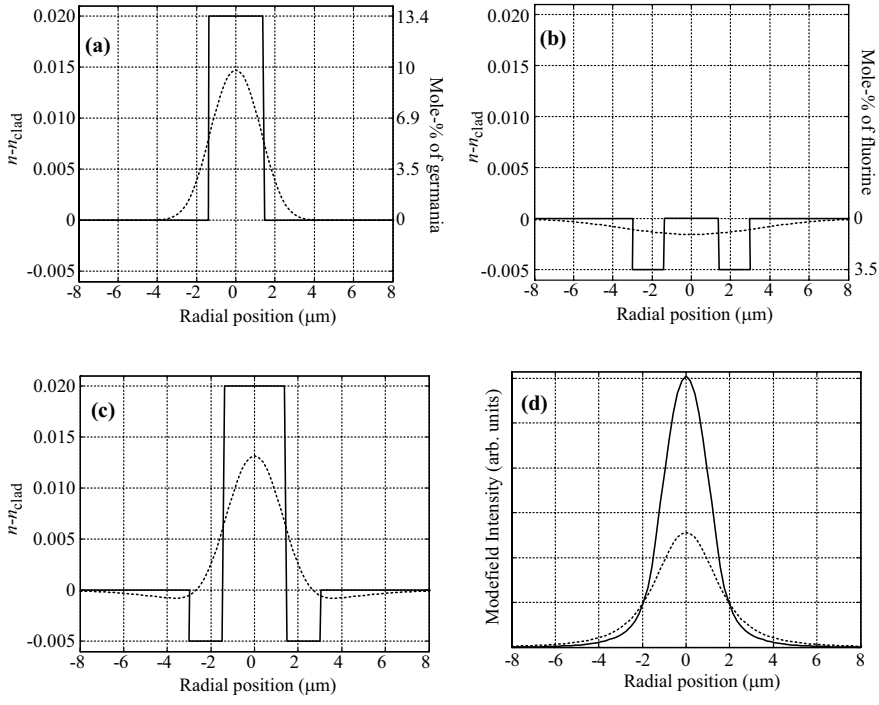

Fig. 3.24. Illustration of multiple dopant diffusion. The diffusion was computed with (3.39) and the traces in the plots correspond to the original state of the fiber (*solid line*) and the fiber following dopant diffusion (*dotted line*). The difference between the local refractive index and the cladding refractive index, $n - n_{\text{clad}}$, is assumed to be linearly proportional to the local dopant concentrations. The cladding refractive index, n_{clad}, is assumed to be equal to the refractive index of pure silica (about 1.444 at 1550 nm). (**a**) Germania concentration and corresponding refractive index profiles. (**b**) Fluorine concentration and corresponding refractive index profiles. (**c**) Total fiber refractive index profile. (**d**) Corresponding mode fields computed according to the methods described in Sect. 4.4.3

the fiber [3.66–3.71]. High temperatures experienced during fusion splicing changes the fiber's residual stress and strain state in the immediate vicinity of the splice and can thus change the fiber's optical and mechanical properties [3.72–3.74]. A good introduction to stresses, strains, and elasticity theory is available in [3.30]. Good reviews of the stresses and strains in optical fibers are available in [3.65, 3.75–3.77]. In this section we will discuss how fusion splicing interacts with the fiber's residual stress and strain state.

3.4.1 Source of Stress and Strain in Optical Fibers

There are two main mechanisms for inducing residual stresses and strains in optical fibers: *thermal stress* and *draw-induced mechanical stress*. Ther-

mal stress results from radial variations in the thermal expansion coefficient of the fiber. These radial variations in thermal expansion result from radial variations in dopant concentration. Silica has a thermal expansion coefficient of about $5.5 \times 10^{-7}\,\mathrm{K}^{-1}$ from room temperature up to its strain point [3.20]. Most dopants, such as germania, phosphorus, and boron increase the thermal expansion coefficient of silica glass. A few dopants, notably fluorine and titania, lower the thermal expansion coefficient of silica glass. The change in thermal expansion coefficient scales linearly with the dopant concentration when the concentration is low [3.78].

When a fiber preform is fabricated or a fiber is drawn, the various glass components are initially in mechanical equilibrium at a high temperature. As the glass cools and solidifies, it thermally contracts. The glass regions with a higher thermal expansion coefficient attempt to contract a larger amount upon cooling. Other glass regions with a lower thermal expansion coefficient resist this large thermal contraction. The end result is a residual state of thermal stress in which the pure silica fiber regions generally experience compressive axial stress while the highly doped regions of the fiber generally experience tensile axial stress (Fig. 3.25a). In order to satisfy mechanical equilibrium, the residual thermal stress in the cladding is much smaller than that in the core since the cladding has a much larger cross sectional area than the core. Axial thermal residual stresses in an SMF core are generally on the order of 20 MPa. General solutions to thermal residual stress in an optical fiber are available in [3.75, 3.77].

Most PM fibers derive their birefringence from thermal stress. The cladding of many PM fibers includes regions of cladding glass with a particularly large thermal expansion coefficient, termed stress-applying members. When these fibers cool down following the draw process, substantial residual stresses result from the difference in thermal expansion between the low- and high-thermal expansion regions. The regions are distributed in a non-radially symmetric manner to impart a non-radially symmetric stress field that causes birefringence in the fiber. PM fibers are discussed in more detail in Sect. 9.2.

The other mechanism for generating residual stress in optical fiber is draw-induced mechanical stress discussed in [3.65, 3.69, 3.76, 3.79]. Variations in the dopant concentration leads to variations in the viscosity of the glass. During the fiber draw process, the draw tension is initially borne by the entire fiber preform. As the drawn fiber cools, the highest viscosity glass in the fiber, typically the pure silica cladding, solidifies first while the low-viscosity glass, typically the doped core, remain relatively soft. At this point, the draw tension is mostly borne by the high-viscosity glass so it elastically stretches. The low viscosity glass flows to conform to the dimensions of the elastically stretched high-viscosity glass. As the fiber cools further, the low-viscosity glass solidifies and the draw tension is removed. Once the tension

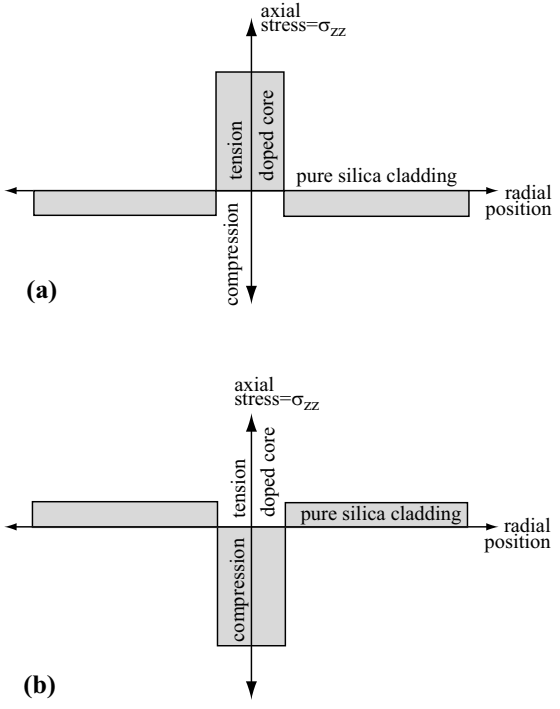

Fig. 3.25. Schematic illustration of stress fields in a step-index optical fiber with a small diameter (small area) core and a large diameter (large area) cladding. σ_{zz} refers to the axial stress in the fiber. When $\sigma_{zz} > 0$ stress is tensile and when $\sigma_{zz} < 0$ stress is compressive. (**a**) Residual thermal stresses resulting from large thermal expansion coefficient in the core and small thermal expansion coefficient in the cladding. (**b**) Draw-induced mechanical residual stress resulting from low-viscosity core and high-viscosity cladding

is removed, the high-viscosity glass elastically contracts but it is opposed by the solidified low-viscosity glass. Thus the low-viscosity glass is in axial compression and the high-viscosity glass is in axial tension (Fig. 3.25b).

Since the cross sectional area of the high-viscosity pure silica glass cladding is much larger than that of the low-viscosity glass core, the draw-induced residual mechanical stresses are much larger in the core than in the cladding. Another important observation is that the magnitude of draw-induced residual stresses and strains scale linearly with the draw tension. When fibers are drawn at low draw tension (<100 g) the residual stresses and strains usually result from differential thermal contraction. In fibers drawn at higher draw tension, the residual stresses and strains usually result from draw-induced effects. When the fibers are drawn at extremely high tension, the axial draw-induced residual compressive mechanical stresses in the core can be as large as 200 MPa [3.82–3.84].

3.4.2 Fusion Splicing and Its Relationship to Residual Stress and Strain

Changes to the fiber's residual stress and strain state resulting from fusion splicing can have an impact on the mechanical and optical properties of the splice. During a fusion splice, the fiber tips are usually heated to temperatures which rival the original fiber draw temperatures. Thus fusion splicing erases any "memory" of the original draw-induced residual stress and strain. However, residual thermal stresses will be restored to the fiber as it cools down from splicing temperatures [3.72]. Restoration of the original thermal stress field is of critical importance for some types of splicing. For example, PM fiber splices exhibit low-loss and low polarization crosstalk because the residual thermal stress state that gives rise to the fiber's birefringence is not altered by the thermal cycling experienced during the fusion splice.

Residual stress in an optical fiber affects the refractive index through the *stress-optic* effect. If the unstressed fiber refractive index is considered to be isotropic and is denoted by n, then the refractive index components of the stressed fiber may be expressed as [3.75]

$$n_{\mathrm{r}} = n + p\sigma_{\mathrm{rr}} + q(\sigma_{\phi\phi} + \sigma_{\mathrm{zz}}) \,, \tag{3.45a}$$

$$n_{\mathrm{z}} = n + p\sigma_{\mathrm{zz}} + q(\sigma_{\phi\phi} + \sigma_{\mathrm{rr}}) \,, \tag{3.45b}$$

$$n_{\phi} = n + p\sigma_{\phi\phi} + q(\sigma_{\mathrm{rr}} + \sigma_{\mathrm{zz}}) \,, \tag{3.45c}$$

where p and q are the stress-optic coefficients, and n_{r}, n_{z}, and n_{ϕ} are the refractive indices for light polarized in the radial, axial, and azimuthal directions respectively. Furthermore, σ_{rr}, σ_{zz}, and $\sigma_{\phi\phi}$ are the normal stresses in the radial, axial, and azimuthal directions, respectively. The radial and axial symmetry of an optical fiber ensures that only the normal stress components are non-zero [3.75, 3.76]. The stress optic coefficients for silica have been measured to be $p = -6.5\times10^{-13}\,\mathrm{Pa}^{-1}$ and $q = -4.2\times10^{-12}\,\mathrm{Pa}^{-1}$ [3.85].

The residual stress field in an optical fiber manifests itself as birefringence which can be measured with a polarscope [3.86]. Chu and Whitbread were the first to report that fusion splicing altered the residual stress in optical fibers [3.72]. They measured the birefringence of an optical fiber in the vicinity of a fusion splice and showed that the splicing process removed the draw-induced residual mechanical stresses leaving behind only residual stresses from differential thermal contraction. Volotinen and co-workers also used birefringence to measure the residual mechanical stress in the vicinity of a fusion splice and corroborated Chu's results [3.74]. Mohanna measured the rate of stress relaxation by monitoring the rate of change of the birefringence of an optical fiber and used this to estimate the temperature achieved during fusion splicing [3.73].

The stress changes associated with relaxation of draw-induced residual mechanical stresses are on the order of the residual stresses them-

selves [3.83]. Since these stresses can be as large as 200 MPa in the core of a fiber [3.82–3.84], the refractive index change associated with their relaxation is on the order of 0.00013. A localized refractive index change of this magnitude has a negligible impact on the wave guiding characteristics of most fibers.

The refractive index of certain optical fibers can be changed by localized heating [3.70, 3.71, 3.87]. These refractive index changes can be as large as 0.0015 [3.70] and are thought to result from thermal relaxation of large draw-induced mechanical stresses. Equations (3.45a-3.45c) suggest that the corresponding change in the core residual stress must be on the order of 2 GPA! Similar refractive index changes are expected when fusion splicing fibers with such large draw-induced residual stresses. In any case, these refractive index changes are not as large as those typically result from dopant diffusion.

The strength of an optical fiber fusion splice, as well as an optical fiber, is primarily determined by the condition of the outer surface of the fiber (see Chap. 6). Defects on the fiber's outer surface can serve as nucleation sites for crack growth. The strength of an optical fiber can be increased by imparting a residual compressive stress to the outermost portion of the fiber cladding [3.68, 3.80, 3.81, 3.88–3.91]. This residual compressive stress suppresses crack growth. Differential thermal contraction can impart just such a compressive stress to the outer surface of the fiber cladding, providing that the outer surface is fabricated from a glass with a lower thermal expansion coefficient than that of the interior glass. Most silica fibers consist of a high thermal expansion coefficient core that is overclad by low thermal expansion coefficient high-purity silica glass so they enjoy some benefit from small amounts of compressive stress on their outer surface.

However, when fibers are drawn at high tension, the high silica cladding can experience residual tensile stresses. Since fusion splicing does not substantially alter the residual thermal stress but does destroy any residual draw-induced stresses in the vicinity of the splice, fusion splicing will not make the cladding residual stress more tensile, providing the fiber has a high viscosity glass at its outer surface. In fact, fusion splicing induced changes to the fiber residual stress state can only make the residual axial stress in the cladding (and on the cladding surface) more compressive, and thus more crack resistant [3.72]. However, this benefit is typically outweighed by surface defects incurred on the surface of the fiber during fusion splicing, especially in the region immediately adjacent to the fusion splice that is heated to intermediate temperatures. As discussed in Sect. 2.1, fiber surface damage can also result from stripping the fibers polymer coating, from careless handling, or from dirty or worn arc electrodes. The effect of externally applied mechanical stress on the long term reliability of optical fiber fusion splices is discussed in detail in Chap. 6.

Residual thermal stresses can impair fusion splices between certain combinations of optical fibers. For example, it is very difficult to fusion splice silica based optical fibers to optical fibers fabricated from lower temperature glasses including fluoride [3.92–3.94], bismuth oxide [3.95–3.97], chalcogenide, borosilicate, or phosphate [3.98] glasses because the thermal expansion coefficient of these glasses is very different from that of silica glass. Moreover, the lower melting temperature of these glasses necessitates lower splicing temperatures, at which the silica glass fiber tip remains solid. The lower temperature glass will flow around, and possibly bond to, the solid silica fiber tip. Although a joint can be formed at elevated temperatures, as the joint cools down, the differential thermal contraction between the two fibers is so large that large thermal stresses result so that fusion splices between silica fibers and low temperature glasses exhibit very poor mechanical strength and are often too fragile to be handled.

3.5 Summary

Heat transfer during optical fiber fusion splicing is a complex nonlinear mixture of unsteady radiation, convection, and conduction. The fiber tips in an arc discharge are heated by radiation and convection while conduction and radiation in the axial direction carry some of this heat away from the splice. The fiber tips heat up and cool down within a few hundred milliseconds. The fiber temperature is largely uniform with respect to radial position, but varies as a function of axial position. The characteristic width of the heated zone depends on the width of the heat source but is typically on the order of a millimeter.

Mechanical forces such as those applied by the splicer's chucks as well as surface tension and viscosity play a critical role in shaping the fusion splice process. A variety of important phenomena such as bending, buckling, tapers, bubbles, and fiber neckdown depend on the mechanical forces occurring during fusion splicing. Producing a low-loss, high-strength optical fiber splice requires some understanding of these phenomena and the forces that control them.

High temperatures during fusion splicing can result in substantial amounts of dopant diffusion that can significantly change the refractive index profile and hence the optical and mechanical properties of a fiber in the vicinity of a fusion splice. Linear dopant diffusion is relatively easy to quantify, although the diffusion coefficients for common dopants in silica are not well characterized in the literature. An understanding of dopant diffusion is particularly important when splicing fibers with small cores and highly mobile dopants such as fluorine. Dopant diffusion can be either detrimental or advantageous to fusion splice quality.

Fusion splicing can alter the fiber's residual stress and strain, which can alter the optical and mechanical characteristics of the fibers in the vicin-

ity of the splice. The effect on the refractive index profile is thought to be quite small but the effect on mechanical strength may be more substantial. Relaxation of draw-induced residual mechanical stresses can reduce surface tensile stress in the vicinity of a splice and thus increase the fiber's mechanical strength and long term reliability. However, this effect is typically outweighed by other effects influencing a fiber's mechanical strength such as surface damage incurred during fiber stripping or handling.

4. Optics of Fusion Splicing

An optical fiber fusion splice is a permanent joint between two fibers that enables the optical signal, an electromagnetic wave, to pass from one fiber to another. At a fusion splice, the optical signal may be radiated out of the fiber, reflected back into the launching fiber, or transmitted into one or more guided modes in the receiving fiber (Fig. 4.1). Typically optical absorption is minimal in the fiber itself so the fusion splice joint may be thought of as a purely scattering element. The optics of a fusion splice are entirely determined by the refractive index experienced by the optical signal in the vicinity of the splice. The refractive index in the vicinity of the splice depends in turn upon the geometry of the splice and upon materials effects such as dopant diffusion and residual stress, both of which were discussed in the preceding chapter.

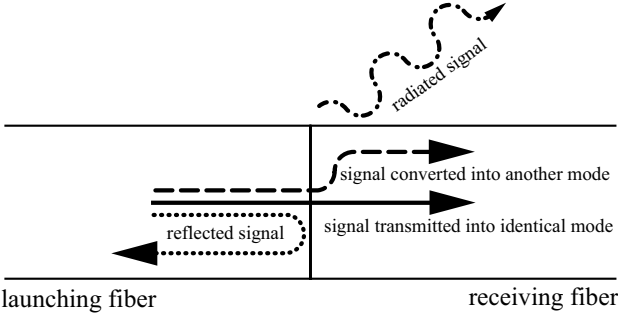

Fig. 4.1. Schematic illustration of the effect of a fusion splice joint on an optical signal propagating from left (launching fiber) to right (receiving fiber). The signal can be transmitted from the launching fiber into an identical mode (if there is one) in the receiving fiber at the splice joint (*solid arrow*), it can be converted into different modes in the receiving fiber (*dashed arrow*), it can be reflected back into the launching fiber (*dotted arrow*), or it can be completely radiated out of the fiber (*dot/dashed arrow*)

Splice loss is the most common, and usually the most important, optical characteristic of a fusion splice. Splice loss usually refers to the fraction of the incident optical signal power that is not transmitted across the joint because it is either reflected or radiated away. The portion of signal power converted

into other guided modes at a multimode fiber splice may or may not be considered "lost." In single-mode fibers, any portion of the optical signal that is not transmitted into the fundamental guided mode of the receiving fiber is considered to be lost. By convention the splice loss, Γ_{splice}, is measured in dB units according to the following equation

$$\Gamma_{\text{splice}} = 10 \log_{10} \frac{P_{\text{inc}}}{P_{\text{trans}}} \tag{4.1}$$

where P_{inc} is the total optical power incident upon a fusion splice and P_{trans} is the desirable portion of the optical power transmitted across the fusion splice. Since $P_{\text{inc}} > P_{\text{trans}}$, the splice loss will be a positive number.

The fundamental mechanisms responsible for fusion splice loss can be organized into two categories: extrinsic and intrinsic loss. *Extrinsic loss* refers to splice loss that results from imperfectly formed splice joints, usually from geometric misalignment or deformation at the joint. *Intrinsic splice loss* refers to splice loss that results from differences in the propagating characteristics of the launching and receiving fibers. Extrinsic splice loss can be minimized by proper fabrication of the fusion splice including careful attention to cleave quality and optimizing splicing parameters as discussed in Sect. 8.1. Intrinsic losses can be minimized through splice parameter optimization as well as by exploiting special splicing strategies, which modify the propagation characteristics of the fibers at the splice. These strategies include splice tapering, splice fattening, bridge fibers, diffusion of core dopants, offset heating, and fire polishing (Sect. 8.2).

One important advantage of fusion splices over competing fiber interconnection technologies, such as free space coupling, connectors, or mechanical splices, is the relatively small amount of optical power reflected by fusion splices. Since the performance of many optical sources, devices, and transmission systems can be sensitive to even minute amounts of reflected power [4.1–4.3], fusion splices are often the only viable option. *Reflectance* is a measure of the amount of optical power reflected by an individual component, such as a fusion splice, whereas *return loss* is a measure of the total optical power reflected by an optical fiber span containing many individual components (Sect. 7.2.1). By convention the reflectance of a fusion splice, R_{splice}, is expressed in dB units as

$$R_{\text{splice}} = 10 \log_{10} \frac{P_{\text{refl}}}{P_{\text{inc}}} \tag{4.2}$$

where P_{refl} is the optical power reflected at the fusion splice. Since P_{refl} must be less than P_{inc}, R_{splice} will always be a negative number. A lower (more negative) value for the reflectance is nearly always preferred.

The propagation of optical signals in optical fibers may be approached from two perspectives: *ray optics* (also known as *geometrical optics*) and the *modal description* (also known as *wave optics* or *physical optics*). In the ray-optic description, photons are assumed to follow straight trajectories like

ballistic particles. In the modal description, the signal propagates in discrete modes which are spatial envelopes of oscillating electromagnetic waves. The ray-optic description of signal propagation is valid when the wavelength of light is very small compared to the characteristic length scale of the fiber, which can be very loosely defined as the fiber's core radius. Thus the ray-optic approach is valid for most multimode optical fibers, especially when their normalized frequency, V, is larger than 10 [4.4]. The modal description of optical fibers is essential for analyzing single-mode fibers, whose normalized frequency is less than 2.5.

In this chapter we discuss the optical characteristics of fusion splices. First we introduce relevant aspects of optical waveguide theory for both single- and multimode fibers. Analytical techniques for describing single- and multimode optical fiber splice loss are derived and then approximate splice loss prediction formulae are presented. We conclude with an introduction to the beam propagation method (BPM), a numerical techniques for describing the optical characteristics of a fusion splice based on the refractive index in the vicinity of the splice.

4.1 Modal Description of Fusion Splices

In this section we will examine the optical characteristics of fusion splices with the aid of the *modal description* perspective and discuss the interactions between optical fiber modes and fusion splices. A complete review of optical waveguide theory is beyond the scope of this book but excellent introductions are available in [4.4–4.8, 4.10]. In this section we will develop the scalar wave equation which will serve as the foundation for our analysis of the optics of fusion splicing. This scalar analysis is approximately correct for single-mode fiber fusion splices. A rigorous description of multimode fusion splices requires solving the full vectorial wave equation, which is also beyond the scope of this book. However, the scalar approximation captures the essence of the full vectorial solution so that the general results derived using the scalar analysis are valid for multimode fibers. The specific optical characteristics of single- and multimode fiber fusion splices will be addressed in Sects. 4.2 and 4.3 respectively.

4.1.1 The Scalar Wave Equation

The optical signal carried in a fiber is an oscillating electromagnetic wave governed by Maxwell's equations. In isotropic, linear, non-conducting, source-free, and non-magnetic media such as silica glass Maxwell's Equations may be written as [4.7]

$$\nabla \times \boldsymbol{E} = -\mu_0 \frac{\partial \boldsymbol{H}}{\partial t} \,, \tag{4.3a}$$

$$\nabla \times \boldsymbol{H} = \varepsilon \frac{\partial \boldsymbol{E}}{\partial t} \,, \tag{4.3b}$$

$$\nabla \cdot (\varepsilon \boldsymbol{E}) = 0 \,, \tag{4.3c}$$

$$\mu_0 \nabla \boldsymbol{H} = 0 \,, \tag{4.3d}$$

where $\boldsymbol{E}$ is the electric field vector, $\boldsymbol{H}$ is the magnetic field vector, t is time, ε is the dielectric constant of the material and μ_0 is the magnetic permeability of free space ($4\pi \times 10^{-7}$ Vs/Am). The electric field, $\boldsymbol{E}$, is measured in the SI units V/m. The dielectric constant, ε, is in general a function of position, denoted by the vector $\boldsymbol{r}$, and may be expressed as

$$\varepsilon(\boldsymbol{r}) = \varepsilon_0 n^2(\boldsymbol{r}) \,, \tag{4.4}$$

where $n(\boldsymbol{r})$ is the local index of refraction. A rigorous description of the optical properties of a fusion splice require a complete solution to Maxwell's equations, (4.3a-4.3d), which yields the vector quantities $\boldsymbol{E}$ and $\boldsymbol{H}$ as a function of position, $\boldsymbol{r}$, and time, t, given refractive index geometry, $n(\boldsymbol{r})$ and the boundary conditions. Unfortunately, (4.3a-4.3d) are a coupled set of partial differential equations, which can only be solved with certain important assumptions. If we take the curl of (4.3a) and substitute in (4.3b) we obtain

$$\nabla \times (\nabla \times \boldsymbol{E}) = -\mu_0 \varepsilon \frac{\partial^2 \boldsymbol{E}}{\partial t^2} \,. \tag{4.5}$$

Equations (4.3c) and (4.5) may be combined with the vector identity $\nabla \times \nabla \times \boldsymbol{E} \equiv \nabla(\nabla \cdot \boldsymbol{E}) - \nabla^2 \boldsymbol{E}$ to yield [4.8]

$$\nabla^2 \boldsymbol{E} - \mu_0 \varepsilon \frac{\partial^2 \boldsymbol{E}}{\partial t^2} = -\nabla\left(\frac{1}{\varepsilon} \boldsymbol{E} \cdot \nabla \varepsilon\right) \,. \tag{4.6}$$

The right hand side of (4.6) may be neglected when the fractional change in ε, and hence n^2, is much less than one over a distance of one optical wavelength [4.8]. With this simplification we obtain the *vector wave equation*

$$\nabla^2 \boldsymbol{E} = \mu_0 \varepsilon \frac{\partial^2 \boldsymbol{E}}{\partial t^2} \,. \tag{4.7}$$

The solution to this wave equation is the vector quantity $\boldsymbol{E}$ as a function of position $\boldsymbol{r}$, and time t. When the refractive index variation in a fiber is small (i.e. $\frac{n_{\text{core}} - n_{\text{cladding}}}{n_{\text{core}}} \ll 1$) the electric field oscillates almost entirely in the transverse direction. In other words, the component of $\boldsymbol{E}$ in the z direction is negligible. This *weakly guiding* or *scalar approximation* permits us to express the electric field as the scalar quantity $E(\boldsymbol{r}, t)$ which is understood to oscillate in the transverse direction [4.4–4.6, 4.8–4.10]. This assumption results in the *scalar wave equation*, also termed the *Helmholtz equation* [4.11]

$$\nabla^2 E = \mu_0 \varepsilon \frac{\partial^2 E}{\partial t^2} \,. \tag{4.8}$$

In general, $E(\boldsymbol{r}, t)$ is a complex valued function. This equation is sufficiently rigorous for analyzing the optical characteristics of most single-mode and multimode fusion splices.

Most optical fibers exhibit cylindrical symmetry ($n{=}n(r,z)$ where r is the radial coordinate and z is the axial coordinate) so it is convenient to express (4.8) in cylindrical coordinates while substituting in (4.4)

$$\frac{\partial^2 E}{\partial z^2}+\frac{\partial^2 E}{\partial r^2}+\frac{1}{r}\frac{\partial E}{\partial r}+\frac{1}{r^2}\frac{\partial^2 E}{\partial \phi^2}=n^2(r,z)\mu_0\varepsilon_0\frac{\partial^2 E}{\partial t^2}\ , \tag{4.9}$$

where ϕ is the azimuthal angle. If we assume that the fiber does not change along its length the electric field may be expressed by [4.4]

$$E(r,\phi,z,t)=\psi(r,\phi)\exp\left(\mathrm{i}(\omega t-\beta z)\right)\ , \tag{4.10}$$

where $\mathrm{i}{=}\sqrt{-1}$, $\psi(r,\phi)$ is the envelope of the oscillating electric field, ω is the angular frequency, and β is the *axial propagation constant*, also termed the *phase constant* [4.10]. Consider a real valued function $\psi(r,\phi)$ such that

$$\psi(r,\phi)=R(r)\Phi(\phi)\ , \tag{4.11}$$

where $R(r)$ and $\Phi(\phi)$ are also real-valued functions. If we substitute (4.10) and (4.11) into (4.9) we find a sufficiently general expression for Φ is

$$\Phi(\phi)=\cos(l\phi)\ , \tag{4.12}$$

where l is an integer (0,1,2...). We also find [4.4]

$$\frac{\partial^2 R}{\partial r^2}+\frac{1}{r}\frac{\partial R}{\partial r}+\frac{1}{r^2}\frac{\partial^2 R}{\partial \phi^2}+[k_0 n^2(r,z)-\frac{l^2}{r^2}-\beta^2]R=0\ , \tag{4.13}$$

where k_0 is the vacuum wavenumber given by $k_0=\omega/c_{\mathrm{light}}=\omega\sqrt{\mu_0\varepsilon_0}=2\pi/\lambda$ and c_{light} is the speed of light in a vacuum.

If we assume that the magnetic field is a linear function of the local electric field, then the optical intensity in the fiber, I, can be related to the magnitude of an electric field as follows [4.12]

$$I(r,\phi)=\frac{n}{2}\sqrt{\frac{\varepsilon_0}{\mu_0}}E^*E\ , \tag{4.14}$$

where * denotes the complex conjugate. Unlike the electric field E, the optical intensity, I, may be directly measured by an optical detector and is usually quantified in the SI units $\mathrm{W/m^2}$. Given that the refractive index in silica optical fibers is approximately 1.444 at 1550 nm and exhibits relatively small variations over the radius of most fibers, we can choose special units for electric field magnitude, which incorporate the leading coefficients of (4.14). If we do this, we can express the optical intensity $I(r,\phi)$ associated with an arbitrary electric field envelope $\Psi(r,\phi)$ in very simple terms

$$I(r,\phi)=\Psi^*\Psi\ . \tag{4.15}$$

Of course, $\Psi^*\Psi$ reduces to Ψ^2 when Ψ is real valued. Equation (4.15) shows that the units of Ψ can be expressed as $\sqrt{\mathrm{W}}/\mathrm{m}$. The total optical power carried by the electric field envelope $\Psi(r,\phi)$ is denoted by P_Ψ and can be obtained by integrating (4.15) over the entire cross sectional area of the electric field envelope, A_{cs}

$$P_{\Psi} = \int \Psi^* \Psi \mathrm{d}A_{\mathrm{cs}} \, . \tag{4.16}$$

4.1.2 Modes

There are two types of solutions to (4.13): the first type of solution has $\beta > k_0 n_{\mathrm{cladding}}$ and the second solution has $\beta < k_0 n_{\mathrm{cladding}}$ [4.4].

The first type of solution exhibits only discrete values of β, each of which is associated with a distinct *guided mode* designated as LP_{lm} where l is the azimuthal mode number, an integer (0,1,2...) in (4.12) and (4.13) and m is the radial mode number, another integer (1,2,3...) that differentiates between the various modes for each value of l. LP stands for "linearly polarized" since the electric field is assumed to oscillate in the transverse linear direction. Each discrete value of β, the axial propagation constant, corresponding to a solution of (4.13) is related to the propagation velocity of that particular mode so that each distinct guided mode propagates along the fiber at a unique velocity.

For every guided mode, LP_{lm}, the function $\psi_{lm}(r, \phi)$ defined in (4.11) denotes the envelope of the oscillating electric field comprising that mode. This envelope function, $\psi_{lm}(r, \phi)$, is known as the *mode field shape*, or simply the *mode field* function since it defines the spatial distribution of the electric field associated with a particular mode. Note that according to our definitions, $\psi_{lm}(r, \phi)$ will be real because R and Φ are real valued. The mode field, and hence the optical intensity distribution, exhibits $2l$ zeros in the azimuthal (ϕ) direction and $m-1$ zeros in the radial (r) direction (excluding the possibility of a zero at $r = 0$) [4.4]. The optical intensity distributions for some low-order modes in a multimode fiber are depicted in Fig. 4.2.

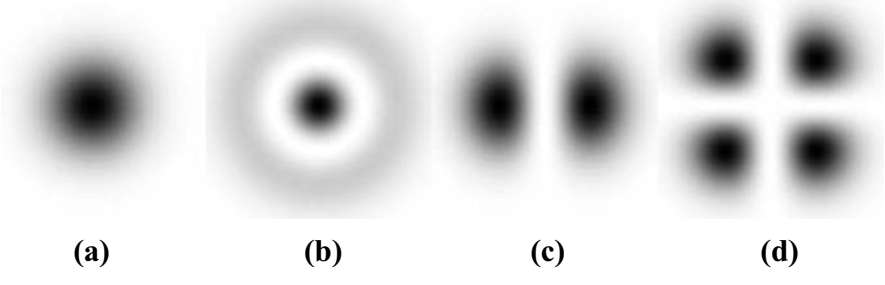

Fig. 4.2. Some low-order modes (mode intensity patterns, not electric fields) for a parabolic graded-index multimode fiber with Δ of 0.01, core radius of 25 µm, and wavelength of 850 nm, which is typical for this type of fiber. The normalized frequency of this fiber, V, is about 37 which corresponds to about 720 guided modes. Darker regions correspond to regions of higher optical intensity. Low-order modes for a step-index fiber are very similar, (**a**) LP_{01}; (**b**) LP_{02}; (**c**) LP_{11}; (**d**) LP_{21}. Note how the mode fields have $2l$ zeros in the azimuthal (ϕ) direction and $m-1$ zeros in the radial (r) direction (excluding the possibility of a zero at $r = 0$)

The normalized frequency, V, introduced in (1.6), determines the number of distinct guided modes in a fiber. When V is between 0 and 2.405 the fiber is single-mode meaning that there is only one discrete solution to (4.13) with $\beta > k_0 n_{\text{cladding}}$. This unique solution is known as the LP_{01}, or *fundamental*, mode. Some sample LP_{01} mode fields are depicted in Fig. 4.3. The number of distinct guided modes in a multimode fiber, N_{modes}, may be estimated as [4.4]

$$N_{\text{modes}} \approx \frac{V^2}{2} \,. \tag{4.17}$$

Commercial multimode fibers typically exhibit $V \geq 15$ so they guide hundreds of modes.

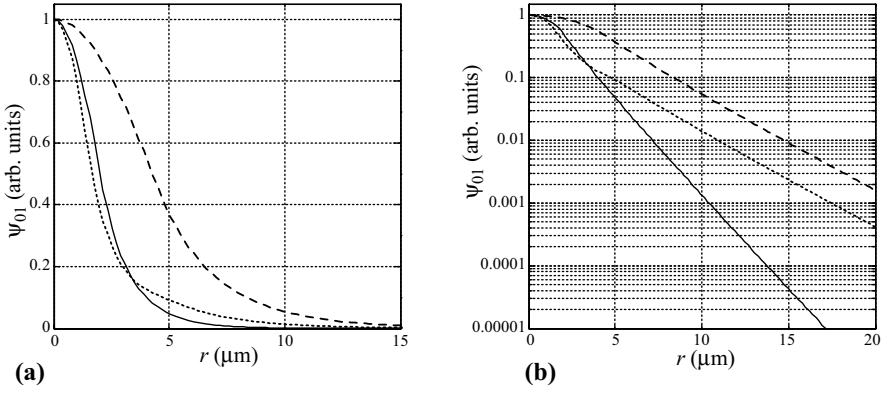

Fig. 4.3. Sample LP_{01} mode fields at 1550 nm for three different types of SMF. The ψ_{01} are not orthonormal as they have been scaled such that $\psi_{01}|_{\text{r=0}} = 1$. ψ_{01} for standard SMF (*dashed line*) with 8.3 μm core diameter, Δ=0.33%, 10.5 μm MFD; ψ_{01} for a small core SMF such as an erbium-doped gain fiber (*solid line*) with 4 μm core diameter, Δ=1.4%, 5 μm MFD; and ψ_{01} for a DCF (*dotted line*) with core, trench, and ring index structure, 5 μm MFD. (**a**) Linear scale and (**b**) Logarithmic scale. Note how all ψ_{01} drop off exponentially at large r (linearly on logarithmic plot). Mode fields calculated with the method described in Sect. 4.4.3

The second type of solution to (4.13) occurs when $\beta < k_0 n_{\text{cladding}}$ and this type of solution exhibits a continuous set of values for β. The set of continuous β are sometimes termed *radiation modes* and they are not guided by the fiber. After a sufficiently long propagation distance in the z direction, the optical power associated with these radiation modes exits the fiber.

Any arbitrary electric field at a particular place in the fiber, $\Psi(r, \phi)$, can be expressed as a linear sum of guided and radiation modes as follows [4.4]

$$\Psi(r, \phi) = \sum_{lm} c_{lm} \psi_{lm}(r, \phi) + \int c(\beta) \psi_\beta(r, \phi) \mathrm{d}\beta \,, \tag{4.18}$$

where c_{lm} and $c(\beta)$ are complex-valued coefficients for the guided modes and a complex-valued function for the radiation modes, respectively.

The guided mode solutions, the ψ_{lm}, are *orthogonal* to each other meaning that

$$\int \psi_{lm}\psi_{l'm'}\mathrm{d}A_{\mathrm{cs}} = 0 \text{ for either } l \neq l' \text{ or } m \neq m' \,. \tag{4.19}$$

Physically this means that the optical power traveling down the fiber in one mode field is completely isolated from, and does not exchange energy with, any other mode field. However, if the fiber index profile changes along its length, then energy may be exchanged between modes. A fusion splice usually results in a local change in the fiber index profile which can permit energy to be exchanged among the mode fields. Manufacturing imperfections in the fiber, such as variations in the fiber index profile or fiber geometry, as well as bends in the fiber, can also cause optical power to be scattered amongst the various modes in the fiber.

To simplify future derivations, we choose our guided mode field solutions, the ψ_{lm}, such that

$$\int \psi_{lm}^2 \mathrm{d}A_{\mathrm{cs}} \equiv 1 \,, \tag{4.20}$$

for all l and m. Thus, the units of measurement for ψ_{lm} is length^{-1} or 1/m. Since Ψ in (4.15) and (4.18) is expressed in the units $\sqrt{\mathrm{W}}$/m, we infer that the coefficients c_{lm} must have the units $\sqrt{\mathrm{W}}$. Note that this choice for normalization of the ψ_{lm} is somewhat non-standard but is particularly convenient for the analysis of fusion splices. When the set of guided modes, ψ_{lm}, satisfies (4.19) and (4.20) they are termed *orthonormal*. For the duration of this chapter, we will assume ψ_{lm} denotes an orthonormal mode field.

In (4.18), the c_{lm} coefficients represent the amount of electric field residing in the associated mode LP_{lm}. These coefficients are termed the electric field amplitude coefficients and can be expressed as

$$c_{lm} = \int \Psi\psi_{lm}\mathrm{d}A_{\mathrm{cs}} \,. \tag{4.21}$$

Note that c_{lm} will be complex when $\Psi(r,\phi)$ is complex; the magnitude of c_{lm} is related to the amount of power carried in the mode while the phase angle of c_{lm} is related to the phase angle of the oscillating electric field. The total power carried in the LP_{lm} mode can then be expressed as

$$P_{lm} = c_{lm}^* c_{lm} \,. \tag{4.22}$$

As mentioned earlier, after a certain distance, the optical power comprising the radiation modes will exit the fiber and the $c(\beta)$ in the final term of (4.18) may then be considered to be zero. At this point, all the optical power in the fiber is comprised of guided modes. Substituting (4.18) into (4.16) and making use of (4.19), one can show that the total amount of guided optical power may be expressed as

$$P_\Psi = \sum_{lm} c_{lm}^* c_{lm} \ . \tag{4.23}$$

It is interesting to note that the guided modes of an optical fiber are analogous to quantum mechanical base states [4.13]. In this sense, the phase of the electric field of a mode is analogous to the probability amplitude associated with a quantum base state. Like probability amplitudes in quantum mechanics, the phase of a guided mode in an optical fiber cannot be directly measured, but can only be inferred from interference experiments. Some of the tools used for analyzing quantum base states, such as the matrix propagation formalism, are applicable to signal propagation in optical fibers, as demonstrated in the next Section.

4.1.3 The Scattering Matrix

In this section we will apply the *scattering matrix* formalism to an idealized fusion splice and derive some basic results concerning optical coupling between two fibers. The mathematics and the notation may seem a bit tedious but the results are well worth the effort since they have important implications for both single- and multimode fiber fusion splices. The general scattering matrix formalism is detailed in [4.7, 4.14].

Consider two different fibers, denoted *left* and *right*, mated together at a planar interface, as shown in Fig. 4.4a. These fibers may be single- or multimode. Let the M orthonormal guided mode fields of the left hand fiber be denoted by $\psi_i^{(\mathrm{L})}$ for $i = 1, 2, 3...M$ and the N orthonormal guided mode fields of the right hand fiber be denoted by $\psi_j^{(\mathrm{R})}$ for $j = 1, 2, 3...N$.

The notation is simplified by identifying each guided mode by a single number, rather than using the LP_{lm} notation introduced earlier. Each individual LP_{lm} will be denoted by a single unique subscript. In fact, the LP_{lm} modes derived earlier from the scalar wave equation, (4.8), may not accurately describe the mode fields when the fibers guide a large number of modes. In that case, the vector wave equation must be solved to obtain exact solutions to the mode fields. Nevertheless, the use of the scalar approximation in the present derivation will still lead us to the same important conclusions.

The refractive index profile of the individual fibers in the vicinity of the splice are assumed to be constant with respect to z, the coordinate along the fiber's axis. Optical energy is assumed to travel into and out of the fusion splice from both fibers. The corresponding electric field incident on the fusion splice from the left fiber is denoted by $E_{\mathrm{L,in}}$, the electric field incident from the right fiber is denoted by $E_{\mathrm{R,in}}$, the electric field exiting from the left fiber is denoted by $E_{\mathrm{L,out}}$, and the electric field exiting from the right fiber is denoted by $E_{\mathrm{R,out}}$.

Figure 4.4b illustrates how this fusion splice joint can be modeled as a *multiport passive* optical device. The various guided modes in the left and right fibers serve as "ports." The radiation modes are all lumped together

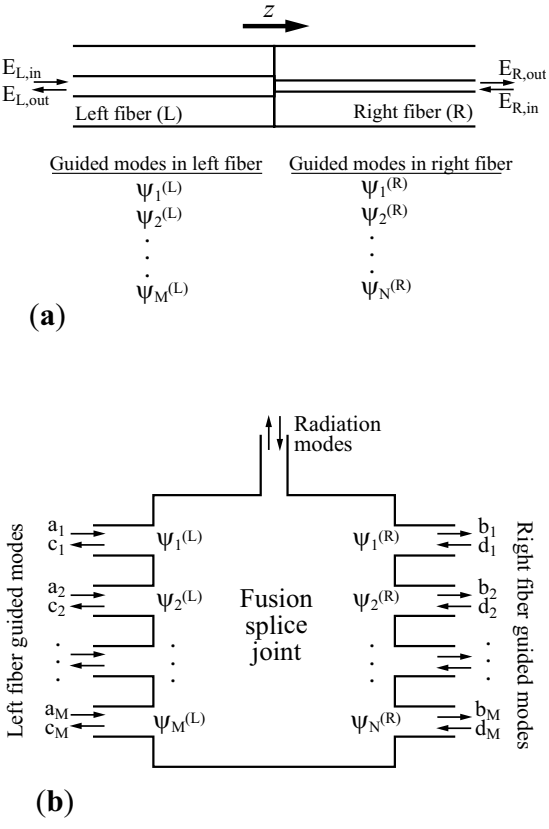

Fig. 4.4. Application of the scattering matrix formalism to the analysis of a fusion splice. (**a**) Illustration of an idealized fusion splice between two dissimilar fibers, left and right, guiding modes $\psi_i^{(\mathrm{L})}$ for $i = 1, 2, 3...M$, and modes $\psi_j^{(\mathrm{R})}$ for $j = 1, 2, 3...N$ respectively. The incident electric field traveling in the left fiber is denoted by $E_{\mathrm{L,in}}$, the exiting electric field in the left fiber is denoted by $E_{\mathrm{L,out}}$, the exiting electric field traveling in the right fiber is denoted by $E_{\mathrm{R,out}}$, and the incident electric field in the right fiber is denoted by $E_{\mathrm{L,in}}$. (**b**) Depiction of the fusion splice joint as a passive multiport optical device in which the various modes of the two fibers comprise ports. In this analysis, radiation modes are grouped together to comprise an additional port

into an additional port. The system is passive in the sense that it does not amplify nor absorb any optical power. Instead, the system scatters the optical energy amongst the various ports. The details of this scattering are determined entirely by the refractive index geometry of the scattering region.

The entering and exiting electric fields associated with the entering and exiting optical signals are decomposed into guided orthonormal modes and their associated amplitude coefficients following (4.18) and (4.21). Consequently, the total electric fields may be expressed as a superposition of the

electric field amplitudes of the individual modes as

$$E_{\mathrm{L,in}} = \sum_{i=1}^{M} a_i \psi_i^{(\mathrm{L})} \,, \tag{4.24a}$$

$$E_{\mathrm{R,out}} = \sum_{j=1}^{N} b_j \psi_j^{(\mathrm{R})} \,, \tag{4.24b}$$

$$E_{\mathrm{L,out}} = \sum_{i=1}^{M} c_i \psi_i^{(\mathrm{L})} \,, \tag{4.24c}$$

$$E_{\mathrm{R,in}} = \sum_{j=1}^{N} d_j \psi_j^{(\mathrm{R})} \,, \tag{4.24d}$$

where the complex amplitude of the electric field entering the system from via the ith mode of the left fiber is denoted by a_i while the complex amplitude of the electric field exiting the system via the left fiber's ith mode is denoted by c_i. Similarly, the complex amplitudes of the electric field entering the system via the jth mode of the right fiber is denoted by d_j while the complex amplitude of the electric field exiting the system via the jth mode of the right fiber is denoted by b_j.

Let the column vectors $\boldsymbol{a}$, $\boldsymbol{b}$, $\boldsymbol{c}$, and $\boldsymbol{d}$ contain the individual complex field amplitudes as their components so

$$\boldsymbol{a} = \begin{bmatrix} a_1 \\ a_2 \\ \vdots \\ a_M \end{bmatrix} \,, \; \boldsymbol{b} = \begin{bmatrix} b_1 \\ b_2 \\ \vdots \\ b_N \end{bmatrix} \,, \; \boldsymbol{c} = \begin{bmatrix} c_1 \\ c_2 \\ \vdots \\ c_M \end{bmatrix} \,, \; \boldsymbol{d} = \begin{bmatrix} d_1 \\ d_2 \\ \vdots \\ d_N \end{bmatrix} \,. \tag{4.25}$$

Following (4.23), the total optical power corresponding to an electric field is given by the sum of the magnitudes of the complex electric field amplitudes which can be written in vector form as

$$P_{\mathrm{L,in}} = \boldsymbol{a}^{+}\boldsymbol{a} \,, \tag{4.26a}$$

$$P_{\mathrm{R,out}} = \boldsymbol{b}^{+}\boldsymbol{b} \,, \tag{4.26b}$$

$$P_{\mathrm{L,out}} = \boldsymbol{c}^{+}\boldsymbol{c} \,, \tag{4.26c}$$

$$P_{\mathrm{R,in}} = \boldsymbol{d}^{+}\boldsymbol{d} \,, \tag{4.26d}$$

where $^{+}$ denotes the operator which takes the transpose and the complex conjugate of the argument, $P_{\mathrm{L,in}}$ denotes the total optical power incident on the fusion splice from the left fiber, $P_{\mathrm{R,out}}$ denotes the total optical power exiting the fusion splice via the right fiber, $P_{\mathrm{L,out}}$ denotes the total optical power exiting the fusion splice via the left fiber, and $P_{\mathrm{R,in}}$ denotes the total optical power incident on the fusion splice from the right fiber.

We can assemble a column vector $\boldsymbol{C}_{\mathrm{in}}$, which contains the electric field amplitudes of all the light entering the fusion splice from the two fibers and

a column vector $\boldsymbol{C}_{\text{out}}$, which contains the electric field amplitudes of all the light exiting the fusion splice

$$\boldsymbol{C}_{\text{in}} = \begin{bmatrix} \boldsymbol{a} \\ \boldsymbol{d} \end{bmatrix}, \quad \boldsymbol{C}_{\text{out}} = \begin{bmatrix} \boldsymbol{c} \\ \boldsymbol{b} \end{bmatrix} . \tag{4.27}$$

Notice the special order of the components comprising $\boldsymbol{C}_{\text{in}}$ and $\boldsymbol{C}_{\text{out}}$. The column vectors must be ordered such that each row of $\boldsymbol{C}_{\text{in}}$ corresponds to the identical port of $\boldsymbol{C}_{\text{out}}$. Since a_i shares the same port as c_j, they must appear in the same row of $\boldsymbol{C}_{\text{in}}$ and $\boldsymbol{C}_{\text{out}}$ respectively.

Since the splice joint is a linear passive optical device, it does not add or subtract optical power but rather distributes that optical power according to linear rules. Thus, we may express the output electric field amplitudes, $\boldsymbol{C}_{\text{out}}$, as a linear functions of the input electric field amplitudes, $\boldsymbol{C}_{\text{in}}$, so

$$\boldsymbol{C}_{\text{out}} = \boldsymbol{S}\boldsymbol{C}_{\text{in}} , \tag{4.28}$$

where $\boldsymbol{S}$ is a special square matrix called the *scattering matrix*. The elements of $\boldsymbol{S}$ are unitless and determined only by the refractive index geometry of the splice and are independent of the actual electric field amplitudes. We will refer to the individual elements of $\boldsymbol{S}$ using two subscripts, the first referring to the input electric field amplitude component of $\boldsymbol{C}_{\text{in}}$ and the second referring to the output electric field amplitude component of $\boldsymbol{C}_{\text{out}}$. Thus, the element of $\boldsymbol{S}$ relating the input electric field amplitude a_i to the output electric field amplitude b_j is denoted by $\boldsymbol{S}_{ai,bj}$.

Since the fusion splice does not contain any magnetic elements, it may be considered *reciprocal* meaning that $\boldsymbol{S}$ is symmetric [4.7]

$$\boldsymbol{S}^{\text{T}} = \boldsymbol{S} , \tag{4.29}$$

where $^{\text{T}}$ denotes the matrix transpose operator. When $\boldsymbol{S}$ is symmetric, the correspondence between the rows of $\boldsymbol{C}_{\text{in}}$ and $\boldsymbol{C}_{\text{out}}$ ensures that

$$\boldsymbol{S}_{ai,bj} = \boldsymbol{S}_{dj,ci} . \tag{4.30}$$

The scattering matrix defined by (4.28) is not complete since we have not accounted for the radiation modes. Thus, the scattering matrix $\boldsymbol{S}$ derived here is not loss less so it is not *unitary* [4.7].

Between fusion splices, a length of optical fiber that does not couple energy between its various guided modes can be modeled as a diagonal matrix whose elements are complex numbers of unit magnitude that produce a phase shift appropriate for each guided mode's unique axial propagation constant. A span of optical fiber containing several splices can be modeled by a cascaded sequence of scattering matrices corresponding to the individual splices and the segments of fiber between them. It is important to note that cascaded scattering matrices are not commutable; they must be applied in the correct order. This fact has implications for multimode fibers discussed in Sect. 4.3.1.

Equation (4.30) is an important result as it implies that the fraction of electric field transformed from input mode $\psi_i^{(\text{L})}$ in the left fiber to output

mode $\psi_j^{(\mathrm{R})}$ in the right fiber is equal to the fraction of electric field transformed from input mode $\psi_j^{(\mathrm{R})}$ in the right fiber to output mode $\psi_i^{(\mathrm{L})}$ in the left fiber. For this reason, the splice loss between two SMFs *must be equal in both propagating directions*.

Some older studies of fusion splice loss between low-NA (large core and low Δ) and high-NA (small core and high Δ) fibers have suggested that splice loss is lower when propagating from the larger-core to the smaller-core fibers [4.15–4.18]. Miller acknowledged that this result is inconsistent with electromagnetic theory and there is no theoretical justification for such an observation [4.16], however Zheng purported to provide one [4.18]. More recent experimental [4.19] and theoretical work [4.19, 4.20] (the latter using a scattering matrix approach similar to that presented here) has confirmed that the splice loss between two purely single-mode fibers is indeed independent of direction.

The fact that splice loss between single-mode fibers is equal in both propagating direction is unrelated to the observation that SMF "splice loss" as measured by an optical time-domain reflectometer (OTDR) depends on the measurement direction. The reason for the "directional dependence" of splice loss measured by an OTDR is that the OTDR actually measures the change in backscattered power across the splice joint, which is a function of both the splice quality and the backscattering characteristics of the fibers themselves. The actual splice loss (for either propagating direction in a single-mode fiber) is given by the average of the loss measured by the OTDR in both directions. This issue is discussed in more detail in Sect. 7.2.2.

Another important implication of (4.28-4.29) is that the splice loss between two multimode fibers is generally *not* the same in both directions. The splice loss between two multimode fibers depends on how the optical energy is distributed (both amplitude and phase) amongst the various modes. This observation makes some physical sense since we can imagine fusion splicing a single-mode fiber to a multimode fiber designed so that the single-mode fiber's guided mode is nearly identical to the multimode fiber's fundamental guided mode. When light is launched from the single mode fiber into the multimode fiber, the splice loss will be extremely low since nearly all the energy from the SMF will couple into the fundamental mode of the MMF. However, if light is launched from the MMF into the SMF, and if this light is well distributed among the many modes in the MMF, most of the light will be lost since it won't couple into the SMF's single guided mode.

The polymer coating of a single-mode fiber usually exhibits a refractive index higher than the glass cladding so that the cladding won't support any guided modes and the radiation modes mentioned earlier will be stripped out of the fiber. During fusion splicing, this polymer coating is removed in the vicinity of the splice and the resulting silica-air boundary on the outside of the cladding actually turns the single-mode fiber into a multimode waveguide in the vicinity of the splice [4.21]. However, the single-mode splice loss is still

the same in both directions in this case since we can choose the boundary of our scattering system such that it includes the entire stripped region of fiber so that the fibers cross the system boundary where they are coated and thus truly single-moded.

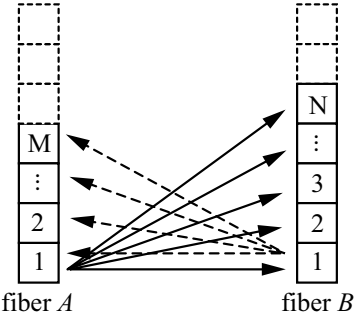

Fig. 4.5. Schematic illustration of the exchange of energy across a fusion splice joint between modes in two different optical fibers. The solid boxes represent guided modes, the dotted boxes represent radiation modes. The solid arrows demonstrate how an optical signal traveling towards the splice in the fundamental mode of fiber A can get distributed into various guided modes in fiber B. The dashed arrows demonstrate how an optical signal traveling towards the splice in fiber B can be distributed into various guided modes in fiber A. After [4.20]

4.1.4 The Overlap Integral

We can use (4.21) to compute the amount of electric field transmitted from orthonormal mode i in the left fiber to orthonormal mode j in the right fiber. To do this, we assume that the electric field in the launching fiber crosses the splice joint into the receiving fiber and is then decomposed into the various orthonormal modes, ψ_{lm}, associated with the receiving fiber. This can be best appreciated by imagining a special situation in which the only non-zero electric field amplitude entering the scattering region is a_i associated with orthonormal mode $\psi_i^{(\mathrm{L})}$ in the launching (left) fiber. In that very special case we may simplify (4.28) for the exiting electric field amplitude b_j associated with orthonormal mode $\psi_j^{(\mathrm{R})}$ in the receiving (right) fiber.

$$b_{\mathrm{j}} = S_{ai,bj} a_i \ . \tag{4.31}$$

However, (4.21) demands that

$$b_j = \int a_i \psi_i^{(\mathrm{L})} \psi_j^{(\mathrm{R})} \mathrm{d}A_{\mathrm{cs}} \ , \tag{4.32}$$

where Ψ, c_{lm}, and ψ_{lm} in (4.21) are analogous to $a_i\psi_i^{(\mathrm{L})}$, b_j, and $\psi_j^{(\mathrm{R})}$ in (4.32), respectively, and A_{cs} is the cross-sectional area of the fiber at the

splice joint. The term a_i may be pulled out of the integral in (4.32) and this expression then combined with (4.30) and (4.31) to reveal

$$S_{ai,bj} = \int \psi_i^{(\mathrm{L})} \psi_j^{(\mathrm{R})} \mathrm{d}A_{\mathrm{cs}} = S_{dj,ci} \ . \tag{4.33}$$

Notice that that (4.33) is independent of propagation direction. Although our derivation assumed that the only non-zero incident electric field amplitude was a_i, the preceding expression must be valid for all choices of input electric field amplitudes a_i and d_j since the scattering matrix itself does not depend on the electric field amplitudes but only on the geometry (refractive index profile) of the system.

Equation (4.33) is a form of the *overlap integral* [4.10], which can be used to compute the energy exchanged between different modes on either side of a discrete interface such as a fusion splice with a high degree of accuracy. Note that the overlap integral has nothing to do with the physical overlap of fibers during the fusion splice process defined in Sect. 1.2. When both fibers are perfectly aligned to each other, there is no lateral offset, and the mode fields are axisymmetric, we may readily express this relationship is cylindrical coordinates

$$S_{ai,bj} = \int_{\phi=0}^{\phi=2\pi} \int_{r=0}^{r=\infty} \psi_i^{(\mathrm{L})} \psi_j^{(\mathrm{R})} r \, \mathrm{d}r \, \mathrm{d}\phi \ . \tag{4.34}$$

If we substitute in (4.11) and (4.12) for $\psi_i^{(\mathrm{L})}$ and $\psi_j^{(\mathrm{R})}$ we may write

$$S_{ai,bj} = \int_{\phi=0}^{\phi=2\pi} \cos(l_i\phi)\cos(l_j\phi)\mathrm{d}\phi \int_{r=0}^{r=\infty} R_i^{(\mathrm{L})} R_j^{(\mathrm{R})} r \, \mathrm{d}r \ , \tag{4.35}$$

which is zero unless $l_i{=}l_j$. In other words, a perfectly aligned fusion splice between perfectly rotationally symmetric fibers will only couple energy from LP_{lm} in the launching fiber to $\mathrm{LP}_{l'm'}$ in the receiving fiber when $l{=}l'$.

Equation (4.33) describes how the electric field in an input mode is transformed into the electric field of an output mode. In the case of a single-mode fiber splicing, we are often interested in the total optical power transmitted from the input fundamental mode to the output fundamental mode. If the mode fields ψ are orthonormal, then the fraction of power transmitted from mode $\psi_i^{(\mathrm{L})}$ in the left fiber to mode $\psi_j^{(\mathrm{R})}$ in the right fiber, $F_{ai,bj}$, is a number between zero and one given by the square of the magnitude of the complex number $S_{ai,bj}$

$$F_{ai,bj} = S_{ai,bj}^{*} S_{ai,bj} = \left| \int \psi_i^{(\mathrm{L})} \psi_j^{(\mathrm{R})} \mathrm{d}A_{\mathrm{cs}} \right|^2 \ . \tag{4.36}$$

We can express the fraction of the optical power incident on the splice from mode $\psi_i^{(\mathrm{L})}$ in the left fiber but not transmitted to mode $\psi_j^{(\mathrm{R})}$ in the right fiber, $\Gamma_{ai,bj}$, to be

$$\Gamma_{ai,bj} = -10 \log_{10} \left(F_{ai,bj} \right) \ , \tag{4.37}$$

where $\Gamma_{ai,bj}$ is expressed in decibels.

When both the left and right fibers are single-mode fibers, there is only one guided mode in each fiber thus there are only two electric field amplitudes associated with each fiber, an input and an output. In this case, we may use the overlap integral to express the fusion splice loss between two perfectly aligned dissimilar single-mode fibers as

$$\Gamma_{\mathrm{SMF}} = -10 \log_{10} \left(\left| \int \psi_1 \psi_2 \mathrm{d}A_{\mathrm{cs}} \right|^2 \right) , \tag{4.38}$$

where Γ_{SMF} is in decibels and ψ_1 and ψ_2 are the orthonormal fundamental guided modes of the two single-mode fibers. Note that (4.38) can be used to predict the transmission loss across a fusion splice joint in the presence of core offset or core eccentricity by using Cartesian coordinates and laterally displacing ψ_1 relative to ψ_2.

4.1.5 The Reflectance of Fusion Splices

The scattering matrix $\boldsymbol{S}$ also quantifies the reflectance of a fusion splice. For example, the component $S_{ai,ci}$ quantifies how much of the incident electric field in mode $\psi_i^{(\mathrm{L})}$ is reflected back into the exiting electric field in mode $\psi_i^{(\mathrm{L})}$. Note that the scattering matrix *does not* require that the reflectivity of an input field into the corresponding output field of the same mode (*i.e.* a_1 into c_1 for mode $\psi_1^{(\mathrm{L})}$) be equivalent to that of any other mode. Thus, although we have shown that the fusion splice loss between any two single-mode fibers must be the same in both propagating directions, the reflectance of such a fusion splice need *not* be the same in both directions. Furthermore, the reflectance of multimode fiber fusion splices certainly need not be identical in both directions.

The magnitude of the reflectance of a fusion splice can be estimated by considering the reflectance of a planar interface between two dielectric materials exhibiting refractive indices n_1 and n_2, respectively. When a plane wave crosses such an interface at normal incidence, the reflectivity can be expressed as [4.23]

$$R_{\mathrm{planewave}} = \frac{(n_1 - n_2)^2}{(n_1 + n_2)^2} . \tag{4.39}$$

The refractive index profiles of the launching and receiving fibers are usually not uniform, but instead exhibit some form of higher index core surrounded by a lower index cladding, possibly with additional trenches or rings surrounding the core (see Figs. 1.6 and 1.7). Therefore, an upper bound on the fusion splice reflectance can be obtained by substituting the highest refractive index present in either fiber for n_1 and the lowest refractive index present in either fiber for n_2 of (4.39) and (4.2) to yield

$$R_{\text{splice}} < 10 \log_{10} \left(\frac{(n_2 - n_1)^2}{(n_2 + n_1)^2} \right) \tag{4.40}$$

where reflectance follows the convention of (4.2) so it is represented as a negative number when expressed in dB units. A more accurate (and hence lower) estimate for the reflectance can be obtain by choosing n_2 to be the cladding refractive index and n_1 to be the approximate value of the core refractive index.

Since reflectance at a fusion splice arises from abrupt transitions in refractive index, it will be maximal at fusion splices between dissimilar optical fibers and minimal between similar or identical fibers. However, the reflectance of a high-quality fusion splices between optical fibers is substantially lower than the upper bound estimate of (4.40), and is nearly always less than -80 dB, regardless of the fiber types [4.24]. For comparison, a planar air-glass interface exhibits a reflectance of about -15 dB whereas conventional optical fiber connectors exhibit reflectance on the order of -55 dB. For example, the reflectance of a typical fusion splice between conventional SMF and erbium-doped fiber has been measured to be less than -100 dB [4.25]. In fact, we shall see in Chap. 7 that the reflectance of most fusion splices is typically so low that it cannot be measured with commercially available splice characterization equipment!

One of the main reasons for the exceedingly small reflectance of optical fiber fusion splices between dissimilar fibers is dopant diffusion (Sect. 3.3) across the boundary between the ends of the two fused fiber tips, which creates a narrow sub-micron graded-index interface region. This effect can be estimated by considering how a graded-index zone separating two uniform regions with different refractive indices reduces the reflectivity of a normally incident plane wave. The reflectivity of such a graded index region may be numerically modeled as a stack of many distinct thin uniform layers using either the wave impedance approach of [4.7] or the layered media analysis of [4.24, 4.26]. Figure 4.6 compares the results of some sample calculations showing how the reflectance of a plane wave is reduced as transition zone width between the two regions is increased where both wavelength and the refractive index difference are parameters. These results shows that the reflectance exhibits a very weak dependence upon wavelength, and that interdiffusion of only about 1 micron, which commonly occurs during normal fusion splicing conditions, results in fusion splice reflectance on the order of -80 dB or less.

Low-temperature fusion splices, discussed in Sect. 8.2.4, significantly limit dopant diffusion so that the observed reflectance between dissimilar fibers connected by low-temperature fusion splices can sometimes approach (4.40). However, the reflectance can be significantly reduced by cultivating a more gradual transition in refractive index that is easily achieved by increasing the temperature and/or the duration of the fusion splice, or reheating an existing fusion splice. Conventional single-mode fibers are most commonly comprised

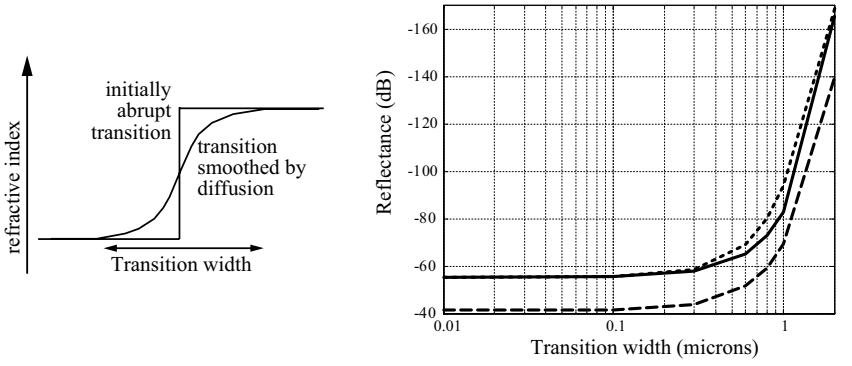

Fig. 4.6. Numerical prediction of the reflectance experienced by a plane wave impinging at normal incidence on an interface between two regions exhibiting distinct refractive index. The figure shows results for a refractive index difference (n_1-n_2) in silica fibers of 0.005 at 1550 nm (*solid line*), a refractive index difference of 0.005 at 1310 nm (*dotted line*) and an index difference of 0.025 at 1550 nm (*dashed line*).

of a pure silica cladding and an up-doped core, but can also be comprised of a pure silica core and a down-doped cladding. A fusion splice between these two different types of fiber will have a refractive index transition across the splice joint on the order of 0.005. Figure 4.6 shows that the reflectance (at both 1310 nm and 1550 nm)will be on the order of -55 dB following a very low-temperature splice of these fibers, or in the early stages of a conventional fusion splice. At the conclusion of a conventional fusion splice process the reflectance will be reduced below -80 dB. Similarly, Fig. 4.6 shows that an abrupt refractive index difference on the order of 0.025, which can occur when fusion splicing a large-core graded-index multimode fiber to conventional SMF at low temperature, can result in nearly -40 dB of reflectance. Conventional fusion splicing parameters will induce enough diffusion to reduce the splice's reflectance below -80 dB.

4.2 The Optics of Single-Mode Fiber Fusion Splices

The analysis of single-mode fiber fusion splices is much simpler than the analysis of multimode fiber fusion splices. Although we have noted in Sect. 4.1.3 that scattering matrices are non-commutable, in most cases we can ignore this rule when dealing with fusion splices between strictly single-mode fibers. In particular, the total fusion splice loss of a single-mode fiber span will be equal to the sum of the individual fusion splice losses within the span, irrespective of their particular order. The only exception to this generalization occurs when higher order modes are guided by the nominally single-mode fibers (an uncommon occurrence discussed in Sect. 4.2.4). Fusion splices be-

tween single- and multimode fibers are more complex than those between strictly single-mode fibers, and this topic is discussed in Sect. 4.3.4.

In a single-mode fiber fusion splice, the main concern is the amount of power transmitted across the splice from the launching fiber to the receiving fiber. In the previous section we derived the important result that the splice loss between single-mode fibers is the same in both direction. Single-mode splice losses between similar fibers are generally below 0.1 dB and in many cases are so low as to be undetectable and unmeasurable (<0.005 dB or <0.1% of the optical signal lost). However, single-mode fiber splices between very different fibers, such as between standard single-mode fiber (SMF) and dispersion-compensating fiber (DCF) can amount to several tenths of a dB (5% to 10% of the optical power lost).

It is helpful to organize single-mode fiber fusion splice loss into three general categories: *geometric deformation* (an extrinsic loss); *fiber mismatch loss* (an intrinsic loss); and *transition loss* (an extrinsic loss). As the name suggests, geometric deformation losses (Fig. 4.7a) result from physical perturbations to the fibers during the fusion splicing process. During the hot push and the ensuing joint formation, forces such as surface tension and viscosity often distort the shape of the fiber tips and their core structure. Poor cleaves are also likely to result in a fusion splice with core deformation. Generally speaking, geometric deformation of the fiber can be controlled and suppressed with proper fiber preparation and splicing parameters. In Sect. 4.2.2 we present a relatively simple formula for estimating single-mode splice loss based on simple geometrical deformations. A more accurate description of how geometrical deformation influences single-mode splice loss is presented in Chap. 5.

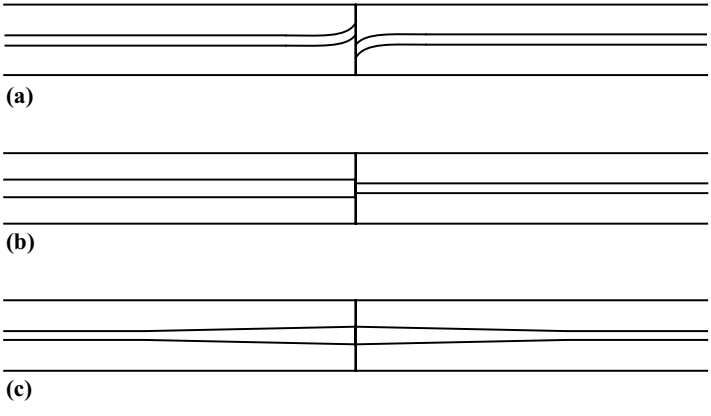

Fig. 4.7. The three general categories for single-mode fusion splice loss: (**a**) geometric deformation; (**b**) fiber mismatch; and (**c**) transition loss

Fiber mismatch loss (Fig. 4.7b) can only occur when splicing dissimilar fibers. In rare cases, two different batches of the same fiber design are so different that fiber mismatch splice loss results when splicing them together. Splice loss resulting from core eccentricity can be considered a fiber mismatch loss since the fibers are "different" on either side of the splice. The splice loss resulting from fiber mismatch can be estimated with the overlap integral in (4.38). Along with careful splice parameter optimization, several specialized strategies have been developed for reducing fiber mismatch loss (Sect. 8.1).

Transition splice loss (Fig. 4.7c) refers to loss resulting from heat-induced changes to the fibers in the vicinity of the splice. It is important to note that transition loss can occur between two identical fiber tips with perfect core alignment. In certain fibers, dopant diffusion can causes substantial transition loss, which manifest itself even when splicing identical fibers to each other. Along with careful splice parameter optimization, special strategies can be used to minimize transition losses (see Chap. 8.1).

4.2.1 The Mode Field Diameter

The mode field diameter (MFD) of a single mode fiber plays an important role in determining the fusion splice loss between fibers. Typical measurements for the MFD of single-mode fiber range from 4 to 12 μm. In general, fusion splice loss between fibers with very different MFD values is higher than fusion splice loss between fibers with similar MFD values. Furthermore, average splice loss is usually higher when the fiber's MFD is small since the splice loss will be more sensitive to lateral misalignments resulting from geometric deformation at the splice or core eccentricity in the fiber.

The fundamental mode field of a conventional single-mode fiber, ψ_{01}, exhibits no azimuthal dependence since $l = 0$, so we can describe it as $\psi_{01}(r)$. This mode field is usually a maximum at the center of the fiber where $r = 0$ and falls off exponentially at large r in the cladding of the fiber. Equation (4.13) actually predicts that the mode field only reaches zero as $r \to \infty$ because of this exponential behavior. In reality, $\psi_{01}(r)$ grows so weak at large r that it is undetectable and negligible. Characterizing the effective diameter of a mode field is not straightforward since the mode field asymptotically approaches zero at large radius. The MFD sensitively depends on the criteria employed for deciding where the "outside boundary" of the mode field is found.

Nevertheless, several practical definitions for the mode field diameter have been proposed, but the most common one, and the one we employ here, is termed the *Petermann II spot size* that was first proposed by Petermann in 1983 [4.4, 4.27, 4.28]

$$w_{\mathrm{p}} = \frac{2\int_0^\infty \psi_{01}^2(r)\mathrm{d}r}{\int_0^\infty (\frac{\mathrm{d}\psi_{01}(r)}{\mathrm{d}r})^2 r\mathrm{d}r} \,, \tag{4.41}$$

where w_{p} is the mode field radius so $2w_{\mathrm{p}}$ is the MFD.

Most manufacturers provide MFD data for their fibers, usually according to (4.41). Equation (4.41) can be used to compute the MFD based on an analytical expression for the mode field or a numerical data set. A high quality near field measurement of the mode field can also be used in (4.41), although the derivative in the denominator can cause trouble with noisy measurements. Pask and Ghatak describe methods for measuring the MFD based on the far field, or diffracted, intensity pattern of SMF [4.4, 4.28].

The MFD depends on the wavelength of the optical signal and longer wavelengths generally have larger MFD values. For example, standard SMF has an MFD of about 9.5 μm at 1310 nm and 10.5 μm at 1550 nm. Non-zero dispersion-shifted fibers (NZ-DSF) usually exhibit a slightly smaller MFD, around 9 μm at 1550 nm. Large-effective-area NZ-DSF exhibit MFD values as high as 12 μm at 1550 nm. Dispersion-compensating fibers (DCF) and erbium-doped amplifier fibers (EDF) usually exhibit small MFD values on the order of 5 μm. In fibers with large negative dispersion, such as DCF, the MFD may be particularly sensitive to wavelength. The unique dispersion characteristics of such fibers results from a MFD that changes rapidly with wavelength so that the optical power at different wavelengths samples different amounts of various cladding regions.

A common error is to assume that because two fibers have identical MFD values, their mode fields are identical. That is a bit like assuming two people are indistinguishable because they are the same height. It is critical to remember that the MFD is a single number that cannot possibly capture the details of the mode field shape, which is a continuous function that is very sensitive to the refractive index profile. Splice loss between dissimilar waveguides ultimately depends on the difference in shape between two mode field via the overlap integral equation, (4.38). In some cases, such as when both mode fields are very nearly Gaussian, the MFD is a very accurate indicator of the similarity between two mode fields. More generally, mode fields are not well characterized by a Gaussian and so they may have very different shapes, even when their MFD is identical. A good example of this is the small core SMF (*solid line*) and the DCF (*dotted line*) in Fig. 4.3 which have identical MFD values computed according to (4.41) but exhibit an overlap integral loss of 0.2 dB.

4.2.2 The Gaussian Approximation

Equation (4.13) cannot usually be solved analytically for the fundamental guided mode, ψ_{01}. Fortunately, the fundamental mode field of an optical fiber, $\psi_{01}(r)$, is often well approximated by a Gaussian function $\psi_{\mathrm{g}}(r)$. This Gaussian approximation was originally developed by Marcuse [4.29] and is a powerful tool for quantifying how mode field size, lateral core offset, and angular misalignments affect fusion splice loss. In this section we will introduce the Gaussian approximation to the mode field and cite some commonly used formulae for estimating single-mode fusion splice loss.

The Gaussian approximation to the fundamental mode of a fiber, $\psi_{01}(r)$, is expressed as

$$\psi_{\mathrm{g}}(r) = \frac{1}{\pi w_{\mathrm{g}}^2} \mathrm{e}^{-r^2/w_{\mathrm{g}}^2} , \tag{4.42}$$

where w_{g} is termed the Gaussian spot radius and is equal to w_{p} when (4.41) is applied to $\psi_{\mathrm{g}}(r)$. The Gaussian spot diameter is denoted by $2w_{\mathrm{g}}$. Marcuse developed an empirical relation for w_{g} of a single-mode step-index fiber based on the normalized frequency, V, of the fiber [4.4, 4.30]

$$\frac{w_{\mathrm{g}}}{R_{\mathrm{core}}} \approx \left(0.65 + \frac{1.619}{V^{3/2}} + \frac{2.870}{V^6} \right) , \tag{4.43}$$

where R_{core} is the core radius and $0 \leq V \leq 2.5$ which is approximately the range of V values for single-mode fibers.

Fusion splice loss between two Gaussian mode fields can occur when the spot sizes are different (dissimilar fibers), there is an angular misalignment at the splice, or there is a lateral offset at the splice. The Gaussian approximation for two dissimilar fibers with Gaussian spot radii w_{g1} and w_{g2}, lateral offset δ_{core} (which could be attributed to core eccentricity), and angular misalignment θ (Fig. 4.9), can be substituted into the overlap integral equation (4.38), and analytically solved to yield the fusion splice loss, $\Gamma_{\mathrm{Gaussian}}$ [4.10, 4.16, 4.29, 4.31]

$$\Gamma_{\mathrm{Gaussian}} = -10 \log \left[\frac{4 w_{\mathrm{g1}}^2 w_{\mathrm{g2}}^2}{\left(w_{\mathrm{g1}}^2 + w_{\mathrm{g2}}^2 \right)^2} \exp \left(- \frac{4\delta_{\mathrm{core}}^2 + k_0^2 n^2 w_{\mathrm{g1}}^2 w_{\mathrm{g2}}^2 \sin^2 \theta}{2(w_{\mathrm{g1}}^2 + w_{\mathrm{g2}}^2)} \right) \right] , \tag{4.44}$$

where $\Gamma_{\mathrm{Gaussian}}$ is in dB, n is the refractive index, and k_0, the vacuum wavenumber, is given by $2\pi/\lambda$. As expected for the case of single-mode fibers, (4.44) does not depend on propagation direction. When the two fibers are identical or there is no angular or no lateral misalignment, (4.44) may be further simplified (Figs. 4.10 and 4.11). Equation (4.44) suggests that when considered in units of dB, the loss contribution of mode field diameter mismatch, angular misalignment, and core offset are additive and do not interact.

Equation (4.44) is useful for understanding how the Gaussian spot size influences geometrical misalignments. For example, when the wavelength is kept constant smaller Gaussian spot sizes result is lower sensitivity to angular misalignments but increased sensitivity to lateral misalignments. Equations (4.43) and (4.44) can be used to show that as the V-parameter of an optical fiber increases, the splice loss due to tilted or offset cores increases as well [4.16]. Figure 4.12 shows that for a fixed fiber design, as the V-parameter increases due to a lower operating wavelength, the splice loss due to lateral core offset or angular core misalignment increases.

It is critical to understand that (4.44) is only an approximate estimate for fusion splice loss. Surface tension will often act to prevent real fusion splices

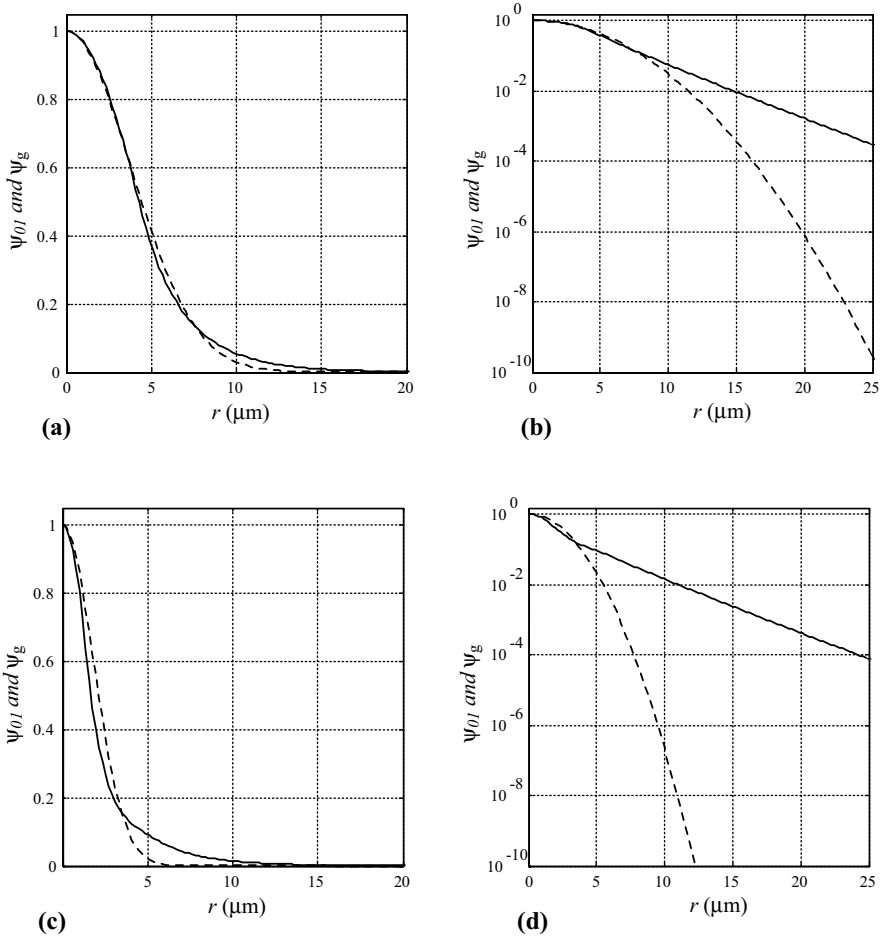

Fig. 4.8. The Gaussian approximation to SMF mode fields showing how the Gaussian approximation is much more accurate for standard SMF than it is for a DCF. The ψ_{01} are not orthonormal as they have been scaled such that $\psi_{01}|_{r=0} = 1$ to enhance the comparison. Note how the actual ψ_{01} drops off exponentially at large r (linearly on logarithmic plots) while $\psi_{\rm g}$ drops off much faster (quadratically on logarithmic plots). (**a**) linear scale and (**b**) logarithmic scale depictions of ψ_{01} for standard SMF (*solid line*) with 8.6 μm core diameter, Δ=0.33%, 10.5 μm MFD; and the corresponding Gaussian approximation $\psi_{\rm g}(r)$ (*dashed line*) with 10.6 μm MFD. The overlap integral loss between ψ_{01} for standard SMF and its Gaussian approximation is less than 0.03 dB. (**c**) linear scale and (**d**) logarithmic scale depictions of ψ_{01} for a DCF (*solid line*) 5.1 μm MFD and the Gaussian approximation $\psi_g(r)$ (*dashed line*) also with a 5.1 μm MFD. The overlap integral loss between ψ_{01} for DCF and its Gaussian approximation is 0.37 dB

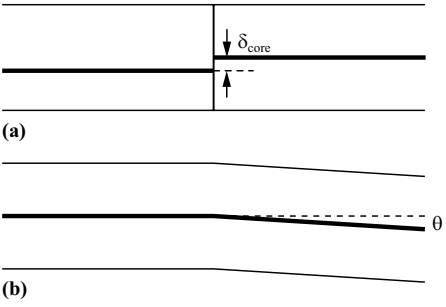

Fig. 4.9. Illustration of (**a**) lateral offset and (**b**) angular misalignment in a fusion splice between single-mode fibers

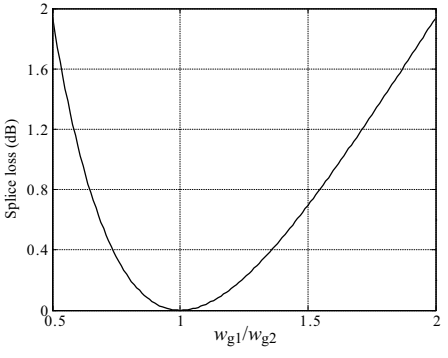

Fig. 4.10. Fusion splice loss for dissimilar fibers computed using (4.44). After [4.4]

from exhibiting truly discrete lateral core offsets δ_{core} or angular misalignments θ. The relationship between real core deformations and fusion splice loss in single mode fibers is more accurately described by coupled-mode theory (CMT) discussed in Chap. 5.

Splices involving certain types of SMF, especially those with complex refractive index profiles and relatively non-Gaussian mode fields, such as dispersion-compensating fiber (DCF) and dispersion-shifted fiber, are not well approximated by the equations presented in this section [4.32]. For example, (4.44) suggests that the fusion splice loss between standard SMF and the DCF from Fig. 4.8 is on the order of 1.8 dB but the more accurate overlap integral computation yields 1.1 dB. Fibers with a larger V-parameter have a more Gaussian fundamental mode field [4.33] and thus their splice loss is more accurately modeled by (4.44). Equation (1.6) shows that the V-parameter increases as the core radius or core diameter in increased and decreases as the operating wavelength is increased. Thus, (4.44) is more accurate at shorter wavelengths and becomes less accurate when a fiber is physically tapered to a smaller diameter.

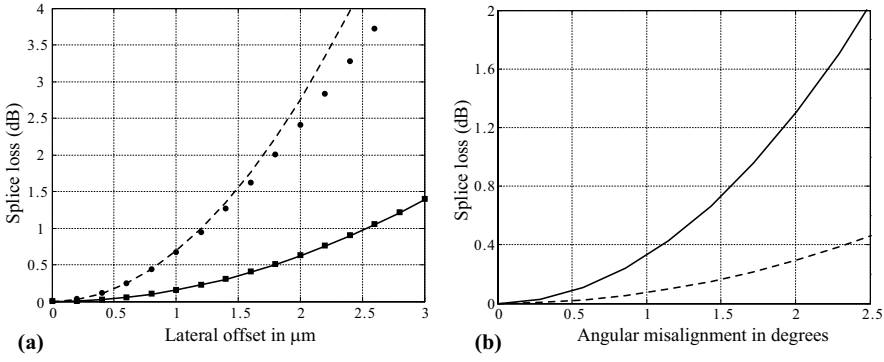

Fig. 4.11. Fusion splice loss between identical fibers as a function of (**a**) lateral offset and (**b**) angular misalignment both according to (4.44). Standard SMF at 1550 nm directly computed using the overlap integral (*squares*) and its Gaussian approximation (*solid line*) ; a DCF at 1550 nm directly computed using overlap integral (*circles*) and its Gaussian approximation (*dashed line*). Note how the DCF is much more sensitive to lateral offset than the SMF but SMF is much more sensitive to angular misalignments. The overlap integral calculations are performed using a numerical solution to (4.13) and are thus more accurate than the Gaussian approximation. Note how the Gaussian approximation for lateral offset splice loss is more accurate for standard SMF than it is for the DCF

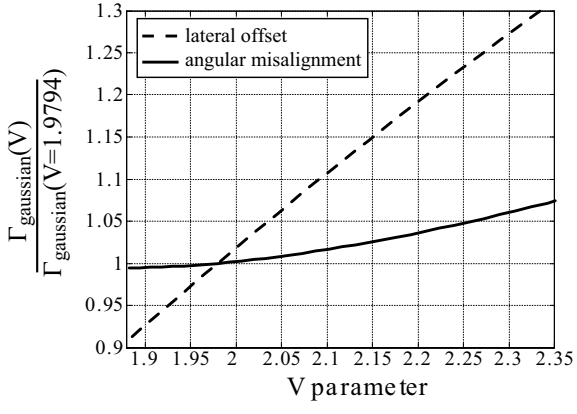

Fig. 4.12. Illustration of the effect of V-parameter on splice loss predicted by (4.44) using (1.6) and (4.43). The amount of Gaussian splice loss is normalized to the amount of splice loss that would occur when V=1.9794 (V-parameter for standard step-index SMF at 1550 nm). This plot can be used to estimate the variation of splice loss with operating wavelength for a given fiber design. For example, if V=1.9794 at 1550 nm, and if we assume a cladding refractive index of about 1.444 and a core radius of about 4.15 μm (which are typical values for standard SMF), (1.6) reveals that Δ is about 0.332%. Again using (1.6), we calculate that V is 2.342 at 1310 nm and thus we read off this plot that splice loss due to lateral core offset is about 30% higher and splice loss due to angular misalignment is about 7% higher at 1310 nm compared to 1550 nm. This plot is somewhat more useful than the one in [4.16] which was normalized to V=2.8 which is an unusual V-parameter for SMF

4.2.3 Reflectance of Single-Mode Fusion Splices

Competing fiber interconnection technologies such as connectors or mechanical splices can exhibit reflectances as high as -40 dB. As noted in Sect. 4.1.5, the reflectance of a high quality fusion splice is nearly always below -80 dB, which is so low that it is both difficult to measure and of little consequence for most optical fiber transmission systems [4.2, 4.3]. Moreover, the inherent distributed Rayleigh backscatter that is found in all optical fibers induces a reflectance on the order of -70 dB/meter (for conventional SMF) [4.25] so that the total optical power reflected by a single km of conventional SMF carrying a continuous wave signal is on the order of -40 dB, which is much greater than typical fusion splices.

However, it is important to note that low-temperature fusion splices discussed in Sect. 8.2.4 can result in elevated reflectances between dissimilar fibers because the low-temperature of the fusion splice limits dopant diffusion across the splice joint thus yielding a more abrupt refractive index transition. Furthermore, severe misalignments of low-temperature fusion splices between dissimilar or even similar fiber types can have the same effect.

Generally speaking, fusion splice reflectance is minimized when the two constituent fibers have similar refractive index profiles and similar mode field shapes. Kweon et al suggests the following relation to approximate the reflectance between two perfectly aligned but dissimilar single-mode fibers [4.20]

$$R_{SMF} = -10 \log_{10} \left[\frac{|\beta_1 - \beta_2|^2}{(\beta_1 + \beta_2)^2} \right] , \tag{4.45}$$

where β_1 and β_2 and are the axial propagation constants of the fundamental modes of the two constituent fibers. This relation is really just a restatement of (4.39) where the refractive index has been replaced by the effective refractive index of the guided modes, which is then simplified in terms of their axial propagation constants. Note that this approximate equation implies that the reflectance of a single-mode fusion splice is identical in both directions, which, as we saw earlier in Sect. 4.1.5, is not necessarily accurate. More importantly, (4.45) ignores the reduction in reflectance that results from dopant diffusion across the splice joint so this expression can be considered an upper bound estimate, albeit a better one than (4.40).

4.2.4 Modal Noise and Single-Mode Fiber Splices

Although single-mode fibers can theoretically only guide their fundamental mode, in practice higher order modes can travel a short distance before they dissipate [4.34]. If two low-quality single-mode fusion splices are too close to each other, it is possible for some amount of the original LP_{01} optical signal to be scattered into a higher-order mode at the first splice and then recoupled

back into the LP_{01} at the second splice (Fig. 4.13). This higher order mode is most commonly the LP_{11}, which can be strongly excited at a splice exhibiting substantial lateral core offset such as in a splice between eccentric core fibers. Since the LP_{11} mode travels at a slightly different velocity than the LP_{01} mode, one signal will be delayed with respect to the other, so the two signals will interfere to produce noise that reduces the bandwidth of the optical transmission system. This interference noise is termed *modal noise* [4.10,4.34–4.36].

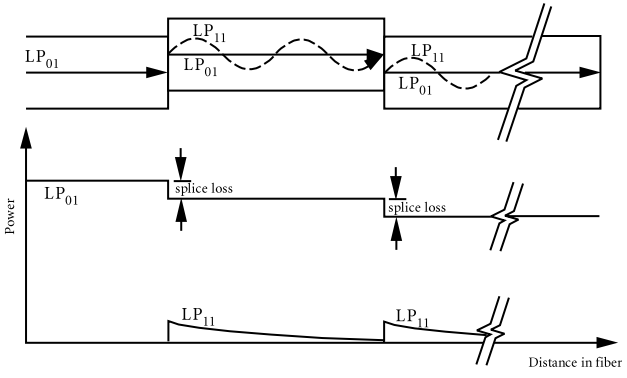

Fig. 4.13. Schematic illustration of modal noise arising from two closely spaced lossy fusion splices. The optical signal initially occupies the LP_{01} mode. At the first lossy splice some of the energy from the LP_{01} mode is converted into the LP_{11} mode where it is slowly attenuated. However, there is still some power remaining in the LP_{11} at the second lossy fusion splice where it interferes with the original signal in the LP_{01} thus degrading the system signal-to-noise ratio. After [4.35]

All optical fibers exhibit a cutoff wavelength, below which they guide more than one mode, above which they guide only the fundamental mode. Modal noise is naturally more pronounced at shorter wavelengths, where a single-mode fiber is closer to guiding multiple modes. For a modern telecommunications fiber designed for operation at 1550 nm, this corresponds to wavelengths shorter than about 1350 nm. Modal noise can be identified by measuring the variation of splice loss with wavelength since the splice loss exhibits strong wavelength dependent fringes at shorter wavelengths which grow weaker at longer wavelengths (Fig. 4.14). The spacing of the fringes shrinks when the spacing between the two splices increases [4.37].

Since modal noise depends on converting energy from the LP_{01} mode to the LP_{11} mode at the splice joint, it can be suppressed by ensuring that the splice is high quality (low-loss in the LP_{01} mode and minimal power exchanged between the LP_{01} and LP_{11} modes). Experimental and theoretical results indicate that splice losses on the order of 0.5 dB are sufficient to result in substantial modal noise [4.37, 4.38]. Optical fiber fusion splices between

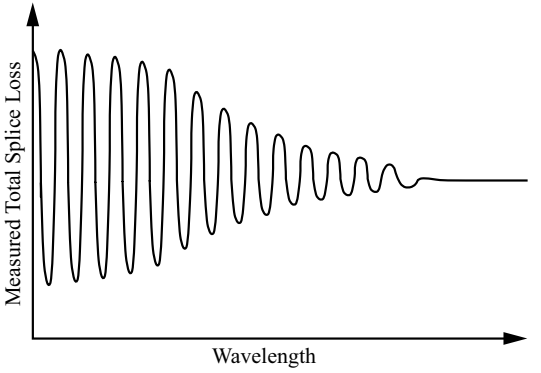

Fig. 4.14. Interference fringes characteristic of modal noise in a single-mode fiber near the cutoff wavelength. After [4.37]

very dissimilar fibers such as DCF and SMF can be this lossy, but if the fiber cores are well aligned to each other, the lost power won't couple into the LP_{11} mode so modal noise shouldn't be a problem.

When the spacing between single-mode fiber fusion splices is greater than about two meters, the natural attenuation of higher-order modes is typically sufficient to suppress modal noise [4.39]. Consequently, pigtails and bridge fibers should be longer than 2 m, when possible. Modal noise can also be suppressed by putting a bend in the fiber between the two splices that will attenuate the LP_{11} mode much more than the more strongly guided LP_{01} mode [4.34].

Another type of interference noise can occur when two highly reflective splices interact with each other. In this phenomenon, termed *multipath interference* or MPI, a fraction of the optical power is delayed by reflection at the two splices and then interferes with the original optical signal (Fig 4.15) [4.34, 4.36, 4.40]. Unlike modal noise, the interference signal responsible for MPI remains in the fundamental mode. Fusion splices usually do not induce such MPI because, as we saw earlier in Sect. 4.1.3, fusion splices usually exhibit extremely low reflectance.

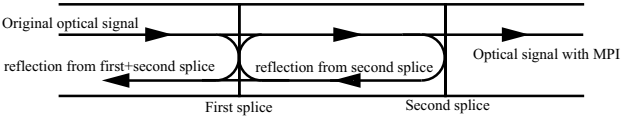

Fig. 4.15. Illustration of multipath interference (MPI) arising from two highly reflective splices. Unlike modal noise, the interference signal responsible for MPI remains in the fundamental mode

4.3 The Optics of Multimode Fusion Splices

The optical characteristics of multimode fiber splices are much more complex than single-mode fiber splices. This is because a multitude of individual modes interact with each other both at the splice joint and also along the length of the fiber. The distribution of energy amongst the various guided modes slowly evolves along the length of a multimode fiber. Thus, the optical characteristics of an individual multimode fiber splice depends on its proximity to other multimode splices, connectors, and sources as well as upon the propagation direction and the geometry of splice itself.

Detailed treatments of multimode optical fiber splices are available in [4.16, 4.41]. In this section we will provide an introduction to the optics of multimode fiber splices. We begin with a discussion of some of the unique properties of multimode fibers. We will then present some approximate formulae for the estimation of fusion splice loss in multimode fibers. We conclude this section with a discussion of the reflection properties of multimode fiber fusion splices and an analysis of fusion splices between single- and multimode fibers.

4.3.1 Propagation Characteristics

In order to properly understand the optics of multimode fiber fusion splices, a basic understanding of optical propagation in multimode fiber is required. When the normalized frequency, the V-parameter, of multimode fiber is larger than about 10 (as it is for most commercial multimode fiber), ray optics (also termed geometrical optics) can be used to describe the path of the propagating signal [4.4]. Ray optics ignores interference or wave phenomena and treats the optical signal as if it were comprised of individual ballistic photons following a path determined by the refractive index of the medium they travel through.

According to this ray optics approach, a step-index multimode fiber guides light due to total internal reflection at the core-cladding interface. Light propagating inside the fiber at an angle (measured relative to the fiber axis) that is less than a critical angle (Sect. 1.3.1) will be guided in the fiber's core. The fiber's numerical aperture (NA) is the sine of the critical angle for light impinging on the fiber's end face in air. In other words, the NA defines the cone of incident light that is successfully coupled into the fiber's core. The NA is also defined for graded-index multimode fibers and also describes the sine of the critical acceptance angle at the fiber's end face.

Fusion splices will exhibit loss when the receiving fiber has a smaller core diameter or a smaller NA than the launching fiber. In such a case, some of the incident photons won't be captured by the receiving fiber. This helps to explain why multimode fiber splice loss, unlike single-mode fiber splice loss, depends on propagation direction. When the V-parameter of the fiber is less than 10, this ray optic picture is inadequate for describing the propagation characteristics of multimode fiber so the modal description is necessary.

As we saw in Sect. 4.1.3, scattering matrices are non-commutable, meaning that their order is important. This implies that the optical performance of a multimode fiber span can depend on the precise order and spacing of the fusion splices within. By definition, multimode fibers guide a large number of individual modes which are orthogonal to each other. The electric field, and hence the optical intensity, of lower-order guided modes are confined to the central region of the fiber's core and do not penetrate deeply into the fiber's cladding. Meanwhile, the higher-order modes tend to sample regions of the fiber at larger radius where the fiber's cladding, and the interface between the core and cladding, is more lossy. Thus, energy in the higher order modes is gradually depleted as it propagates down the fiber. However, as higher order modes are depleted, energy is scattered from the lower order modes to populate the higher order modes. This mode mixing is unavoidable and results from imperfections and microbends in the multimode fiber. These competing phenomena will tend to establish an equilibrium distribution of power amongst the various modes. Many km of multimode fiber are required to establish a steady-state population of the modes.

As Fig. 4.16 demonstrates, a fusion splice can change the amount of power distributed amongst the various modes. Generally speaking, some power will be scattered from lower-order modes into higher-order modes at a splice joint. The excess power in the higher-order modes will gradually be scattered amongst the various modes, as well as completely out of the fiber in the portion of fiber downstream of the splice. If another fusion splice is situated close to this first splice, the amount of loss measured at the second splice may be different than that measured at the first splice since the population of the modes is different at the second splice.

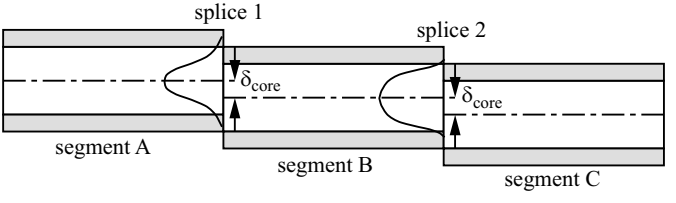

Fig. 4.16. Schematic illustration of how fusion splice loss in multimode fiber can depend on proximity to other fusion splices. The power in fiber segment A is assumed to conform to the equilibrium distribution amongst the modes. The Gaussian curve is intended to schematically illustrate how the intensity might depend on radial position in fiber segment A. At splice number 1, there is a small offset, δ_{core}, which causes power to be scattered to higher-order modes. Fiber segment B is assumed to be short enough (on the order of meters) so that the power does not achieve an equilibrium mode distribution. The same amount of offset δ_{core} at splice number 2 will result in a different amount of loss than δ_{core} at splice number 1 because the modal power distribution is different. Thus the splice loss depends on the proximity of the splices as well as the geometry of the splice itself. After [4.42]

Since splices tend to scatter energy from the lower-order modes into the higher-order modes, and since higher-order modes are in general more lossy than lower-order modes, a large number of closely spaced multimode fusion splices will tend to exhibit more loss per splice than fusion splices spaced by long lengths of fiber. Moreover, a large number of closely spaced splices can tend to increase the dispersion of a multimode fiber link by encouraging a larger fraction of energy to travel in the higher order modes. In rare cases, the mode scrambling behavior of a fusion splice can actually increase the bandwidth of a multimode fiber by fostering a more desirable distribution of power amongst the modes [4.16, 4.34].

The fusion splice loss between dissimilar multimode fibers has been found to exhibit a wavelength dependence that oscillates about some constant value [4.43]. The amplitude and period of the oscillation increases with increasing wavelength and results from the fact that the receiving fiber cannot accept all the modes from the launching fiber [4.34].

4.3.2 Splice Loss Approximation Formulae

We may express the power lost at a multimode splice using the scattering matrix formalism developed in Sect. 4.1.3. A precise description of optical propagation across a multimode fiber fusion splice requires considering the interaction of hundreds or even thousands of modes via the scattering matrix in (4.28). From (4.26b) and (4.26c) we see that the total power lost at a multimode splice, L_{total}, may be expressed as

$$L_{\text{total}} = P_{\text{L,in}} - P_{\text{R,out}} = \boldsymbol{a}^{+}\boldsymbol{a} - \boldsymbol{b}^{+}\boldsymbol{b} \,. \tag{4.46}$$

Now consider the subset of the scattering matrix $\boldsymbol{S}$, termed $\boldsymbol{S}_{\text{sub}}$, which relates $\boldsymbol{a}$ to $\boldsymbol{b}$ in the same manner as (4.28)

$$\boldsymbol{b} = \boldsymbol{S}_{\text{sub}}\boldsymbol{a} \,. \tag{4.47}$$

Note that unlike $\boldsymbol{S}$, $\boldsymbol{S}_{\text{sub}}$ is not necessarily square nor is it symmetric. With some algebraic manipulation of (4.46) and (4.47) we can write

$$L_{\text{total}} = \boldsymbol{a}^{+}\left(\mathbf{I} - \boldsymbol{S}_{\text{sub}}^{+}\boldsymbol{S}_{\text{sub}}\right)\boldsymbol{a} \,, \tag{4.48}$$

where $\mathbf{I}$ is the identity matrix. If define a new matrix $\boldsymbol{L}$ such that $\boldsymbol{L} \equiv \mathbf{I} - \boldsymbol{S}_{\text{sub}}^{+}\boldsymbol{S}_{\text{sub}}$ we may write

$$L_{\text{total}} = \boldsymbol{a}^{+}\boldsymbol{L}\boldsymbol{a} \,, \tag{4.49}$$

which can be written as

$$L_{\text{total}} = \sum_{j=1}^{M} a_j^{*}\left(\sum_{i=1}^{M} a_i L_{ij}\right) \,, \tag{4.50}$$

where L_{ij} is the component from the i^{th} column and j^{th} row of matrix $\boldsymbol{L}$. Equation (4.50) may then be written out as

$$L_{\text{total}} = L_{11}a_1^*a_1 + L_{12}a_2^*a_1 + L_{22}a_2^*a_2 + L_{21}a_1^*a_2 + \cdots \ . \tag{4.51}$$

When the number of modes is very large and the relative phase angle of the modal amplitude coefficients are randomly distributed, the cross terms in (4.51) are negligible [4.16, 4.41]. Physically this means that the phases of the various propagating modes are uncorrelated so that they do not interfere with each other on a time averaged basis. With this assumption we may approximate the total multimode fiber loss as

$$L_{\text{total}} = L_1P_1 + L_2P_2 + L_3P_3 + \cdots = \sum_{i=1}^{M} L_iP_i \ , \tag{4.52}$$

where $P_i = a_i^*a_i$ and thus denotes the amount of power carried in mode i whereas L_i denotes the fraction of mode i lost at the splice. We drop the second subscript in L_i to simplify the notation since we are neglecting all cross terms.

Equation (4.52) suggests that the amount of power lost at a multimode fusion splice is a linear function of the power carried in the various modes of the fibers. This relationship implies that, in contrast to single-mode splice loss, multimode splice loss depends on the relative amount of power in the various modes. Since typical multimode fibers carry hundreds of modes, it is very difficult to estimate the values for the hundreds of L_i and P_i at an arbitrary fusion splice so even the approximate expression (4.52) is still far to complex to yield practical estimates for multimode fusion splice loss.

In response to these difficulties, Sekai derived the following simple approximation formulae to predict the fusion splice loss of multimode fibers with [4.41, 4.44]

$$\Gamma_{\text{offset}} \approx 3\frac{\delta_{\text{core}}}{D_{\text{core}}} \ , \tag{4.53a}$$

$$\Gamma_{\text{diam}} \approx 4.5\left(1 - \frac{D_{\text{core2}}}{D_{\text{core1}}}\right) \ , \tag{4.53b}$$

$$\Gamma_{\text{index}} \approx 1.6\left(1 - \frac{\Delta_2}{\Delta_1}\right) \ , \tag{4.53c}$$

where Γ_{offset} refers to the splice loss resulting from a lateral offset of the fiber cores, Γ_{diam} refers to a mismatch in the multimode core diameters, Γ_{index} refers to a mismatch in the fibers' core Δ, D_{core} is the core diameter, δ_{core} is the lateral offset, and the subscript 1 refers to the launching fiber and 2 refers to the receiving fiber. Other approximate formulae for predicting multimode fiber splice loss are available in [4.16, 4.41]. All the splices losses in (4.53) are expressed in units of dB. Obviously (4.53b) is only applicable when $D_{\text{core2}} < D_{\text{core1}}$.

4.3.3 Reflections from Multi-Mode Fusion Splices

Quantifying the reflectance of a multimode fusion splice is just as difficult as quantifying its splice loss since an exact determination requires considering the interaction between hundreds, and possibly thousands of modes at the splice joint. Theoretically, multimode fusion splice reflectance depends upon the amount of energy populating each mode, as well as upon the reflectivity coefficients for the individual modes. Kashima *et al* has found that in practice, the reflectance of a fusion splice between graded index fibers is not particularly sensitive to the mode power distribution [4.22, 4.41]. As is the case with single-mode fusion splices, lower loss multimode fusion splices generally exhibit lower reflectance as well. Reflectance values well below -60 dB are typical [4.22, 4.41]. As discussed in Sect. 4.1.5, dopant diffusion plays an important role suppressing the reflectance of multimode fusion splices.

4.3.4 Fusion Splices Between Single- and Multimode Fibers

Fusion splices between single- and multimode fibers are rare, but are sometimes used to connect a single-mode system to a multimode fiber that is coupled to either a source or a detector. Although the joint between a single- and multimode fiber will be optically reciprocal, the fusion splice loss sensitively depends upon propagation direction [4.10].

When the single-mode fiber is the launching fiber and the multimode fiber is the receiving fiber, the fusion splice loss (defined as optical power radiated out of the fiber) will generally be quite low since the energy from the single-mode fiber will be scattered amongst the many guided modes of the multimode fiber. The overlap integral, (4.33), can be used to compute this partitioning of the energy [4.10].

The overlap integral also governs the characteristics of a fusion splice in which the multimode fiber launches into the single-mode fiber. However, the amount of energy in each guided mode of the multimode fiber, as well as the relative phase angle of each mode, is generally unknown, so overlap integral computation is impossible. Since the distribution of energy in a multimode fiber, and especially the relative phase angle between the various modes, varies with time, the splice loss from the multimode fiber into the single-mode fiber will also vary with time. Neumann crudely estimates the transmitted power from a general multimode fiber into a general single-mode fiber to be 2 divided by the number of modes in the multimode fiber, which is usually on the order of 150. This works out to a splice loss on the order of 20 dB [4.10] whereas Shumate [4.45] has measured it to be on the order of 15 dB in one particular case. This measurement will be sensitive to the precise distribution of the modal energy.

As noted in Sect. 4.1.5, the reflectance of a low-temperature fusion splice between a large-core graded-index multimode fiber and a single-mode fiber can be relatively large (on the order of -40 dB) because of the relatively

large refractive index difference normally occurring between the two fibers. As Fig. 4.6 shows, much lower reflectance values (<-80dB) are easily attained by performing the splice at a sufficiently high temperature such that diffusion across the interface between the two fibers creates a more gradual transition in refractive index.

4.4 The Beam Propagation Method (BPM)

In many cases we would like to predict how the optical characteristics of a fusion splice depend on the particular refractive index profile in the vicinity of the splice. For example, we may wish to compute how dopant diffusion, physical tapering, or dissimilar fiber designs affect splice loss or mode conversion. We may wish to understand why fusion splices between certain fiber types is unusually lossy or to gain insights that will speed the tedious process of splice optimization. Finally, we may want to predict the loss of a fusion splice based on knowledge of its geometric deformation, a process termed loss estimation.

To accomplish these tasks, we require a computational tool that can predict the evolution of an initial optical signal as it propagates along a changing waveguide. The *Beam Propagation Method* (BPM) is a numerical simulation tool that can provide an accurate description of optical propagation in a fiber based solely on the refractive index profile. In fact, BPM can be used to numerically solve for the guided modes of an arbitrary refractive index profile. Furthermore, BPM can be effective for a wide variety of initial optical fields and fiber index profiles. As numerical computation becomes faster and cheaper, simulation tools such as BPM become more attractive strategies for understanding and optimizing fusion splicing. Several good general reviews of BPM are available in the literature [4.46–4.50]. In this section we will introduce BPM and demonstrate its utility for analyzing optical fiber fusion splices.

4.4.1 Introduction to BPM

The original version of the BPM, termed the Fourier transform BPM (FT-BPM), was developed by Feit and Fleck during the early days of optical fiber [4.6, 4.51–4.54]. Their algorithm provided a solution to the scalar wave equation using a Cartesian coordinate system, which is useful and efficient for solving a wide variety of optical wave propagation (including optical fiber) problems. However, the FT-BPM is not efficient for strictly radially symmetric optical fibers. Since their invention of the original FT-BPM, a wide variety of BPM techniques have been developed including finite-difference BPM (FD-BPM), finite-element BPM (FE-BPM), as well as full-vectorial,

partial-vectorial, and scalar techniques [4.48–4.50, 4.55]. One universal limitation of the BPM is that it cannot model reflections or backward propagating waves. Time-domain algorithms such as the finite-difference time-domain (FDTD) approach are a more rigorous solution to Maxwell's Equations and can model reflectance, but they require more computation time and data storage [4.50, 4.56–4.58]. Several BPM software packages are commercially available. In this section, we will focus on one particular BPM implementation developed by Yamauchi and coworkers [4.59, 4.60].

Yamauchi's BPM is a scalar FD-BPM with a radially symmetric domain, which is appropriate for analyzing radially symmetric fibers. Since the technique is based on the scalar wave equation, (4.8), it is not appropriate for waveguides with large refractive index gradients or large electric field components in the axial direction, which require a vectorial BPM. Yamauchi's BPM is particularly well suited to analyzing fusion splices of contemporary single-mode fiber such as standard SMF, erbium-doped fiber (EDF), and dispersion-compensating fiber (DCF). As a BPM, it cannot handle reflected waves but this is not a problem since reflections from a fusion splice are usually weak enough to be neglected. This BPM assumes a perfectly radially symmetric fusion splice so it cannot model lateral core misalignment or radially asymmetric core deformation. This is not a disadvantage since we are usually interested in understanding how radially symmetric fiber refractive index profiles, such as those resulting from dopant diffusion, splice tapering, splice fattening, or dissimilar fiber designs, affect the optical characteristics of fusion splices. The BPM described here utilizes a uniform radial grid spacing, but non-uniform grid version are also available in the literature [4.61].

The derivation of the BPM assumes that the electric field in the fiber varies along the z-direction so instead of (4.10) we postulate a scalar electric field of the form

$$E(r, \phi, z, t) = R(r, z)\Phi(\phi) \exp \mathrm{i}(\omega t - k_0 n_{\mathrm{clad}} z) \,, \tag{4.54}$$

where ϕ is the azimuthal coordinate, ω is the angular frequency, $\Phi(\phi) = \cos(l\phi)$, k_0 is the vacuum wavenumber, n_{clad} is the refractive index of the fiber's cladding, and l is an integer (0,1,2...). However, the radial electric field envelope, R, is a now function of *both* radius, r, and axial position, z. By separating the field envelope functions R and Φ from the exponential phase variation term, $\exp(\mathrm{i}k_0 n_{\mathrm{clad}} z)$, we can utilize a relatively coarse grid spacing in the z direction which contributes to the efficiency of the BPM [4.50].

We discretize the function $R(r, z)$ into $N + 1$ equally spaced radial nodes and an unlimited number of axial nodes such that

$$R(r, z) = R((i - 1)\Delta r, k\Delta z) = R_i^k \tag{4.55}$$

where the subscript i and the superscript k are integers denoting the radial and axial node numbers, respectively, and Δr and Δz are the uniform radial and axial node spacings, respectively. (Note that k_0 refers to the vacuum wavenumber, $2\pi/\lambda$, whereas k is the axial mode number. Also note that i

is the axial node number whereas i denotes $\sqrt{-1}$) We define a vector, $\boldsymbol{R}^k$, which denotes the discretized electric field envelope at axial node k (Note that the superscript does not denote an exponent but rather is an index)

$$\boldsymbol{R}^k = \begin{bmatrix} R_1^k \\ R_2^k \\ R_3^k \\ \vdots \end{bmatrix} = \begin{bmatrix} R(0, k\Delta z) \\ R(\Delta r, k\Delta z) \\ R(2\Delta r, k\Delta z) \\ \vdots \end{bmatrix} . \tag{4.56}$$

For the purposes of our BPM, this vector is a complete description of the electric field at axial node k. Note that the $\boldsymbol{R}^k$ will generally be a vector of complex numbers. Likewise, we define a vector $\boldsymbol{R}^{k+1}$ which denotes the vector of electric field amplitudes at the next axial node, $k+1$

$$\boldsymbol{R}^{k+1} = \begin{bmatrix} R_1^{k+1} \\ R_2^{k+1} \\ R_3^{k+1} \\ \vdots \end{bmatrix} = \begin{bmatrix} R(0, (k+1)\Delta z) \\ R(\Delta r, (k+1)\Delta z) \\ R(2\Delta r, (k+1)\Delta z) \\ \vdots \end{bmatrix} . \tag{4.57}$$

Put succinctly, the objective of the BPM is to predict $\boldsymbol{R}^{k+1}$ based on $\boldsymbol{R}^k$ and the known refractive index profile. This way, we can launch an arbitrary electric field (optical signal) and observe how it evolves as it moves through a region of optical fiber in which the refractive index profile changes along its length, such as at a fusion splice.

To accomplish this goal (4.54) is substituted into (4.9) to arrive at

$$-\frac{\partial^2 R}{\partial z^2} + 2\mathrm{i}k_0 n_{\mathrm{clad}} \frac{\partial R}{\partial z} = \left\{ \frac{\partial^2}{\partial r^2} + \frac{1}{r}\frac{\partial}{\partial r} - \frac{l^2}{r^2} + k_0^2(n^2 - n_{\mathrm{clad}}^2) \right\} R \, , \tag{4.58}$$

where the refractive index of the fibers is given by $n = n(r, z)$. When we neglect the first term in (4.58), the second derivative with respect to z, we obtain the *paraxial equation* which is valid for small values of $n^2 - n_{\mathrm{clad}}^2$

$$2\mathrm{i}k_0 n_{\mathrm{clad}} \frac{\partial R}{\partial z} = \left\{ \frac{\partial^2}{\partial r^2} + \frac{1}{r}\frac{\partial}{\partial r} - \frac{l^2}{r^2} + k_0^2(n^2 - n_{\mathrm{clad}}^2) \right\} R \, . \tag{4.59}$$

This simplification reduces the problem from a second-order boundary value problem to a first order initial value problem which can be solved by stepping along in the z-direction [4.50]. The paraxial equation, (4.59), may be rewritten with the Padé (1,1) approximant as [4.60]

$$\frac{\partial R}{\partial z} = \frac{\frac{\mathrm{i}P}{2k_0 n_{\mathrm{clad}}}}{1 + \frac{P}{4k_0^2 n_{\mathrm{clad}}^2}} R \, , \tag{4.60}$$

where P is the operator

$$P = \frac{\partial^2}{\partial r^2} + \frac{1}{r}\frac{\partial}{\partial r} - \frac{1^2}{r^2} + k_0(n - n_{\mathrm{clad}}^2) \, . \tag{4.61}$$

The Padé approximant is useful because it can accurately model waves propagating at relatively large angles to the z-axis. A set of finite difference equations can be constructed from (4.60-4.61) using a Crank-Nicholson implicit differencing algorithm [4.60, 4.62]. We can express the resulting finite difference algorithm as [4.60]

$$\boldsymbol{M}^{k+1}\boldsymbol{R}^{k+1} = \boldsymbol{M}^{k}\boldsymbol{R}^{k}\ , \tag{4.62}$$

where $\boldsymbol{M}^k$ is the tridiagonal matrix [4.60]

$$\boldsymbol{M}^k = \begin{bmatrix} \chi+\xi\iota & b\xi & 0 & & & & \\ \xi a^+ & \chi+\xi\zeta & \xi a^- & 0 & & & \\ 0 & \xi a^+ & \chi+\xi\zeta & \xi a^- & 0 & & \\ & 0 & \xi a^+ & \chi+\xi\zeta & \xi a^- & 0 & \\ & & 0 & \ddots & \ddots & \ddots & 0 \\ & & & 0 & \xi a^+ & \chi+\xi\zeta & \xi a^- \\ & & & & 0 & 0 & 0 \end{bmatrix}, \tag{4.63}$$

and [4.60]

$$a^{\pm} = 1 \mp 1/2(i-1) \tag{4.64a}$$

$$\chi = (4k_0^2 n_{\text{clad}}^2 \Delta r^2)/(1 + \mathrm{i}k_0 n_{\text{clad}} \Delta z) \tag{4.64b}$$

$$\zeta = \Delta r^2 k_0^2 (n^2 - n_{\text{clad}}^2) - \Delta r^2 \frac{l^2}{r^2} - 2 \tag{4.64c}$$

$$\xi = (1 - \mathrm{i}k_0 n_{\text{clad}} \Delta z)/(1 + \mathrm{i}k_0 n_{\text{clad}} \Delta z) \tag{4.64d}$$

$$b = (1 + e^{\mathrm{i}l\pi}) \left(2 - \frac{l^2}{2}\right) \tag{4.64e}$$

$$\iota = \Delta r^2 k_0^2 (n^2 - n_{\text{clad}}^2) - 2\left(2 - \frac{1^2}{2}\right)\ . \tag{4.64f}$$

Notice that the first and last rows of $\boldsymbol{M}^k$ appearing in (4.63) are different than the middle rows. The first row is different because L'Hôpital's rule and the symmetry of the electric field are used to derive the difference relation at the origin (where r=0) [4.60]. The special nature of the final row is discussed in the next section which presents the transparent boundary condition.

$\boldsymbol{M}^{k+1}$ is the tridiagonal matrix [4.60]

$$\boldsymbol{M}^{k+1} = \begin{bmatrix} \chi+\iota & b & 0 & & & & \\ a^+ & \chi+\zeta & a^- & 0 & & & \\ 0 & a^+ & \chi+\zeta & a^- & 0 & & \\ & 0 & a^+ & \chi+\zeta & a^- & 0 & \\ & & 0 & \ddots & \ddots & \ddots & 0 \\ & & & 0 & a^+ & \chi+\zeta & a^- \\ & & & & 0 & k_{\text{r}}'\Delta r & -1 \end{bmatrix}. \tag{4.65}$$

As in (4.63), the first and last rows of $\boldsymbol{M}^{k+1}$ appearing in (4.65) are different from the interior rows. The last row of $\boldsymbol{M}^{k+1}$ will be explained in the next section.

Tridiagonal matrices such as (4.63) and (4.65) are particularly attractive since they can be solved very efficiently, often with commercially available numerical routines. A reduced equation relating $\boldsymbol{R}^{k+1}$ to $\boldsymbol{R}^{k}$ may be expressed as

$$\boldsymbol{R}^{k+1} = \boldsymbol{T}\boldsymbol{R}^{k} \,, \tag{4.66}$$

where

$$\boldsymbol{T} = \left(\boldsymbol{M}^{k+1}\right)^{-1} \boldsymbol{M}^{k} \,, \tag{4.67}$$

and $\left(\boldsymbol{M}^{k+1}\right)^{-1}$ is the matrix inverse of $\boldsymbol{M}^{k+1}$. Thus, given an initial field distribution $\boldsymbol{R}^{0}$, $\boldsymbol{R}^{1}$ is obtained by first assembling the matrix $\boldsymbol{T}$ and then multiplying this matrix by $\boldsymbol{R}^{0}$. This process is repeated at each successive axial node to propagate the field through the fusion splice region. Note that the matrix $\boldsymbol{T}$ depends on the refractive index profile so it will change as the refractive index profile changes.

Δz usually is chosen to be on the order of 1 μm so about 1000 computation steps are required to propagate an electric field through a distance of 1 mm. A typical value for Δr is about 200 nm which means that about 330 radial nodes are required to model a 62.5 μm radius fiber. A 3 GHz Pentium IV PC using efficient tri-diagonal matrix routines can propagate a field through a fiber splice at a rate of about 4 mm/minute with this choice of Δz and Δr.

Notice that there is a different set of $\boldsymbol{M}^{k}$ and $\boldsymbol{M}^{k+1}$ matrices for each value of l in (4.59). Thus, to handle a completely arbitrary input electric field (exhibiting both r *and* ϕ variation), we must first decompose it into components which exhibit $l\phi$ variation and propagate each of these components with the appropriate $\boldsymbol{M}^{k}$ and $\boldsymbol{M}^{k+1}$ separately. Usually, we are only interested in input electric fields exhibiting radial symmetry (i.e. l=0).

Another implication of the dependence of $\boldsymbol{M}^{k}$ and $\boldsymbol{M}^{k+1}$ on l is that this BPM formulation does not allow electric field with $l\phi$ dependence to exchange energy with electric field exhibiting with $l'\phi$ dependence if $l \neq l'$. In other words, the LP_{lm} mode cannot exchange energy with the $\mathrm{LP}_{l'm'}$ mode if $l \neq l'$. This feature of this BPM makes physical sense since the domain is assumed to be radially symmetric. Exchanging power between LP_{lm} modes with different values for l requires a refractive index profile that is *not* radially symmetric, such as a splice with laterally offset cores.

4.4.2 The Transparent Boundary Condition

At the outer boundary of the computational domain, where $r = N\Delta r$, we desire a boundary condition that will allow any outgoing electric field to escape the domain without being reflected. Such a boundary condition is

termed a *transparent boundary condition* (TBC) and was first developed by Hadley [4.63, 4.64]. The TBC is dynamic, meaning that it depends on the electric field vector of the previous axial step, rather than depending directly on the refractive index profile of the fiber.

Once the vector $\boldsymbol{R}^k$ is computed from the previous computation step, we define a wavenumber k_r based on the two vector elements R^k_{N-1} and R^k_{N-2} [4.63]

$$\exp(\mathrm{i}k_\mathrm{r}\Delta r) = \frac{R^k_{N-1}}{R^k_{N-2}} \; . \tag{4.68}$$

Generally k_r will be complex. We adjust the value of the last element of $\boldsymbol{R}^k$, R^k_N, so that [4.63]

$$R^k_N = R^k_{N-1}\exp(\mathrm{i}k_\mathrm{r}\Delta r) \; . \tag{4.69}$$

To obtain k'_r, we reject the positive, real portion of k_r

$$\begin{aligned} &\text{if } \; \mathrm{Re}(k_\mathrm{r}) \le 0 \; , \; \text{ then } \; k'_\mathrm{r} = k_\mathrm{r} \; , \\ &\qquad\qquad \text{else } \; k'_\mathrm{r} = \mathrm{i}\,\mathrm{Im}\,(k_\mathrm{r}) \; . \end{aligned} \tag{4.70}$$

Note that we reject the positive, real portion of k_r while Hadley rejects the negative, real portion because we chose an $\exp(-\mathrm{i}k_0 z)$ dependence in (4.54) whereas Hadley chose a $\exp(\mathrm{i}k_0 z)$ dependence [4.63]. In the ensuing propagating step, R^{k+1}_N is given by

$$R^{k+1}_N = R^{k+1}_{N-1}\exp(\mathrm{i}k'_\mathrm{r}\Delta r) \tag{4.71}$$

which corresponds to the final row of $\boldsymbol{M}^{k+1}$ appearing in (4.65).

4.4.3 Mode Solving with BPM

The BPM algorithm described here can also be used to numerically solve for the guided mode fields $\psi_{lp}(r)$ of a particular refractive index profile. By definition, the eigenvectors of the matrix $\boldsymbol{T}$, denoted by $\boldsymbol{T}_\mathrm{eig}$, are special vectors which do not change when multiplied by matrix $\boldsymbol{T}$. In other words, they are the guided modes of the local refractive index distribution since they propagate through the system unchanged. The eigenvalues associated with these eigenvectors, λ_eig, are related to the propagation constants of the guided modes. Most commercial numerical software packages include efficient routines for computing the eigenvalues and eigenvectors of a matrices such as $\boldsymbol{T}$.

The procedure for numerically computing the guided modes of an arbitrary refractive index profile is to assemble the $\boldsymbol{M}^k$ and $\boldsymbol{M}^{k+1}$ matrices according to (4.63) and (4.65) using the appropriate $n(r)$, then compute $\boldsymbol{T}$, and solve for the eigenvectors $\boldsymbol{T}_\mathrm{eig}$. Δz may be chosen to be 1 μm even though no real propagation will occur. The transparent boundary condition cannot

be applied when mode finding since we are not propagating the matrix. Instead, the final rows of $\boldsymbol{M}^k$ and $\boldsymbol{M}^{k+1}$ differ from (4.63) and (4.65). We choose the last rows of both matrices to be zero, except for the last element in the last row of $\boldsymbol{M}^k$, and the second to last element in the last row of $\boldsymbol{M}^{k+1}$, both of which we set equal to 1. This is equivalent to forcing the last two elements in $\boldsymbol{T}_{\text{eig}}$ to be equal to each other. This is not the true behavior of the guided mode but the error is negligible since the guided modes must have negligible electric field near the domain boundary anyway.

As the electric field envelope, $\boldsymbol{R}$, propagates through the system, energy may be exchanged among the various modes. At a particular axial step k, the fraction of power carried in mode m, F_m^k, is given by

$$F_m^k = \frac{\left| \int_0^{N\Delta r} \left(\boldsymbol{T}_{\text{eig},m}^k\right)^{\text{T}} \boldsymbol{R}^k \mathrm{d}r \right|^2}{\int_0^{N\Delta r} \left(\boldsymbol{T}_{\text{eig},m}^k\right)^{+} \boldsymbol{T}_{\text{eig},m}^k \,\mathrm{d}r \int_0^{N\Delta r} \left(\boldsymbol{R}^k\right)^{+} \boldsymbol{R}^k \,\mathrm{d}r} \,, \tag{4.72}$$

where $^{\text{T}}$ denotes the transpose operator, $^{+}$ denotes the transpose of the complex conjugate, $\boldsymbol{R}^k$ is the electric field at axial step k, $\boldsymbol{T}_{\text{eig},m}^k$ is the eigenvector of the m^{th} mode at axial step k, N is the number of radial nodes, and the integration is understood to be a numerical integration over the radial positions.

4.4.4 Computing Splice Loss with BPM

BPM can be used to compute splice loss based on knowledge of the local refractive index profile. First, an analytical or measured data set defines the refractive index profiles at each axial position near the splice. Then an initial mode envelope $\boldsymbol{R}^0$ is chosen. If the splice joins two single-mode fibers, $\boldsymbol{R}^0$ is usually chosen to be the fundamental mode for one of the two fibers. This mode is then propagated across the entire domain. The total power propagating in a particular mode m at a particular axial step k, P_m^k, may be computed by multiplying the fraction of power in mode m at step k, F_m^k, given in (4.72) by the total power in the domain at step k, P^k, as follows

$$P_m^k = F_m^k P^k \,. \tag{4.73}$$

The total power in the domain, P^k, may be computed with the aid of (4.16). An appropriate choice of units yields the numerical integration

$$P^k = \int_0^{N\Delta r} \left(\boldsymbol{R}^k\right)^{+} \boldsymbol{R}^k r \mathrm{d}r \int_0^{2\pi} \cos^2\left(l\phi\right) \mathrm{d}\phi \,. \tag{4.74}$$

The integral over the azimuthal angle, ϕ, in (4.74) evaluates to 2π when l=0 and evaluates to π for all other values of l.

The overlap integral, (4.38), applied to the relevant mode fields is a much simpler way to predict fusion splice loss between two single-mode fibers whose refractive index profiles are constant near the splice. The real power of BPM

is to handle cases where the refractive index profiles in one or more fibers changes near the splice. This capability is illustrated by the example in the next section.

4.4.5 A Practical BPM Example

In this section we illustrate the capability of the FD-BPM to analyze the optical characteristics of fusion splices. Consider an optical fiber fusion splice between standard single-mode fiber (SMF) and erbium-doped fiber (EDF) at an operating wavelength of 1550 nm. The standard SMF is assumed to have a step-index profile with a Δn of 0.0048 (Δ=0.33%) and a core radius of 4.15 μm while the EDF is assumed to have a step-index profile with a Δn of 0.02 (Δ=1.4%) and a core radius of 2 μm. Using (1.6) we find that the normalized frequency is about 2 for both fibers.

The fundamental mode fields for each fiber can be obtained with the methods discussed in Sect. 4.4.3. With these numerical mode fields, we can numerically compute the overlap integral, (4.38), and find that the predicted splice loss is about 1.6 dB, a very high value. Since the normalized frequency of both fibers is very similar, and since both fibers have step-index profiles, it seems reasonable to try to find a lower-loss fusion splice solution exploiting dopant diffusion in the EDF. In fact, the core of EDF usually includes dopants such as aluminum as well as erbium, both of which tend to diffuse more rapidly than the germania dopant in the standard SMF core. Thus, if a fusion splice between EDF and SMF is held at a high temperature for a sufficient amount of time, the core dopants comprising the EDF core will diffuse until the EDF mode field size and shape approaches the size and shape of the guided mode in the standard SMF.

For the sake of simplicity, we assume that the EDF core is comprised of a single dopant that diffuses much faster than the germania in the standard SMF so that we may neglect diffusion in the standard SMF. Experiments reveal this to be a reasonable assumption. Using (3.40) we solve for the dopant distribution in the EDF for a variety of τ_{D}. We then solve for ψ_{01} for these various dopant distributions and predict the splice loss using the overlap integral, (4.38).

With this technique we find that when τ_{D} is about 0.5, the overlap integral computation predicts a splice loss as low as 0.02 to SMF, much better than the 1.6 dB predicted between the original (undiffused) EDF and standard SMF. Not surprisingly, the MFD of the diffused EDF mode field is about 10 μm which is very close to the 10.4 μm MFD of the standard SMF.

Now we apply the BPM to predict what length for the transition region between the original (undiffused) EDF and the splice, $L_{\mathrm{transition}}$, results in a low-loss fusion splice. In other word, we are interested in predicting how long a region of the EDF must be heated to minimize transition losses (see Fig. 4.7). For simplicity, we assume that τ_{D} will vary linearly along the length of the

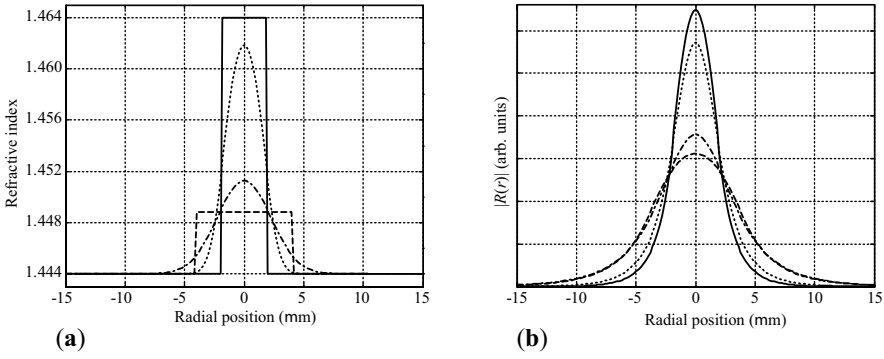

Fig. 4.17. The effect of dopant diffusion on the index profiles and mode fields of EDF compared to standard SMF. Traces correspond to standard SMF (*dashed lines*), EDF with τ_{D}=0 (*solid lines*), EDF with τ_{D}=0.1 (*dotted lines*), and EDF with τ_{D}=0.5 (*dash-dot lines*). (**a**) index profiles and (**b**) corresponding mode fields computed using Sect. 4.4.3. Notice the good match between the shape of the standard SMF mode field and the mode field corresponding to EDF with τ_{D}=0.5

fiber from τ_{D}=0 to τ_{D}=0.5 at the splice. With this assumption, the problem is reduced to determining the length of fiber required for this transition.

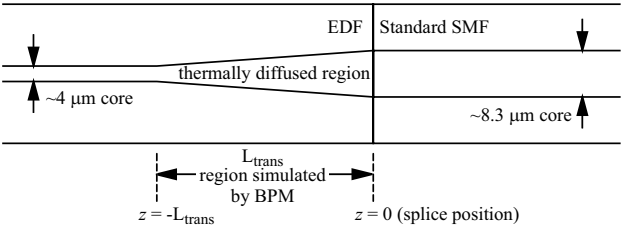

Fig. 4.18. Schematic illustration of the geometry for the BPM analysis of a fusion splice between EDF (*left fiber*) and standard SMF (*right fiber*). The figure schematically shows the core radius growing linearly in the transition region but in reality it is the normalized diffusion, τ_{D} that is modeled as growing linearly in the transition region. The BPM is used to model the transition region in the EDF which runs from $z=-L_{\mathrm{transition}}$ to the splice at z=0

We numerically solve for the guided mode of the original, undiffused EDF using the method of Sect. 4.4.3 and use this mode field as the input mode field, $\boldsymbol{R}^0$. Using an efficient tri-diagonal matrix solving routine we propagate the initial field step by step through the region of EDF where the amount of diffusion, τ_{D}, varies from 0 to 0.5. We take l = 0, Δr=0.2 μm, N=326, Δz=1 μm, and refractive index profiles based on dopant distributions computed from (3.40). Once we have propagated through the section of EDF fiber we overlap the resulting electric field with the fundamental guided mode field of the standard SMF and obtain the results listed in Table 4.1.

Table 4.1. Fusion splice losses predicted for EDF to standard SMF for a variety of transition lengths. $L_{\text{transition}}$=0 corresponds to the case of no dopant diffusion

$L_{\text{transition}}$ (μm)	BPM predicted splice loss (dB)
0	1.58
125	0.43
250	0.11
500	0.03

These results show that a transition length of about 500 μm is sufficient to achieve a very low fusion splice loss, a result that is consistent with experimental data. Note that we have assumed that τ_{D} of the erbium fiber varies linearly over the transition length. This linear variation is probably not the most efficient transition profile compared to other possibilities such as a quadratic or square root dependence. The BPM analysis demonstrated here can be used to determine the most efficient variation of τ_{D} so that a low-loss transition can be achieved over a shorter transition length. Figure 4.19 depicts the electric field amplitudes, $R(r, z)$, predicted by a BPM simulation of a 500 μm transition length. The figure clearly shows how the effective diameter of the electric field amplitudes smoothly expand over the 500 μm transition length. A small discontinuity is the electric field amplitudes is visible right at the splice joint where z=0. The energy lost in the transition region and at the splice joint manifests itself as radiation modes which slowly leak out of the boundary of the computational domain. Since the refractive index profile of the SMF is assumed to be constant along its length, energy coupled into the standard SMF guided mode at the splice remains in that guided mode.

Recall that in Sect. 4.1.3 we showed that fusion splice loss between single mode fibers, such as EDF and standard SMF, is the same regardless of propagation direction. Indeed when the BPM is applied to an electric field propagating in the opposite direction, from the standard SMF to the EDF, the splice loss is also predicted to be about 0.03 dB by the BPM.

A similar strategy can be used to analyze other types of fiber splices, including tapered or fattened splices (Sect. 8.2). Other versions of the BPM can be used to predict fusion splice losses or mode conversion in a radially asymmetric geometry. The BPM described here utilized a uniform radial mesh but non-uniform grid schemes are available for cases in which the mode field is concentrated in a local region [4.61].

Note that alternative strategies such as coupled-mode theory (CMT), described in Sect. 5.2, can also be used to analyze the optical characteristics of fusion splices. For example, Snyder and Love have developed general relationships for predicting the transition length required to preserve the optical signal in the fundamental mode [4.5, 4.65].

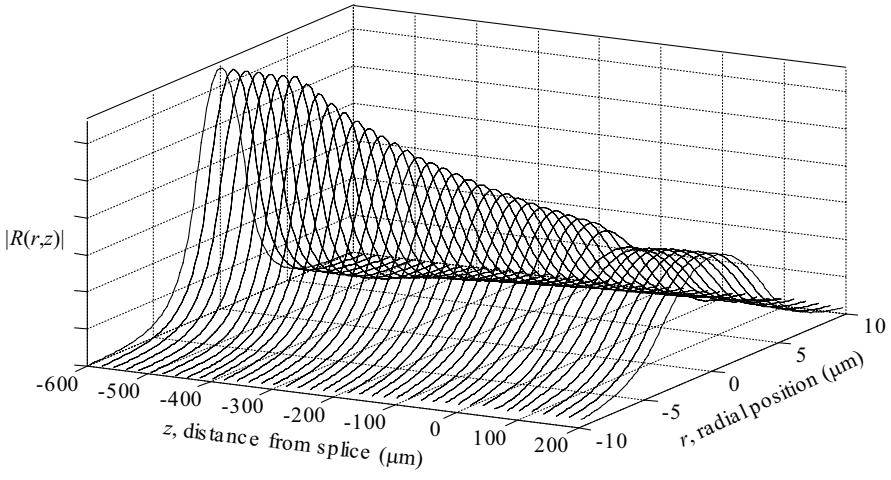

Fig. 4.19. FD-BPM simulation of a fusion splice between erbium-doped fiber (EDF) and standard single-mode fiber (SMF). The axial coordinate, z, is chosen to be 0 at the fusion splice. At the input, $R(r,z\text{=-}600\,\mu\text{m})$ is the fundamental guided mode of the EDF. From z=-600 μm to z=-500 μm the fiber is assumed to be EDF with a core Δn of 0.02 (Δ=1.4%) and a core radius of 2 μm. The amount of non-dimensional core dopant diffusion, measured by (3.41), is assumed to increase linearly from τ_D=0 to τ_D=0.5 over the region from z=-500 μm to z=0. From z=0 to z=200 μm the fiber is assumed to be standard SMF with a core Δn of 0.0048 (Δ=0.33%) and a core radius of 4.15 μm. The conditions for the BPM are as follows: n_{clad}=1.444, Δr=0.2 μm, N=326 radial nodes, and Δz=1 μm. The predicted splice loss for this example is only 0.03 dB (compare to a splice loss of about 1.6 dB without any diffusion of the EDF dopants)

4.5 Summary

The optical characteristics of fusion splices, such as optical transmission, loss, and reflectance, are entirely determined by the refractive index of the fiber in the vicinity of the splice. These optical characteristics can be described using a ray-optic approach when the fiber's normalized frequency is sufficiently large (as in a multimode fiber). However, the modal description is preferred since it is a more rigorous approach and is applicable when the normalized frequency is small, as in a single-mode fiber. With the aid of the scattering matrix formalism, one can show that single-mode fusion splice loss is independent of propagation direction while multimode splice loss is generally directionally dependent. Reflectance from single- and multimode fusion splices are much lower than those of connectors or mechanical splices and are nearly always so small that they may be considered negligible.

Single mode fusion splice loss results from geometric deformation, fiber mismatch, or transition losses near the splice. In many cases, the Gaussian approximation based on the mode field diameter (MFD) is useful for predicting

fusion splice loss in the presence of lateral core offsets, angular misalignments, and dissimilar mode field diameters. The most accurate description of splice loss between dissimilar single-mode fibers is provided by the overlap integral. Interference effects such as modal noise and multipath interference can arise when single-mode splices are particularly lossy and can degrade overall system performance.

The optical characteristics of multimode fibers are difficult to predict analytically due to the interaction of hundreds of distinct modes. The optical characteristics of a fusion splice between multimode fiber depends on the distribution of optical power amongst the various modes. This distribution depends on the launch condition at the fiber input and varies along the length of a multimode fiber. Greatly simplified splice loss formulae are useful for estimating splice loss based on fiber parameters and the geometry of the splice.

The beam propagation method (BPM) is a useful numerical technique for simulating the optical characteristics of a fusion splice given a hypothetical or a measured refractive index profile. It can be a powerful tool for understanding the performance of an existing splice or for providing insight for splice optimization.

5. Splice Loss Estimation and Fiber Imaging

Among the optical characteristics of a fusion splice, the splice loss is typically the most important. Unfortunately, direct measurement of the splice loss is often impractical, or perhaps even impossible. In such situations, *loss estimation* is used to help guarantee that the splice loss is below some maximum threshold. Loss estimation is attractive since it is applicable to almost any fusion splice, it is inherently non-destructive, and it does not require access to the ends of the fiber as most other loss measurements do.

Loss estimation is integrated into most contemporary fusion splice hardware, including single fiber splicers and mass fusion splicers [5.1–5.3]. Loss estimation is most commonly applied to single-mode fiber (SMF) since SMF typically exhibits higher splice loss than multimode fiber (MMF), and SMF communication systems are typically less tolerant of splice loss than MMF communication systems. Loss estimation has been applied to specialty fiber fusion splicing, including splicing of erbium-doped fiber (EDF) [5.4].

Practical implementation of loss estimation usually amounts to detecting unacceptably high loss single-mode fusion splices. For this reason, underestimating the splice loss (a false negative) is usually more dangerous that overestimating the splice loss (a false positive). False positives may reduce fusion splice yield, but false negatives can result in the installation of a high-loss splices that will compromise system performance.

It is important to understand that loss estimation is fundamentally an *estimation* rather than a measurement. There are numerous opportunities for inaccuracies to creep into the loss estimation process so that loss estimation should never be construed as a substitute for actual loss measurements. It is also important to understand that loss estimation requires certain assumptions about the optical characteristics of the fibers participating in the splice, so accurate loss estimation requires accurate supporting information about the fusion splice, which may include the refractive index profile, operating wavelength, and mode field shape of the fibers comprising the splice.

In most cases, loss estimation is used to differentiate the splice loss between splices fabricated with identical (and usually optimized) splicing parameters. The main source for variation among such splices is geometric deformation of the fibers rather than fiber mismatch or transition loss (see

Fig. 4.7). Consequently, loss estimation strategies must be able to estimate loss resulting from geometric deformation, but will often ignore splice loss resulting from fiber mismatch or transition losses. Note that core eccentricity can be thought of as a form of geometric deformation.

The performance of loss estimation routines varies somewhat from splicer to splicer. Various standards bodies have sought to define loss estimation accuracy requirements. One commonly cited standard is the Telcordia (formally Bellcore) GR-1095-CORE [5.5]. This requirement was originally formulated for mass fusion splicing so it can be considered to be relatively non-stringent when applied to single fiber fusion splicers, which are typically more accurate than mass fusion splicers. The GR-1095-CORE requirement is summarized in Table 5.1.

Table 5.1. Loss estimation accuracy specified by Telcordia GR-1095-CORE. The second and third columns detail the required estimation accuracy while the final two columns detail the objective for the loss estimation, which may not be achievable in all cases

Actual Loss	Accuracy req. for 90% of splices	Accuracy req. for 100% of splices	Objective for 90% of splices	Objective for 100% of splices
$\leq$0.40 dB	$\pm$0.10 dB	$\pm$0.25 dB	$\pm$0.05 dB	$\pm$0.10 dB
>0.40 dB	$\pm$25%	$\pm$50%	$\pm$15%	$\pm$30%

The basic problem of loss estimation can be summarized as follows: predict the optical loss of a fusion splice at its operating wavelength(s) based solely on images of the splice. The solution to this problem involves two main tasks (Fig. 5.1): (1) *image processing* and (2) *loss computation*. A tremendous amount of information is included in an image of a fusion splice, but extracting this information requires sophisticated image processing algorithms as well as an understanding of the unique features occurring in an image of a fusion splice. It is worth noting that many of the imaging and image processing issues relevant to splice loss estimation are also relevant to other aspects of fusion splicing such as fiber alignment. In this chapter we will discuss fiber imaging primarily within the context of loss estimation but its significance for fiber alignment should not be overlooked.

Once information about the geometry of a fusion splice is extracted from images of the fusion splice, this geometry must be used to predict the splice loss with the aid of a suitable theoretical model. In Sect. 4.2.2 we introduced the Gaussian approximation, which can be used for loss computation in special situations. In this Chapter we will perform loss computation with coupled-mode theory, which is more accurate and can be used under much more general conditions than the Gaussian approximation.

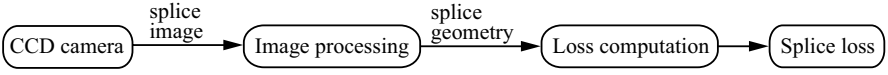

Fig. 5.1. Illustration of the steps comprising loss estimation

5.1 Fusion Splice Imaging and Image Processing

Imaging an optical fiber is an important component of both fiber alignment and loss estimation. When performing loss estimation, the goal of the imaging system is to determine the refractive index geometry in the vicinity of the splice. When aligning fibers in preparation for splicing, the goal of the imaging system is to determine the relative position and orientation of the fiber tips.

5.1.1 The Imaging System

Commercial fusion splices always include an *imaging system*, which provides a magnified transverse image of the optical fiber. This imaging system (Fig. 5.2) generally consists of an illumination source, an objective lens for capturing and focusing the image, and a charge-coupled device (CCD) camera to digitize the resulting image. Most fusion splicers employ a light-emitting diode (LED) to illuminate the fibers. An LED is attractive because it provides relatively monochromatic illumination thus minimizing chromatic aberrations in the lens. The emission from the illuminating LED is often collimated, meaning that the illuminating rays travel in nearly parallel paths to further improve the image quality.

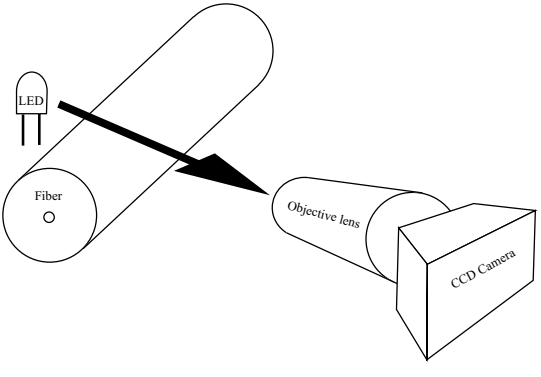

Fig. 5.2. Schematic illustration of a generalized fiber imaging system consisting of an illumination source (in this case an LED), an optical fiber, an objective lens to capture and focus the image, and a CCD camera to digitize the image

The imaging system usually incorporates lenses and mirrors which allow it to visualize the fiber from two perpendicular viewing directions, thus pro-

viding orthogonal views of the fiber. This is not only important for fiber alignment (see Sect. 2.3) but also for loss computation as we shall see in Sect. 5.2.

Sophisticated techniques are employed to achieve two orthogonal, high-magnification views when performing loss estimation on ribbon fiber in a mass fusion splicer [5.2, 5.3, 5.6, 5.7]. Figure 5.3 depicts two common strategies for providing orthogonal views of ribbon fiber. Older mass fusion splicing equipment utilized moving mirrors and objectives (Fig. 5.3a) but more contemporary mass fusion splicers typically use a compact system of multiple fixed position objective lenses and CCD cameras (Fig. 5.3b) to rapidly acquire multiple orthogonal images of the fiber ribbon tips with a minimum of moving parts [5.7].

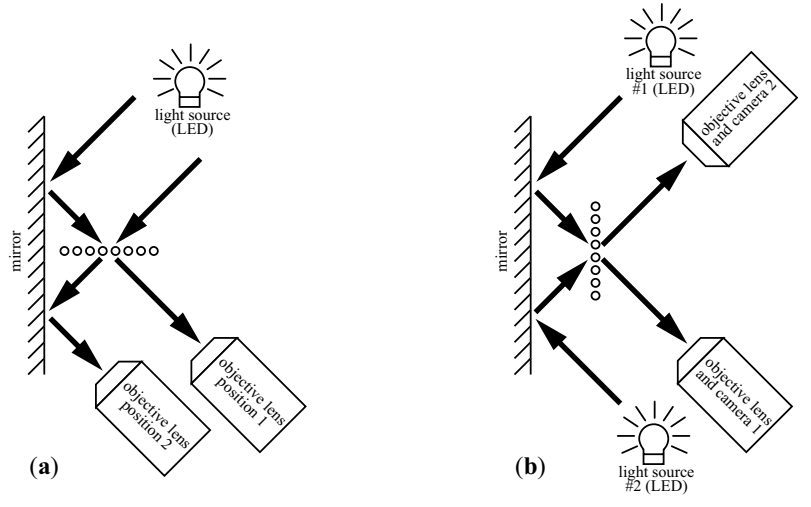

Fig. 5.3. Strategies for obtaining orthogonal views of ribbon fiber in a mass fusion splicer. The heavy arrows denote the two orthogonal paths of light through the imaging system. The figure depicts an eight fiber ribbon, but contemporary ribbons consist of as many as 24 ribbons. (**a**) An older design using a single objective lens which is physically translated between two possible viewing positions. Note that this strategy requires the objective lens position to be adjusted to preserve the same working distance. (**b**) A more contemporary design using two LEDs, two objective lenses, and two CCD cameras to minimize moving parts and reduce the time required for splicing by instantaneously switching views. Note that in both (**a**) and (**b**) each fiber has a slightly different distance to the objective lens. This defocusing effect can be corrected by specialized objective lenses. After [5.2, 5.3, 5.6, 5.7]

One challenge when imaging a fiber ribbon is ensuring that all the fiber strands are in proper focus since the need for two orthogonal views usually dictates that the distance from the fibers to the objective lens varies from fiber

to fiber (Fig. 5.3). This challenge grows more difficult with higher fiber count ribbon cables. Special objective lenses can compensate for this effect [5.3,5.7].

5.1.2 Introduction to Fiber Imaging

Interpreting the image of an optical fiber or fusion splice requires an understanding of the unique features present in such images. Figure 5.4 highlights some of these features. When imaged transversely, the cladding of an optical fiber exhibits a wide bright band running down its center sandwiched between two dark bands above and below. If the imaging system has sufficient magnification and resolution, the core of a single-mode fiber (SMF) is visible inside the central bright band. When the fiber is exactly in focus, the core becomes nearly invisible (see Fig. 5.6b), so the fiber is often deliberately defocused a bit to maximized visibility of the fiber core. The curved surface of the fiber's cladding actually magnifies the core region so that the core diameter appears out of proportion to the cladding diameter. Diffusion of the core during a splice causes the core to appear larger and more diffuse (dopant diffusion is discussed in Sect. 3.3). Recently, both the size of the fiber's core and the extent of any dopant diffusion was extracted from images of a fusion splice and used to improve the accuracy of loss estimation [5.8]. However, most commercial loss estimators only take into account the contribution of core deformation, which is typically the main source of loss variation from splice to splice.

The refractive index geometry of an optical fiber determines how it interacts with illumination during imaging. The polymer coating is stripped from the optical fiber since it cannot tolerate the heat of the fusion splice and furthermore will distort the image. Most optical fibers can be conveniently described as radially symmetric cylinders of glass with a small amount of refractive index contrast defining the core region. However, certain fibers, such as microstructured fiber, polarization-maintaining (PM) fibers, or cladding-pumped fibers have a complex, non-radially symmetric structure which complicates interpretation of the image. The large refractive index contrast between the silica glass and the vacuum or air occupying the holes in microstructured fiber make images of such fiber particularly difficult to interpret.

5.1.3 Characteristics of Fiber Images

The circularly shaped cross section characteristic of most optical fibers complicates the interpretation of transverse fiber images. The cladding surface acts as a kind of lens because the large refractive index contrast between the cladding and the surrounding air strongly refracts the illumination. Snell's law, (1.3), can be used to trace the trajectory of a light ray as it travels through the fiber. Figure 5.5 depicts a large number of such ray traces for a standard 125 μm diameter SMF. Such a ray trace is useful for understanding a transverse fiber image.

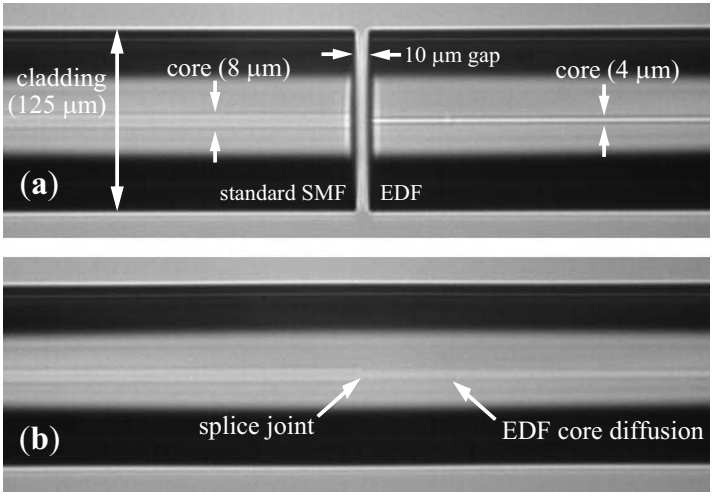

Fig. 5.4. Sample images acquired (**a**) before and (**b**) after a fusion splice between ordinary SMF and erbium-doped fiber (EDF). This a low loss splice (∼0.1 dB at 1550 nm) obtained with the aid of substantial core diffusion, which is discussed in Sects. 3.3 and 9.3. These images contain key features that are characteristic of fusion splice images. For example, the images are not truly in focus since when they are focused, it is nearly impossible to see the core of the fiber (see Fig. 5.6b). A little bit of defocusing makes the cores much more visible. The cladding of the fibers exhibits a bright region in the middle of two dark bands. The cores of the fiber are actually magnified by the curvature of the cladding so that they are out of proportion to the cladding diameter. The lower image acquired after the splice shows how the SMF core was not affected by the heat of the splice while the EDF core exhibits substantial diffusion of the core dopants causing the core to appear both larger and more diffuse

Notice how the rays that are incident on the center of the fiber's axis travel along a straighter trajectory than the rays which are incident at more oblique angles. In fact, some of the rays traveling through the cladding are refracted so strongly that they are not actually captured by the objective lens. These "missing" rays are responsible for the dark sections of the fiber cladding that sandwich the core region in fiber images such as those in Fig. 5.4. The NA and the aperture diameter of the objective lens determine the fraction of strongly refracted rays that are captured. A larger NA and a larger aperture lens captures more rays which results in a wider bright band in the core region and narrower dark bands above and below it [5.11]. The shaded region in Fig. 5.5 corresponds to the portion of the cladding containing rays which are not captured resulting in dark bands in the cladding. No information about these portions of the fiber is detected by the CCD. This is usually not a problem since, when working with single-mode fibers, we are primarily concerned with the core region. Of course, if a fiber is immersed in refractive index matching oil, there is a minimal amount of re-

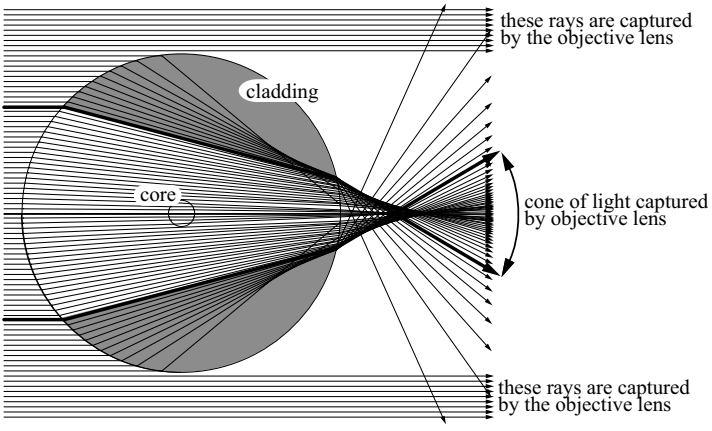

Fig. 5.5. Collimated rays of illumination traced through a simple 125 μm diameter step-index single-mode fiber with the aid of Snell's law. The two thick rays represent the marginal rays which are just barely captured by the imaging system. Rays passing through the shaded portion of the fiber's cladding are not captured by the optical system because they are refracted at a sharp angle by the fiber. This phenomenon gives rise to the dark bands in the outer regions of the cladding. Note that the relatively small index difference (Δ is about 0.33%) between the core and cladding results in minimal refraction of the rays passing through the fiber's core. After [5.9, 5.10]

fraction at the cladding-oil boundary so the bright and dark bands are not observed.

As noted earlier, when the cladding surface is a perfect cylinder, as is the case for most optical fibers, it has the peculiar effect of magnifying the core region relative to the other portions of the image (such as the cladding diameter). The magnification is equal to the refractive index of the cladding [5.12]. For a silica fiber illuminated by visible light, this amounts to a magnification factor of about 1.46. This phenomenon can be physically explained by considering that the wavelength of light inside the fiber is reduced in scale by an amount equal to the refractive index. This effect is identical to that occurring in a *solid immersion lens* or an *oil-immersion microscope* [5.13, 5.14]. When a fiber is immersed in refractive index matching oil, the entire core and cladding can be considered to be approximately magnified by the magnitude of the index of refraction, but the effect goes unnoticed since the cladding and core region are both magnified by the same amount.

Just as the strong refractive index contrast between the cladding and the surrounding air strongly refracts the illuminating rays, the weak refractive index contrast between the core and the cladding has a relatively small impact on the trajectory of the illumination. This fact is evident from the ray trace in Fig. 5.5 and is demonstrated in images of a lossy fusion splice depicted in Fig. 5.6. In fact, when the objective lens is exactly focused on the optical

fiber, the core is nearly invisible (Fig. 5.6b). In order to make the core more visible, the image of the fiber is deliberately defocused by 10 to 30 microns (Fig. 5.6d).

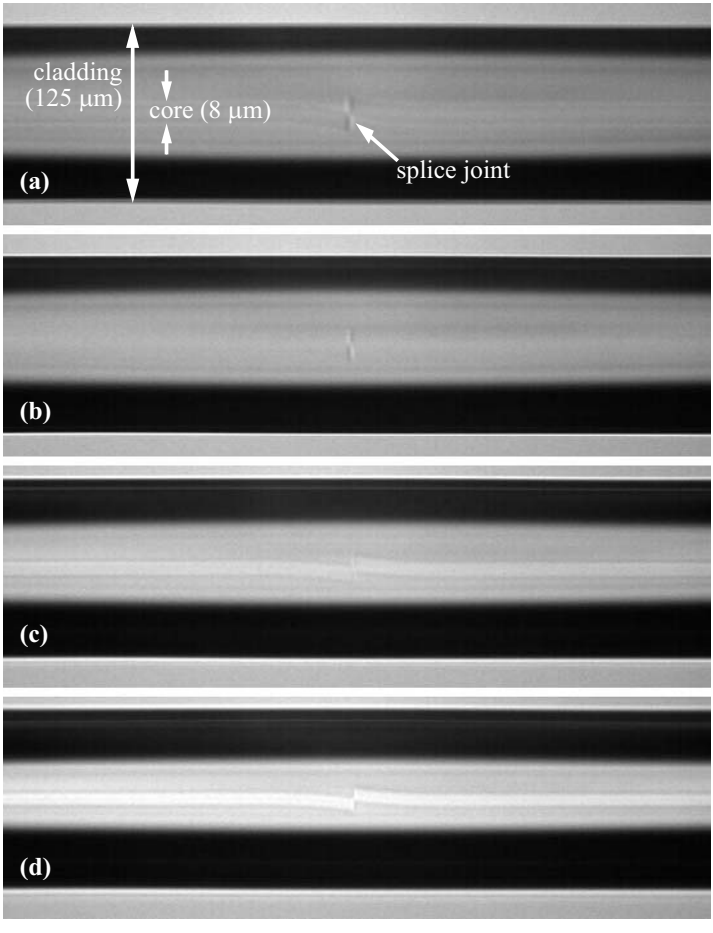

Fig. 5.6. Images of a lossy (∼0.2 dB at 1550 nm) single-mode fiber (SMF) fusion splice acquired at several focal positions: (**a**) microscope lens 10 μm too close to fiber, (**b**) microscope lens focused exactly on fiber, (**c**) microscope lens 10 μm too far from fiber, (**d**) microscope lens 20 μm too far from fiber. The images are each about 500 microns wide and the cladding and core regions are annotated in the top image. Note how the core is nearly invisible when the fiber is in focus (b) and how the core region becomes much more distinct as the microscope objective is pulled away from the fiber (c-d)

Note the characteristic shape of the core distortion of the splice depicted in Fig. 5.6. This sort of core deformation often results when the fiber tips shear

across one another during joint formation as a result of surface tension acting on a lateral misalignment (see Sect. 3.2.3). A large initial cleave angle can also cause this kind of core deformation. At the splice joint itself, the lateral displacement between the cores is seen to be several microns, whereas the core displacement decays to zero away from the splice in a roughly exponential manner. In Sect. 5.2 we will derive a general model that estimates splice loss based on core deformation.

The magnification of the fiber's core region is only given by the cladding refractive index when the core is precisely in focus (and invisible). When the image is defocused by moving the objective a short distance away from the fiber, the magnification of the core region is reduced. Ray tracing can be used to compute the amount of defocus [5.11]. Such a computation was used to produce the plot of core magnification versus defocus depicted in Fig. 5.7. This phenomenon must be kept in mind when measuring features in the core region such as the core diameter or the core eccentricity.

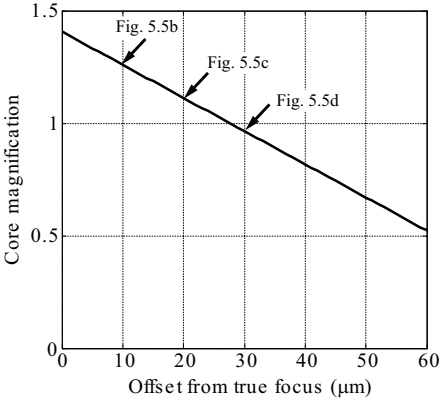

Fig. 5.7. Variation of core magnification as a function of focal position when the fiber is viewed with collimated illumination. This plot was generated for a standard single-mode fiber (SMF) with a cladding diameter of 125 μm. Most fusion splicers image the core about 20 μm from the true focus in order to more readily detect it. This amount of defocus reduces the effective magnification of the core caused by the curved cladding surface. Similar to [5.11]

Most loss estimation and the associated splice imaging occurs after the splice is completed and the fibers have cooled to room temperature. Zheng and coworkers developed a novel method for imaging the core of single-mode fibers during the actual joint formation process without using any external illumination [5.15]. This method relies on the fact that germania doped silica emits more radiation than undoped silica when heated to splicing temperatures (∼2100 C) [5.12]. During joint formation, a neutral density filter can be placed in front of the objective lens to suppress radiant emission from the

heat source and undoped silica while permitting radiation from germania-doped portions of the fiber to illuminate the CCD. Crude images of the fiber core during joint formation can then be used to tailor the alignment of the fusion splice during joint formation. Disadvantages of this technique include the fact that the image quality is often poor compared to standard transverse illumination, it may not work well with fibers lacking germania in the core, and it cannot be used once the fiber has cooled down to room temperature.

5.1.4 Basic Image Processing

When performing either fiber alignment or loss estimation, the image processing algorithm must detect certain features in the image and convert those features into quantitative data. During fiber alignment, tasks such as edge detection are critically important and must be performed on the fiber end faces as well as on the cladding edges [5.9, 5.16].

Loss estimation, and sometimes alignment, in single-mode fibers depends on detecting the core position in the vicinity of the splice. This can be a difficult task due to the weak refractive index contrast between the core and cladding. When the image is suitably defocused, as in Fig. 5.6c–d, special image processing routines can detect the core location as a function of distance along the fiber. Figure 5.8 shows the digital brightness data corresponding to a particular column of pixels in Fig. 5.6d.

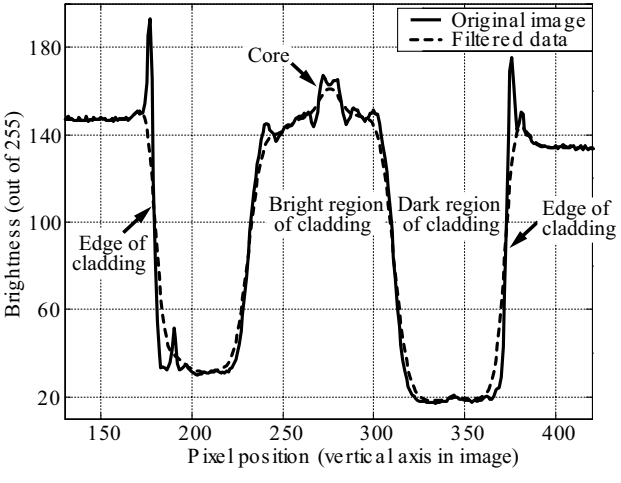

Fig. 5.8. Graphical representation of the image data from a column of pixels in Fig. 5.6d showing both the original image data (*solid line*) and filtered data (*dashed line*). The filtering was accomplished using a Gaussian filter in the Fourier domain

The raw image data typically contains large amounts of noise which can be removed through filtering. Various image processing texts provide detailed information on noise filtering strategies (see for example [5.16]).

Once the image data is filtered, image processing algorithms can detect features such as the cladding edges, or the core region, which appears as a small hump in the filtered image data (Fig. 5.8). Features such as the edge of the fiber's core or cladding can be detected by differentiating the (noise-filtered) brightnesses in a vertical slice of the fiber's image and searching for locations where the derivative is maximized. Interpolation can permit sub-pixel measurement accuracy [5.9]. Figure 5.9 shows the core positions detected by image processing overlaid onto the splice image from Fig. 5.6d.

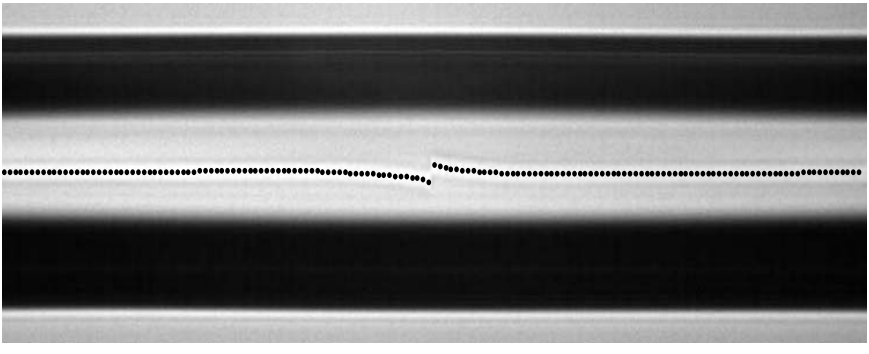

Fig. 5.9. Detected core positions (*black spots*) overlaid onto image of fusion splice

5.2 Loss Computation

The specific geometry of a fusion splice determined by image processing is converted into an estimated loss via a suitable loss estimation model in a process termed *loss computation*. Loss estimation models range in complexity from simple analytical expressions, such as those described in Sects. 4.2.2 and 4.3.2, to more sophisticated modal methods, such as coupled-mode theory, to numerical techniques, such as the beam propagation method (BPM), which was already discussed in Sect. 4.4.

The accuracy of loss computation depends on the accuracy of the model as well as the accuracy of the information input to the model. All loss estimation models require some amount of externally provided information about the fibers comprising the splice and the wavelength of operation. This information may be as limited as the mode field diameter (MFD) of the fiber or as detailed as the full refractive index profile of the fiber. Some fusion splices use the splice image to estimate the fiber core diameter or mode field diameter. Loss

computation is sometimes performed with loss estimation models that are calibrated against experimentally measured splice loss data to tune their accuracy.

More complex loss estimation models, especially those which can take advantage of detailed information about the fibers comprising the splice, are generally more accurate. However, simple models require less computation time and fewer computational resources. Full vectorial solutions to the propagation of an optical signal through a splice is generally beyond the capability of laboratory, as well as commercial fusion splice hardware. Recent work has demonstrated a particularly efficient form of the BPM which is quite effective for loss estimation [5.17]. As the cost of embedded computation power falls, the cost of including sophisticated loss estimation models in commercial fusion splicers falls as well.

In this section we will focus our attention on one particular loss computation technique that is ubiquitous in commercial equipment and represents a successful balance between sophistication, accuracy, and computation power: *coupled-mode theory* (CMT). Coupled-mode theory is more powerful than the Gaussian approximation because it is can be used when the mode field is not Gaussian in shape and can account for a wider variety of geometric deformations. In this Section we show how coupled-mode theory can be used as a loss computation model for single-mode fusion splices.

5.2.1 Introduction to Coupled-Mode Theory

As its name suggests, coupled-mode theory is an analytical description of how various modes in a waveguide *couple*, or exchange energy, with each other. As such, it is inherently a modal, rather than ray-optic, description of the optical fiber waveguiding. Coupled-mode theory was first developed to describe the interaction of modes in microwave systems and has since been successfully used to analyze numerous optical fiber devices such as waveguide couplers and gratings [5.18], as well as optical fiber characteristics such as microbends [5.19]. Coupled-mode theory was first applied to describe fusion splice loss by White and Kuhl [5.20], was further developed by Miller et al [5.21], and made especially convenient by Zheng [5.22]. Coupled-mode theory is particularly appropriate for describing fusion splice loss because unlike the simple loss formulas presented in Sect. 4.2.2, it is valid for non-Gaussian mode fields and can account for subtle geometric deviations as well as core offset or angular misalignments. Excellent general treatments of coupled-mode theory are available in [5.23] and particularly [5.19], which is the seminal reference for coupled-mode theory applied to optical fibers.

In this section we will present a limited introduction to coupled-mode theory which will subsequently be applied to fusion splice loss computation. The results of this subsection are completely general and thus applicable to multimode as well as single-mode fibers. We follow the derivation in [5.19]

although for simplicity we use scalar, rather than vector fields, and we employ a different normalization for the orthonormal mode fields.

In Sect. 4.1 we saw that any electric field distribution, and hence any optical signal, in an optical fiber can be described as a superposition of guided modes and radiation modes. According to this view, if the transverse refractive index profile of the fiber remains perfectly constant along its length, then the individual modes do not exchange energy as they travel along the fiber because they are, by definition, orthogonal. Consequently, the amount of power carried in each guided mode remains constant as it propagates along the fiber's length, although energy carried in the radiation modes will naturally dissipate into the medium surrounding the fiber (such as the polymer coating). However, a perturbation to the fiber's refractive index can induce energy to be coupled amongst the various modes. In the presence of such perturbations, it is convenient to express the modal amplitudes, which quantify the amount of energy carried within each mode, as functions of axial position.

Our theoretical description begins with the Helmholtz equation, (4.8), also known as the scalar wave equation, which was derived in Sect. 4.1. To account for the possibility of energy exchange between modes along the length of the fiber, we postulate an electric field, E, of the form

$$E(r, \phi, z, t) = \psi(r, \phi, z) \mathrm{e}^{\mathrm{i}(\omega t - \beta z)} \,, \tag{5.1}$$

where t is time, r is the radial coordinate, ϕ is the azimuthal coordinate, z is the axial coordinate, β is an axial propagation constant describing the phase of the field as it propagates down the length of the fiber, and ω is the optical frequency. Equation (5.1) differs from (4.10) in that the envelope of the oscillating electric field, ψ, varies along the fiber length z, whereas in (4.10) it does not.

When (5.1) is substituted into (4.8) we obtain

$$\nabla_{\mathrm{T}}^2 \psi + \omega^2 \mu_0 \varepsilon \psi - \beta^2 \psi - 2\mathrm{i}\beta \frac{\partial \psi}{\partial z} + \frac{\partial^2 \psi}{\partial z^2} = 0 \,, \tag{5.2}$$

where ε is the electric field permittivity, which is given by the square of the refractive index, n^2, μ_0 is the magnetic permeability (the fiber is assumed to be non-magnetic), and ∇_{T}^2 is the transverse Laplacian operator defined by

$$\nabla_{\mathrm{T}}^2 = \nabla^2 - \frac{\partial^2}{\partial z^2} \,. \tag{5.3}$$

For most optical fields of interest, we can assume that the electric field envelope, ψ, varies slowly enough with z that we may neglect the second derivative term in (5.2) and obtain

$$\nabla_{\mathrm{T}}^2 \psi + \omega^2 \mu_0 \varepsilon \psi - \beta^2 \psi - 2\mathrm{i}\beta \frac{\partial \psi}{\partial z} = 0 \,. \tag{5.4}$$

Equation (4.18) describes how any arbitrary electric field, Ψ, can be expressed as a superposition of bound modes ψ_{lm}, and radiation modes, ψ_β. We extend this expression by permitting the modal amplitude coefficients,

c_{lm} and $c(\beta)$, to vary as a function of z. We also explicitly include the phase of each mode oscillating along the length of the fiber according to its own unique axial propagation constant,

$$\Psi(r,\phi,z) = \sum_{lm} c_{lm}(z)\psi_{lm}(r,\phi)\exp\left(-\mathrm{i}\beta_{lm}z\right) + \int c(\beta,z)\psi_{\beta}(r,\phi)\exp\left(-\mathrm{i}\beta z\right)\mathrm{d}\beta \ . \tag{5.5}$$

To simplify the notation of the derivation that follows, we rewrite (5.5) as follows

$$\Psi(r,\phi,z) = \sum_{\nu} c_{\nu}(z)\psi_{\nu}(r,\phi)\exp\left(-\mathrm{i}\beta_{\nu}z\right) \ , \tag{5.6}$$

where the subscript ν distinguishes between different modes and the discrete summation sign is understood to refer to an integration when radiation modes are considered.

Since the modal amplitude coefficients, the c_{ν} in (5.6), are functions of z, we can think of the product formed by the modal amplitude coefficients and the mode fields in (5.6), the $c_{\nu}\psi_{\nu}$, as individual z-varying electric field envelopes analogous to the ψ in (5.1). It is worth noting that, by definition, the ψ_{ν} are solutions to the Helmholtz equation for a z-independent waveguide, so that

$$\left(\nabla_{\mathrm{T}}^2 + \omega^2\mu_0\varepsilon_{\mathrm{const}} - \beta_{\nu}^2\right)\psi_{\nu} = 0 \ , \tag{5.7}$$

where we denote the electrical permittivity of the z-independent waveguide with $\varepsilon_{\mathrm{const}}$.

The actual electric field permittivity, ε, is assumed to be a function of axial coordinate, z, as well as a function of transverse coordinates r and ϕ. However, we assume that the variation of ε, and hence n, with z is small enough that at any location the permittivity may be approximated as the sum of the constant electrical permittivity $\varepsilon_{\mathrm{const}}(r,\phi)$, for which the ψ_{ν} are a solution, and a perturbation term, $\varepsilon'(r,\phi,z)$, as follows

$$\varepsilon(r,\phi,z) = n^2(r,\phi,z) = \varepsilon_{\mathrm{const}}(r,\phi) + \varepsilon'(r,\phi,z) \ . \tag{5.8}$$

When (5.6) and (5.8) are substituted into (5.4), and (5.7) is used to cancel terms, we obtain

$$2\mathrm{i}\sum_{\nu}\beta_{\nu}\psi_{\nu}(r,\phi)\frac{\partial c_{\nu}(z)}{\partial z}\exp\left(-\mathrm{i}\beta_{\nu}z\right) = \omega^2\mu_0\varepsilon'(r,\phi,z) \times \sum_{\nu} c_{\nu}(z)\psi_{\nu}(r,\phi)\exp\left(-\mathrm{i}\beta_{\nu}z\right) \ , \tag{5.9}$$

where the functional dependencies are explicitly included for clarity. This equation can be simplified by multiplying both sides by the complex conjugate

of another mode envelope function from the set of ψ_ν, denoted by ψ_μ^*, and integrating over the entire cross sectional area, $A_{\rm cs}$, of the domain,

$$2\mathrm{i}\sum_\nu \beta_\nu \frac{\partial c_\nu}{\partial z}\exp\left(-\mathrm{i}\beta_\nu z\right)\int_{\mathrm{A_{cs}}}\psi_\mu^*\psi_\nu \mathrm{d}A_{\rm cs} = \omega^2\mu_0\sum_\nu c_\nu \exp\left(-\mathrm{i}\beta_\nu z\right)\int_{\mathrm{A_{cs}}}\varepsilon'\psi_\mu^*\psi_\nu \mathrm{d}A_{\rm cs}\ . \tag{5.10}$$

Mode orthogonality (Sect. 4.1.2) ensures that

$$\int_{\mathrm{A_{cs}}}\psi_\mu^*\psi_\nu \mathrm{d}A_{\rm cs} = 0\,,\ \text{for}\ \nu \neq \mu\ . \tag{5.11}$$

As in Sect. 4.1.2, we choose our modes here such that they are orthonormal so that

$$\int_{\mathrm{A_{cs}}}\psi_\mu^*\psi_\mu \mathrm{d}A_{\rm cs} = 1\ . \tag{5.12}$$

Equations (5.11) and (5.12) permit (5.10) to be simplified into a coupled set of linear first order differential equations

$$\frac{\partial c_\mu}{\partial z} = \sum_\nu \kappa_{\nu\mu} c_\nu \exp\left(\mathrm{i}\left(\beta_\mu - \beta_\nu z\right)\right)\ , \tag{5.13}$$

where

$$\kappa_{\nu\mu} = \frac{-\mathrm{i}\omega^2\mu_0}{2\beta_\mu}\int_{\mathrm{A_{cs}}}\varepsilon'\psi_\mu^*\psi_\nu \mathrm{d}A_{\rm cs}\ . \tag{5.14}$$

Equations (5.13) and (5.14) are the central equations for scalar coupled-mode theory. The $\kappa_{\nu\mu}$ are known as the coupling coefficients because they quantify how strongly the two modes ψ_μ and ψ_ν are coupled together by a perturbation ε'. Notice that when the perturbation ε' vanishes, so do the coupling coefficients, so that there is no energy exchanged between modes and thus the modal amplitudes, the c_μ, are constant with respect to z.

5.2.2 Coupled-Mode Theory in a Single-Mode Fiber: Microbend Theory

The coupled-mode theory developed in the preceding section is a general theory that is applicable to multimode as well as single-mode fibers. In this section we will specialize the coupled-mode theory for application to single-mode fibers. Much of the analysis presented in this section was originally developed by Marcuse [5.19] for analyzing the optical effects of *microbends*, which are microscopic random deviations in the core of an optical fiber [5.24]. Thus, the theory developed in this section is also called *microbend theory*. Microbends can result when an optical fiber is improperly wrapped around a spool, packaged into a poorly fitting cable assembly, or strained by differential thermal expansion [5.24].

Most loss estimation problems are concerned with single-mode fibers. Coupled-mode theory applied to single-mode appears to be an oxymoron – by definition, a single-mode fiber can only guide the fundamental, or LP_{01}, mode! However, in some single-mode fibers low-order cladding modes can travel a relatively long distance (several centimeters) before they are attenuated. Furthermore, during the fusion splice process, the polymer coating which normally surrounds the glass cladding is removed so that the glass-air interface at the cladding surface in the vicinity of the splice locally transforms a single-mode fiber into a multimode fiber in the vicinity of the splice. Finally, even in a purely single-mode fiber, splice-induced perturbations to the fiber can couple energy from the fundamental mode to radiation modes. Thus coupled-mode theory is an appropriate formalism for modeling single-mode fusion splices.

In a single-mode fiber, we may safely assume that the vast majority of the optical signal remains in the fundamental mode. Thus, we may neglect mode coupling between radiation or cladding modes and restrict our attention to coupling between the fundamental mode and other modes (cladding or radiation). Moreover, for relatively small amounts of loss, we may assume that the energy carried in the fundamental mode is nearly constant. If we restrict our attention to the fundamental mode, whose amplitude coefficient and axial propagation constant we denote by c_{fund} and β_{fund} respectively, we may integrate (5.13) with respect to z to obtain

$$c_\mu|_{z=L} = \int_{z=0}^{z=L} \left[\kappa_{\mathrm{fund}\mu} c_{\mathrm{fund}} \exp\left(\mathrm{i}\left(\beta_\mu - \beta_{\mathrm{fund}}\right)\right)\right] \mathrm{d}z \ . \tag{5.15}$$

Since we are assuming that the loss in the fundamental mode is small, we approximate it as a constant and pull it out of the integral to obtain

$$c_\mu|_{z=L} = c_{\mathrm{fund}} \int_{z=0}^{z=L} \left[\kappa_{\mathrm{fund}\mu} \exp\left(\mathrm{i}\left(\beta_\mu - \beta_{\mathrm{fund}}\right)\right)\right] \mathrm{d}z \ . \tag{5.16}$$

In a typical single-mode fusion splice, a significant fraction of the optical loss can result from geometric deformation of the fiber cores (see Fig. 4.7). Moreover, when the splicing parameters are kept constant, the main source of loss variation from splice to splice is geometric deformation. Modeling this source of loss will yield a loss estimation process that is particularly effective at discriminating between low loss and high loss splice.

The geometric deformation of the core in a single-mode fiber fusion splice can be described as a displacement in the r-ϕ plane (or x-y plane) as a function of axial position, z. We will describe this as the *core deviation function*, $f(z)$, such that

$$f(z) = f_{\mathrm{x}}(z)\hat{x} + f_{\mathrm{y}}(z)\hat{y} \ , \tag{5.17}$$

where f_{x} is the core deviation function projected on the x-z plane, f_{y} is the core deviation function projected on the y-z plane, and $\hat{x}$ and $\hat{y}$ denote unit

vectors in the x and y directions, respectively. We have chosen to use Cartesian coordinates since most fusion splicers use image processing to detect the core deviation in two orthogonal viewing axes. In some cases, we may also wish to account for changes in the core diameter, for example resulting from dopant diffusion. In such cases we denote the core diameter as $D_{\text{core}}(z)$.

Some sample core deviation functions are depicted in Fig. 5.10. We have already considered core offset, illustrated in Fig. 5.10b, with the Gaussian approximation in Sect. 4.2.2. However, core offset can also be modeled with coupled-mode theory by using a step function to describe the core deviation function. Sheared cores, Fig. 5.10c-d, are a common occurrence, and often result from poor cleave angles or surface tension effects (see Sect. 3.2.3). A decaying exponential can serve as the core deviation function for a sheared core [5.20, 5.22]. Such a deviation can be expressed as [5.21]

$$f_{\text{x}}(z) = A_{\text{shear}} \exp\left(-\gamma_{\text{shear}} |z|\right); \tag{5.18}$$

where the splice is situated at z=0, A_{shear} is the amplitude of the shearing (lateral displacement), and γ_{shear} is the exponential decay constant, which is typically 0.05 to 0.25 μm^{-1} [5.21]. It is important to recognize that a splice can simultaneously exhibit core offset and sheared cores. Moreover, the deviation function can appear very different when viewed from orthogonal direction (in x-direction versus y-direction). For example f_{x} could look like Fig. 5.10c, while f_{y} could look like Fig. 5.10d.

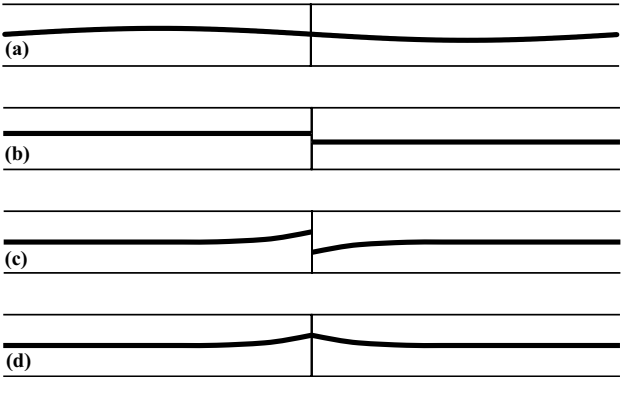

Fig. 5.10. Core deviation function shapes useful for illustrating loss computation via coupled-mode theory. The significance of the sine wave, (**a**), will be explained in an ensuing section. Core offset, (**b**), and sheared cores, (**c**) and (**d**), are particularly common sources of single-mode fiber fusion splice loss

The coupling coefficients between the fundamental mode and any of the cladding or radiation modes can be expressed as [5.19, 5.20, 5.22]

$$\kappa_{\text{fund}\mu}(z) = \hat{\kappa}_{\text{fund}\mu} f(z) \,, \tag{5.19}$$

where $f(z)$ could be f_{x}, f_{y}, or a combination of both, and $\hat{\kappa}_{\mathrm{fund}\mu}$ is constant with respect to z that depends on which particular mode is coupling with the fundamental. In other words, the coupling coefficient scales linearly with the core deviation function. Also note that the $\hat{\kappa}_{\mathrm{fund}\mu}$ are independent of the particular core deviation function. When (5.19) is substituted into (5.16) we obtain

$$c_{\mu}|_{z=L} = c_{\mathrm{fund}}\hat{\kappa}_{\mathrm{fund}\mu}\int_{z=0}^{z=L} f(z)\exp\left(\mathrm{i}\left(\beta_{\mu}-\beta_{\mathrm{fund}}\right)\right)\mathrm{d}z\ . \tag{5.20}$$

Following Marcuse [5.19], we define the Fourier transform, $\mathcal{F}(\beta)$ of a function $f(z)$ as

$$\mathcal{F}(\beta) = \frac{1}{\sqrt{L}}\int_{0}^{L} f(z)\mathrm{e}^{-\mathrm{i}\beta z}\mathrm{d}z\ . \tag{5.21}$$

The Fourier transform depicts the spectral frequencies present in the original function. For example, the Fourier transform of a pure sine wave is zero everywhere except at the frequency of the sine wave, where it is proportional to the sine wave's amplitude.

Substituting (5.21) into (5.20) yields

$$c_{\mu}|_{z=L} = c_{\mathrm{fund}}\hat{\kappa}_{\mathrm{fund}\mu}\mathcal{F}\left(\beta_{\mu}-\beta_{\mathrm{fund}}\right)\sqrt{L} \tag{5.22}$$

where

$$\mathcal{F}\left(\beta\right) = \mathcal{F}_{\mathrm{x}}\left(\beta\right) + \mathcal{F}_{\mathrm{y}}\left(\beta\right)\ , \tag{5.23}$$

and $\mathcal{F}_{\mathrm{x}}$ and $\mathcal{F}_{\mathrm{y}}$ are understood to refer to the Fourier transform pairs of f_{x} and f_{y}, respectively. Note that the squared magnitude of the Fourier transform, $\left|\mathcal{F}\left(\beta\right)\right|^2$, is commonly called the *power spectrum* of the function since it is a measure of the power present in each frequency component. The power spectrum of the total core deviation function, $f(z)$, can be expressed in terms of the power spectra of $f_{\mathrm{x}}(z)$ and $f_{\mathrm{y}}(z)$ as

$$\left|\mathcal{F}\left(\beta\right)\right|^2 = \left|\mathcal{F}_{\mathrm{x}}\left(\beta\right)\right|^2 + \left|\mathcal{F}_{\mathrm{y}}\left(\beta\right)\right|^2\ . \tag{5.24}$$

5.2.3 Coupled-Mode Theory for Loss Computation

In this section we will apply the microbend theory developed in the preceding section to the specific problem of computing fusion splice loss based on knowledge of the geometric deformation of the fiber cores.

According to (4.22), the total power carried in a guided mode (fundamental or cladding) is given by the squared magnitude of the modal amplitude coefficient. Likewise, the total power carried in a radiation mode is given by the squared magnitude of its modal amplitude coefficient. Thus, we may express the initial power in the fundamental mode upstream of the splice as

$$P_{\mathrm{initial}} = c_{\mathrm{fund}}^{*}c_{\mathrm{fund}}\ , \tag{5.25}$$

whereas the power lost from the fundamental mode may be expressed as

$$P_{\text{lost}} = \sum_{\mu} c_{\mu}^{*} c_{\mu} \ . \tag{5.26}$$

Combining (5.20-5.26) we find that the fraction of power lost at the splice is

$$\begin{aligned} \Gamma_{\text{cmt}} &= -10 \times \log_{10} \left(\frac{P_{\text{initial}} - P_{\text{lost}}}{P_{\text{initial}}} \right) \\ &= -10 \times \log_{10} \left(1 - \sum_{\mu} \left| \hat{\kappa}_{\text{fund}\mu} \right|^2 \left| \mathcal{F} \left(\beta_{\mu} - \beta_{\text{fund}} \right) \right|^2 L \right) \ , \end{aligned} \tag{5.27}$$

where L is understood to be a distance spanning the entire region containing geometric core deformation, from the region upstream of the splice where the core deviation begins, to the region downstream of the splice where is ends. Notice how (5.27) depends on the squared magnitude of the core deviation function's Fourier transform.

When the splice loss is small, this expression can be simplified to

$$\Gamma_{\text{cmt}} = 4.34 \sum_{\mu} \left| \hat{\kappa}_{\text{fund}\mu} \right|^2 \left| \mathcal{F} \left(\beta_{\mu} - \beta_{\text{fund}} \right) \right|^2 L \ . \tag{5.28}$$

This equation is significant since it demonstrates that the splice loss resulting from geometric core deformation in a single-mode fiber is purely a function of the power spectrum of the core deviation function and the coupling coefficients (which don't depend on the core deviation function but rather on the operating wavelength and the fiber design). Furthermore, this expression for single-mode fusion splice loss does not depend on propagation direction which is consistent with our derivation in Sect. 4.1.3. Note that when the fundamental mode is being coupled to radiation modes, the summation is really an integration over a continuous set of radiation modes. For a given combination of fibers and operating wavelength, the only parameter that varies from splice to splice is the power spectrum of the core deviation function.

In order to better understand (5.28), it is worthwhile to consider the relative magnitudes of the axial propagation constant, β, of the various modes (including cladding modes) of a standard single-mode fiber. These can be visualized by considering their relative locations on the β-axis (Fig. 5.11). As Fig. 5.11 shows, the fundamental mode exhibits the largest axial propagation constant in a standard single-mode fiber while the axial propagation constant of the cladding modes are smaller and grow dense near where β takes on the value $2\pi n_{\text{clad}}/\lambda$ (n_{clad} refers to the cladding refractive index). There are an infinite number of radiation modes, all exhibiting an axial propagation constant that is less than $2\pi n_{\text{clad}}/\lambda$. Note that when $\beta < 0$, the optical signal is propagating in the backward direction.

We can now appreciate the physical significance of (5.28) by considering the Fourier power spectra of a few sample core deviation functions such as

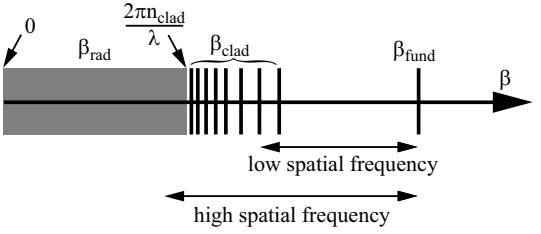

Fig. 5.11. Schematic illustration of the axial propagation constant, β, for a standard single-mode fiber. When the spatial frequency (measured in radians per unit length) of a perturbation, such as core deviation function, matches the spatial frequency difference between the fundamental mode and a cladding or radiation mode, energy will be coupled between them. The amount of coupling depends on the magnitude of the perturbation. The figure illustrates how a lower spatial frequency can couple energy from the fundamental mode to a low order cladding mode while a higher spatial frequency can couple energy from the fundamental mode to a radiation modes

those depicted in Fig. 5.10. Consider an idealized pure sine wave core deviation function such as that depicted in Fig. 5.10a. The corresponding Fourier power spectrum is zero, except for delta functions at the positive and negative spatial frequencies of the pure sine wave, as depicted in Fig. 5.12a. In fact, real sine waves are never "pure" – real core deviation functions have imperfections which broaden their delta functions into frequency spikes with a small, but finite, linewidth. When the axial propagation constant of the fundamental mode differs from that of a cladding mode (or radiation mode) by a spatial frequency very close to that of the sine wave (see Fig. 5.11), energy will be coupled between them, and the resulting splice loss will be proportional to the amplitude of the sine wave. However, if there are no radiation modes or cladding modes with an axial propagation constant that differs from the fundamental by the appropriate range of spatial frequencies, no energy will be lost (coupled) from the fundamental.

Now consider a core deviation function that resembles a step offset, as in Fig. 5.10b, which exhibits a power spectrum similar to that of Fig. 5.12b. This power spectrum contains a series of delta functions which grow weaker as the magnitude of the spatial frequency increases. As is the case for a sine wave, a real core offset has imperfections that ensure that the individual delta functions are actually narrow linewidth features. Once again, energy will be coupled if any cladding or radiation modes have an axial propagation constant that differs from the fundamental's axial propagation constant by an amount matching one of those spectral lines. The amount of energy coupled will be proportional to the strength of the spectral line. We are guaranteed that some energy will be coupled out of the fundamental mode by (1) the generally large number of spectral lines and (2) the fact there is a continuity of radiation modes whose axial propagation constant differs from the fundamental by a relatively high spatial frequency (Fig. 5.11).

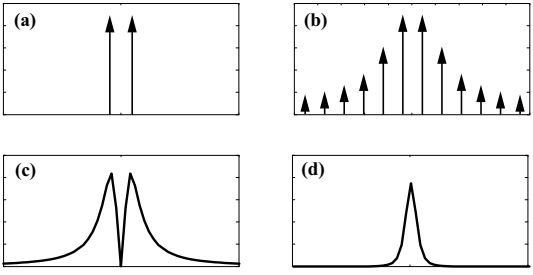

Fig. 5.12. Sample Fourier power spectra corresponding to the core deviation functions depicted in Fig. 5.10. The x-axis represents spatial frequencies and the zero frequency (DC component) is centered in each axis. The y-axis represents the amount of power contained in a given spatial frequency. Note that the graphs are not to scale. (**a**) A pure sine wave, such as the core deviation function depicted in Fig. 5.10a, corresponds to delta functions at the positive and negative frequencies of the sine wave. (**b**) A core offset, such as the core deviation function depicted in Fig. 5.10b, corresponds to an infinite series of equally spaced (harmonic) delta functions which grow weak at high frequencies. (**c**) Sheared cores, such as those depicted in Fig. 5.10c, yield a Fourier power spectrum that resembles a smoothed version of the power spectrum for offset cores. (**d**) When the cores are sheared in the same direction, as in Fig. 5.10d, the Fourier power spectra is more tightly concentrated near the zero frequency. The broader spectrum of Fig. 5.10c causes it to couple more energy out of the fundamental mode than Fig. 5.10d which explains the observation that splice loss is typically higher when the cores are sheared in opposite directions [5.20]

Figure 5.12c is the power spectrum for a core deviation function where the cores are sheared in opposite directions, as in Fig. 5.10c. Because the core deviation function is a kind of decaying exponential, it represents a superposition of a continuity of spatial frequencies, so that the power spectrum is also continuous, in contrast to Figs. 5.10a-b. This ensures that there will be some spectral power found at the spatial frequency differences between the fundamental and cladding modes. When the cores are sheared in the same direction, as in Fig. 5.10d, the power spectrum resembles Fig. 5.12d. This is also a continuous distribution of spatial frequencies but since it is inherently more narrow than Fig. 5.12d, it couples between a smaller set of modes and will typically exhibit lower splice loss.

Generally speaking, most single-mode splice loss results from coupling to the lowest order cladding modes which typically exhibit axial propagation constants very close to that of the fundamental mode. For a typical SMF, the relevant axial propagation constant difference is about 8300 rad/m. This corresponds to perturbations with a period on the order of 750 μm or perturbations with a spatial frequency of about 1300 perturbations per meter.

By considering the coupling between the fundamental mode and cladding modes in a specifically step-index single-mode fiber, Zheng was able to derive a closed form solution expressing Γ_{cmt} in terms of the fiber parameters and operating wavelength that also takes into account core diameter fluctuations

(for example due to dopant diffusion) [5.22]

$$\Gamma_{\mathrm{cmt-si}} = \frac{8.68\Delta}{R_{\mathrm{fiber}}^2 w^2} \sum_{\mu} \left\{ \left| D_{\mathrm{core}} \left(\beta_\mu - \beta_{\mathrm{fund}} \right) \right|^2 \frac{J_0^2 \left(\frac{j_{0\mu} R_{\mathrm{core}}}{R_{\mathrm{fiber}}} \right)}{J_1^2 (j_{0\mu})} \right.$$

$$\left. + \left[\left| \mathcal{F}_{\mathrm{x}} \left(\beta_\mu - \beta_{\mathrm{fund}} \right) \right|^2 + \left| \mathcal{F}_{\mathrm{y}} \left(\beta_\mu - \beta_{\mathrm{fund}} \right) \right|^2 \right] \frac{J_1^2 \left(\frac{j_{1\mu} R_{\mathrm{core}}}{R_{\mathrm{fiber}}} \right)}{J_0^2 (j_{1\mu})} \right\} , \tag{5.29}$$

where $\Gamma_{\mathrm{cmt-si}}$ is the coupled-mode theory splice loss for a step-index fiber in dB, Δ is the familiar fractional refractive index difference between core and cladding, w is the mode field radius of the fundamental mode, R_{fiber} is the radius of the fiber (cladding), $\mathcal{F}$ denotes the Fourier transform of the core deviation function, D_{core} denotes the Fourier transform of the core diameter variation $f_{\mathrm{core}}(z)$, J_0 is the ordinary Bessel function of the first kind with order 0, J_1 is the ordinary Bessel function of the first kind with order 1 and the $j_{0\mu}$ and $j_{1\mu}$ are eigenvalues defined by

$$J_0(j_{0\mu}) = 0 \tag{5.30a}$$

$$J_1(j_{1\mu}) = 0 \tag{5.30b}$$

In actual practice, the closed form solution (5.29) is not always accurate, in part because of the many assumptions used to derive it. Moreover, it does not apply to fibers that do not have a step-index profile, such as dispersion-shifted fibers (DSF), dispersion-compensating fibers (DCF), or fibers with substantially diffused cores. However, (5.28) shows that the actual loss resulting from geometric deformation can be expressed as a series of coefficients (the $\hat{\kappa}_{\mathrm{fund}\mu}$) multiplied by the power carried in each frequency of the core deviation function. We may express this concept as

$$\Gamma_{\mathrm{cmt}} = \sum_{\upsilon} \left[a_\upsilon \left(\left| \mathcal{F}_{\mathrm{x}}(\upsilon) \right|^2 + \left| \mathcal{F}_{\mathrm{y}}(\upsilon) \right|^2 \right) + b_\upsilon \left| D_{\mathrm{core}}(\upsilon) \right|^2 \right] \tag{5.31}$$

where a_υ and b_υ are coefficients that depend on the fiber design and the operating wavelength and υ is a spatial frequency (with units of radians per unit length). As expected, this expression for single-mode fusion splice loss does not depend on propagation direction. This expression reveals that we can calibrate a loss estimation model for a particular combination of fibers at a particular wavelength by performing a large number of splices and determining the best fit set of a_υ and b_υ coefficients. This calibration strategy leads to the most accurate loss estimation model. When estimating the loss, we take the Fourier transform of the detected core positions in two orthogonal axes and sum the squares of the magnitudes of the Fourier coefficients. This yields a power spectrum for the core deviation which can be multiplied by the previously determined coefficients and summed to rapidly yield an accurate estimate of the splice loss.

The dimensions (or severity) of a core deformation can be normalized to the operating wavelength, which suggests that the same splice will exhibit

higher loss at shorter wavelengths. Indeed in Sect. 4.2.2 we showed that according to the Gaussian approximation, the loss of a fusion splice with a fixed amount of core offset or angular misalignment increases with decreasing wavelength. Although this behavior is not obvious from (5.29) or (5.31), these equations do generally predict that fusion splice loss increases with decreasing wavelength for core deformation functions such as those depicted in Fig. 5.10. Thus, for a given core deformation, the loss at 1310 nm is generally higher than the loss at 1550 nm

The performance of an exemplary commercial loss estimation system (including image processing and loss computation) is illustrated in Fig. 5.13. This loss estimation utilized a coupled-mode theory loss computation model, was performed on standard single-mode fiber at 1550 nm, and was calibrated against a different sample set of data points. About 95% of the estimated losses are within 0.03 dB of the actual measured losses. The accuracy of the estimation is remarkable, easily satisfying the requirements of the Telcordia GR-1095-CORE specification [5.5].

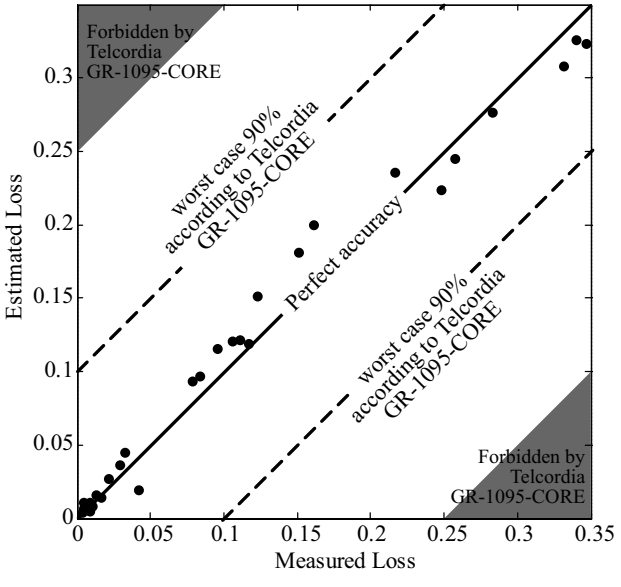

Fig. 5.13. Performance of a sample loss estimation system on standard step-index single-mode fiber (SMF) at 1550 nm. The accuracy and effectiveness of the loss estimation is evident from the proximity of the data points to perfect accuracy (*solid line*). About 95% of the estimated losses are within 0.03 dB of the actual measured losses. Also shown is the boundary of the 90% accuracy requirement (*dashed lines*) and the forbidden region (*shaded*), both mandated by Telcordia GR-1095-CORE [5.5]. Data obtained on *Vytran FFS-2000* and provided by *Vytran Corp.*

5.3 Summary

Loss estimation provides an estimate of the loss of a fusion splice based on digital images of the splice without explicitly performing a loss measurement. Loss estimation should not be misconstrued as a substitute for accurate splice loss measurement. Loss estimation is comprised of two tasks: (1) extracting the refractive index geometry of the splice from images, termed image processing, and (2) predicting the splice loss based on the detected refractive index geometry, termed loss computation. Most single-mode fusion splice loss results from the deformation or distortion of the fiber core. Such perturbations to the fiber core can be characterized by a core deviation function.

Correctly determining the core deviation function of a fusion splice requires an understanding of subtleties in the splice image, such as the ray paths of light traversing the fiber, or the magnification of core features. Filtering and averaging of the image can be improve core detection accuracy.

In special cases, the Gaussian approximation can be used to compute the loss of a fusion splice based on knowledge of the refractive index geometry. Coupled-mode theory is a more general and more accurate formalism for loss computation. Coupled-mode theory shows that the Fourier power spectrum of the core deviation function determines the amount of energy coupled from the fundamental mode into cladding and radiation modes, and thus lost at a single-mode fusion splice. By comparing the measured loss of a large number of splice samples to the power spectrum of the corresponding core deviation functions, one can perform a calibration procedure, which is specific to a particular fiber combination and operating wavelength, that results in highly accurate loss estimation.

6. Splice Strength, Reliability, and Packaging

Since their initial deployment in communications systems more than two decades ago, optical fibers have exhibited a reliability record that is superior to that of conventional copper cables [6.1]. Extensive research and development concerning the mechanical integrity, protection, and long-term reliability of optical fiber fusion splices is partly responsible for this success. Even if only a single fusion splice fails, an entire optical fiber span or optical fiber device, as well as adjacent devices or spans, could be rendered inoperable. Proper fusion splice reliability, lifetime estimation, and splice packaging minimizes the risk of such failures. Fortunately, the exemplary reliability record of optical fiber fusion splices has permitted the construction of high reliability communications networks.

The main failure mode of an optical fiber fusion splice is a mechanical fracture, which usually occurs very near to, but often not exactly at, the splice joint itself. When we refer to a fusion splice fracture in this chapter, we refer not only to the specific case of a fracture at the exact splice joint, but also to any case in which a fracture occurs near the splice joint. The likelihood of a fracture primarily depends on the condition of the fiber surface in the vicinity of the splice, the humidity of the fusion splice environment, and the mechanical load experienced by the splice. The condition of the fiber surface depends in turn on the stripping technique employed to remove the original fiber polymer coating, the splicing equipment and splicing parameters, the splice package, and the ambient environment. As for mechanical loads, only tensile stress can contribute to a fracture, but tensile stresses are present whenever a splice is stretched, bent, twisted, or buckled. Residual elastic stresses in the fiber may encourage, or inhibit, fracture.

An optical fiber fracture is usually easy to detect since the optical loss will suddenly increase by multiple decibels when the fiber cores fall out of alignment at the fracture site. An optical time-domain reflectometer (OTDR), which is described in Chap. 7, can identify the location of a fractured splice from kilometers away. However, it is theoretically possible for a fusion splice fracture to exhibit minimal change in optical loss if the cores happen to remain in alignment at the fracture site, and thus go undetected by an OTDR.

Optical fiber fusion splices must be protected from the environment to ensure their long-term reliability. A good fusion splice package will shield

the surface of the fiber from mechanical or chemical degradation. It must also be relatively cheap, easy to apply, and compact. Various splice protection strategies have been developed over the years to meet these needs. Some splice packages incorporate splints or other load-bearing members to minimize mechanical loads applied to the splice whereas others, such as acrylate recoats, rely on the mechanical strength of the fusion splice itself.

Reliability is inherently a statistical quantity so it is impossible to predict whether an individual splice will be reliable [6.3]. However, the reliability of a large set of fusion splices can be statistically predicted. Suitable physical models combined with tensile strength tests of fusion splice strength can estimate the probability of a fracture and estimate the lifetime of a fusion splice exposed to a known mechanical load. The statistical reliability requirements for optical fiber fusion splices depends on their environment and the costs associated with their repair. Fusion splices in a trans-oceanic communication system must exhibit both exceptional long-term reliability and high tensile strength. The cost of repairing a failed submarine fiber optic cable is enormous since a specialized ship must haul the cable up from the ocean floor. Furthermore, the repair process will subject the cable, and the splices within, to significant mechanical stresses which could lead to other failures. On the other hand, the physical characteristics of an undersea environment, such as temperature or applied load, can be considered to be relatively stable compared to most terrestrial environments [6.4]. Terrestrial fusion splices are much easier and cheaper to replace, but seasonal or even daily temperature fluctuations can stress optical fiber cables and devices, and in turn stress the fusion splices contained within them.

Good reviews of optical fiber reliability, mechanical strength, and the effects of fusion splicing are available in [6.5–6.8]. In this chapter we present a detailed analysis of the mechanical strength and reliability of optical fiber fusion splices, as well as strategies for packaging splices. In the first section, we introduce important concepts pertaining to the mechanical integrity, packaging, and reliability of optical fiber fusion splices. Following this, we show how crack growth in optical fibers is analyzed with fracture mechanics. Weibull statistics are introduced for analyzing the statistical nature of fusion splice strength. Theoretical and practical aspects of fusion splice proof testing are presented. Proof testing hardware is discussed. Finally, we discuss some contemporary optical fiber fusion splice packaging technologies.

6.1 Introduction to Splice Strength and Reliability

The strength and reliability of fusion splices in silica fibers is mainly determined by the material properties of silica glass. Silica is a brittle material meaning that it fractures rather than deforming plastically, like a ductile material, such as copper wire. The main failure mode of an optical fiber fusion splice, as well as an optical fiber, is mechanical fracture, which requires

tensile stress. Silica glass is extremely strong with a theoretical ultimate fracture strength on the order of 20 GPa [6.8]! However, the real failure strength is much lower because of the inevitable presence of cracks and flaws on the fiber's surface. Short lengths of commercial 125 μm diameter optical fiber usually fracture at a tensile load of about 69 N, which is equivalent to about 5.5 GPa of tensile stress. The axial tensile load applied to an optical fiber is often measured in an industry unit termed *kpsi* which stands for *kilo-pound-force per square-inch*. For a standard 125 μm diameter telecommunication fiber, 1 kpsi is about equal to 6.9 MPa so 5.5 GPa is equivalent to about 800 kpsi.

Fracture is the ultimate conclusion to the process of crack growth. Cracks in silica fiber grow continuously under normal ambient conditions. Surface cracks, rather than internal cracks, are nearly always responsible for optical fiber fracture for several reasons. Firstly, cracks are created on the surface of the optical fiber by abrasion. Secondly, crack growth at the fiber surface is accelerated by the presence of ambient moisture. Finally, certain types of loading, such as bending, apply the greatest amount of tensile stress on the fiber surface. For these reasons, the surface of any optical fiber is riddled with microscopic cracks or flaws introduced during the initial fabrication of the fiber. Very high strength optical fibers exhibit very small (sub-micron) cracks whereas lower strength optical fibers exhibit larger crack sizes. The fact that the surface condition of an optical fiber determines its strength is apparent from experiments showing that a low-strength optical fiber can be transformed into a high-strength optical fiber by etching away a ∼1 μm thick surface layer with hydro–fluoric acid [6.9–6.11].

Since the mechanical integrity of a glass fiber is controlled by the quality of its surface, proper handling of optical fibers during fusion splicing is critical to obtaining high strength splices. Once the protective polymer coating is stripped from an optical fiber, it immediately becomes vulnerable to surface damage. Even the gentlest physical contact of a bare glass fiber can cause a flaw which significantly reduces the strength and reliability of the fiber. Many fusion splicer manufacturers have introduced fully automatic splicing equipment that eliminates the need for a human operator to manipulate stripped fibers, thus minimizing the risk that the bare fiber surface will be inadvertently damaged.

Aside from the handling of the stripped optical fiber, the stripping process is a common source for the introduction of new surface flaws which reduce the strength of the subsequent fusion splice. Generally speaking, mechanical coating stripping techniques produce more fiber surface damage than solvent based (i.e. methylene chloride or hot sulphuric acid) stripping techniques. The high temperatures occurring during joint formation can encourage residual coating debris left behind by the stripping process to chemically interact with the glass, also reducing the splice's mechanical strength. Techniques for stripping the optical fiber are discussed in detail in Chap. 2.

Water has long been implicated as a contributor to crack growth in silica; in fact glass blowers sometimes breathe on a scribed piece of glass to encourage it to fracture more easily [6.12]. Water is thought to contribute to crack growth via the following reaction [6.5]

$$\begin{array}{cccc} | & | & | & | \\ -\mathrm{Si}-\mathrm{O}-\mathrm{Si} & + \mathrm{H_2O} & \Rightarrow & -\mathrm{Si}-\mathrm{O}-\mathrm{H} + \mathrm{H}-\mathrm{O}-\mathrm{Si}- \\ | & | & | & | \end{array} . \tag{6.1}$$

Thus, long-term exposure to high humidity, especially at elevated temperatures, can greatly accelerate crack growth in optical fibers. Splice packages can also decompose after long term exposure to high humidity (100%) and elevated temperatures ($> 60^\circ$ C) [6.13].

Numerous investigators have observed that optical fiber fusion splices often fracture in a region of fiber adjacent to the splice joint rather than exactly at the joint itself (Fig. 6.1). This region approximately ranges from 500 µm to 1.5 mm from the splice joint. The stripping process may have introduced new flaws or left coating debris behind in this region. Unlike the fiber at the splice joint itself, this section of fiber is heated during the splice to a temperature well above room temperature, but not hot enough for surface tension to heal surface flaws. The elevated temperatures experienced by this region of fiber can accelerate moisture-induced crack growth [6.14].

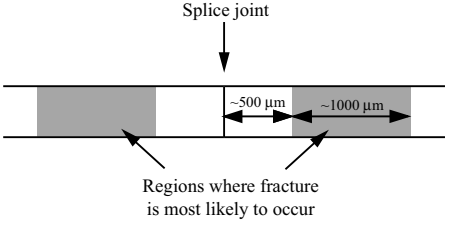

Fig. 6.1. Illustration of the most common location for fracture in an optical fiber fusion splice

Devitrification, meaning the growth of localized silica crystals, has been proposed as a mechanism for strength reduction of optical fiber fusion splices [6.9, 6.16]. The lowest energy state of room temperature silica is a crystalline structure, but optical fibers are amorphous (meaning glassy or non-crystalline) because they are cooled from their molten state too rapidly for crystals to form. However, if fused silica is held for long periods of time at elevated temperatures, crystals can begin to form at nucleation sites. As discussed in Sect. 3.1, fusion splice joints in silica fibers are formed at temperatures on the order of 2100° C. The glass on either side of the fusion splice joint is heated to intermediate temperatures that are high enough to permit devitrification of the glass. However, the glass is held at these intermediate

temperatures for only a few seconds. Some researchers have concluded that this short time interval is long enough to permit localized devitrification that weakens the fusion splice [6.9,6.16]. However, this conjecture is contradicted by other data showing that acid stripping and suppression of ambient moisture is sufficient to achieve splices whose failure stress nearly matches that of the original as-drawn fibers [6.17–6.19].

During normal operation, silica vaporized off the fiber surface can condense onto the electrodes of an arc fusion splicer when the arc is terminated. The resulting silica particles can be ejected from the electrodes during a subsequent fusion splice and deposited onto the fiber surface [6.19–6.23]. Particles deposited onto the splice joint itself will be melted into the surface by the high temperatures experienced there, but particles deposited a little further away from the joint, in the intermediate temperature region, can serve as crack nucleation sites, thus weakening the splice. Proper cleaning and maintenance of splicer electrodes can minimize this undesirable phenomenon.

Some fusion splicers perform a *fire polish* at the conclusion of the fusion splice in order to improve the surface quality in the vicinity of the splice [6.14,6.15]. During a fire polish, the fusion splice heat source is scanned over the vicinity of the splice joint in an effort to encourage surface tension to seal up any surface cracks in the vicinity of the splice. Such a fire polish may also re-vitrify any devitrified regions in the vicinity of the splice. Fusion splice manufacturers have reported that a fire polish improves the splice strength and consequently its long term reliability. Fire polishing is discussed in Sect. 8.2.1.

6.2 Crack Growth Theory

The tensile stress required to fracture an optical fiber depends on the density and severity of microscopic cracks on its surface. Microscopic surface cracks are inevitably introduced to the surface of optical fibers during fabrication, and these cracks determine the inherent tensile strength of as-drawn fiber. New surface cracks can be introduced during fusion splicing by the stripping process, joint formation, splice packaging, or simply by inappropriate handling of the bare fiber.

Surface cracks inevitably grow in size over time, especially in the presence of moisture or tensile stress, thus weakening the mechanical strength of the fiber. Crack growth in the absence of mechanical stress is termed *zero-stress aging* and can be minimized by splice packages which prevent ambient moisture from reaching the splice. Modeling and predicting zero-stress aging in optical fiber fusion splices is difficult and there is little published work concerning the matter. In contrast, crack growth resulting from mechanical stress, termed *stress corrosion*, is extensively discussed in the technical literature. Stress corrosion can be minimized by limiting the amount of tensile stress applied at the splice as well as moisture in the vicinity of the splice.

Unlike a ductile material, such as copper, a brittle material, such as silica glass, responds to an increasing tensile load by elastically stretching until a slow-growing microscopic crack exceeds a certain threshold at which point the crack grows rapidly and the material *fractures*. *Fracture mechanics* is concerned with the formation and growth of cracks which cause such fractures in brittle materials. Good general reviews of fracture mechanics are provided in [6.24,6.25]. In this section we will use fracture mechanics to analyze crack growth in silica and the strength of optical fiber fusion splices.

The *stress intensity factor* of a crack, K_{I}, is defined as [6.5, 6.7, 6.8, 6.24, 6.26]

$$K_{\mathrm{I}} = \sigma_{\mathrm{a}} Y \sqrt{a_{\mathrm{c}}}\,, \tag{6.2}$$

where σ_{a} is the local tensile stress applied in the vicinity of the crack, Y is a dimensionless constant on the order of unity that depends on the crack geometry, and a_{c} is the length of a surface crack. Y has been variously cited as $\sqrt{\pi}$ [6.5,6.7,6.8,6.24], 1.2 [6.27], or about 0.8 [6.8]. When the stress intensity factor, K_{I}, is equal to the *fracture toughness* of the material, K_{Ic}, the crack grows rapidly and the fiber immediately fractures. The fracture toughness of fused silica has been estimated to be about $0.8\,\mathrm{MPa}\sqrt{\mathrm{m}}$ [6.5, 6.8, 6.26, 6.27].

The *failure stress*, or *ultimate tensile strength*, of an optical fiber, σ_{f}, is the applied tensile stress required for K_{I} to equal K_{Ic} and can be expressed as

$$\sigma_{\mathrm{f}} = \frac{K_{\mathrm{Ic}}}{Y\sqrt{a_{\mathrm{c}}}}\,. \tag{6.3}$$

To measure the ultimate tensile strength of a fusion splice, the stress applied to a fusion splice is continuously ramped upwards until the splice fractures. The tensile load required to fracture an optical fiber is simply given by σ_{f} times its cross sectional area. Equation (6.3) shows how the strength of an optical fiber depends on the size of a surface crack. Furthermore, a length of optical fiber is only as strong as its weakest portion so the largest crack determines the fracture stress of the fiber. We define the *critical crack size*, a_{critical}, to be the crack length required to cause fracture in the presence of an applied tensile stress σ_{a}. Thus, the critical crack size is a function of the applied stress. Rearranging (6.2) and substituting K_{Ic} for K_{I} yields

$$a_{\mathrm{critical}} = \left(\frac{K_{\mathrm{Ic}}}{Y\sigma_{\mathrm{a}}}\right)^2\,. \tag{6.4}$$

Equation (6.3) suggests that the observed failure stress of short lengths of commercial 125 µm diameter fiber, 5.5 GPa, corresponds to surface cracks on the order of 10 nm in length. The small variation in the measured failure stress across large numbers of fiber samples suggests that all silica fibers are covered with a large number of surface cracks of this size. Most commercial 125 µm diameter optical fiber is only rated to survive a 700 MPa (100 kpsi)

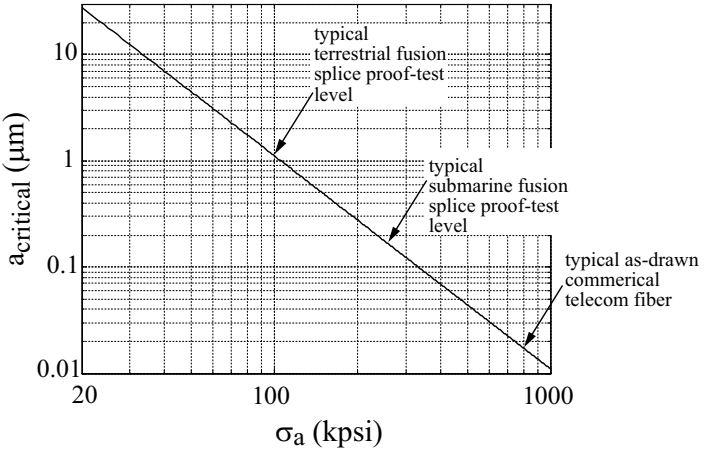

Fig. 6.2. Critical crack size, a_{critical}, plotted against corresponding applied tensile stress, σ_{a} according to (6.4). Y was taken to be 0.806. After [6.8]

tensile stress which corresponds to about 9 N of load. This suggests that the largest surface crack in such commercial fiber is on the order of 1 μm.

Modeling crack growth due to zero-stress aging is difficult as it depends on the chemical environment of the fiber surface. However, various simple models exist for modeling the crack growth due to stress corrosion. The rate of crack growth is usually expressed as a function of the crack length. Exponential models are thought to be more physically realistic but power law models are more mathematically convenient and are sufficiently accurate for most purposes [6.5, 6.26]. A commonly used crack growth power law is [6.7, 6.8, 6.26, 6.27]

$$V_{\text{crack}} = \frac{\mathrm{d}a_{\text{c}}}{\mathrm{d}t} = A_{\text{c}} K_{\text{I}}^{n_\sigma} \ , \tag{6.5}$$

where V_{crack} is the crack growth velocity and A_{c} and n_σ are material constants. The parameter n_σ denotes the *stress corrosion susceptibility factor*. In contrast to most of the technical literature, which denotes the stress corrosion susceptibility factor by n, we have chosen the symbol n_σ to avoid confusion with the refractive index. For practical optical fiber applications, n_σ ranges from about 16 in humid environments (which are conducive to crack growth) to about 25 in very dry environments [6.28]. Since K_{I} is less than one in conventional units, larger values of n_σ correspond to slower crack growth. Measurement of the stress corrosion susceptibility factor is discussed in [6.28,6.29]. The constant A_{c} is not as well characterized but has been cited to be $1{\times}10^{19}$ to $8.5{\times}10^{36}$ when n_σ varies from about 10 to 20 (note that the units of A_{c} depend on n_σ) [6.28]. In Sect. 6.4 we will show how practical results for splice lifetime estimation and reliability can be obtained without a detailed knowledge of A_{c}.

If we raise σ_f from (6.3) to the $n_\sigma - 2$ power, then differentiate with respect to time, and finally substitute in (6.5), we obtain

$$\frac{d(\sigma_f^{n_\sigma-2})}{dt} = \left(\frac{2-n_\sigma}{2}\right) A_c Y^2 K_{Ic}^{n_\sigma-2} \sigma_a^{n_\sigma} \ , \tag{6.6}$$

where σ_a is the applied stress and is in general a function of time. This equation can be integrated over time to yield

$$\sigma_{f,initial}^{n_\sigma-2} - \sigma_{f,final}^{n_\sigma-2} = \left(\frac{n_\sigma-2}{2}\right) A_c Y^2 K_{Ic}^{n_\sigma-2} \int_{t_{initial}}^{t_{final}} \sigma_a^{n_\sigma}(t) dt \ , \tag{6.7}$$

where $\sigma_{f,initial}$ is the initial failure stress of the fiber prior to the application of a tensile load, $\sigma_{f,final}$ is the final failure stress, and $\sigma_a(t)$ is the applied stress as a function of time between times $t_{initial}$ and t_{final}. Equation (6.7) is significant since it quantifies how an applied stress, σ_a, reduces the ultimate tensile strength, $\sigma_{f,final}$, of an optical fiber as a function of the initial ultimate tensile strength, $\sigma_{f,initial}$. More specifically, the ultimate tensile strength of a fiber is degraded by an amount proportional to the time integral of the applied stress raised to the n_σ power.

If the applied stress, σ_a, is approximately constant over time, (6.7) may be rearranged to estimate the lifetime of the optical fiber, t_s. Since the applied load is a constant, it may be pulled out of the integral in (6.7). Furthermore, we assume that at the end of the fiber's lifetime, it fractures because its ultimate failure strength, $\sigma_{f,final}$, is equal to the applied load, σ_a. Based on these assumptions, the fiber's lifetime when exposed to a constant applied stress may be estimated as

$$t_s = \frac{(n_\sigma-2)}{2A_c Y^2} K_{Ic}^{2-n_\sigma} \sigma_a^{-n_\sigma} \left(\sigma_{f,initial}^{n_\sigma-2} - \sigma_a^{n_\sigma-2}\right) \ . \tag{6.8}$$

Since the exponent of the final terms of (6.8) will be larger than 10, we may neglect the final term when $\sigma_{f,initial}$ is much larger than σ_a to obtain a simplified lifetime equation

$$t_s = \frac{(n_\sigma-2)}{2A_c Y^2} K_{Ic}^{2-n_\sigma} \sigma_a^{-n_\sigma} \sigma_{f,initial}^{n_\sigma-2} \ . \tag{6.9}$$

This equation predicts the lifetime of a fiber with initial strength $\sigma_{f,initial}$ exposed to a constant tensile stress of σ_a.

6.3 Characterizing Splice Failure Strength: Weibull Statistics

The statistical distribution of the ultimate tensile strength of a set of fusion splices can be approximated by a normal distribution which is characterized by a mean value and a standard deviation. However, real fusion splice strength

data is usually poorly described by a normal distribution. The Weibull distribution is a better choice because it more accurately captures the underlying physics responsible for fiber fracture. In this section we will describe how the Weibull distribution can be used to characterize fusion splice strength, and even provide some interesting insight into the failure mode of a fusion splice.

Weibull proposed a simple relationship for the strength of a material based on a distribution of flaws inside its bulk. This relationship was predicated on a "weakest link" model for fracture meaning that a sample is assumed to fracture at the site of the largest flaw. The resulting statistical description of failure probability can be applied to the problem of optical fiber failure strength in general and optical fiber fusion splice fracture in particular.

As we have already seen, empirical evidence and theoretical arguments show that the failure strength of an optical fiber depends on the distribution of scratches and flaws on its surface. A longer length of optical fiber will exhibit a lower ultimate tensile strength than a shorter length of fiber because its larger surface area is more likely to contain a larger flaw. The probability that a piece of fiber with surface area A_0 will survive a proof test, P_S, can be expressed as [6.25]

$$P_S(A_0, \sigma_f) = \exp\left[-\left(\frac{\sigma_f}{\sigma_0}\right)^m\right] , \tag{6.10}$$

where σ_f is the applied stress and σ_0 and m are constants that depend on the state of the glass surface. Equation (6.10) can also be thought of as the probability that the particular fiber sample exhibits a failure stress of σ_f. We can express (6.10) in terms of the failure probability, P_F, since the failure probability is the complement of the survival probability, P_F=1-P_S, so

$$P_F(A_0, \sigma_f) = 1 - \exp\left[-\left(\frac{\sigma_f}{\sigma_0}\right)^m\right] . \tag{6.11}$$

Note that these equations imply that the probability of the failure stress, σ_f, equaling or exceeding σ_0 is about 37%. We will denote σ_0 as the *nominal failure stress* of the fiber. Equation (6.10) is an empirical relationship that has been found to agree well with experimental data for a variety of materials in a variety of contexts. Some researchers have attempted to provide a physical justification for (6.10) [6.30].

The utility of the Weibull distribution is apparent by considering how (6.10) can be used to describe the survival probability of another identical fiber sample with a different surface area. The survival probability of an identical sample with the arbitrary surface area A, where $A = \upsilon A_0$, can be written as

$$P_S(A, \sigma_f) = [P_S(A_0, \sigma_f)]^{\upsilon} = [P_S(A_0, \sigma_f)]^{A/A_0} . \tag{6.12}$$

If we take the natural logarithm of (6.10) twice we obtain the following [6.25]

$$\ln\left[\ln\left(\frac{1}{P_{\mathrm{S}}(A_0,\sigma_{\mathrm{f}})}\right)\right] = m\ln\left(\frac{\sigma_{\mathrm{f}}}{\sigma_0}\right) \ . \tag{6.13}$$

Thus, if $\ln\left(\frac{\sigma_{\mathrm{f}}}{\sigma_0}\right)$ is plotted against $\ln\left[\ln\left(\frac{1}{P_{\mathrm{s}}(A_0,\sigma_{\mathrm{f}})}\right)\right]$, a straight line with slope m, now termed the *Weibull slope*, results. Note that we can also express (6.13) in terms of the failure probability, P_{F}. Furthermore, the surface area of fiber affected by the fusion splice is usually the same for all splices so we can neglect the dependence on A_0 to obtain

$$\ln\left[\ln\left(\frac{1}{1-P_{\mathrm{F}}(\sigma_{\mathrm{f}})}\right)\right] = m\ln\left(\frac{\sigma_{\mathrm{f}}}{\sigma_0}\right) = m\ln\left(\sigma_{\mathrm{f}}\right) - m\ln\left(\sigma_0\right) \ . \tag{6.14}$$

As-drawn commercial optical fibers with a 125 μm cladding diameter typically exhibit a nominal failure stress, σ_0, of about 5.5 GPa (800 kpsi) and a Weibull slope, m, ranging from about 25 to 125 [6.5]. Sample data for the failure probability of such as-drawn commercial optical fiber is presented in Fig. 6.3.

The parameters characterizing the Weibull distribution, σ_0 and m, can be estimated from the parameters characterizing a normal distribution for the same data. Typically, σ_0 is comparable to the mean value of a normal distribution while m is approximately 1.28 times the mean divided by the standard deviation [6.5].

The Weibull distribution of failure stresses for a particular type of optical fiber fusion splice can be compiled by measuring the failure strength of a large enough set of splices. At least 20 splice failure stress measurements are required for a practical Weibull representation, but at least measurements 30 are recommended. The raw data is initially a simple list of failure stresses. To transform this relationship into the form of (6.14), one must first compute the failure probabilities associated with each strength measurement. If the N_{weib} measured failure stresses are listed in size order from lowest to highest, the failure probability for the ith measurement can be estimated as

$$P_{\mathrm{F}} = \frac{i-\frac{1}{2}}{N_{\mathrm{weib}}} \ . \tag{6.15}$$

A Weibull plot, such as Fig. 6.3, is prepared by plotting the left hand side of (6.14) computed with the aid of (6.15) on the y-axis against the logarithm of the measured failure stress on the x-axis. An estimate for m can be obtained from the slope of the resulting data set

$$m = \frac{\Delta\left(\ln\left(\ln\left(\frac{1}{1-P_{\mathrm{F}}(\sigma_{\mathrm{f}})}\right)\right)\right)}{\Delta\left(\ln\sigma_{\mathrm{f}}\right)} \ , \tag{6.16}$$

while an estimate for σ_0 is given by the stress where $\ln\left(\ln\left(\frac{1}{1-P_{\mathrm{F}}}\right)\right)=0$.

A Weibull plot of fusion splice data can be a helpful tool for characterizing the performance of particular splice parameters or splicing equipment. It can also provide insight into the failure mode of the fusion splice. As long as all

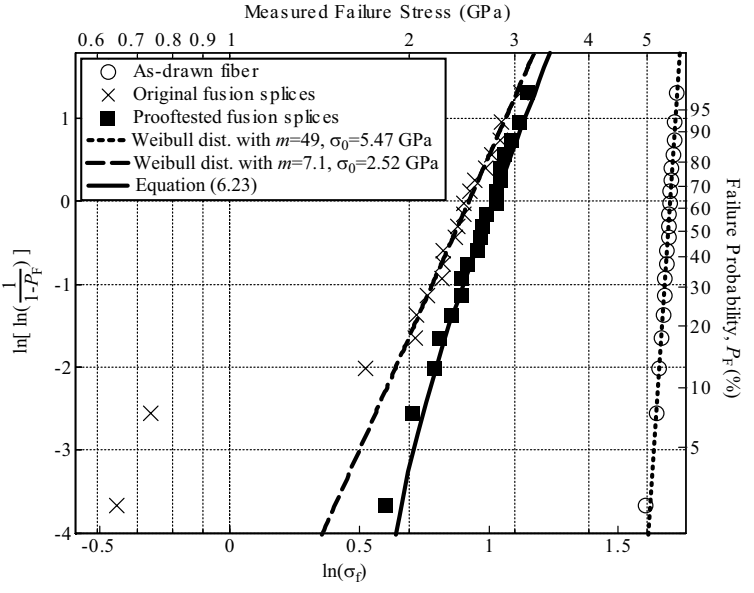

Fig. 6.3. Weibull plot of failure stress for as-drawn commercial optical fiber (*circles*), fusion spliced fiber (x *'s*), and fusion spliced fiber following a 1.6 GPa (235 kpsi) proof test (*squares*). Note that $\ln(\sigma_f)$ is plotted on the x-axis and $\ln\left[\ln\left(\frac{1}{1-P_F}\right)\right]$ on the y-axis. To provide a more physical appreciation for the data, σ_a is indicated in GPa by the (non-linearly spaced) tick marks above the plot while P_F is indicated in % by the (non-linearly spaced) tick marks to the right of the plot. The as-drawn fiber data and the fusion splice data were both fit to Weibull distributions (*dotted line* and *dashed line* respectively). σ_0 and m for the as-drawn fiber are 5.47 GPa and 39 while σ_0 and m for the spliced fiber are about 2.51 GPa and 7.1. The two outliers on the low-strength end of the fusion spliced fiber probably incurred surface flaws due to inappropriate handling or stripping procedures. The solid line represents the failure strengths predicted by (6.23) in Sect. 6.4

of the fusion splice samples exhibit a similar distribution of surface flaws, the data can be expected to approximate a Weibull distribution, thus yielding a straight line in a Weibull plot. However, if a few fusion splice samples are mishandled, or weakened by some extrinsic phenomenon, those samples will not conform to the same distribution, so the data will be poorly approximated by a Weibull distribution. Excessive departure from linear behavior indicates that there are significant extrinsic sources of strength reduction, such as improper handling or improper fiber stripping procedures.

The 20 fusion splice samples (x's) depicted in Fig. 6.3 include 2 data points at the low end which do not line up with the others. These outliers probably incurred extra surface flaws due to inappropriate handling or stripping procedures. The amount of splice-induced strength reduction relative to the original as-drawn fiber is substantial, but is typical even for high quality

fusion splices. About 90% of the fusion splice samples in Fig. 6.3 exceed the stringent proof test requirement for submarine fiber splices, which is about 1.6 GPa.

Fusion splices exhibiting no measurable strength degradation, meaning that both their nominal failure stress and their Weibull slope matches that of the original fiber, have been documented in the literature [6.17]. These splices were performed with a very clean burning oxy-hydrogen torch in the presence of chlorine gas on fibers stripped by hot sulphuric acid. Such an hazardous and complex apparatus is not very practical for most laboratory fusion splicing, let alone factory splicing or field splicing! Nearly equivalent results have also been achieved using a conventional arc splicer on fibers stripped with hot sulphuric acid [6.19]. However, since commercial as-drawn optical fiber is rarely proof tested to greater than 1.6 GPa, achieving such high fusion splice strengths is not of much practical interest. Consistently achieving a minimum proof test threshold such as 700 MPa for terrestrial fiber applications and 1.6 GPa for submarine applications is far more important. This consistency can be achieved with a large Weibull slope, m, as well as with a high nominal failure stress, σ_0.

6.4 Theory of Proof Testing for Long-Term Reliability

An optical fiber fusion splice must not only be strong enough to survive handling during splice packaging and installation, but also must withstand zero-stress aging and stress corrosion over its long service life, often 25 years or more. Proof testing is the main method for ensuring mechanical robustness and long term reliability of fusion splices because it requires relatively simple, low-cost equipment and can be preformed in less than a minute. Proof test stress levels must be set high enough to ensure the robustness and reliability of a splice, but not so high that the proof test yield, or fraction of splices surviving the proof test, is too low. Moreover, the failure rate of other components in the optical network, such as the optical fiber or cable itself, puts an upper limit on the long term reliability requirements of optical fiber splices. For example, the reliability of optical fiber cables in the United States has been cited to be on the order of 2 failures per thousand km per year [6.1]. These failures are overwhelmingly due to causes other than fusion splices.

In this section, we will show how the results of the preceding two sections, crack growth theory and Weibull statistics, have been combined to create a theory which quantifies the strength and reliability of proof tested fusion splices. The interested reader is referred to many important treatments of this topic in the literature [6.11, 6.28, 6.29, 6.31–6.35, 6.37–6.39].

When an optical fiber fusion splice is proof tested, a tensile stress σ_p is applied to the fiber for a time duration t_p. In practice, there will be a finite time interval, t_l, at the beginning of the proof test when the applied load is ramped up to σ_p and a finite time interval, t_u, at the end of the proof

test during which the applied load is ramped back down to zero (Fig. 6.4). Clearly the fusion splice will fracture during the proof test if σ_p exceeds the ultimate tensile strength of the splice, σ_f. On this basis, a proof test would appear to be an obvious way to eliminate fusion splices which do not satisfy the fracture stress requirement σ_p. However, we have already seen that the presence of tensile stress induces crack growth via stress corrosion so it is logical to suspect that during the unloading phase of the proof test, cracks could grow to the point that the ultimate tensile strength of a fusion splice, which previously survived the peak proof test stress of σ_p, may be less than σ_p after the proof test is completed.

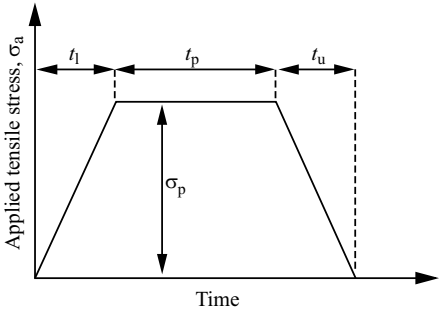

Fig. 6.4. Schematic illustration of the tensile stress applied to an optical fiber fusion splice during a proof test. The loading time is σ_l, the proof stress σ_p is applied for time t_p, and the unloading time is σ_u. The time axis is not to scale and in a real proof test, the loading and unloading may not be linear

Ideally we would like to quantify the long term reliability and strength benefits of proof testing while accounting for the possibility of strength reduction during the unloading phase. In other words, we would like to predict the probability of fusion splice fracture as a function of applied stress following a proof test. Building on the important work of Kalish and Tariyal [6.28], Mitsunaga and coworkers [6.29] showed how the failure probability of an optical fiber following a proof test could be predicted from the Weibull distribution of the fiber prior to the proof test and the stress corrosion susceptibility factor, n_σ. Remarkably, this prediction accounts for the possibility of crack growth during the unloading phase of the proof test and does not require knowledge of the crack growth parameter A_c, geometric parameter Y, or fracture toughness K_{Ic} appearing in (6.2–6.8). Mitsunaga's result can be expressed as [6.29]

$$P_F = 1 - \exp\left\{-N_p\left[\left(1 + \frac{k_s}{\sigma_p^{n_\sigma} t_{pe}}\right)^{m/(n_\sigma - 2)} - 1\right]\right\}, \tag{6.17}$$

where k_s is a parameter characterizing the amount of tensile stress applied to the splice during its service life, m is the Weibull slope of a distribution

of an equivalent group of (non-proof tested) fusion splices, N_p is the fraction of splices that fail the proof test, σ_p is the proof test level, and t_pe is the effective proof test time, given by [6.29]

$$t_\mathrm{pe} \equiv t_\mathrm{p} + \frac{t_\mathrm{l} + t_\mathrm{u}}{n_\sigma + 1} \,, \tag{6.18}$$

accounting for the influence of loading and unloading. N_p can either be directly measured, or computed from the Weibull statistics determined from a large set of fusion splice samples. Note that the failure probability of proof tested splice samples given by (6.17) is not a true Weibull distribution.

The fusion splice experiences a strength degradation resulting from the (potentially time varying) service stress, σ_s over the course of its service life t_s. This phenomenon is captured by the parameter k_s [6.29]

$$k_\mathrm{s} = \int_0^{t_\mathrm{s}} \sigma_\mathrm{s}^{n_\sigma} \mathrm{d}t \,. \tag{6.19}$$

This expression is essentially a restatement of (6.7): it states that the strength degradation of an optical fiber fusion splice is proportional to the time integral of the applied tensile stress raised to the n_σ power. When the applied stress is constant over the entire service life, (6.19) simply reduces to $k_\mathrm{s}{=}\sigma_\mathrm{s}^{n_\sigma} t_\mathrm{s}$.

Equations (6.17–6.19) are the central equations for describing the long term reliability of fusion splices experiencing stress corrosion. They are extremely powerful because they relate the probability of fusion splice fracture to the tensile stresses experienced during the splice's service life and to other well characterized parameters (inherent Weibull slope of the fusion splice m, stress corrosion susceptibility parameter n_σ, proof test level σ_p, proof test failure rate N_p, and effective proof test time t_pe). Note that the inherent Weibull slope for a fusion splice is easily computed from measurements of the failure strength of 20 (non-proof tested) sample fusion splices while the stress corrosion susceptibility factor of silica fibers is a well characterized function of ambient humidity [6.28].

If the service stress σ_s is constant over the entire service lifetime, (6.17) can be rearranged to estimate the service lifetime, t_s, as a function of the other parameters

$$t_\mathrm{s} = \left\{ \left(1 - \frac{\ln(1 - P_\mathrm{F})}{N_\mathrm{p}} \right)^{(n_\sigma - 2)/m} - 1 \right\} \left(\frac{\sigma_\mathrm{p}}{\sigma_\mathrm{s}} \right)^{n_\sigma} t_\mathrm{pe} \,. \tag{6.20}$$

An example of a service stress that is constant over the lifetime of a fusion splice is the tensile stress resulting from wrapping a fusion splice around a spool. As we shall soon discuss in Sect. 6.6, some splice packages contain a rigid splint which prohibits bending and limits packaging options whereas other splice packages, such as a recoat, are as flexible as the original polymer coating and permit the splice to be coiled in the manner of an ordinary fiber. Bending a fiber into a loop of radius R_bend (Fig. 6.5) results in a maximum tensile stress $\sigma_\mathrm{bend,max}$ given by [6.40, 6.41]

$$\sigma_{\text{bend,max}} = \frac{R_{\text{fiber}}}{R_{\text{bend}}} E_{\text{y}} \ , \tag{6.21}$$

where R_{fiber} is the fiber radius and E_{y} is Young's modulus for silica glass, which is about 73 GPa. A typical bend radius for a fusion splice coiled inside an optical fiber device is on the order of 10 cm which implies a maximum bending stress on the order of 46 MPa (6.6 kpsi) for a 125 μm diameter fiber.

If we assume typical values such as σ_{p}=700 MPa (100 kpsi), $n_\sigma \sim 20$ (for a reasonably dry environment), $m \sim 4$, $N_{\text{p}} \sim 0.1$ (10% of the initial splices fail the proof test), and $t_{\text{pe}} \sim 15$ s, then (6.17) predicts a vanishingly small fracture probability P_{F} after 25 years of service. The stress corrosion susceptibility factor, n_σ, has been measured to be on the order of 18 in the case of recoated fusion splices [6.36]. Even a very moist environment resulting in n_σ=16, a failure probability of only 0.1%, and a tight bend radius of 2.5 cm inducing a service stress of about 185 MPa (26.7 kpsi) is predicted by (6.20) to have a service life to be about 25 years. In reality, we expect an actual fusion splice to be much more reliable than these examples since bending only induces high tensile stress on the small portion of the fiber surface at the outside of the fiber loop – most of the fiber surface experiences a much lower tensile stress.

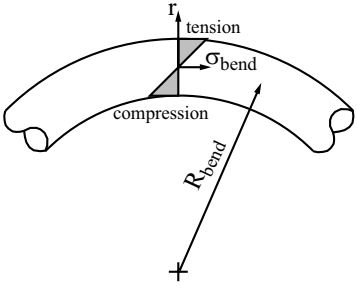

Fig. 6.5. Stress resulting from a bend in an optical fiber. The outer surface of the loop experiences the highest tensile stress while the inner surface of the loop experiences compressive stress which does not induce stress corrosion

The validity of the preceding theory can be established by evaluating its ability to predict the ultimate tensile strength of fusion splices that have been previously proof tested. We can approximate a measurement of the ultimate tensile strength of a fusion splice as the application of a service stress which is continuously ramped upwards at a rate of $\dot{\sigma}$ until the splice fails at σ_{f}. Substituting into (6.19) and integrating yields

$$k_{\text{s}} = \int_0^{t_{\text{s}}} (\dot{\sigma} t)^{n_\sigma} \, \mathrm{d}t = \frac{\sigma_{\text{f}}^{n_\sigma + 1}}{(n_\sigma + 1)\, \dot{\sigma}} \ . \tag{6.22}$$

This expression can be substituted into (6.17) to yield

$$P_{\mathrm{F}} = 1 - \exp\left\{-N_{\mathrm{p}}\left[\left(1 + \frac{\sigma_{\mathrm{f}}^{n_\sigma+1}}{(n_\sigma+1)\dot{\sigma}\sigma_{\mathrm{p}}^{n_\sigma} t_{\mathrm{pe}}}\right)^{m/(n_\sigma-2)} - 1\right]\right\} . \quad (6.23)$$

The solid line in Fig. 6.3 was computed with (6.23) for fusion splice samples proof tested at 1.61 GPa (235 kpsi) and agrees well with experimentally measured fracture strengths (*squares*). Notice that since (6.23) is not a true Weibull distribution it appears as a curved, rather than straight, line in Fig. 6.3. The agreement between the predicted (*dashed line*) and the experimentally measured (*x's*) ultimate failure strengths of proof tested fusion splice samples in Fig. 6.3 confirms the accuracy of the theory [6.37].

Proof test requirements for optical fiber fusion splices are derived by considering the maximum tensile stress expected to be experienced by the fusion splice and ensuring that the proof test exceeds this level by a safe margin. Furthermore, (6.17–6.19) can be used to estimate the lifetime of proof tested fusion splices experiencing stress corrosion resulting from known levels of tensile stress. Various standards bodies have issued publications detailing specific tensile strength requirements for fusion splices. Published standards generally require proof test loads ranging from 50 to 100 kpsi [6.42–6.44]. Other standards require the packaged splice to withstand tensile loads on the order of 5 N [6.45], which is equivalent to tensile stress on the order of 50 kpsi if all the load is borne by the fiber itself.

High tensile loads are applied to submarine optical fiber cables during their initial deployment on the ocean floor, during subsequent recovery of the cable from the ocean floor, and while they are suspended from a cable ship for repair [6.27]. When typical submarine cable values are used, (6.17-6.19) reveal that the appropriate proof test stress, σ_{p}, must be on the order of 1.2 to 1.6 GPa (160 to 235 kpsi) [6.27,6.33]. When all safety margins are factored in, proof test requirement is set to about 1.6 GPa (235 ksi). If proper fiber stripping, handling, and splicing procedures are followed, proof test yields, even at these high proof test stress levels, can exceed 90%. Corresponding computations for terrestrial fiber cables yield proof test requirements on the order of 700 MPa (100 kpsi), which are much easier to satisfy.

6.5 Proof Testing Methods and Hardware

A fusion splice can be proof tested either by applying an axial tensile load across the splice or bending the splice through a tight radius. Commercial strength testing equipment usually employs the axial tensile method since bending only exposes a portion of the optical fiber to high tensile stresses (Fig. 6.5).

Short lengths of standard as-drawn 125 μm diameter silica fibers are very strong: they typically fail at tensile loads of about 69 N or 5.5 GPa (800 kpsi). High strength fusion splices can approach this strength [6.17,6.19]. It is difficult to apply such high loads to a fusion splices without damaging the fiber's

polymer coating. Usually, both ends of the fiber to be tested are wrapped around mandrels (Fig. 6.6). However, at the lower tensile stress levels typical for fusion splice proof testing, the fiber gripping chucks can be much simpler in design.

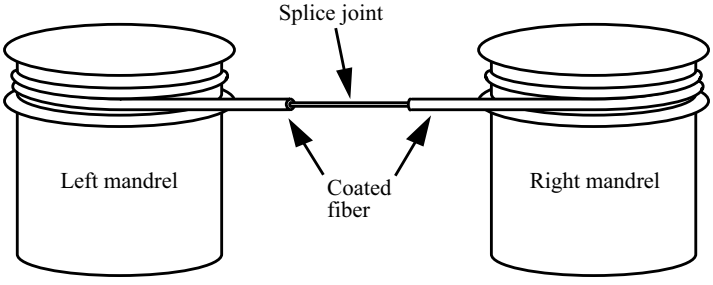

Fig. 6.6. Illustration of fusion splice strength testing geometry. Rotary mandrels can apply tensile forces in excess of 69 N, which is the ultimate tensile strength of most commercial telecommunication fibers. In this diagram, the proof test is performed on a fusion splice prior to packaging. When a splice is recoated, the recoat should always be applied prior to the proof test to ensure that the splice strength is not compromised by the recoating process

Standard proof testing of a fusion splice usually involves three stages: linearly ramping the tension up to a desired level; holding the fiber at the desired tension for a short time interval; and ramping the tension back down to zero (Fig. 6.4). The entire process usually takes about 15 seconds. As we have seen, stress corrosion can weaken fusion splices during the unloading phase so the fiber is usually unloaded within one second [6.1].

When an optical fiber fractures at stresses of 1.4 GPa (200 kpsi) or greater, the fiber usually shatters violently. For this reason, safety precautions such as eye-goggles and a shatter shield should always be used when proof testing optical fibers. Small shards of shattered optical fiber have been known to embed themselves in exposed skin. When the fiber fails at lower tension and it does not shatter, the root cause of the crack leading to the fracture of a fusion splice can often be identified by analyzing the end face of the fractured fiber with a scanning electron microscope (SEM). However, analyzing the cause of high strength fractures is impossible when the fiber shatters since the end faces of the fractured fiber are destroyed.

6.6 Splice Packaging

Optical fiber fusion splices are nearly always protected from the environment by a packaging technology. In this context, splice packages refers to coatings, tubes, cases, and splints applied to protect the specific portion of the optical

fiber exposed or modified during the fusion splice process. Multiple fusion splices are sometimes further packaged in a splice tray or splice housing.

Fusion splice protection is designed with some or all of the following goals in mind

- protect surface of fusion splice from mechanical degradation (i.e. abrasion)
- protect surface of fusion splice from chemical degradation (i.e. humidity)
- low cost
- easy and quick to apply
- withstand thermal cycling
- minimize optical loss resulting from geometric distortion of splice
- minimize tensile, bending, or torsion loads applied to the splice joint
- record data about splice (i.e. date of manufacture, optical loss, etc.)

Fusion splice packages may be divided into two general categories: *recoats* and rigid *splice protectors*. A recoat restores a flexible polymer coating onto the bare fusion splice but does not satisfy the last three items in the list above. The polymer comprising the recoat is usually similar in composition to the original fiber polymer coating. Since a recoat is soft and flexible like the original fiber coating, the mechanical integrity of the splice entirely depends upon the fusion splice itself. In contrast, a splice protector is designed to satisfy all the items in the list by employing a rigid splint to transfer tensile, bending, and torsional loads across the splice joint.

6.6.1 Splice Recoating Technology

A recoat is a fusion splice packaging technology in which a polymer coating similar to the original polymer coating is restored to the original fiber. Typically this is a UV-cured urethane acrylate although thermally cured polyimide is occasionally used. The mechanical integrity of the recoated splice is entirely dependent on the fusion splice joint itself so successful recoating requires high strength splices. Several commercial optical fiber recoating systems have been introduced in recent years. Even ribbon fibers spliced on a mass fusion splicer can now be recoated. Recoated ribbon fiber splices often need not be high strength since any applied load is distributed over a larger number of fibers (up to 24). Typical single fiber recoated splices are depicted in Fig. 6.7.

Recoated splices can usually be coiled into a tight radius because the recoat is just as flexible as the original polymer coating. The ability to coil a recoated splice makes recoating attractive for applications in which the finished splice must be wound around a fiber spool or tightly coiled to fit inside a small fiber device package. Recoats are typically employed in the assembly of undersea optical fiber cables where high fusion splice strength is already necessitated by stringent reliability requirements. Recoats are also attractive for submarine optical fiber cables since their cross section matches that of the original coated fiber.

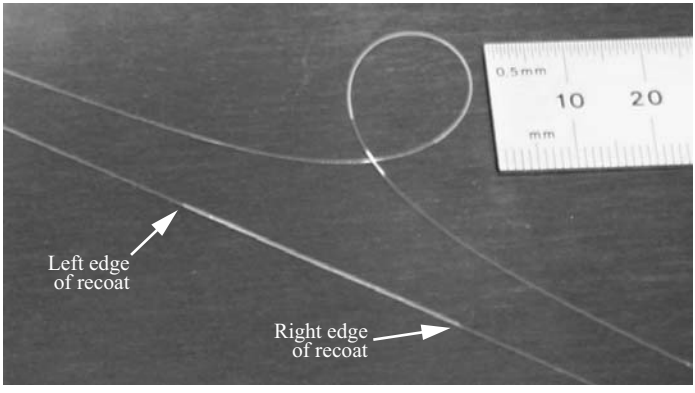

Fig. 6.7. Recoated fusion splices illustrating how they may be bent into very tight radii. Fiber shown here is 125 μm diameter standard SMF with a 250 μm diameter UV-curable acrylate coating applied using a *Vytran* model *PTR-100* recoater. Note how similar the recoated portion is to the original fiber coating

To recoat a fusion splice, the completed fusion splice is loaded into a mold and liquid acrylate material is injected into the mold around the bare glass surface of the fiber (Fig. 6.8). The recoat material envelopes the fusion splice and overlaps or mates against the edge of the original polymer coating. Once the mold is filled, high intensity UV-radiation is used to cure the liquid polymer. Recoat diameters can range from as little as 100 μm to as much as 1 mm depending on the size of the recoat mold and the original coating diameter of the fiber, but 260 μm is the most common diameter for a single fiber recoat

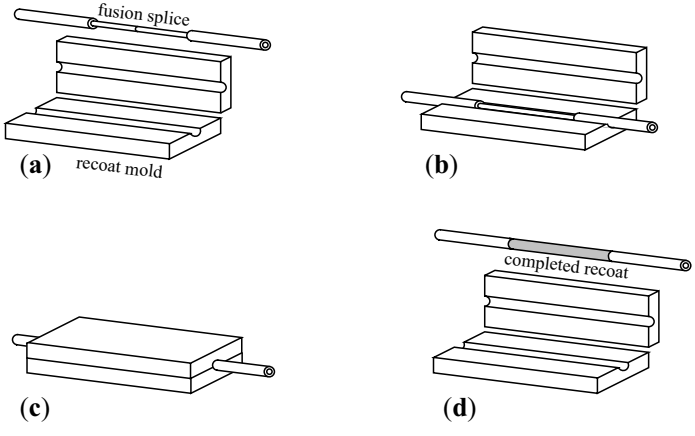

Fig. 6.8. Schematic illustration of fusion splice recoat process. (**a**) Completed fusion splice positioned above recoat mold. (**b**) Completed fusion splice laying in open recoat mold. (**c**) Recoat mold closed as recoat material is pumped into the mold and cured, typically using high-intensity UV lamps. (**d**) Completed recoat (shaded) after removal from mold

(the recoat is typically slightly larger than the coated fiber diameter so a portion of the coated fiber can fit into either end of the mold). Depending on the application, special recoat material may be chosen to have a refractive index that is either higher or lower than the fiber's glass cladding. Some fusion splicers have fiber recoating equipment integrated into their design.

Sometimes the quality of a recoat is so good that it is difficult to distinguish it from the rest of the fiber. In such cases, the recoat material can be dyed to facilitate identification of the recoat location.

6.6.2 Rigid Splice Protectors and Splints

Fusion splices are often packaged in rigid splice protectors, two examples of which are depicted in Fig. 6.9. These splice protectors can be divided into two categories: heat shrinkable tubes and clam-shell designs. Splice protectors are inexpensive and easy to apply and are designed to carry tensile, bending, and torsional loads across the splice joint. Splice protectors should enable a fusion splice to withstand the equivalent of several hundred kpsi of tensile load. However, their rigid design means that they cannot be easily wound around a fiber spool and are difficult to accommodate inside a small fiber device housing.

Heat shrinkable splice protector tubes must be slipped onto one of the fiber tips prior to splicing. Once the splice is completed, the tube is then slid back over the spliced region and after a few minutes of gentle heating contracts around the fiber including the coated fiber far from the splice. These heat shrink splice protectors typically include a rigid metal pin to act as a strength member. Many commercial fusion splicers include a special heating oven for

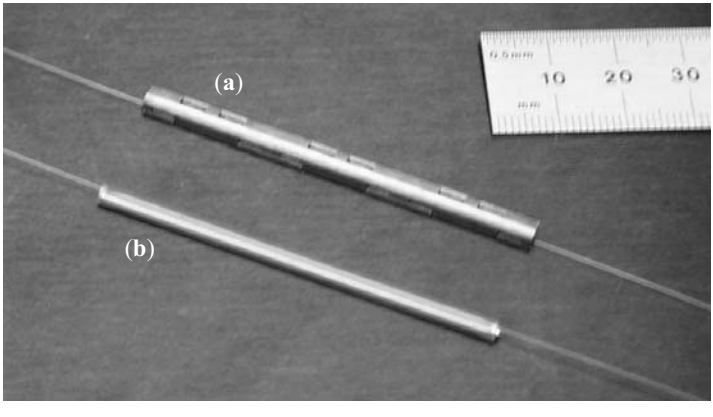

Fig. 6.9. Two examples of typical fusion splice protectors: (**a**) *ULTRAsleeve*^{TM} rigid clam-shell style splice protector and (**b**) typical heat-shrinkable fusion splice sleeve containing a metal splint. These splice protectors are rigid and cannot be readily wound around a fiber spool like a recoat. Fusion splice protectors like these are available in several lengths from 10 to 60 mm

curing the heat shrinkable splice protector. Heat shrink splice protectors are available for mass fusion splices as well [6.46, 6.47].

Recently, fusion splicer and splice protector manufacturers have sought to reduce the total length of stripped fiber required to perform a fusion splice so as to minimize the require length for rigid splice protectors. Shorter splice protectors yield smaller component packages by permitting tighter coiling radii. Splice protectors can be as short as 10 mm [6.15].

An alternative to heat shrinkable protectors are clam-shell designs that do not need to be prepositioned on the fiber prior to splicing. These clam-shell designs are typically fabricated from rigid plastic and fold down over the bare fusion splice and neighboring coated fiber regions to carry tensile loads across the splice joint and prevent bending or torsion.

6.7 Summary

The reliability of an optical fiber communication system depends on the reliability of the numerous fusion splices within the transmission cable and optical fiber components comprising the system. The main failure mode of an optical fiber fusion splice is a mechanical fracture. The likelihood of a fracture depends on the humidity of the ambient environment, the stress applied at the fusion splice, and the condition of the fiber surface in the vicinity of the fusion splice. The surface quality of an optical fiber fusion splice, and the resulting mechanical strength of the splice, can be maximized by minimizing damage to the fiber's surface when stripping the polymer coating from the fiber, or otherwise handling the fiber. Fire polishing the surface of a completed fusion splice can also improve its surface quality and therefore its reliability.

Fracture mechanics describes how the surface condition of an optical fiber interacts with applied stress to cause a fracture. The Weibull distribution and Weibull plots are useful tools for characterizing the mechanical strength of optical fiber fusion splices and can provide insights into the failure mode of fusion splices.

Proof testing is an important technique for ensuring the mechanical robustness and long-term reliability of an optical fiber fusion splice. Fracture mechanics and Weibull statistics can be combined to yield equations which predict the failure probability and service lifetime of a fusion splice exposed to a known tensile stress. Such equations can be used to determine the appropriate stress level for a fusion splice proof test.

Many splice packaging technologies are available for satisfying the various fusion splice packaging requirements. Recoating restores a flexible polymer coating in place of the original, stripped, coating and relies on the splice joint itself for mechanical strength. Recoated splices can be wrapped around spools and coiled in tight loops to facilitate packaging the splice. Rigid splice protectors employ a splint to transfer axial, torsional, and bending loads across the splice joint.

7. Splice Measurement and Characterization

As we have seen, the quality of a fusion splice depends on a variety of characteristics such as mechanical strength, reliability, reflectance, and transmission loss. In this chapter we review technologies for measuring the optical quality of a fusion splice. Since the optical transmission loss of a fusion splice is almost always its most important performance characteristic, it is the most commonly performed fusion splice measurement. Some of the measurement technologies we discuss are specific to fusion splicing, but most are general optical fiber measurement techniques that can also be applied to other types of optical fiber interconnections, such as connectors.

The choice of measurement technology depends upon the type of fusion splice. Sophisticated measurements for understanding fusion splice loss, such as spatially-resolved index profiling or optical low-coherence reflectometry (OLCR), might be useful in a research laboratory, but are inappropriate for characterizing fusion splices during assembly and installation of an optical fiber cable in the field. In contrast, an optical time-domain reflectometer (OTDR), is preferred for such field splicing situations since they can efficiently characterize fusion splices during field installation, even from a remote location many kilometers from the fusion splice. In a factory or production environment, insertion loss or cutback type measurements often offer the best compromise between speed, accuracy, and cost.

Mechanical proof testing is a common approach for measuring the mechanical integrity and long-term reliability of a fusion splice. Both the theory and practical implementations of mechanical proof testing have already been discussed together in Chap. 6. Polarization crosstalk and polarization extinction ratio are important factors controlling the optical quality of polarization-maintaining (PM) fiber fusion splices, and they are discussed in Sect. 9.2.

Often the reduction in signal power associated with fusion splice loss is not the only concern. In certain cases, the "lost" signal power can itself have deleterious effects. Most optical fibers are manufactured with a polymer coating whose refractive index is higher than that of the cladding glass, so that the energy lost from the waveguiding core is stripped out into the polymer coating. When a fusion splice conducts extremely high optical powers, for example in the case of an optical fiber laser or amplifier, the optical energy dissipated into the fiber's coating can cause localized heating and damage, even including fiber breakage. Furthermore, certain specialty single-mode fibers

are manufactured with a low refractive index coating that deliberately traps optical energy in the cladding. In this case, energy lost from the core of the fiber can be guided by the low-index polymer coating in the fiber's cladding for long distances. When this cladding energy is recoupled into the fiber's core, modal noise can result.

It is worthwhile to consider some fundamental measurement concepts. All measurements include some amount of *error*, which is the difference between the actual and measured value. *Systemic error*, also known as *bias error*, is an error whose magnitude and direction are repeated from one measurement to the next. As its name suggests, *random error* varies with each measurement, and truly random error can be reduced by averaging many repeated measurements. The *uncertainty* associated with a measurement is an estimate of the magnitude of the measurement error. There are mathematical rules for computing the uncertainty of a quantity that is calculated from several separate measurements, each with their own uncertainty [7.1].

The *precision* and the *accuracy* of a measurement are distinct concepts. Precision refers to the variation in the measured value observed when repeating the same measurement many times. An accurate measurement is a measurement in which the error is small. Thus, a precise measurement can also be inaccurate. When a manufacturer specifies the accuracy of a measurement device, they are typically referring to the maximum error expected between the true and measured value [7.1].

Excellent general reviews of optical fiber measurements are available in [7.2,7.3]. In addition to a general review of optical fiber measurements, [7.4] also contains an excellent discussion of contemporary equipment used to perform measurements of optical fibers and fusion splices, including various sources and detectors. We begin this chapter with a discussion of transmission measurements followed by a discussion of reflection measurements. We conclude with a discussion of refractive index profiling.

7.1 Transmission Measurements

As its name suggests, transmission measurements of fusion splices measure optical energy that is transmitted across a fusion splice. Transmissive measurements usually require access to both ends of an optical fiber span, although light-injection and detection (LID), introduced in Sect. 2.3.4, does not have this requirement [7.5]. In this section we will review insertion loss and cutback measurements, as well as spectral measurements and special approaches for measuring fusion splice loss between dissimilar fibers.

7.1.1 Insertion Loss and Cutback Measurements

Among the most common methods to measure fusion splice loss in the laboratory are *insertion loss* and *cutback* measurements. Both of these measurement

schemes consist of a calibration step and a measurement step (Fig. 7.1), and differ only in the order in which these steps are executed. Calibration is performed first during insertion loss measurement (since the splice is "inserted") whereas measurement is performed first during the cutback measurement (since the fiber is "cutback" to excise the splice). The splice loss, Γ_{splice} can be expressed in dB units as (compare with (4.1))

$$\Gamma_{\text{splice}} = 10 \log_{10} \frac{P_{\text{cal}}}{P_{\text{meas}}}, \tag{7.1}$$

where P_{meas} and P_{cal} are the powers measured during the measurement and calibration stages, respectively. Since the optical power measured during calibration must exceed that during measurement, Γ_{splice} will be a positive number.

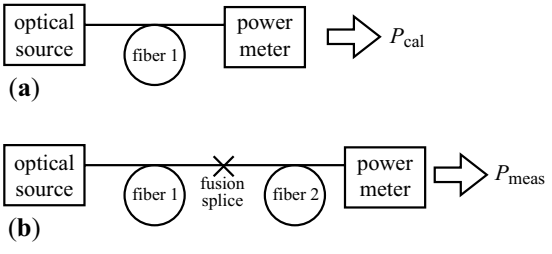

Fig. 7.1. Insertion loss and cutback measurements. Figure depicts (**a**) calibration stage and (**b**) measurement stage. In a cutback measurement the measurement stage is performed first while in an insertion loss measurement the calibration is performed first. Adapted from [7.6]

Several factors can reduce the accuracy of insertion loss and cutback measurements. Firstly, the optical power emitted by the source and the responsivity of the detector may vary slightly during the time between calibration and measurement. This error may be estimated my monitoring the stability of the power measured during the calibration stage. Most temperature-controlled laser diode (LD) and light-emitting diode (LED) sources as well as most power meters are found to exhibit variations on the order of 0.01 dB or less during the relatively short timescales of insertion loss and cutback measurements. However, if the calibration is performed only once and many splice loss measurements are performed sequentially, the source or the detector may drift by a substantial amount, so the stability of the source and the detector can be important considerations.

Ideally the power meter captures and measures all of the optical signal during both calibration and measurement. The accuracy of both insertion loss and cutback measurements is reduced if the power meter does not register all of the emerging optical power and this effect can be quantified by comparing the variation in measured power when a fiber tip is repeatedly reconnected to

the optical power meter. This variation is usually about 0.1 dB. An *integrating sphere* can help to capture all of the power in the fiber. Since the variation observed when reconnecting an optical power meter is usually much less than the variation when reconnecting an optical source to a fiber, insertion loss and cutback measurements nearly always involve reconnecting the power meter rather than the source.

When the goal is to verify the splice loss or loss estimation performance of a particular fusion splicer, the calibration (Fig. 7.1a) can be performed on a single-continuous fiber, which can then be broken and respliced at a single location. Since the power meter and source need not be disconnected or reconnected, this is a particularly accurate method for measuring fusion splice loss, providing the source and detector are stable over time. However, this approach is not practical for assembling a fiber span or a fiber device from individual lengths of fiber.

The loss in an optical fiber also depends on local bends and twists in the fiber. Ensuring that the optical fibers are not inadvertently tangled, kinked, or bent through a tight radius is important when striving for accurate loss measurements. Clamps and fixturing equipment must not grip too tightly on the fibers or they will induce loss as well. Conventional single-mode fiber should be arranged in neat loops at least 7 cm in diameter, whereas specialty fibers may require much larger loop diameters, especially if they are known to have elevated bend loss.

Most optical fibers are coated with a polymer whose refractive index is higher than that of the cladding and so they effectively strip out of the cladding any energy lost at a fusion splice. In the case of such conventional high-index coatings, single-mode fiber splices should be separated by a minimum of several cm of coated fiber to ensure that any energy lost at the fusion splice is stripped out into the coating before interacting with a subsequent fusion splice and resulting in modal noise (Sect. 4.2.4). Certain specialty optical fibers have a low-index coating that traps light in the cladding so that optical energy lost from the core at a fusion splice remains in the cladding and can corrupt cutback or insertion loss measurements. In these special cases, the optical energy lost at the fusion splice must be stripped out of the cladding by surrounding it with a high-index medium (such as index oil or gel) downstream of the fusion splice.

Accurate measurement of multimode fusion splices pose additional challenges since the splice loss can depend on the amount of energy populating the various modes of the fiber. In such a case we are usually interested in the fusion splice loss when the modal intensities are in equilibrium (also termed a steady-state modal distribution), which can be achieved by ensuring the launching fiber in Fig. 7.1 is very long (multiple kilometers). Unlike single-mode fiber fusion splice loss, which cannot depend on propagation direction (Sect. 4.1.3), the fusion splice loss of multimode fibers *can* depend on propagation direction, especially when fusion splicing dissimilar multimode fiber types.

7.1.2 The "Pre-Splice" Technique

The fiber itself can be a source of uncertainty in the measurement. Most transmission fibers experience a signal attenuation on the order of a few tenths of a dB per km in the near infrared telecommunications bands of 1310 and 1550 nm. Thus, if fiber 2 in Fig. 7.1b is a low-loss transmission fiber with a length on the order of a hundred meters or more, the effect of the fiber's attenuation will be on the order of several hundredths of a dB and must be subtracted from the splice loss computed in (7.1) to yield a high-accuracy measurement. When the attenuation in fiber 2 cannot be computed to high accuracy, or when the output end of fiber 2 is located a long distance from the fusion splice, such as during optical fiber cable installation, the "pre-splice" approach can be used. Alternatively, an optical time-domain reflectometer (OTDR), which is described later in Sect. 7.2.2, can be used to measure fusion splice loss from a remote location.

The pre-splice technique involves the fabrication of a temporary splice between Fibers 1 and 2 and is graphically depicted in Fig. 7.2. First, the power transmitted by Fiber 1 alone, P_{cal1}, is recorded (Fig. 7.2a). Then a temporary splice (mechanical or fusion) is made between the fibers and the total transmitted power, P_{cal2}, is measured at the output of fiber 2 (Fig 7.2b). When the output of Fiber 2 is a long distance from the splice location, a separate power meter can be used to measure this power. Next, Fiber 2 is broken a short distance downstream of the temporary presplice and the power there, P_{cal3}, is measured (Fig 7.2c). Finally, the temporary presplice is broken and Fibers 1 and 2 are connected with a permanent fusion splice. The total transmitted power, P_{cal4}, is measured at the output of Fiber 2 and the fusion splice loss, Γ_{splice}, is then given in dB by [7.7]

$$\Gamma_{\text{splice}} = 10 \log_{10} \left(\frac{P_{\text{cal1}} P_{\text{cal2}}}{P_{\text{cal3}} P_{\text{cal4}}} \right) . \tag{7.2}$$

The optical attenuation of fiber 2 as well as any differences between the two power meters are cancelled out and do not contribute to the measured splice loss.

7.1.3 The Two-Splice Technique

When the error introduced by reconnecting the optical power meter between the calibration and measurement stages of a cutback or insertion loss measurement is too high, the two-splice insertion loss measurement can serve as an alternative. The two-splice approach is depicted in Fig. 7.3 [7.8].

The calibration step, which must be performed first, is identical to that of a conventional insertion loss measurement. Once the calibration power is recorded, fiber 1 is deliberately broken some distance away from the power meter so that a length of a second fiber can be inserted into it with two fusion splices. Once again, any additional loss resulting from the added portion of

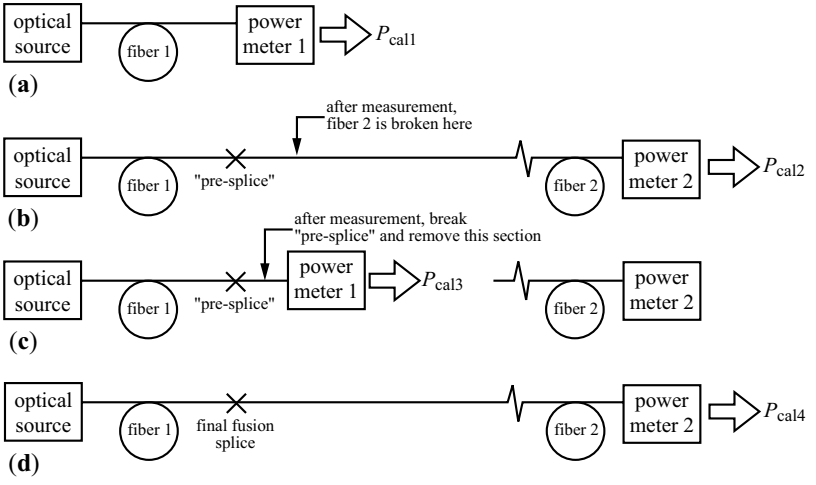

Fig. 7.2. The "pre-splice" approach for measuring splice loss when the attenuation in the fiber is unknown. In (**a**), the power transmitted by Fiber 1 alone, P_{cal1}, is measured. Following this, (**b**), a "pre-splice" is used to connect Fiber 1 to Fiber 2 and the total transmitted power P_{cal2} is recorded. Next, (**c**), Fiber 2 is broken a short distance downstream of the pre-splice and power P_{cal3} is measured there. Finally in (**d**), the pre-splice is broken apart and Fiber 1 is permanently fusion spliced to the main portion of Fiber 2. The total transmitted power P_{cal4} is recorded and the fusion splice loss is computed with (7.2). The figure shows two distinct power meters, which are convenient during optical fiber cable installation, but it should be clear that in the laboratory or factory environment, a single power meter can be used. Adapted from [7.7]

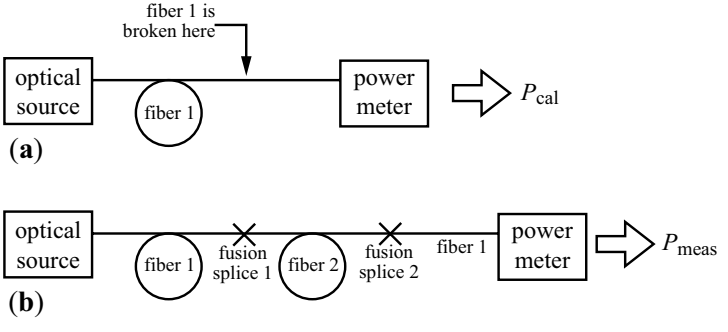

Fig. 7.3. Schematic illustration of the two-splice loss measurement technique showing (**a**) calibration and (**b**) measurement

fiber 2 must be accounted for. The need for an extra fusion splice is an obvious disadvantage of this technique, but at least it avoids the need to disturb either the launch or detection arrangement.

7.1.4 Spectral Splice Loss Measurements

The wavelength dependence of fusion splices can be an important parameter, such as when the splice will be utilized in a wavelength-division-multiplexed (WDM) telecommunications system. The origins of wavelength dependent loss in single-mode fiber fusion splices are discussed in Sects. 4.2.2 and 5.2.3. The wavelength dependent loss of a fusion splice can be measured by using a narrow wavelength tunable source with a broadband detector, or by using a broadband source and a wavelength sensitive detector following the arrangements depicted in Figs. 7.1–7.3.

An optical spectrum analyzer (OSA) is a wavelength sensitive detector that allows the operator to set the wavelength range and resolution of the measurement. Increasing the wavelength resolution results in lower sensitivity and hence an inferior signal-to-noise ratio (SNR). Tungsten-halogen light bulbs, light-emitting diodes (LEDs), and amplified spontaneous emission (ASE) emitted by an erbium-doped optical amplifiers (EDFAs) can all serve as broadband light sources. An EDFA is a much brighter than either a tungsten-halogen bulb or an LED but also exhibits a much narrower spectrum, only about 35 nm wide. In contrast to the other two types of broadband sources, the emission of LEDs is typically somewhat polarized and exhibits spectral widths on the order of 75 nm [7.6]. A tungsten halogen lamp, unlike other sources, covers the entire visible and near-infrared wavelength range and can easily span the spectral distance between the 1310 nm and 1550 nm telecommunications windows but it produces a relatively weak signal. Special optical sources that incorporate both 1310 and 1550 nm laser diodes can be used to make splice loss measurements inside both transmission windows. A narrow-linewidth tunable laser can serve as a tunable source over a wavelength range of about 100 nm.

7.2 Reflection Measurements

As the name suggests, reflection measurements of fusion splices involve measuring reflected optical energy. Reflection measurements can assess both the transmission loss as well as the reflectance of a fusion splice. Reflective measurements can be attractive since in principle they only require access to one end of a fiber. However, as we shall see below, practical reflective measurements do sometimes require access to both ends of an optical fiber span.

A plethora of reflective measurement strategies have been developed over the years. Optical continuous wave reflectometers (OCWRs), also known as return-loss meters, are very common commercially available measurement instruments, but they cannot measure transmission loss, nor can they discriminate between individual sources of reflection, and they are not sensitive enough to measure the minute reflectance of most fusion splices. Optical time-domain reflectometers (OTDRs), which directly detect energy backscattered

from short-duration pulses, are by far the important commercially available devices for measuring optical fiber fusion splices. More sophisticated and more sensitive reflective measurements, such as optical frequency-domain reflectometers (OFDR) and optical low-coherence reflectometry (OLCR), are available commercially, but are only suitable for laboratory or production environments.

The reflectance of many high quality fusion splices is so low (below −110 dB) that even the most sensitive technologies, such as OLCR, are actually unable to measure it. The inherent Rayleigh backscatter in the fiber can reflect more power than high quality fusion splices. However, the reflectance of low quality fusion splices and low-temperature fusion splices, can sometimes be measured with OTDRs as well as by OFDRs or OLCRs. Even though the reflectance of many fusion splices is unmeasurable, a reflectance measurement may still be required to verify that a specific reflectance specification is satisfied.

An introduction to the reflection properties of optical fiber fusion splices was already provided in Sects. 4.1.5, 4.2.3, and 4.3.3. In addition to optical energy reflected by fusion splices, optical fibers also contain reflections from other interconnections such as mechanical splices or connectors, from other components such as optical fiber gratings, and from inherent Rayleigh backscatter that results from minute density fluctuations distributed throughout all optical fibers. At high optical powers, non-linear scattering such as Brillouin scattering [7.18] can also contribute to backreflected energy. The presence of so many sources for reflections make reflection measurement of optical fiber fusion splices more difficult.

An excellent general review of optical fiber reflection measurements is available in [7.17]. In this section we begin with a brief introduction to OCWRs followed by an extended treatment of direct detection OTDRs. We conclude with a description of two sophisticated high resolution reflection measurement devices that can be useful for measuring fusion splice reflectance, the OFDR and OLCR.

7.2.1 Optical Continuous Wave Reflectometers (OCWRs)

An *optical continuous wave reflectometer (OCWR)*, also termed a *return loss meter*, is a simple device which measures the return loss of an optical fiber span illuminated by a continuous wave signal (Fig. 7.4). *Return loss*, RL, is a measure of the total reflected optical power and by convention is expressed in dB units as [7.10]

$$\mathrm{RL} = 10 \log_{10} \left(\frac{P_{\mathrm{inc}}}{P_{\mathrm{refl}}} \right) \tag{7.3}$$

where P_{inc} is the total incident optical power and P_{refl} is the total reflected optical fiber. Because $P_{\mathrm{inc}} > P_{\mathrm{refl}}$ RL will always be greater than zero, unlike

reflectance, which was defined in (4.2) and is by convention always less than zero.

Since an OCWR does not spatially resolve the sources of reflection, the relative contribution of various reflection sources, such as connectors, mechanical splices, cleaved end faces, Rayleigh backscatter, and fusion splices, are indistinguishable. Fusion splices are typically among the weakest sources of reflection so OCWRs are usually not particularly useful for measuring fusion splice reflectance, but are included in this Section for the sake of completeness. OCWRs can measure reflectances down to approximately -70 dB [7.17], which is only sufficient to detect the most highly reflective fusion splices, such as low-temperature splices between very dissimilar fibers.

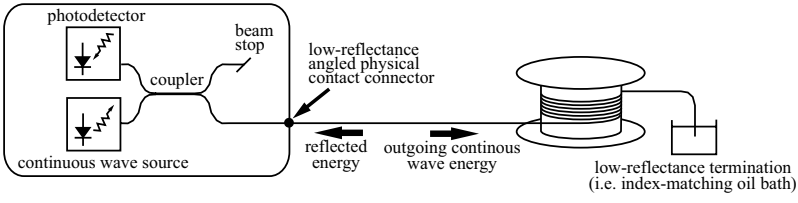

Fig. 7.4. Schematic illustration of an optical continuous wave reflectometer (OCWR). Note the low-reflectance angled physical contact connector connecting the device to the optical fiber span. The reflectance of such connectors is typically on the order of -80 dB, which overwhelms the minute reflectance of high-quality fusion splices. The inherent Rayleigh backscatter of moderate or long length (>500 m) optical fiber spans will also overwhelm the reflectance of nearly all fusion splices

7.2.2 Optical Time-Domain Reflectometer (OTDR) Measurements

An optical time-domain reflectometer (OTDR) sends short duration pulses into a fiber and directly detects the time-delayed backscattered signal. Unlike OCWRs, the time-resolved measurement of an OTDR enables it to identify the spatial location of a reflective event and thus discriminate between reflections resulting from fusion splices, Rayleigh scattering, or other sources. Moreover, unlike an OCWR, an OTDR can actually measure the transmission loss of a fusion splice. OTDRs can be effective for either single- or multimode fibers but since the backscattered signal from single-mode fibers is much stronger than that of multimode fibers, OTDRs are more versatile when applied to single-mode fibers.

OTDRs are particularly useful for troubleshooting and verifying the performance optical fiber spans. They are used to measure fusion splice loss in optical fiber transmission cables either before or after field installation since an OTDR can measure splice loss from a remote location many kilometers away. Although they are indispensable for the analysis of long lengths of

optical fibers and cables, OTDRs are more expensive than most individual optical sources and detectors and are not useful when analyzing short fiber lengths or fibers with many closely spaced splices or components. Figure 7.5 schematically illustrates the components of a typical OTDR.

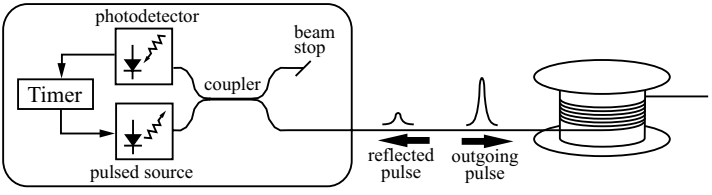

Fig. 7.5. Schematic illustration of an optical time-domain reflectometer (OTDR). Adapted from [7.4]

Figure 7.6 illustrates several features commonly observed in a single-mode OTDR measurement trace. The trace decays nearly monotonically and is expressed in dB units as a function of distance in the fiber span, although it is actually acquired as a function of time. The velocity of an optical pulse in the fiber, termed the group velocity, relates the time delay to the location of the source of the reflection. The group velocity of light in a fiber can be approximated to within a couple of percent accuracy by c_{light}/n where c_{light} is the speed of light in a vacuum and n is the refractive index of silica at the relevant wavelength [7.9]. Since the optical fibers included in telecommunications cables generally include some amount of slack inside the cable, the actual physical location of features observed in an installed optical fiber cable are slightly closer than the OTDR measurement would suggest [7.3].

Even though the OTDR sends out discrete pulses, it receives a continuous stream of backscattered pulse energy resulting from the normal Rayleigh scattering distributed throughout an optical fiber. This Rayleigh scattering is usually the main contributor to optical signal attenuation in the 1550 nm telecommunications transmission window. The strength of the detected backscattered signal depends on the pulse width, τ_{pw}, and is quantified by the backscatter factor, R_{bs}, which can be expressed as [7.10]

$$R_{\text{bs}} \equiv 10\log_{10}\left(\frac{P_{\text{inc,local}}}{P_{\text{refl}}}\right) = R_{\text{bs,1 }\mu\text{s}} + 10\log_{10}\left(\frac{1\,\mu s}{\tau_{\text{pw}}}\right) \tag{7.4}$$

where $P_{\text{inc,local}}$ is the local forward propagating power in the pulse (not the originally launched optical power), P_{refl} is the locally backreflected optical power, and $R_{\text{bs,1 }\mu\text{s}}$ is the backscatter factor for a 1 µs pulse width, which is about 48 dB for conventional SMF.

The fiber attenuation manifests itself as the slope of they decay in the detected backscattered signal strength. Conventional SMF usually exhibits an attenuation on the order of 0.25 dB/km at 1550 nm. Specialty low-loss transmission fiber can be as low as 0.16 dB/km, while other specialty fibers such

as dispersion-compensating fiber (DCF) can exhibit attenuation in excess of 0.5 dB/km. An optical fiber span can be composed of several fiber types so the decay slope can vary along the fiber length as depicted in Fig. 7.6.

The optical detector in an OTDR will be saturated by strong back reflections resulting in a *dead zone*. Depending on the response time of the optical detector, this dead zone can hide details from nearby portions of the measured trace. For example, the dead zone in the vicinity of an optical fiber connector, which is usually present at the input to an OTDR, can exceed 50 m. For this reason, a long pigtail of fiber is usually fusion spliced to the span to be tested in order to ensure that the connector at the OTDRs input does not interfere with the measurement.

Since most of the noise in an OTDR trace is randomly distributed, averaging many traces over a long period of time can significantly improve the precision of a measurement. The maximum fiber length measurable with an OTDR is controlled by the dynamic range of the OTDR, as well as by the backscatter strength and attenuation in the fibers. The dynamic range is the ratio in power between the initial backscatter level and the background noise, which can be improved with several minutes of trace averaging [7.10]. The larger the dynamic range, the further the distance the OTDR can probe.

If the fiber span measured by an OTDR contains relatively strong reflectors, such as highly reflecting connectors or a perpendicularly cleaved fiber at the end of the span, echoes resulting from multiple reflections can produce spurious "ghost" features in the OTDR trace [7.10]. This problem can be eliminated by ensuring that all the interconnections in the span exhibit reasonably low reflectances (<-40 dB). Reflections from the fiber end face at the end of the span can be reduced with an angled cleave (8° for conventional SMF) or by immersing it in index matching oil.

Amplifier fibers, such as erbium-doped fiber (EDF), exhibit extremely high signal absorption (> 100 dB/km) in their amplification band when there is no pump energy present. Moreover, unlike transmission fibers, the signal absorption can be non-linear with distance. For these reasons, OTDRs are not effective for measuring fusion splice loss in the amplification band of amplifier fibers. However, OTDRs can be designed to operate at a variety of wavelengths including 850, 1310, and 1550 nm, so they can be applied outside of the amplification band, for example at 1310 nm for EDF. Even so, the real strength of an OTDR is its ability to remotely measure splice loss from a long distance away. This capability is usually not needed when testing or characterizing EDF spans that are typically less than 10 m long.

OTDR Splice Loss Measurement. Measuring fusion splice loss between similar or identical fibers is relatively straightforward. A line is fit to the backreflected trace before and after the fusion splice using a least-squares fit as shown in Fig. 7.7a and the difference between the vertical position of these two lines directly reveals the fusion splice loss. However, measuring splice loss

between dissimilar fibers with an OTDR requires either consideration of the fiber properties or a bi-directional measurement.

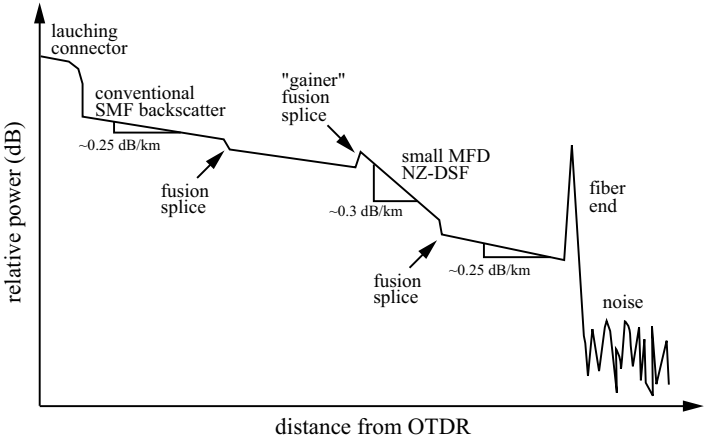

Fig. 7.6. Illustration of several typical features in an OTDR measurement trace of a section of small mode field diameter (MFD) non-zero dispersion-shifted fiber (NZ-DSF) fusion spliced between two sections of conventional single-mode fiber (SMF). Figure not to scale

The strength of the backscattered signal depends not only on the pulse width, but also upon the mode field diameter (MFD) of the fiber. A smaller MFD in a single-mode fiber leads to a stronger backscattered signal for several reasons. Firstly, a smaller MFD exhibits a larger numerical aperture (NA), so the fiber's core captures a larger fraction of the Rayleigh scattered photons. Secondly, the core of smaller MFD fibers usually have a larger core Δ resulting from higher dopant concentrations that also lead to larger amounts of Rayleigh scattering (and more signal attenuation) [7.3, 7.10].

Since the strength of the backreflected signal depends upon the MFD of a single-mode fiber as well as upon the strength of the forward propagating pulse, the measurement trace of an OTDR does not necessarily decline monotonically with distance. As shown in Fig. 7.6, the backreflected signal received by an OTDR can actually *increase* when a smaller MFD fiber is situated downstream of a larger MFD fiber. When the MFD discrepancy is large enough, the apparent fusion splice loss can be a negative number, also termed a *gainer*. Of course, there is no real gain at the fusion splice, and this effect is merely an artifact of the discrepancy between the MFDs. Similarly, when a smaller MFD fiber is followed by a larger MFD fiber, the apparent splice loss can be much larger than the actual splice loss due to the difference in backscattered signal. If the fiber characteristics are known, these effects can be corrected to reveal the true splice loss. The difference in backreflected

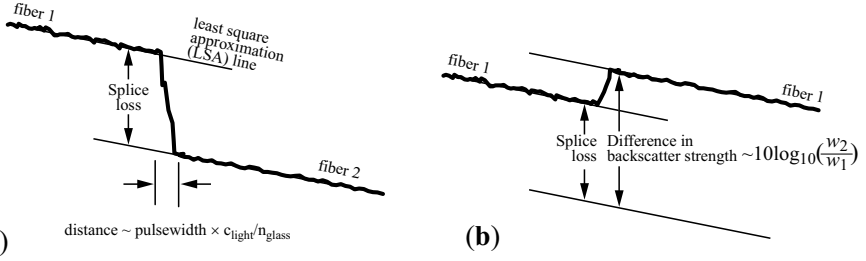

Fig. 7.7. Detailed depiction of fusion splice loss measurement with OTDR between (**a**) similar fibers and (**b**) dissimilar single-mode fibers. In (**b**) the second fiber's MFD is smaller than the first so that the fusion splice is a gainer in which the apparent splice loss is shifted by (7.5). Adapted from [7.3, 7.10]

signals between two dissimilar fibers, Δ_{bs}, at a fusion splice can be expressed as [7.11]

$$\Delta_{\mathrm{bs}} = 10 \log_{10} \frac{w_2}{w_1} , \tag{7.5}$$

where $2w_1$ and $2w_2$ are the MFDs of the first and second fibers, respectively. When conventional SMF exhibiting a MFD of about 10.5 μm is fusion spliced to a non-zero dispersion-shifted fiber (NZ-DSF) exhibiting a MFD of about 9 μm, the mode field mismatch can lead to several tenths of a dB difference in backscattered signal, which can easily overwhelm the actual fusion splice loss since it is typically only about 0.1 dB in high-quality fusion splices between such fibers. Even nominally similar fibers can have small discrepancies in MFD, on the order of a few hundred nanometers, which when substituted into (7.5) yields backscatter differences on the order of 0.1 dB. Instead of using (7.5), the difference in backreflection between dissimilar fiber types can also be empirically measured and then used as a correction factor [7.12].

The most common solution to the problem of MFD-dependent backreflection is to measure the apparent splice loss from both directions, and then average the results to obtain the true value. Measuring fusion splice loss from both directions can be inconvenient since it requires access to both ends of an optical fiber cable span, which may be separated by tens of km. Some investigators have developed probabilistic descriptions of fusion splice loss that can be used to estimate the true splice loss from single-direction measurements when the total span loss rather than the individual fusion splice losses are of primary interest [7.11, 7.13]. Alternatively, a single OTDR attached to one end of a fiber span can be used to acquire bi-directional data when the other end of the fiber is highly reflecting (for example coated with a metallic layer) [7.14, 7.15].

The duration of the pulse and the bandwidth of the backscattered light detection system controls the spatial resolution of the OTDR, which in turn controls its ability to discriminate between neighboring fusion splices [7.9].

A typical 1 μs pulse width will yield a spatial resolution on the order of 300 m. Pulses can be as short as 10 ns, which corresponds to a spatial resolution as fine as a few meters of fiber. However, shorter pulses carry less optical energy so they result in weaker signals and lower signal-to-noise ratios (SNR). When two fusion splices are within a few meters of each other, most OTDRs will be unable to discriminate between them, so the measured splice loss will be the sum of both fusion splices. For this reason, elevated loss detected in the vicinity of a fusion splice may not be due to the fusion splice itself, but could be caused by a nearby fiber break or kink. Unlike fusion splices or fiber breaks, fiber bends or kinks normally exhibit strong wavelength dependent loss so a multi-wavelength OTDR can be used to discriminate between these features [7.3]. The limited spatial resolution of OTDRs mean that they are not useful for measuring fusion splice loss in optical fiber spans containing a large number of closely situated splices or components, such as in a local area network (LAN) or inside an optical fiber device such as an erbium-doped fiber amplifier (EDFA).

OTDR Reflectance Measurement. The spatial resolution of an OTDR can make it relatively easy to identify the reflectance of individual fusion splices separated by hundreds of meters or more. However like an OCWR, the minimal detectable reflectance of an OTDR is limited to about -75 dB [7.20] so only the most strongly reflecting fusion splices, such as low-temperature fusion splices, can be measured. If the temporal profile of the OTDR's pulse shape can be approximated as a rectangle, then the reflectance of an individual fusion splice can be related to the difference between the background Rayleigh scattering and the height of the reflected signal at the fusion splice, δ_{refl}, with [7.10, 7.21]

$$R_{\text{splice}} \approx -R_{\text{bs}} + 10 \log_{10} \left(10^{0.2\delta_{\text{refl}}} - 1\right) \tag{7.6}$$

where the backscatter factor, R_{bs}, is given by (7.4) and δ_{refl} is expressed in dB units. Note that δ_{refl} must be measured with respect to the background Rayleigh scattering of the trace on the side closer to the OTDR.

Figure 7.8 shows the application of (7.6) to estimated the reflectance of a low-temperature fusion splice between two dissimilar fibers, a conventional matched clad SMF and a pure-silica core depressed-clad SMF. The refractive index difference between the cores and the claddings of these two fibers is estimated to be about 0.005, so the reflectance of a fusion splice between these two fibers is expected to be at most -55 dB using (4.40) and Fig. 4.6. After a low-temperature fusion splice, δ_{refl} is found to be about 0.7 dB and since R_{bs} is about -48 dB/μs, R_{splice}, is estimated to be about -62 dB using (7.6). Reheating the fusion splice at splice temperatures for just a few seconds reduces the reflectance below the instrument's detection limit (about -70 dB) because dopant diffusion smoothes out the refractive index transition at the fusion splice joint between the two fibers (Sect. 4.1.5).

When the magnitude of the computed reflectance is on the same order or smaller than the magnitude of the inherent Rayleigh backscatter factor, R_{bs},

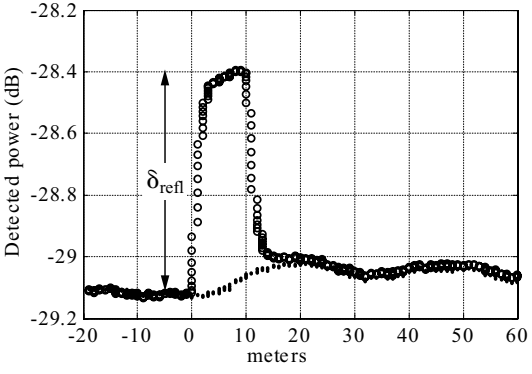

Fig. 7.8. Example of OTDR reflectance measurement of a fusion splice between a matched clad conventional SMF and a pure-silica core depressed-clad SMF using a 100 ns pulsewidth at 1310 nm. The detected signal following a low-temperature fusion splice (*open circles*) is directly compared to the detected signal following a few extra seconds of reheating at splice temperatures (*solid points*). The difference between these two traces is primarily due to the reflectance of the fusion splice joint. The physical appearance of the fiber corresponding to both traces is shown in Fig. 8.6. The height of the low-temperature fusion splice reflectance above the background signal, δ_{refl}, is about 0.7 dB and since the inherent backscatter of the matched clad SMF, R_{bs}, is around -48 dB/μs, the reflectance of the low-temperature fusion splice, R_{splice}, is estimated to be about -62 dB using (7.6). Since there is no detectable δ_{refl} for the fusion splice following the reheat, its reflectance is below the detection sensitivity of the OTDR, so it is <70 dB. Note that δ_{refl} must be measured with respect to the background Rayleigh scattering on the side closer to the OTDR, and as this figure shows, the background Rayleigh scattering can be very different on both sides of the splice. Figure adapted from [7.10]

as is the case in Fig. 7.8 where the inherent Rayleigh backscatter of the 100 ns pulse is about 58 dB, the reflectance measurement will be less accurate. Equation (7.4) shows that R_{bs} is substantially reduced when the pulsewidth, τ_{pw}, is reduced. However, very short pulsewidths result in weaker pulses and thus a weaker SNR. Furthermore, at very short pulsewidths the finite bandwidth of the optical detector can distort the amplitude of discrete reflections [7.10]. Thus, direct detection OTDRs capable of producing pulsewidths as short as 10 ns, which is predicted to have a backscatter factor of about 68 dB using (7.4), usually cannot accurately measure fusion splice reflectances when they are below about -65 dB.

7.2.3 High Resolution Reflection Measurements

Commercial OCWRs and direct detection OTDRs are widely available but are not sensitive enough to measure the reflectance of most fusion splices. More sophisticated measurement techniques, including photon-counting optical time-domain reflectometry, coherent optical time-domain reflectometry,

optical frequency-domain reflectometry, and optical low-coherence reflectometry, can measure very weak levels of reflectance with extraordinary spatial resolution. In this section we will briefly introduce optical frequency-domain reflectometers (OFDRs) and optical low-coherence reflectometers (OLCRs), which have recently become commercially available. Application of these strategies are largely limited to the laboratory environment, although some of the commercial instruments may be suitable for a production environment. General reviews of a variety of high-resolution reflection measurements are available in [7.17, 7.22, 7.23].

Fig. 7.9 schematically depicts an OLCR containing a Michelson interferometer constructed using a low-coherence (broadband) optical source. The interferometer contains a sample arm, which includes the fiber being tested, and a reference arm, which contains a reference length of fiber, L_{coil}, terminated with a movable mirror. The coherence length of the source is chosen to be so low ($\sim$10 µm) that the optical interference fringes seen by the photodetector exclusively result from optical energy reflected by features in the sample arm whose optical distance from the source is within a few microns of the total optical path length of the reference arm. The total length of fiber sampled by the OLCR is limited, but the moving mirror generally allows the OLCR to scan through on the order of 10 cm of fiber. For this reason, the length of the reference arm must be carefully controlled to ensure that it will permit the OLCR to probe the section of fiber in the sample arm containing the fusion splice in question. OLCR is noted for remarkable spatial resolution, on the order of 2 µm, which permits OLCR to discriminate between closely spaced components or interconnections. Furthermore, OLCR achieves extraordinary sensitivity and can detect reflectance values as low as -150 dB [7.17], which is low enough to measure most fusion splices. OLCR has been used to show that the reflectance of high quality fusion splices between conventional SMF and erbium-doped fiber (EDF) are below -110 dB [7.19].

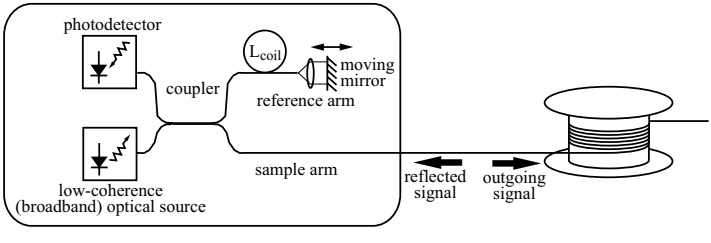

Fig. 7.9. Schematic illustration of a OLCR in which a Michelson interferometer in combination with a low-coherence (broadband) optical source and a movable mirror is used to spatially resolve the sources of reflection in an optical fiber span. L_{coil} refers to the length of the fiber in the reference coil. After [7.17]

OFDRs can be divided into two categories: coherent and incoherent, and it is the coherent version that provides the high resolution and high sensitivity

necessary for measuring the reflectance of optical fiber fusion splices. Fig. 7.10 schematically depicts an OFDR containing a Michelson interferometer constructed using a chirped narrow-linewidth laser source. The chirp applied to the laser frequency ensures that optical interference between the reference and sample arms has a beat frequency that is proportional to the time delay between the signals returning from the sample and reference arms [7.17]. An OTDR-like trace indicating reflectivity as a function of distance can be generated from the Fourier transform of the detected signal. The spatial resolution of OFDR is on the order of 10 μm, which is about an order of magnitude inferior to OLCR, whereas the measurement range is about 10 m [7.17], which is substantially higher than OLCR. The minimum measurable reflectance of a coherent OFDR is on the order of -150 dB, which is comparable to OLCR.

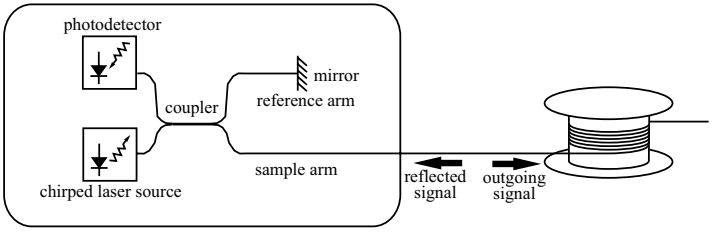

Fig. 7.10. Schematic illustration of a coherent OFDR in which a Michelson interferometer in combination with a linearly chirped laser source. After [7.17]

7.3 Refractive Index Profiling of Fibers and Fusion Splices

The optical characteristics of a fusion splice are entirely determined by the refractive index profile of the optical fibers in the vicinity of the splice. Consequently, understanding the refractive index profile of a fusion splice can be helpful during splice optimization of difficult fusion splices, such as those between dramatically dissimilar fiber types. Refractive index profiling is particularly useful for measuring and understanding transition splice loss, which was described in Sect. 4.2. When excessive fusion splice loss cannot be ascribed to core deformation, poor cleaves, or poorly optimized fusion splice parameters, refractive index profiling can be an effective diagnostic tool. However, refractive index profiling of fusion splices is a tedious and complex process that is not applicable to field or even factory fusion splicing, and is only practical in the laboratory.

In Sect. 4.4 we showed how the beam propagation method (BPM) can be used to numerically compute how an axial variation in refractive index profile affects a propagating signal. In Sect. 5.2 we showed how coupled-mode theory

(CMT) can be used to compute the effect of core deformation on fusion splice loss. In this section, we describe how to obtain measurements of the fiber's refractive index profile in the vicinity of the splice that can subsequently be used in conjunction with either CMT or BPM to estimate the optical characteristics of fusion splices.

Several different approaches for measuring the refractive index profile of optical fibers have been developed, including the refracted near field (RNF) [7.2,7.9,7.16], the transmitted near field (TNF) [7.2,7.9,7.16], the focusing method [7.2,7.9], and the transverse interferometric method (TIM) [7.2]. RNF is the dominant commercial approach for measuring the refractive index of optical fibers. However, both RNF and TNF are destructive measurements in the sense that they require access to a cleaved end of the optical fiber. Moreover, both RNF and TNF measurements average the refractive index over a length of several hundred microns in the vicinity of the cleave. This is a disadvantage when analyzing fusion splices where large variations in the fiber's refractive index profile occur within a few hundred microns of the fusion splice joint due to dopant diffusion (Sect. 3.3), viscous deformation (Sect. 3.2), or stress relaxation (Sect. 3.4).

Although they are not commercially available, the focusing method and TIM, are nevertheless attractive because they can non-destructively measure fiber index profiles in the immediate vicinity of a fusion splice. Individual measurements can be made on axial segments of fiber as thin as 50 microns, so axial variations in the refractive index profile due to dopant diffusion, viscous deformation, or stress relaxation can be measured in the vicinity of a splice. Refractive index profiles measured by TIM or the focusing method can be fed into CMT, BPM, or another numerical algorithm to predict the optical characteristics of a fusion splice. TIM is preferred due to its superior accuracy and so it will be detailed here.

TIM is accomplished with the aid of an interferometer that measures the optical path length difference experienced by light rays traversing an optical fiber (Fig. 7.11a). Probe light is divided by a beam splitter into two beams, one of which passes transversely across the fiber, which is immersed in index matching oil to minimize refraction, while the other beam passes through an empty bath of identical index matching oil. A beam splitter recombines these two beams into a single beam that is imaged onto a CCD camera yielding an interferogram. By adjusting the optical elements in the interferometer, the light and dark bands, termed *interference fringes*, can be made to run transversely across the image of the fiber as shown in Fig. 7.11b.

The relative shifts in the bright and dark bands of the interferogram are detected by a computer and can be directly related to the optical path length. A computer implementing the Abel integral transform reconstructs the fiber's refractive index profile from the detected fringe shifts. Details concerning the algorithm relating the fringe shifts to the fiber index profile are described in [7.2]. Note that because of a typo, the final plus sign in equation (4.5-25) of [7.2] should in fact be a minus sign.

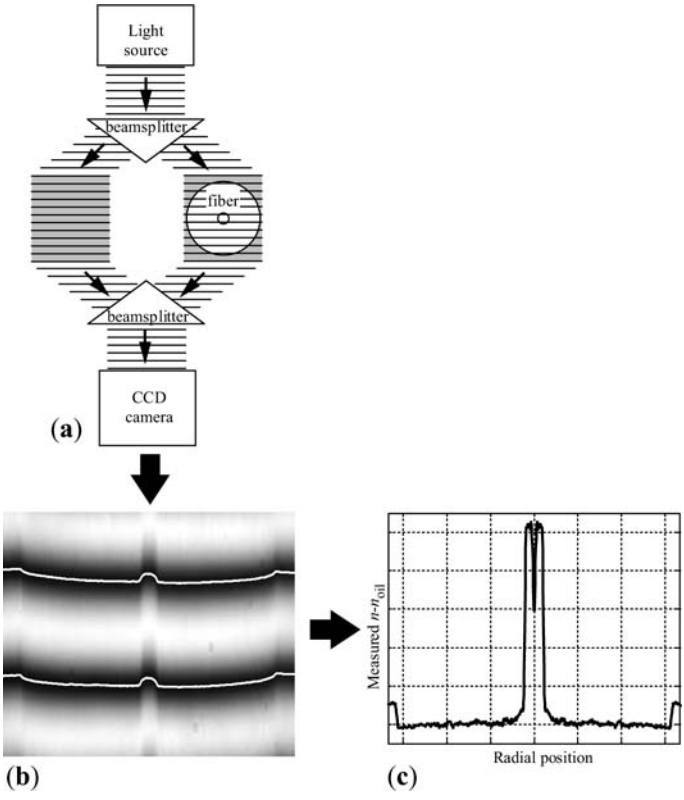

Fig. 7.11. Schematic illustration of refractive index profiling using the TIM method. The shading in each arm of the Mach-Zehnder interferometer depicted in (**a**) shows the location of refractive index matching oil. The parallel lines indicate the phase fronts of the probing light while the arrows indicate light propagation direction. In the interferogram, (**b**), heavy white lines overlaid on the dark fringes indicate computer-detected fringe positions. The shift in the detected fringe positions can be related to the optical path length, which is converted into the refractive index profile depicted in (**c**)

By axially translating an optical fiber fusion splice across the field of view of the interferometer, the refractive index profile can be measured as a function of distance from the fusion splice. In this way, axial variations in a fiber's index profile can be nondestructively measured and combined with numerical techniques such as BPM or CMT to estimate splice loss and mode coupling effects.

The algorithm described in [7.2] to extract the refractive index profile from the interferogram assumes that the light rays traversing the fiber are not refracted by the relatively small refractive index differences encountered as they traverse the fiber. In reality, some refraction does occur and this reduces the accuracy of the measurement. TIM is not effective for microstructured optical fibers described in Sect. 9.5 because the large refractive index difference

between the glass and the voids causes too much refraction. The algorithm described in [7.2] assumes that the fiber is axisymmetric, so radial asymmetries will also reduce the accuracy of the index profile. For this reason, TIM is not effective for polarization-maintaining (PM) optical fibers described in Sect. 9.2.

7.4 Summary

Fusion splice loss is usually the most important optical performance characteristic of a fusion splice. It can be measured using transmission or reflection measurements. The choice of measurement technology depends on whether the fusion splice is analyzed in a research laboratory, in a factory environment, or during field installation of optical fibers.

The insertion loss or cutback techniques can be used to accurately measure fusion splice loss. The "pre-splice" approach yields accurate splice loss measurements even when the attenuation in the fibers themselves is significant yet unknown, or when distinct power meters must be used because the end of the fiber span is situated far from the fusion splice. The two-splice approach can eliminate measurement inaccuracies associated with reconnecting optical fibers to a source or detector. The wavelength dependence of splice loss can be measured with a broadband source and a wavelength sensitive detector or alternatively with a wavelength tunable source and a broadband detector.

Optical time-domain reflectometers (OTDRs) are indispensable for measuring single-mode or multimode fusion splice loss in optical fiber transmission cables either before or after installation. The apparent single-mode splice loss measured by an OTDR can sensitively depend upon the relative size of the fibers' mode field diameters (MFD) and so accurate splice loss measurement between dissimilar fibers usually requires that they be measured by the OTDR in both propagating directions. Most OTDRs are not effective at discriminating the individual loss contributions of closely spaced splices or components.

Although low-temperature fusion splices between dissimilar fibers can exhibit relatively high values of reflectance, the reflectance of most other fusion splices is well below the measurement limit of OTDRs or optical continuous wave reflectometers (OCWRs), which is on the order of -70 dB. More sophisticated devices, such as optical low-coherence reflectometers (OLCR) or coherent optical frequency-domain reflectometers (OFDR) can be used to measure fusion splice reflectance down to about -150 dB with sub-mm spatial resolution.

Refractive index profiling of a fusion splice using the transverse interferometric method (TIM) can be a powerful tool for splice optimization and for understanding otherwise unexplained splice loss, especially when combined with a numerical method such as coupled-mode theory (CMT) or the beam propagation method (BPM).

8. Splice Process Optimization and Special Splicing Strategies

The quality of a fusion splice can be defined by both optical characteristics, such as insertion loss or reflectance, and mechanical characteristics, such as failure strength or long term reliability. These fusion splice characteristics are in turn determined by the details of the splice process, including the splicing parameters as well as by the properties of the fibers themselves. The equipment used to fabricate the splice and their associated splice parameters, must be carefully chosen to meet the quality requirements, which are dictated by the environment and the particular application of the fusion splice. *Splice optimization* refers to the process of determining the best choice of splice parameters for achieving the highest quality fusion splices. The proliferation of a wide variety of specialty optical fibers, including dispersion-compensating fiber (DCF), non-zero dispersion-shifted fiber (NZ-DSF), erbium-doped fiber (EDF) and polarization-maintaining (PM) fiber, has elevated the importance of splice optimization, since fabricating high quality fusion splices with these fibers usually requires specialized splicing strategies and carefully tuned splice parameters.

The splice parameters of an arc fusion splicer typically include one or more arc fusion currents and their associated durations, as well as the overlap distance and the hot push delay. In addition, the procedures and parameters used for coating removal (stripping), cleaning, cleaving, and protecting the completed splice may also affect the fusion splice quality. The relationship between these various parameters and the resulting splice quality is difficult to predict, partly because of the large number of splice parameters, and partly because of interactions between them. In some of the earlier chapters we presented physical models describing how the characteristics of a fusion splice depend upon processing conditions, but the relationship between the general set of splice parameters and the overall quality of the resulting splice is almost always too complex to capture with a physical model. For these reason, efficient splice optimization often requires an empirical strategy based on specially designed experiments.

Aside from splice optimization, the quality of certain types of fusion splices can also be improved by employing one of several special splicing strategies that have been developed over the past few decades. For example, dopant diffusion has proved to be a very important technique when fusion splicing erbium-doped fiber (EDF) to standard single-mode fiber (SMF). Special splic-

ing strategies are also associated with their own set of process parameters, which also may benefit from optimization using designed experiments.

In the first Section of this Chapter, we will describe strategies for efficient splice optimization, including an introduction to designed experiments. In the second Section we will discuss several special fusion splice strategies that can improve the quality of certain types of fusion splices. Explanations for the effectiveness of these strategies are provided based on fundamental concepts introduced in earlier chapters. The reader is cautioned that certain specialized fusion splice strategies may be patent protected.

8.1 Design of Experiments for Splice Optimization

The fusion splice process is associated with a large number of distinct splice parameters that affect the quality of the resulting splice. Parameters common to most commercial fusion splicing equipment include fusion splice heating power (or arc current), fusion splice duration, hot push delay, overlap distance, and the maximum allowed initial cleave angle. The hot push delay is the time delay between when the heat is first applied to the fiber tips and when the two tips are fed together (see Sect. 1.2 and especially Fig. 1.3). The overlap distance is the amount of extra distance the fibers are fed together beyond the original gap spacing between them. Many fusion splicers can be programmed to apply several distinct sequential heatings, each with a unique duration and power level. One application for multiple heating periods is the case where a relatively high initial temperature is applied during joint formation and then a subsequent lower temperature and longer duration heating period induces beneficial dopant diffusion. The large number of fusion splice parameters, the presence of underlying physical interactions between them, and naturally occurring random splice quality variations make splice optimization a challenging and tedious task.

A typical fusion splice takes on the order of a few minutes to perform and since the total number of distinct splice parameter combinations varies exponentially with the number of splice parameters, an exhaustive search of every possible splice parameter combination is impossible. Moreover, it may be necessary to perform several splices at the same parameter settings since there is always uncertainty associated with splice measurements as well as naturally occurring random variations in splice quality (for example due to cleave angle variation or minute alignment variations). These challenges are common to the general problem of optimizing a manufacturing process. One solution to the general problem of process optimization is to perform specially *designed experiments*, which can more efficiently elucidate the important process parameters and determine their optimal settings compared to an exhaustive search through all possible parameter settings.

Parameter optimization and experimental design is a mathematical subject whose complete description is beyond the scope of this book. Instead,

we provide an introduction to how designed experiments can be useful for splice optimization. We provide an example that demonstrates the power of the methodology, but the interested reader is referred to several excellent texts that more thoroughly describe experimental design and process optimization [8.1–8.5].

8.1.1 The Splice Parameter Space

Each individual splice parameter can be thought of as an axis on a graph (Fig. 8.1a) with a quantitative value denoted by p_i where i is an index identifying the splice parameter. If we temporarily restrict our attention to only two splice parameters, we can imagine that one comprises the x-axis, say fusion current, and the other parameter comprises the y-axis, say fusion time (splice duration). The available parameter space can be thought of as a two dimensional area defined by these two splice parameters. Practical constraints, such as the available settings on a commercial fusion splicer, may not only restrict the available range of these parameters, but also may discretize the available settings, so that only certain loci in the theoretical parameter space are actually accessible.

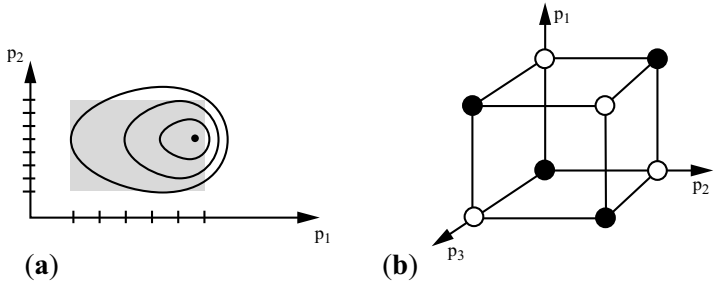

Fig. 8.1. Graphical depictions of splice process optimization and designed experiments. (**a**) Two dimensional parameter space defined by two splice parameters, p_1 and p_2. The equipment restricts the splice parameters to be set to one of the discrete values indicated by the tic marks on the axes. The shaded region is the range of the parameter space. The solid lines indicate contours of equal splice quality (*i.e.* splice loss). The optimum quality and splice parameters are indicated by the solid dot. (**b**) A simple scheme for performing a reduced set of orthogonal experiments for three splice parameters p_1, p_2, and p_3, each with only 2 levels. There are eight circles corresponding to the eight possible parameter combinations. The dark circles are the experiments to be performed in a designed experiment

Clearly certain parameter combinations, meaning certain regions in the two dimensional area of Fig. 8.1a, will yield better quality fusion splices than others. Splice optimization can be described as the process of searching for the region in the parameter space that yields the highest quality fusion splices. When three splice parameters are considered, the parameter space becomes

a three dimensional volume instead of a two dimensional area. As even more parameters are added, it becomes much harder, even impossible, to visualize the shape of the parameter space. Nevertheless, the same mathematical rules applicable to optimizing a two dimensional parameter space can be extended to optimize a higher dimension parameter space.

The two dimensional parameter space depicted in Fig 8.1a contains only one general region where the splice quality is optimal, and this region can be described as the global maximum of fusion splice quality. Unfortunately, a parameter space sometimes contains several distinct regions, termed local quality maxima, where the local fusion splice quality higher than the immediate surroundings. Usually the goal of splice optimization is to find the global quality maximum, but optimization procedures can sometimes be distracted by local maxima and consequently overlook the global maximum. Occasionally, a local quality maximum is preferable to the global maximum; for example if it occupies a much larger area in the parameter space and is consequently more robust to disturbances, such as a poor cleave angle.

To simplify our search for the optimum splice parameters, we can reduce the number of choices for each parameter by choosing discrete values that approximately span the range of interest. For example, instead of allowing the fusion current of a conventional arc fusion splicer to continuously vary from less than 6 mA to more then 20 mA, we can restrict our choice to one of three discrete *levels*, for example 10 mA, 12 mA, and 14 mA, which are expected to be in the vicinity of the optimum parameter set. This significantly reduces the number of different combinations of splice parameters. However, even if we consider only three different splice parameters, each associated with three possible levels, there are still 3^3=27 possible combinations for all of the different splice parameters! This simple example illustrates how the total number of available parameter combinations grows exponentially as the number of levels or the number of different splice parameters is increased.

8.1.2 Orthogonal Arrays

The splice parameters that control the splice quality are known as *factors* in experimental design and process optimization literature. A *full factorial array* is an experimental design in which at least one experiment (fusion splice) is performed for every combination of factors (fusion splice parameters). As we saw in the preceding section, when there are several factors, full factorial arrays usually require too many individual trials to be practical.

To overcome this difficulty, we can reduce the required number of experiments by only performing them at certain specific combinations of factors, which is termed a *fractional factorial* experimental design. In a fractional factorial design, many (or all) of the splice parameters are varied simultaneously during the set of experiments, instead of performing single valued experiments in which only one splice parameter is changed at a time. Fractional factorial experiments are usually designed to comprise an *orthogonal*

array, meaning that a particular splice parameter level occurs an equal number of times in the experimental array [8.5]. Fractional factorial designs are particularly useful for efficiently identifying which fusion splice parameters are of primary importance, as well as the general effect of these primary splice parameters on splice quality. Once the main splice parameters are identified, a full factorial optimization iteration is often performed on these parameters alone. In this way, a relatively large number of fusion splice parameters can be efficiently optimized. One disadvantage of fractional factorial experimental designs compared to full factorial designs is that they can hide interactions between two splice parameters [8.1].

The principle behind fractional factorial experimental design can be illustrated graphically (Fig. 8.1b). Consider three splice parameters such that the parameter space is a three dimensional volume in which each parameter is chosen from one of two possible levels. There are 2^3=8 possible distinct combinations of splice parameters, which would require a total of eight experiments if we perform one experiment at each possible combination. However, if we vary multiple parameters at a time, we can perform only four experiments and obtain much of the same information. Notice how the reduced set of experiments (*dark circles*) appearing in Fig. 8.1b appears to efficiently sample much of the three dimensional volume comprising the parameter space. Also note how each parameter level appears exactly twice in the course of all four experiments. Once we have decided which splice parameters are likely to be most worthy of consideration, and how many levels are needed to span the parameter space, we can choose an orthogonal array and perform a series of different fusion splices according to the array's specifications.

Special mathematical rules can be used to design a set of orthogonal experiments for a given number of splice parameters, each of which is restricted to a given number of levels. Prearranged tables detailing many such orthogonal arrays have been compiled [8.1–8.5]. Fig. 8.1b is a graphical portrayal of the so-called *Taguchi* L_4 *orthogonal array* designed for up to three splice parameters, each restricted to two levels [8.5]. Table 8.1 describes an orthogonal array which can be used for up to four splice parameters, each varied amongst three possible levels. Only nine separate combinations of parameters are required for this orthogonal array, which is much less that the total number of possible combinations (3^4=81 when varying all four splice parameters). This orthogonal array can be used with fewer than four splice parameters by simply ignoring the unnecessary final columns of Table 8.1. When only the first two columns of Table 8.1 are used, the array is really a full factorial experimental design for two splice parameters with three levels each.

The levels chosen for a particular splice parameter are important. We usually do not choose the levels to span the entire physical parameter space, but instead we initially search the parameter space in the vicinity of known fusion splice conditions. This is partly because spanning the entire parameter space is likely to coarsely sample widely disparate regions governed by

Table 8.1. Orthogonal array experiment design for up to four splice parameters (p_1 through p_4), each varied amongst three possible levels, denoted as low, medium, and high. The quality of the i^{th} experiment is denoted by Q_i, and this quantity is assumed to be the mean value if there is replication of experiments at the same parameter combinations. This particular experiment design is sometimes called a *Taguchi L_9 array* [8.5]

Experiment number	p_1	p_2	p_3	p_4	Outcome
1	low	low	low	low	Q_1
2	low	medium	medium	medium	Q_2
3	low	high	high	high	Q_3
4	medium	low	medium	high	Q_4
5	medium	medium	high	low	Q_5
6	medium	high	low	medium	Q_6
7	high	low	high	medium	Q_7
8	high	medium	low	high	Q_8
9	high	high	medium	low	Q_9

very different physical phenomena. Interpreting data that span such widely dissimilar regions can be difficult. If we discover that the optimum conditions are on the edge of the parameter space used for the orthogonal array, we can repeat the optimization process with parameter levels that bracket the splice parameters found to be optimal by the first optimization.

In order to optimize fusion splice parameters, we must quantify the quality of the fusion splice. If we are simply interested in minimizing the splice loss, we may use the splice loss measured in a convenient unit, such as dB, to quantify the splice quality. In other cases, the fusion splice quality may be a combination of splice loss, reflectance, or tensile strength. In such cases, one approach is to define a mathematical quality function, Q, which depends on the measured value of the splice's optical loss, reflectance, and tensile strength. In our notation, Q_i denotes the quality of the i^{th} experiment. During splice optimization the splice quality measurement must remain relatively accurate and must not drift over time. This can be a problem when a large number of splices is required and the stability of an optical source or power meter drifts over this time period. Splice loss measurement strategies are discussed in Chap. 7.

Since both the actual fusion splice quality and its measured value is subject to a certain amount of random variation, multiple experiments (fusion splices) can be performed at each combination of parameters comprising the orthogonal array. Multiple experiments performed at the same parameters settings are termed *replications* or *repetitions*, and can be particularly help-

ful when deciding if the difference in splice quality between two different combinations of parameters is statistically significant. Given a limitation in the total number of fusion splices that can be performed during a particular splice optimization, the enhanced statistical confidence resulting from replications must be weighed against the desire to fully cover the parameter space with a sufficient number of parameters and their associated levels [8.2, 8.3].

The overall mean value of Q resulting from all of the various experimental combinations in the orthogonal array, $\bar{Q}$, can be computed from the quality measured for each experimental combination, Q_i,

$$\bar{Q} = \frac{1}{N_{\text{exp}}} \sum_{i=1}^{N_{\text{exp}}} Q_i \,. \tag{8.1}$$

where N_{exp} is the total number of experiments comprising the orthogonal array (in Table 8.1, $N_{\text{exp}} = 9$) and Q_i is the measured quality or the mean quality value if experiments are replicated.

The splice *parameter effect* resulting from setting parameter p_j to level k, $Q_{p_j=k}$, is given by

$$Q_{p_j=k} = \frac{1}{N_{p_j=k}} \sum_{i=1}^{N_{p_j=k}} \left(Q_i \,\big|_{p_j=k} - \bar{Q} \right) , \tag{8.2}$$

where $Q_i \,\big|_{p_j=k}$ denotes the outcome of experiments in which parameter p_j was set to level k and $N_{p_j=k}$ is the number of Q_i where p_j was set to level k. Here the parameter effect, $Q_{p_j=k}$, is expressed relative to the overall mean, $\bar{Q}$. Since the parameter effects have been averaged over several different combinations of splice parameter settings, they only provide an approximate indication as to how a variation of a particular splice parameter affects the fusion splice quality.

The relative importance of a particular parameter in determining fusion splice quality can be estimated using the *sum-of-squares* approach. The sum-of-squares resulting from parameter p_j is denoted by SS_{p_j} and is given by

$$SS_{p_j} = \sum_k N_{p_j=k} \left(Q_{p_j=k} - \bar{Q} \right)^2 , \tag{8.3}$$

where the summation $\sum_k$ is understood to occur over only the parameter combinations in which parameter p_j was set to a level of k (of which there are $N_{p_j=k}$ combinations). The total sum-of-squares associated with each individual parameter, SS_{total}, will always obey the identity

$$SS_{\text{total}} \equiv \sum_j SS_{p_j} = \sum_{i=1}^{N} \left(Q_i - \bar{Q} \right)^2 , \tag{8.4}$$

where the summation $\sum_j$ is understood to occur over each splice parameter, p_j. The relative contribution of an individual splice parameter to the splice quality can be crudely estimated by taking the ratio of the sum-of-squares due to that splice parameter, SS_{p_j}, and dividing it by the total sum-of-squares, SS_{total}. One of the most powerful aspects of orthogonal array experimental design is the ability to estimate the relative importance of many different parameters, thus efficiently screening for the most important ones. *Analysis-of-variance* (ANOVA) is a powerful mathematical tool for determining the statistical significance of the parameter effects, their relative importance, and their interactions using the Fisher "F-test" in conjunction with sum-of-squares and replication. ANOVA is beyond the scope of this introductory treatment but detailed descriptions are available in a variety of sources [8.1, 8.2, 8.5].

Aside from the effects of individual parameters, the splice quality can also be controlled by interactions between two or more parameters. For example, an excessively large overlap might lead to relatively high fusion splice loss when the hot push delay is relatively short, since the fiber tips might not have sufficient time to soften and therefore could buckle when fed together during the hot push (Sect. 3.2). On the other hand, such a large hot push might not be detrimental when the hot push delay is relatively long, since there will be ample time for the fiber tips to soften before they are fed together. One disadvantage of fractional factorial experimental designs compared with full factorial designs is that they can sometimes conceal such interactions, if not carefully thought out [8.1, 8.2, 8.4, 8.5].

There are other approaches for parameter optimization aside from orthogonal arrays. *Response surface methodology* (RSM) can be particularly effective for fine tuning the splice parameters when they are known to be near an optimum setting [8.1, 8.4]. In RSM the splice quality is modeled as a Taylor series function of the splice parameters and the local gradient of this quality function is used to direct the search for optimum splice parameters. One disadvantage of RSM is that it can more easily be distracted by a local maximum in quality thereby overlooking the desired global quality maximum.

8.1.3 Example Splice Optimization

In this section we will present a specific splice optimization example demonstrating the general methodology. Consider a fusion splice between standard SMF and a very small core, very high Δ fiber, which could for example be an erbium-doped fiber. Standard SMF has a Δ of about 0.35%, a core diameter of about 8.3 µm, an NA of about 0.12, and a mode field diameter (MFD) of about 10.4 µm at 1550 nm (computed with the aid of Sect. 4.4.3 and (4.41)). In contrast, the high Δ fiber has a Δ of about 1.7%, an NA of about 0.27, and a MFD of about 4.5 µm at 1550 nm (computed in the

same manner). The overlap integral, (4.38), predicts the splice loss resulting from the mismatch in mode field size and shape to be about 1.8 dB. The less accurate Gaussian approximation presented in Sect. 4.2.2 predicts that the splice loss from mode field size mismatch is about 2.6 dB. The goal is to optimize splice quality by minimizing splice loss, hopefully reducing it well below the theoretical values predicted for simple mode field mismatch.

For the purposes of illustration, we will optimize this splice over four common splice parameters: splice heating power, splice duration, overlap, and hot push delay. These four splice parameters are varied over three levels each. We use the Taguchi L_9 orthogonal array presented in Table 8.1. Table 8.2 details the individual experimental conditions and their respective outcomes. There was no replication of the experiments in this example; only one fusion splice was fabricated at each combination of splice parameters. The initial conditions for this splice optimization we taken to be conditions known to be favorable for fusion splicing of standard SMF. We choose the levels of the various splice parameters to bracket the neighborhood of these initial conditions.

Table 8.2. Optimization of a fusion splice between standard SMF and a small core, high Δ fiber using the L_9 orthogonal array first presented in Table 8.1

Experiment number	p_1, Splice Power (W)	p_2, Splice Time (s)	p_3, Overlap (μm)	p_4, Hot Push Delay (ms)	Q, Splice Loss (dB)
1	18	2.5	5	150	1.97
2	18	5	8	300	1.65
3	18	10	11	450	1.34
4	20	2.5	8	450	1.40
5	20	5	11	150	1.15
6	20	10	5	300	.55
7	22	2.5	11	300	.9
8	22	5	5	450	1.8
9	22	10	8	150	.22

The splice heating power is often measured in units of mA of fusion current on an arc splicer, but in this example we use a fusion splicer incorporating a resistively heated tungsten filament heat source (Sect. 10.4) whose heating power is measured in W. Typical fusion current values for an arc fusion splicer are about 16 mA whereas a corresponding setting on a tungsten filament fusion splicer is about 20 W. In this optimization example we choose the splice power levels to be 18, 20, and 22 W. The splice duration is the amount

of time that the heat source is applied to the fibers, and is typically about 5 seconds. In this optimization example, we choose the splice duration levels to be 2.5, 5, and 10 s. Note that these levels are not evenly spaced, and that they do not in general need to be evenly spaced. In this optimization example we only consider a single heating period described by a single power and a single splice duration, although many contemporary fusion splicers can be programmed to perform several different sequential heatings, each with a distinct amount of heat and duration. Overlap, the geometric interference between the fiber tips when they are fed together, is typically about 8 μm. In this optimization example, we choose the overlap to be 5, 8, and 11 μm. The hot push delay, the amount of time between the initiation of heating and when the fiber tips are fed together, is typically on the order of a few hundred ms and here we choose the levels to be 150, 300, and 450 ms. In this example, the individual splice experiments were carefully performed on fiber tips exhibiting high quality cleaves ($< 0.5°$ cleave angle) in an effort to minimize cleave-induced quality variations. Sometimes a deliberate variation in cleave angle can be useful for gauging the sensitivity of the splice quality to cleave angle. Splice parameters can also be optimized so that the resulting splice quality is robust to natural variations in cleave quality.

Figure 8.2 graphically illustrates the parameter effects of the four splice parameters on the splice loss using the data in Table 8.2 and (8.2). Note that the overall mean value, $\bar{Q}$=1.22, was added to the factor effects for clarity and that although the horizontal tic marks in the plot are evenly spaced, the levels of the splice duration are not. These plots show that the splice power and especially the splice time have the strongest and clearest impact on the resulting splice loss. The longest splice durations and highest splice power levels result in the lowest splice losses. These two trends suggest that the optimal splice conditions lie near the edge of the parameter space considered in this designed set of experiments. Thus, another splice optimization iteration bracketing the maximum splice power and maximum splice duration used here may find a better set of splice parameters. Alternatively, RSM could be employed to find the optimal splice conditions starting from the best conditions found by this simple L_9 array.

The sum-of-squares results computed using (8.3) and (8.4) for this sample splice optimization are tabulated in Table 8.3. The table shows that the splice duration exhibits the largest sum-of-squares followed by the splice power. Taking the ratio between the individual parameters sum-of-squares and the total sum-of-squares suggests that the splice duration contributes about 45% of the observed variation in splice quality whereas the splice power contributes about 32%. ANOVA can be applied to this results, especially in the presence of replications, to determine the level of statistical confidence in these results [8.1, 8.2, 8.5]. We may conclude that these two parameters have the most important impact on the fusion splice quality. This is not a surprising result; we might have expected that dopant diffusion would be important

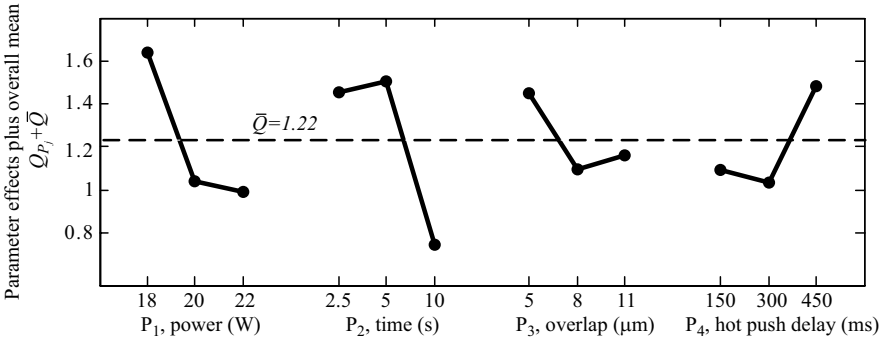

Fig. 8.2. Effect of various parameters on splice loss between standard SMF and a small core high Δ fiber. The overall mean, $\bar{Q}$ is added to the parameter effects, Q_{p_j}, to clarify how the various parameters and levels affect the splice loss. These plots show that the splice power and the splice duration have a strong influence on the resulting splice loss. Note that the levels depicted on the horizontal axes, are not evenly spaced in some cases

when fusion splicing a high-Δ fiber to conventional SMF, so that splice power and splice duration would be the main parameters controlling splice loss.

Table 8.3. Results of initial splice optimization

Parameter	Sum of squares	% Importance ($SS_{p_j}/SS_{\text{total}}$)
1. Power	SS_{p_1}=.85	32%
2. Duration	SS_{p_2}=1.22	45%
3. Overlap	SS_{p_3}=.22	8%
4. Hot Push Delay	SS_{p_4}=0.40	15%
Total	SS_{total}=2.69	

Clearly the relative importance of a splice parameter will depend, in part, on the choice of its levels. If the levels for a parameter are very close, then the resulting variation in splice quality due to this effect would be reduced. Consequently, this example only shows that the fusion splice power and the fusion splice duration are much more important than the overlap and the hot push delay when the levels are selected from range used here. If the levels of overlap or hot push delay were much more widely spaced, their relative importance might very well grow relative to that of splice duration and splice power.

The efficiency of designed experiments with orthogonal arrays is impressive. With only 9 individual combinations of splice parameters, we reduced the fusion splice loss between standard SMF and a high Δ fiber by a huge

margin, from over 1 dB to about 0.22 dB, by performing a total of 9 individual experiments. Moreover, we were able to infer the influence of the various splice parameters over the range spanned by the levels, and found that the splice duration is most important followed by the splice power, the hot push delay, and the overlap. This information is useful when attempting to predict the variability of the splice loss in a production environment, since it indicates the sensitivity of the splicing process to variations in key parameters.

8.2 Special Splicing Strategies

In addition to optimizing splice parameters, the quality of a fusion splice can be improved with the aid of various special processes or strategies that have been developed over the past few decades. Many of these special strategies can be performed with commercial fusion splicing equipment. Most of these special strategies are geared towards single-mode fiber splicing, since the quality requirements of single-mode fibers are usually more stringent than those of multimode fibers. Furthermore, multimode fiber splice loss is generally lower than single-mode fiber splice loss.

In this section we will review the following strategies: fire polishing, bridge fibers, dopant diffusion, low-temperature splices, offset heating, tapered splices, and fattened splices. Sometimes a combination of two or more special strategies yields the best quality fusion splice. Note that aspects of certain specialized strategies may be patent protected.

8.2.1 Fire Polishing and Arc Scanning

Fire polishing is a general term describing a process in which a heat source is scanned over the surface of the fusion splice to improve its quality. Recent arc fusion splicers incorporate *arc scanning*, in which the electric arc can be scanned along the length of the fiber in the vicinity of the splice [8.39]. Fire polishing can be accomplished by scanning a heat source along a stationary fiber, or scanning the fiber past a stationary heat source [8.39]. Fire polishing can potentially improve both the mechanical and optical quality of a fusion splice. Figure 8.3 schematically illustrates an oscillating fire polish.

As discussed in Sect. 6.1, fire polishing can improve the mechanical strength and the long-term reliability of a fusion splice by heating the fiber surface to the point that surface tension heals any surface defects that might otherwise reduce the fiber's strength [8.26]. These defects are often incurred during the fiber stripping process (Sect. 2.1) or even during joint formation (Sect. 6.1).

Fire polishing serves to effectively widen a narrow heat source by distributing the heat over a longer length. The length of silica fiber typically heated to high temperatures by electric arcs is less than 1 mm. By scanning

a narrow electric arc along the fiber, the effective zone of heating can be widened to be several mm or more in length [8.39]. In this way, the process parameters of the fire polish can control the effective width of the heat source. Note that if the heat source emits a constant amount of heat, then increasing its velocity reduces the maximum temperature attained by the heated portion of fiber. A gradual transition in temperature can be achieved by accelerating or decelerating a constant power heat source. Alternatively, such a transition can be achieved by changing the heat emitted by the source while moving the source at a constant velocity.

A fire polish can be effective for cultivating a smooth, low-loss transition between the heat affected region in the immediate vicinity of the fusion splice and the unaffected fiber far from the splice. Such a transition is important when performing dopant diffusion (Sect. 8.2.3) in order to minimize transition loss (Sect. 4.2).

8.2.2 Bridge Fibers

As we saw in Sect. 4.2, the splice loss between dissimilar single-mode fibers is, in many cases, primarily due to mode field mismatch. This mismatch can sometimes be described as a mismatch of the mode field diameters (MFDs), but more generally we may express this splice loss as a result of a mismatch between the *shapes* of the two guided fundamental mode fields. Likewise, splice loss can also occur between dissimilar multimode fibers due to a mismatch in the guiding properties of the two fibers. One generalized strategy for minimizing this mismatch loss is to use a *bridge fiber*, also termed an *intermediate fiber* or *matching fiber*, between the two fibers to be spliced [8.10, 8.21, 8.32, 8.34, 8.37]. Although this requires performing two splices instead of one, if the bridge fiber is properly chosen the total splice loss from the two bridge fiber splices can actually be less than the loss that results when the two fibers are directly spliced together.

Due to the extra costs of fabricating two splices instead of one, bridge fibers are normally employed only when the direct splice loss is unusually high, typically on the order of 0.5 dB or more. Such high direct splice losses

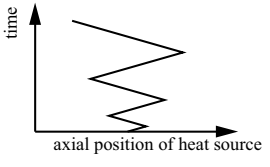

Fig. 8.3. During a fire polish the heat source is scanned axially along the fiber, often in a zigzag trajectory as depicted here. This fire polish can improve the mechanical strength and long-term reliability of the fusion splice by healing surface defects incurred during fiber stripping or joint formation. It can also reduce the transition loss between heat-affected and unaffected fiber.

are common when fusion splicing dispersion-compensating fibers (DCF) to another fiber [8.10, 8.14, 8.34] or when fusion splicing erbium-doped fibers (EDF) [8.21] to another fiber.

In extreme cases, a specialized bridge fiber can actually be designed and fabricated according to the specifications of the two fibers to be spliced. More commonly, the bridge fiber is chosen from one of the variety of commercially available optical fibers. The bridge fiber usually exhibits a MFD that lies between the MFDs of the dissimilar fibers to be spliced.

To illustrate the benefits of a bridge fiber, consider a sample fusion splice between a representative DCF and standard SMF as depicted in Fig. 8.4. Standard SMF is a step-index core with a core diameter of about 8.3 μm and a core Δ of about 0.35%. Using the overlap integral computation of (4.38) applied to the fundamental mode fields of these fibers (computed according to the methodology of Sect. 4.4.3), the direct mode field mismatch fusion splice loss is predicted to be about 1.11 dB at 1550 nm. Note that the overlap integral is a more accurate computation than the Gaussian approximation formula, (4.44), since the mode field shape of DCF is usually non-Gaussian.

If we choose a step-index bridge fiber with a slightly smaller core diameter (7 μm) and slightly higher core Δ (about 0.48%) than standard SMF, the fusion splice loss to the DCF is predicted to be about 0.63 dB and the fusion splice loss to the standard SMF is predicted to be about 0.13 dB. Thus the total splice loss with the bridge fiber is predicted to be about 0.76 dB, which is 0.35 dB less than that of the direct DCF/SMF splice. The bridge fiber exhibits a MFD of about 8.6 μm at 1550 nm, which lies between the mode field diameters of the standard SMF and DCF (10.5 μm and 5 μm respectively). Numerical calculations, such as those described here, can help to determine the optimum choice of bridge fiber.

Equation (4.38), used in this simple example to compute the fusion splice loss, only considers the mode field shape mismatch loss between the fundamental modes of the dissimilar fibers. In reality, the heat from the fusion splice will induce a certain amount of dopant diffusion (Sect. 3.3), especially in the DCF since it exhibits a fluorine-doped refractive index trench around the core, that can increase or decrease the actual mode field mismatch splice loss. This dopant diffusion can also induce transition losses (Sect. 4.2) which occur when the optical signal travels between the unheated portion of the DCF and the heat affected portion of the DCF. Other special fusion splicing strategies, such as dopant diffusion or tapering, could be used to further optimize the bridge fiber splices described here.

Shiraishi has proposed a novel type of bridge fiber that is comprised of a multimode graded-index fiber [8.37]. In this case, the multimode graded-index fiber acts as a graded-index (GRIN) fiber lens that expands or contracts the mode field diameters between two dissimilar fibers. Unlike single-mode bridge fibers, the length of this bridge fiber must be carefully controlled to be within a few microns of a special length to ensure optimum performance.

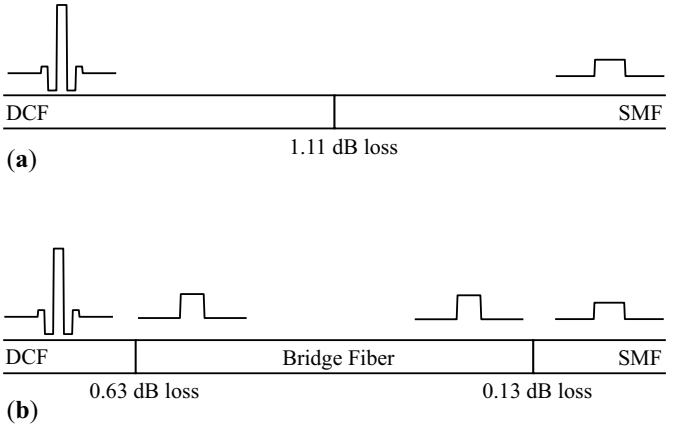

Fig. 8.4. Benefits of a bridge fiber. (**a**) Direct fusion splice between a representative DCF and standard SMF exhibiting about 1.11 dB of loss, computed using the overlap integral approach of (4.38). The MFD of the standard SMF is about 10.5 μm at 1550 nm while the MFD of the DCF is about 5 μm. The refractive index profiles of the fibers are shown above the fibers. (**b**) Step-index bridge fiber exhibits a splice loss of 0.63 dB to the DCF and a splice loss of 0.13 dB to the SMF, reducing the total loss by about 0.35 dB. The MFD of the bridge fiber is about 8.6 μm and the splice losses were also computed using the overlap integral. Note that real splice losses may differ from the overlap integral calculations depicted here

Detailed information concerning GRIN lenses, and their application to fiber optics is available in [8.13]. In Sect. 9.5.2 we discuss the use of GRIN fiber lenses for fusion splicing microstructured optical fibers.

Since bridge fibers introduce two closely situated fusion splices in place of a single direct splice, and since bridge fiber splices can exhibit reasonably high loss (more than 0.1 dB), modal noise (Sect. 4.2.4) can be a concern [8.32]. Two bridge fiber splices can be situated close enough to be packaged in the same splice enclosure [8.32].

8.2.3 Dopant Diffusion and TEC Splices

Dopant diffusion, whose underlying physics were already discussed in Sect. 3.3, can be used to reduce the loss of a fusion splice, especially between certain dissimilar fiber types [8.6,8.9,8.10,8.14–8.16,8.18,8.27,8.32,8.33,8.38,8.40,8.42]. The refractive index structure of conventional silica optical fibers results from the distribution of chemical dopants, such as germania or fluorine, that raise or lower the silica's refractive index. At high temperatures, especially at or above fusion splicing temperatures (on the order of 2000° C), these dopants will diffuse, meaning that they will spread out from regions of higher concentrations to regions of lower concentration. This dopant redistribution alters the fiber's refractive index profile and can either improve or degrade the optical quality of a fusion splice.

Some authors use the term *thermally expanded core (TEC)*, to describe the use of dopant diffusion to reduce splice loss. This term can be misleading and is avoided here, since sometimes the core itself diffuses relatively slowly while a surrounding ring of dopant (typically fluorine) rapidly diffuses into the core.

As we learned in Sect. 3.3, the rate of dopant diffusion scales with the local dopant concentration gradient. Moreover, the rate of dopant diffusion also scales with the square of the characteristic spatial dimension (which can be taken to be the core radius or the thickness of an annular layer). Thus, the dopants diffuse rapidly in a small-core, high-Δ fiber, such as erbium-doped fiber (EDF). Dopants also diffuse rapidly in a dispersion-compensating fiber (DCF) or in a non-zero dispersion-shifted fiber (NZ-DSF) since these fibers typically exhibit fine annular refractive index structures. This accounts for the widespread use of dopant diffusion when fusion splicing such fibers [8.6, 8.9, 8.10, 8.14, 8.15, 8.18, 8.27, 8.32, 8.33, 8.38, 8.40, 8.42]. In contrast, dopant diffusion proceeds very slowly in multimode fibers because the length scales associated with their refractive index profiles are much larger.

As we saw in Sect. 3.3, the diffusion of a dopant in a fiber containing a single chemical species, and the resulting refractive index profile, can be readily modeled. In such a case, either longer heating times or higher temperatures can be used to increase the amount of diffusion to achieve a target refractive index profile. The effect of this diffused refractive index profile on splice loss can then be computed with the aid of numerical techniques such as the beam propagation method (Sect. 4.4). However, when an optical fiber contains multiple chemical dopants, predicting the evolution of the refractive index profile is very difficult, since each dopant species diffuses at its own, temperature-dependent, rate. The local concentration of one dopant may even affect the diffusion coefficient of another dopant. Sect. 3.3.3 includes a sample computation of multiple dopant diffusion. In this case, the Transverse Interferometric Method (TIM, Sect. 7.3) can be used to measured the heat-induced change in the local refractive index profile.

When using dopant diffusion, care must be taken to ensure that the induced transition in the refractive index profile is sufficiently gradual such that the optical signal is not coupled into undesirable higher-order guided modes or radiation modes. When such transition losses are small, the transition is said to be *adiabatic*. The numerical tools introduced in Sect. 4.4 and Sect. 5.2 can be used to predict the required length scale of the transition in the refractive index profile. Alternatively, simple heuristics can also be used although they may be less accurate when applied to specific examples [8.19, 8.20].

Fluorine exhibits a much higher diffusivity in silica than germanium, especially at fusion splice temperatures, as shown in Figs. 3.21 and 3.22. Hence fibers incorporating significant amounts of fluorine, such as dispersion-compensating type fibers (DCF) as well as some non-zero dispersion-shifted-

fiber (NZ-DSF), tend to experience much more dopant diffusion in the vicinity of a fusion splice compared with standard matched-clad SMF, which is primarily doped with germania. If the heat source is narrow, then the transition between the heat-affected dopant-diffused region of fiber and the undiffused region can be abrupt enough to induce large amounts of transition splice loss. This transition loss can be reduced by distributing the heat over a longer distance so that the transition between the undiffused and diffused region of fiber is more gradual. In some cases a more gradual transition can be accomplished with a fire polish (also known as arc scanning), described in Sect. 8.2.1 [8.32]. Once again, BPM can provide guidance as to the required length for the transition region.

Like fluorine, the dopant species comprising the core of erbium-doped fiber (EDF) such as erbium and aluminum are also known to diffuse more rapidly than germania. Moreover, the small core diameter and higher Δ typical of EDF ensures that it experiences much more dopant diffusion than standard SMF during a fusion splice (see Fig. 5.4). This phenomenon can be harnessed when fusion splicing standard SMF to EDF, since the completed splice can be heat treated so as to induce dopant diffusion to match the mode field of the EDF with that of the SMF, as discussed in an earlier example [8.15, 8.40] (Sect. 3.3.3). EDF fusion splicing is discussed further in Sect. 9.3.

Dopant diffusion can be performed on a commercial fusion splicer, especially when fusion splicing a small core, high core Δ fiber (such as EDF) to a larger core, lower core Δ fiber (such as standard SMF) [8.9, 8.10, 8.15, 8.40]. One approach is to use low fusion currents and longer heating times, which can approach a minute or more. Alternatively, extra heat can be applied by the fusion splice heat source to an already completed fusion splice in a process called a *re-arc* (for an arc fusion splicer) or a *reheat* (more generally). Instead of commercial fusion splice heat sources, microburner flames [8.15, 8.25, 8.28] or specially designed tube furnaces [8.17] can be used to heat a fiber to induce dopant diffusion, as shown in Fig. 8.5. However, these specialized systems do not lend themselves to field fusion splicing and can only be employed in a factory environment. Like tapering, dopant diffusion can be

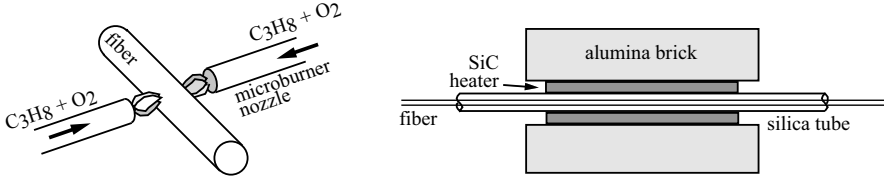

Fig. 8.5. Heat source alternatives to commercial fusion splicers for dopant diffusion. (**a**) Opposing microburners using propane and oxygen. After [8.36]. (**b**) Tube furnace constructed from silica tube positioned within silicon carbide heater in alumina brick. After [8.17]

performed prior to fusion splicing [8.32, 8.41]. The diffused fiber is then cleaved and fusion spliced to another fiber. Dopant diffusion can also be combined with other special splicing strategies such as tapering or bridge fibers.

When heating a fiber to high temperature for dopant diffusion, one must take care that it is not bent or kinked by poor alignment. Moreover, the temperature of the fiber must be kept low enough that surface tension does not squeeze down the fiber diameter (neckdown) and pinch off the fiber into two opposing tips (see Sect. 3.2.5 and especially Fig. 3.15).

The evolution of dopant diffusion performed on a completed fusion splice can be observed by monitoring the optical power coupled across the splice [8.28]. Light injection and detection (LID, Sect. 2.3.4), or simple power measurement, can be used to determine when the dopant diffusion has reduced splice loss to an acceptable level. However, when dopant diffusion is performed prior to fusion splicing, its progress cannot be monitored.

8.2.4 Low-Temperature Splices

In certain cases a *low-temperature splice* may improve the optical or even mechanical quality of a fusion splice. There are three main cases in which a low-temperature splice is advantageous: when fusion splicing similar fibers that are extremely susceptible to diffusion; when fusion splicing standard silica fiber to a fiber exhibiting a much lower viscosity or a much smaller diameter; and when fusion splicing microstructured fibers, which are discussed in Sect. 9.5. The main challenge when fusion splicing at low temperatures is to ensure that the fiber tips form a sufficiently strong joint exhibiting sufficiently low loss.

As discussed in the preceding section, dispersion-compensating type fibers (DCF) typically include thin annular regions that are heavily doped with fluorine to reduce their refractive index. These regions are particularly susceptible to dopant diffusion on account of their small spatial dimensions and the high diffusivity of fluorine in silica. When fusion splicing these fibers to themselves, there is no need for dopant diffusion. Instead, the objective is to minimize thermal damage to the fiber's refractive index profiles in the vicinity of the fusion splice. This can be accomplished with relatively fast fusion times and lower fusion power using a conventional fusion splicer.

In some cases, one may observe a vertical line at the location of a fusion splice performed at low temperatures as in Fig. 3.19. This line indicates that surface tension has not completely formed the joint between the two fibers. Nevertheless, fusion splices with such a "seam" can often pass stringent proof tests (200 kpsi or more) and can also exhibit low splice loss. However, a heavy vertical line appearing between dissimilar fibers fusion spliced at low temperature sometimes indicates the presence of a relatively abrupt refractive index boundary, which can result in elevated fusion splice reflectance, possibly as high as -40 dB. Fig. 8.6a depicts the physical appearance of a low-temperature

fusion splice whose initial reflectance was measured to be about -62 dB in Fig. 7.8 (*open circles*). The same fusion splice is shown in Fig. 8.6b following a few seconds of reheating at fusion splice temperatures, and the reheat reduced the reflectance below -70 dB (*dots* in Fig. 7.8).

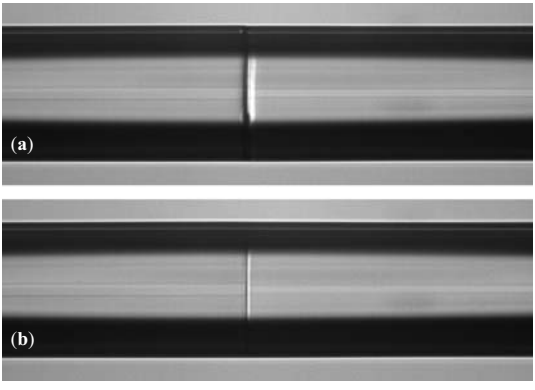

Fig. 8.6. Physical appearance of the fusion splices depicted in Fig. 7.8 showing the fusion splice (**a**) following a low-temperature fusion splice with a reflectance of about -62 dB and (**b**) following several seconds of reheating at fusion splice temperature which resulted in a reflectance substantially lower than -70 dB. The conventional matched clad SMF is on the left whereas the pure-silica core depressed-clad fiber is on the right. Substantial dopant diffusion in the radial direction is evident in the pure-silica core depressed clad fiber following the reheat. The corresponding axial dopant diffusion is responsible for the significant reduction in the reflectance

8.2.5 Offset Heating

Offset heating can facilitate fusion splicing between two fibers exhibiting very different viscosities or diameters. Fusion splices between such dissimilar fibers are more susceptible to neckdown (Sect. 3.2.5) because the smaller diameter fiber or the lower viscosity fiber is less resistant to surface tension forces. As (3.16) shows, larger diameter fibers require more heat to achieve splicing temperatures than smaller diameter fibers. This can be a problem when fusion splicing conventional 125 μm diameter fiber to 80 μm diameter fiber. The temperature distribution between two such fibers can be made more equitable by ensuring that the heat source is closer to the larger diameter fiber. Fusion splice quality can be improved by offsetting the heat source on the order of 50 μm so that the larger diameter fiber is preferentially heated.

Offset heating can also improve fusion splices between fibers exhibiting similar diameters but very different viscosities. For example, many large core multimode fibers are heavily doped and exhibit much lower viscosity than standard single-mode fiber. When fusion splicing a silica single-mode fiber to

a large core multimode fiber, offsetting the heat source to preferentially heat the single-mode fiber can improve the splice quality.

8.2.6 Tapered Splices

An optical fiber heated by a stationary or moving heat source can be *tapered* to a smaller diameter by applying sufficient tensile force (as shown in Fig. 3.8). Tapering can be performed at temperatures lower than fusion splicing as previously discussed in Sect. 3.2.1. Note that when a fiber is tapered, the outer cladding diameter, and the diameter of interior annular structures such as the core, are usually reduced by the same ratio, which is often termed the *taper ratio*. Also note that tapers can be combined with other special splicing strategies such as dopant diffusion or bridge fibers.

Unfortunately, some authors have confused fiber tapering with dopant diffusion by labeling the transition region of a fiber with diffused dopants as a "taper". We use the term taper to only refer to fibers whose outer diameter has been reduced by applying tensile force to the heated fiber.

In this section we will discuss the various mechanisms by which a taper can improve the optical characteristics of a fusion splice. Tapers in single-mode fibers can be categorized as to whether they are "weak" or "strong" in the sense that a weak taper continues to guide the optical signal in the core while a strong taper reduces the core diameter to the point where the optical signal is guided by the cladding surface. Note that optical fibers can be tapered either before or after a fusion splice. However, cleaving and fusion splicing a strongly tapered (thus small diameter) fiber can be challenging so strong tapers are normally performed after the fusion splice. Most commercial fusion splicing equipment has some degree of tapering capability.

Tapers must be made gradual enough to ensure that they are *adiabatic*, meaning that the guided optical signal is not coupled into lossy radiation modes by the taper. This topic has been extensively treated in several publications [8.7,8.8,8.11,8.20,8.29,8.30]. Making a taper more gradual will always reduce its excess loss. Given a fixed taper length, certain taper profiles are less lossy, and thus more efficient, than others.

Depending on the amount of diameter reduction, the mode field diameter (MFD) of the guided mode of a single-mode fiber can be either enlarged or reduced by tapering the fiber. This fact is illustrated in Fig. 8.7 in which the Petermann II mode field diameter given by (4.41) is plotted as a function of the fiber diameter for a standard 125 μm diameter SMF in air. The fraction of power traveling in the core is plotted as well. The fiber core Δ is assumed to be 0.35%, the untapered cladding diameter is assumed to be 125 μm, and the untapered core diameter is assumed to be 8.3 μm. Fig. 8.7 was computed using the scalar wave methodology of Sect. 4.4.3 since the Gaussian approximation introduced by Sect. 4.2.2 is highly inaccurate in the

strong taper region. Although the strong taper region involves strong refractive index contrasts (between the cladding and surrounding air) that violate the assumption of small refractive index contrasts (see Sect. 4.1.1), the scalar solution is sufficient to illustrate the behavior of the mode field. Most other single-mode fibers behave similarly to the standard step-index single-mode fiber depicted in Fig. 8.7.

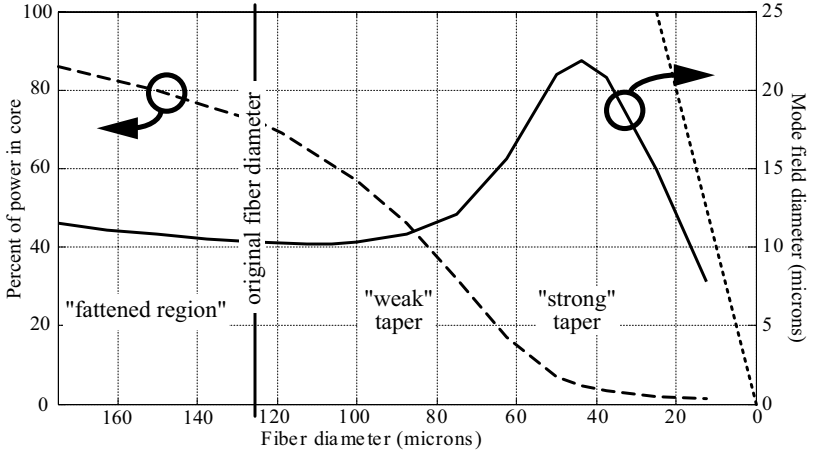

Fig. 8.7. Effect of a taper on the fundamental mode of standard step-index SMF fiber in air showing the percentage of power traveling in the core (*dashed line*) and the mode field diameter (MFD) computed according to (4.41) (*solid line*). The mode fields were computed using the methodology of Sect. 4.4.3. The cladding diameter is also plotted (*dotted*) for comparison to the MFD. The "fattened region" is included for the benefit of Sect. 8.2.7. Notice how the MFD experiences a local minimum in the weak taper region, but in the stronger taper region, the mode field diameter increases rapidly with shrinking fiber diameter until the approach of the cladding surface forces the MFD to shrink as well. The fiber core Δ is assumed to be 0.35%, the untapered cladding diameter is assumed to be 125 μm, and the untapered core diameter is assumed to be 8.3 μm

Figure 8.7 shows that for weak tapers, in which the fiber's diameter is between 80 and 125 μm, the mode field diameter (MFD) is nearly constant whereas a substantial fraction of the optical signal travels in the fiber's core. However, in the strong taper region, where the fiber's diameter is reduced below about 70 μm, the fiber's mode field diameter fluctuates and nearly all the optical signal travels in the cladding. In this strong taper region, the mode is actually guided by the air-glass interface on the surface of the cladding. In the strong taper region, the fundamental mode field is sensitive to the refractive index outside the fiber, and will be stripped out of the fiber if it is surrounded by a lossy medium, such as conventional high refractive index polymer coatings.

In the early days of optical fiber fusion splicing, when core eccentricity, cleave quality, and fiber alignment were significant challenges, tapering a completed fusion splice was an effective method for reducing splice loss by reducing the impact of lateral misalignment caused by core eccentricity or geometric deformation [8.12, 8.24]. Consider that a relatively weak taper that reduces the fiber diameter at the splice from 125 μm to 80 μm also reduces any inherent core eccentricity in the fibers by the same ratio, about 35%, whereas the fiber's MFDs remain substantially unperturbed. Since (4.44) shows the splice loss (in units of dB) resulting from core eccentricity varies with the square of the ratio between the core eccentricity and the fiber's MFD, such a taper can approximately halve the splice loss due to inherent core eccentricity (in units of dB) [8.24].

In addition to reducing the impact of lateral misalignment, tapering can benefit fusion splices in other ways. When splicing dissimilar fibers, tapering can be an effective way to reduce the mismatch in mode field size, or even shape [8.33, 8.38]. If the two fibers' normalized frequencies, their V-parameters given by (1.6), are sufficiently different, then one fiber can be considered "weakly guiding" while the other can be considered "strongly guiding" (weakly and strongly guiding fibers are unrelated to weak and strong tapers). In such a case, weakly tapering the completed fusion splice can cause the mode field diameter of strongly guiding fiber to decrease slightly while also slightly increasing the mode field diameter of the weakly guiding fiber [8.33, 8.38]. In certain cases this effect can reduce fusion splice loss resulting from mode field mismatch.

Sometimes fusion splice loss between dissimilar fibers can be reduced by initially tapering one of the two fibers prior to fusion splicing. This tapered fiber is then cleaved in the tapered region so that the mode field shapes are better matched at the splice joint. In this case, the diameters of the fiber tips may be different at the splice. Most commercial fusion splicers can handle fiber diameter mismatch, and when the smaller fiber is at least 70% of the diameter of the larger fiber, the cladding diameter mismatch usually won't affect the fusion splice. Figure 3.16 depicts a low-loss fusion splice between 100 μm and 125 μm diameter single-mode fibers. If a fiber is tapered to an extremely small diameter, typically less than about 70 μm, it will be very difficult to cleave and fusion splice on conventional splicing equipment.

Strong tapers can be used to achieve low-loss joints between very different optical fibers according to a method developed by Mortimore [8.31]. As Fig. 8.8 demonstrates, when a single-mode optical fiber surrounded by air is strongly tapered, the optical energy, formerly guided by the core, is guided by the cladding-air interface. This occurs because the cross sectional area of the core structure is made extremely small. In such a case, the details of the core refractive index structure have a negligible impact on the guiding properties of the fiber, therefore fibers with radically different refractive

index profiles may be coupled with low loss. The strong taper must occur over a long enough length to ensure that the transitions are adiabatic, thus minimizing lossy coupling to radiation modes.

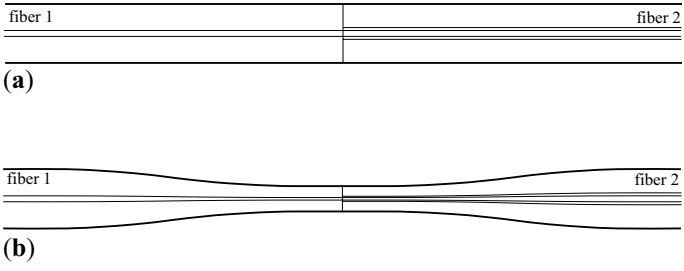

Fig. 8.8. Strong tapers can reduce splice loss between highly dissimilar fibers. (*a*) Completed splice between dissimilar fibers 1 and 2 prior to tapering. (*b*) Fusion splice following strong taper which converts core guided modes into cladding guided modes at splice joint thus reducing mode field mismatch loss. The thin lines represent the core refractive index structures in the fibers, which are different. The strong taper must occur over a long enough length to ensure that the transitions are adiabatic, thus minimizing lossy coupling to radiation modes. After [8.31]

The strong taper requires that the taper must be applied after the splice is completed because it is very difficult to cleave and fusion splice such strongly tapered fibers. Since the mode fields are converted into cladding modes by the strong taper, they are sensitive to the refractive index of the material surrounding the fiber. Consequently these fusion splices cannot be recoated with conventional high refractive index polymer. The mechanical strength of these strongly tapered fusion splices may be substantially reduced by their reduced cross sectional area. When fusion splicing fibers exhibiting substantially different viscosities or initial cladding diameters, it will be difficult to ensure that both sides of the fusion splice are evenly tapered [8.23]. Also, it can be difficult to ensure that the fusion splice remains in the center of the tapered region during the taper process. Most of these disadvantages could be overcome by overcladding the fusion splice with a low refractive index silica capillary tube (such as a heavily fluorine-doped capillary tube) prior to tapering [8.31].

Perhaps surprisingly, tapers are not particularly effective for coupling optical signals between single-mode and multimode fibers (Sect. 4.3.4 and [8.22]). Mode field diameter is not the only difference between single- and multimode fibers. A multimode fiber guides many distinct modes, each traveling at a unique velocity and each exhibiting a unique phase at a splice joint. In contrast, the optical signal in a single-mode fiber by definition exhibits a single mode with a single phase at the splice joint. As a result, even the best physical taper exhibits many dBs of loss when connecting single-mode with multimode fibers. Moreover, the time variation in the relative phases and rel-

ative optical powers in a multimode fiber can cause the splice loss between a single-mode and multimode fiber to vary over time. Finally, unlike the splice loss between two single-mode fibers, the splice loss between a single-mode and a multimode fiber as well as the splice loss between two multimode fibers are directionally dependent.

8.2.7 Fattened Splices

In addition to tapering, fusion splice loss can sometimes be reduced by "fattening" the splice, which is the opposite of a taper (see Fig. 3.7). To fatten a fiber, an axial compressive force is applied to heated fiber. As discussed in Sect. 3.2, the tendency of an optical fiber to buckle limits the amount of compressive force that may be applied, and so fattening a fiber requires temperatures similar to that of fusion splicing. Special heat sources (moving or stationary) may be required to achieve best results [8.23]. Most commercial fusion splicers can fatten a fiber by feeding the fiber chucks together while the fibers are heated. In theory, fibers can be fattened before or after fusion splicing.

As Fig. 8.7 shows, as a standard SMF fiber is fattened from its original diameter of 125 μm, the mode field diameter slowly increases as does the fraction of power traveling in the fiber core. Other fiber designs behave similarly. Thus, fattening a splice can locally increase the size of the mode field diameter. This local increase in the mode field diameter can help to reduce fusion splice loss between dissimilar fibers with very different mode field diameters. Fattened splices have been used to reduce the splice loss between standard SMF and high-NA, small core diameter fibers, which have a smaller mode field diameter [8.23].

The fattened region of a fiber must be sufficiently gradual to prevent energy from coupling to lossy radiation modes or leaky cladding modes [8.20]. Low loss fattened splices may require wide heat sources or moving heat sources to ensure that radiation losses are minimized.

Fattened splicing can be combined with other special splicing strategies such as dopant diffusion. In addition, a weakly tapered fiber of one type could be fusion spliced to a fattened fiber of another type to reduce mode field diameter mismatch induced splice loss.

8.3 Summary

The quality of a fusion splice, including both optical and mechanical characteristics, are determined by the details of the fusion splicing process, which are themselves determined by a plethora of splice parameters. The quality of a fusion splice can be efficiently improved by conducting a series of designed experiments to systematically search the parameter space for the

optimum set of splice parameters (the global quality maximum). Fractional factorial orthogonal arrays are helpful for rapidly identifying the most important splice parameters and their relative contribution to splice quality by fabricating relatively few fusion splices. Full factorial experimental designs may be necessary when there are strong interactions between fusion splice parameters. Analysis-of-variance (ANOVA) is useful for computing the statistical significance of splice parameters on splice quality. Other techniques such as response surface methodology (RSM) can also be used to search for the global quality maximum.

Fusion splice quality can also be improved by employing one of several special splicing strategies including: fire polishing, bridge fibers, dopant diffusion, low-temperature splicing, offset heating, fiber tapering, and fiber fattening. Most of these special strategies are geared towards splicing single-mode fiber, which are governed by more stringent quality requirements than multimode fibers. Many special fusion splicing strategies can be performed with commercial fusion splicing equipment. Each special fusion splicing strategy is defined by its own set of processing parameters, which may require systematic optimization to achieve the best fusion splice quality. Aspects of certain fusion splicing strategies may be patent protected.

9. Fusion Splicing of Specialty Fiber

The development of specialized fusion splicing technologies has been driven by the emergence of a wide variety of specialty optical fibers. In this Chapter we introduce several types of specialty optical fibers and discuss the role of specialized fusion splicing technologies, such as those described in Sect. 8.2. Our discussion of specialty fiber fusion splicing explicitly relies upon the fundamental concepts introduced and developed in earlier chapters.

The most challenging fusion splices are those between dissimilar fibers, such as those between specialty fibers and conventional single-mode fiber (SMF). This is a common problem since conventional SMF is widely used as a *pigtail*, which is a fiber used to terminate specialty fibers or optical fiber devices.

To some extent, the fibers discussed in this chapter are arranged in order of increasing fusion splice complexity, beginning with non-zero dispersion-shifted fiber (NZ-DSF), followed by polarization-maintaining (PM) optical fibers, erbium-doped fibers (EDF), dispersion-compensating fibers (DCF), and concluding with microstructured fibers. These categories of specialty fibers are not mutually exclusive. For example, certain erbium-doped fibers incorporate PM fiber technology so fusion splicing such fibers requires a combination of the EDF and PM fiber splicing technologies described in this Chapter.

9.1 Non-Zero Dispersion Shifted Fibers

Non-zero dispersion-shifted fibers (NZ-DSF) are single-mode fibers designed to exhibit lower chromatic dispersion than conventional SMF in the 1550 nm telecommunications band. These fibers are primarily intended to supersede conventional SMF as high-bandwidth telecommunications transmission fibers for long-distance applications. They are not as challenging to fusion splice as the other more complex specialty fibers described later in this Chapter. However, there are subtleties associated with fusion splicing NZ-DSF, which we describe in this Section.

9.1.1 Introduction to NZ-DSF

Chromatic dispersion distorts optical signals by causing different wavelengths to travel at different group velocities. It accumulates along a length of fiber at a rate that depends on the material composition of the fiber as well as its refractive index profile. In the 1550 nm telecommunications window, conventional SMF has a dispersion of about +17 ps/nm km, which results from a combination of *material dispersion* and *waveguide dispersion*. Material dispersion is, as its name suggests, a property of silica glass, whereas waveguide dispersion depends on the details of the fiber index profile and resulting mode field distribution.

NZ-DSF achieves lower values of chromatic dispersion and hence minimizes the distortion of a propagating optical signal by exploiting a complex refractive index profile exhibiting negative dispersion to offset positive material dispersion. The dispersion of typical NZ-DSF is on the order of +3 to +10 ps/nm km [9.1]. Zero chromatic dispersion is avoided in the transmission band because it leads to undesirable non-linear system impairments in wavelength-division-multiplexed (WDM) transmission systems.

The index profiles of NZ-DSF are more complex than the simple step-index profile of conventional SMF. Figure 9.1 depicts some sample index profiles used to make NZ-DSF. The mode field diameter (MFD) of NZ-DSF is typically on the order of 8.5 to 9.8 μm at 1550 nm [9.1–9.3], which is slightly smaller than that of conventional SMF (whose MFD is about 10.5 μm at 1550 nm). Some types of NZ-DSF are engineered to have a large MFD, on the order of 12 μm [9.4], in order to minimize undesirable intensity-dependent non-linear transmission impairments.

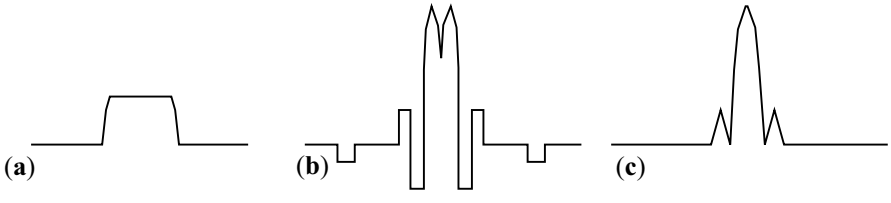

Fig. 9.1. Comparison of index profiles of (**a**) conventional SMF, (**b**) trench-style NZDSF, and (**c**) ring-style NZ-DSF. Index profiles not drawn to scale. After [9.1].

9.1.2 Special Splicing Considerations for NZ-DSF

Acceptably low losses for fusion splices between similar conventional SMFs are on the order of 0.05 dB whereas between similar NZ-DSFs they are often twice as high [9.3]. The higher fusion splice losses of NZ-DSF are tolerated because of their superior dispersion characteristics. Like conventional SMF,

NZ-DSF can be readily spliced by conventional fusion splice equipment in all types of environments: during device or cable manufacturing in a factory; during cable installation in the field; and in the research laboratory.

Optimized splice losses between conventional SMF and NZ-DSF range from about 0.05 dB to as high as 0.15 dB at 1550 nm [9.3]. The relatively small MFD mismatch between NZ-DSF and conventional SMF usually contributes between 0.03 and 0.1 dB to the splice loss [9.5]. The difference in mode field diameter between these dissimilar fibers can cause significant errors when measuring the fusion splice loss with an OTDR in only one direction [9.2, 9.6]. The mode field shape of NZ-DSF is somewhat less Gaussian in shape than conventional SMF, which also contributes to fusion splice loss, and reduces the accuracy of the splice loss approximation formulae developed in Sect. 4.2.2.

As we learned in Sect. 4.2.2, the smaller mode field diameter characteristic of a typical NZ-DSF makes fusion splice loss more sensitive to core eccentricity or lateral misalignment. Moreover, the complex refractive index profiles and correspondingly complex mode field shapes of NZ-DSF usually make these fibers more sensitive to core deformation than conventional SMF [9.6]. As a result, fusion splices involving NZ-DSF are generally more sensitive to manufacturing imperfections as well as improper fusion splice parameters. Fusion splices involving NZ-DSF are much more sensitive to cleave angle than those of conventional SMF and therefore require higher quality cleaves with angles below 1 degree [9.2].

The fusion splice optimization techniques described in Sect. 8.1 are an effective way to overcome some of the challenges associated with fusion splicing NZ-DSF. NZ-DSF fusion splices optimized on conventional equipment may result in a certain amount of dopant diffusion in the vicinity of the splice. However, fusion splicing of NZ-DSF usually does not require explicit implementation of special fusion splicing technologies, such as those described in Sect. 8.2.

9.2 Polarization-Maintaining Fibers

Polarization-maintaining (PM) optical fibers are single-mode fibers designed to preserve the polarization state of a propagating signal, even in the presence of external perturbations such as fiber bends or external forces which would otherwise alter it. The features of PM fibers responsible for this unique capability also necessitate specialized fusion splicing technology. A comprehensive review of PM fiber technology is available in [9.7]. Reviews of contemporary PM fiber fusion splice technology are available in [9.8–9.10]. In this section we discuss the special technologies associated with fusion splicing PM fibers.

Polarizing (PZ) fibers are another category of polarization sensitive fibers that are closely related to PM fibers. Unlike PM fibers, a PZ fiber is an optical fiber version of a linear polarizer, as it only guides a single linear polarization.

Because of their similarities, the fusion splicing subtleties associated with PM fibers also apply to PZ fibers. Consequently, the material presented in this section for PM fibers is also applicable to most PZ fibers.

9.2.1 Introduction to PM Fibers

All optical signals are polarized, meaning that the electric field corresponding to the optical signal oscillates in a direction perpendicular to the direction of signal propagation. Propagating optical signals can be linearly polarized, meaning that their electric field oscillates in a single unchanging transverse direction, circularly polarized, meaning that the direction of electric field oscillation steadily rotates around the direction of signal propagation, or elliptically polarized, which is combination of the preceding two states. The electric field of so-called "unpolarized" optical signals oscillates in a transverse direction that changes randomly at such a rapid rate that no preferred direction can be sensed by the detector.

Conventional single-mode optical fibers are designed to be axisymmetric so that the axial propagation constant (Sect. 4.1.2), and therefore the group velocity of a propagating signal, is independent of polarization state. A perfectly axisymmetric single-mode fiber will preserve the polarization state of a propagating signal since it can't couple energy between optical signals propagating in distinct polarization states. However, an intrinsic asymmetry such as a slightly elliptical core, or an extrinsic asymmetry such as a bend in the fiber, will couple energy between distinct polarization states. In a PM fiber, a strong intrinsic asymmetry in the refractive index profile ensures that distinct polarization states propagate with very different group velocities and modal propagation constants, so that weak extrinsic perturbations have a minimal impact on the polarization state of the propagating signal.

PM fibers exhibit a high degree of *birefringence* resulting from their non-axisymmetric refractive index profile. In a PM fiber, there is a particular axis for which a linearly polarized mode will exhibit a maximal axial propagation constant (and a minimal group velocity), which is termed the slow-axis. The orthogonal linear polarization state exhibits a minimal axial propagation constant (and a maximal group velocity), and is thus termed the fast-axis. The birefringence of a few PM fibers results from a non-axisymmetric distribution of dopants that directly produces a non-axisymmetric refractive index profile, which is termed *form birefringence*. More conventionally, the birefringence of PM fibers results from non-axisymmetric residual thermal stresses that indirectly induce a non-axisymmetric refractive index profile in the vicinity of the core, which is termed *stress birefringence*.

PM fibers were among the earliest specialty fiber types and were available within 10 years of the development of the first low-loss optical fibers. Since that time, several different varieties of PM fibers have been developed, and a few of the more common PM fiber designs are schematically depicted in

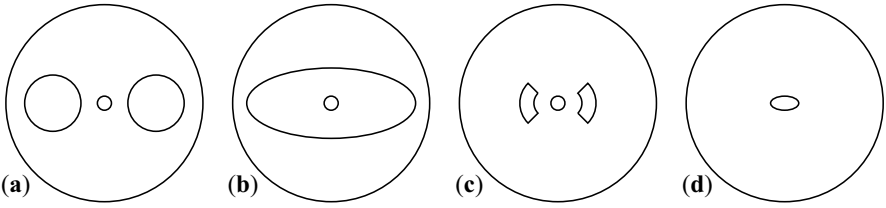

Fig. 9.2. PM fiber designs include (**a**) those with circular stress-applying members in the cladding, also known as *TruePhase*^{TM} or *Panda*^{TM} fibers, (**b**) those with an elliptical stress-applying member in the cladding, also known as *Tiger*^{TM} fibers, (**c**) those with "bow-tie" stress-applying members, and (**d**) those with an elliptical core

Fig. 9.2. PM fibers are widely used for sensing applications, such as in optical fiber gyroscopes, as well as for coherent telecommunications applications and for polarization multiplexing.

The PM fiber designs depicted in Fig. 9.2a-c all derive their birefringence from the presence of *stress-applying members* in the cladding. The stress-applying members are comprised of doped-silica glasses whose thermal expansion coefficients and elastic properties are very different from those of the cladding glass, which is typically comprised of pure silica. These discrepancies in material properties enable the stress-applying members to induce residual thermal stresses that lead to desirable levels of birefringence in the fiber's core.

In addition to conventional performance characteristics such as loss or long-term reliability, PM splice quality also depends on the splice's effect on the polarization state of the optical signal. As we shall see, the splice's effect on the optical fiber's polarization state is in turn largely dependent upon the rotational alignment of the fiber tips.

9.2.2 Cleaving Considerations for PM Fibers

As we learned in Sect. 2.2, a fiber cleave results from a crack that travels across the fiber end face at the sonic velocity. Since the stress-applying members have different elastic properties from the rest of the fiber's cladding, they also have different sonic velocities. As a result, a crack may not grow evenly across the end face of a PM fiber as it does in a conventional single-mode fiber. Moreover, the residual thermal stresses present in PM fibers can perturb the crack propagation direction. Small cracks in the vicinity of the stress-applying members are very common features of a PM fiber cleave.

For these reasons, it is harder to achieve a good quality cleave with PM fiber compared to conventional fiber. Inferior cleave quality can lead to excessive core deformation in a fusion splice and therefore excess splice loss. PM fiber cleave quality is more sensitive to the cleave tension, and may require

a slightly lower cleave tension than the optimum for equivalent conventional fibers. Fig. 9.3 depicts a particularly crack riddled PM fiber cleave resulting from inappropriate cleave tension.

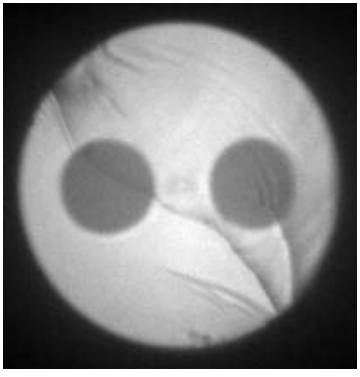

Fig. 9.3. Severe cracks apparent on the end face of a 125 μm diameter polarization-maintaining (PM) optical fiber cleaved under inappropriate conditions

9.2.3 Polarization Crosstalk and Polarization Extinction Ratio

PM fibers are designed to isolate optical signals traveling in orthogonal polarization states. In an ideal PM fiber optical power cannot transfer between orthogonal polarization states. In reality, there is always some small amount of optical power exchanged between orthogonal polarization states, which is termed *polarization crosstalk*, and the amount of polarization crosstalk is typically proportional to the PM fiber length. The ratio between the measured optical power in two orthogonal polarizations is termed the *polarization extinction ratio*, which is typically expressed in dB units. The extinction ratio can measure the extent to which an originally pure polarization state has been degraded by polarization crosstalk in the system.

Extinction ratio and crosstalk are often confused despite the fact that they are quite distinct: the extinction ratio is a parameter that can be directly measured at a discrete location in an optical fiber span, whereas crosstalk is a performance parameter characterizing the coupling between orthogonal polarization states that can occur at a discrete location (such as a fusion splice) or can be distributed over a length of fiber. The extinction ratio measured at a discrete location depends on the polarization crosstalk accumulated from all the components in the optical fiber span upstream of the measurement.

A PM fiber fusion splice manifests itself as localized source of polarization crosstalk. Usually, it is desirable to minimize fusion splice polarization crosstalk in order to minimize the total crosstalk in the entire fiber span and maximize the extinction ratio measured at the end of the span. Minimizing

the polarization crosstalk at a fusion splice requires that the fast and slow axes of the two fiber tips be rotationally aligned to each other, in addition to conventional lateral alignment of the fiber cores (Sect. 2.3). Since conventional fusion splicers generally do not perform rotational fiber alignment, special PM fusion splicers have been developed for this purpose (Chap. 10). As we shall see below, the quality of the rotational alignment is a major determinant of the splice's polarization crosstalk [9.11]. In the next Section we will discuss several approaches for performing rotational fiber alignment. As we learned in Sect. 3.2.3, rotational fiber alignment can also be exploited to mitigate the effect of core eccentricity in conventional (non-PM) fibers.

Figure 9.4 [9.8] depicts a typical setup for estimating the polarization crosstalk of a fusion splice by measuring the effect of a fusion splice on polarization extinction ratio. Accurately measuring polarization crosstalk of an individual fusion splice is difficult, so we are usually concerned with obtaining the best possible polarization extinction ratio measured just downstream of a PM fiber fusion splice. The PM fusion splice polarization crosstalk measurement is performed in two stages (depicted as Fig. 9.4a and b). Since a polarization extinction ratio measurement depends on the polarization crosstalk of each component, the setup must first be calibrated according to Fig. 9.4a [9.8].

Fig. 9.4a depicts a single continuous section (length L_1) of PM fiber with a light source coupled at its input through an input linear polarizer and a detector coupled at its output through an output linear polarizer. To calibrate the system, the rotational orientation of the input polarizer is adjusted such that when the output polarizer is rotated through a large angle (∼180 degrees), the detected power experiences a maximum amount of variation. Once the input polarizer's best rotational alignment is found, it is fixed in place and the output polarizer is then rotated to measure the maximum detected power, which occurs at the *major axis*, and then rotated 90 degrees to the position of minimum detected power, which is termed the *minor axis*. In this case, the extinction ratio measured at point B, ER_{B}, can be expressed as

$$ER_{\mathrm{B}} = 10\log_{10}\left(\frac{P_{\mathrm{major}}}{P_{\mathrm{minor}}}\right) \tag{9.1}$$

where P_{major} is the power measured at the major axis and P_{minor} is the power measured at the minor axis. The major and minor axes will coincide with either the fast and slow axes or the slow and fast axes of the PM fiber, respectively. The measured polarization extinction ratio at position B, ER_{B}, is reduced from infinity by the inherent polarization crosstalk in the fiber itself, α_{c1}, as well as the imperfect nature of the polarizer and the optical couplings [9.8].

Once the baseline polarization extinction ratio of the system is measured, another segment of PM fiber can be fusion spliced onto point B and the output of this second segment of fiber coupled through the output polarizer into the detector (Fig 9.4b). The addition of a fusion splice and a second

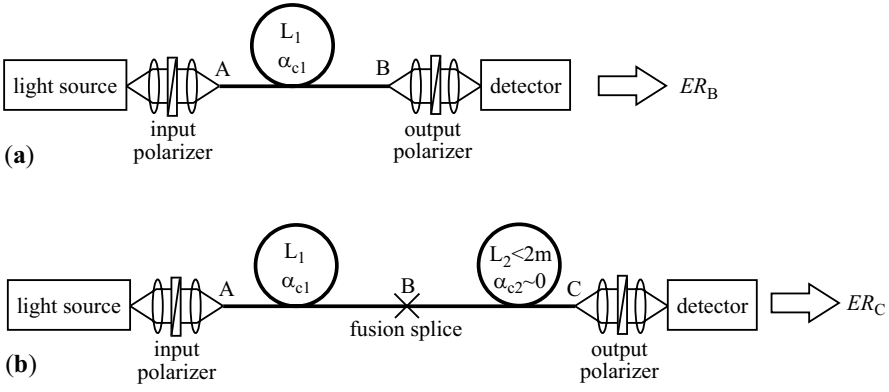

Fig. 9.4. Schematic illustration of a typical setup for estimating the polarization crosstalk of a PM fiber fusion splice by measuring the polarization extinction ratio. Shown is (**a**) measurement of baseline polarization extinction ratio just prior to a fusion splice and (**b**) measurement of extinction ratio just after a fusion splice. Bulk lenses are shown coupling the light across the polarizers. Adapted from [9.8]

segment of PM fiber can only make the situation worse by adding more sources of polarization crosstalk, so ER_{B} is the best possible polarization extinction ratio that can be measured at point C, ER_{C}.

In order to maximize the sensitivity of the measurement, the second PM fiber length, L_2, should be as short as possible (ideally $<\sim 2\,\mathrm{m}$ [9.8]) so that it will have a negligible polarization crosstalk and $\alpha_{\mathrm{c}2} \sim 0$. Then, the extinction ratio measured at point C can be expressed as [9.8]

$$ER_{\mathrm{C}} = 10\log_{10}\frac{1+\rho_{\mathrm{B}}\cos 2\theta_{\mathrm{misalign}}}{1-\rho_{\mathrm{B}}\cos 2\theta_{\mathrm{misalign}}} \tag{9.2}$$

where

$$\rho_{\mathrm{B}} = \frac{10^{|ER_{\mathrm{B}}|/10}-1}{10^{|ER_{\mathrm{B}}|/10}+1} \tag{9.3}$$

and $\theta_{\mathrm{misalign}}$ represents the rotational misalignment of between the two fiber tips at the PM splice.

To accurately measured the angular misalignment at a fusion splice, ER_{B} and ER_{C} are measured according to the procedure described above and then (9.2) and (9.3) are solved for $\theta_{\mathrm{misalign}}$. In reality, the angular misalignment is less important than the resulting measured extinction ration downstream of the fusion splice, ER_{C}.

Equations (9.2) and (9.3) are plotted in Fig. 9.5 for several different values of ER_{B}. The polarization extinction ratio resulting from the polarization crosstalk exclusively contributed by the misalignment of the fusion splice is represented by the solid line in the figure, which would be measurable if the baseline extinction ratio ER_{B} was infinite. In this idealized case we could express the extinction ratio as

$$ER_{\infty} = 10 \log_{10} \left(\tan \theta^2_{\text{misalign}} \right) \ . \tag{9.4}$$

This equation relating rotational misalignment at a fusion splice to the polarization extinction ratio is frequently found in the literature [9.10]. Since the baseline extinction ratio, ER_{B}, will always be finite (typically <40 dB), the portion of the polarization extinction ratio exclusively resulting from the rotational misalignment at the splice is not directly measurable.

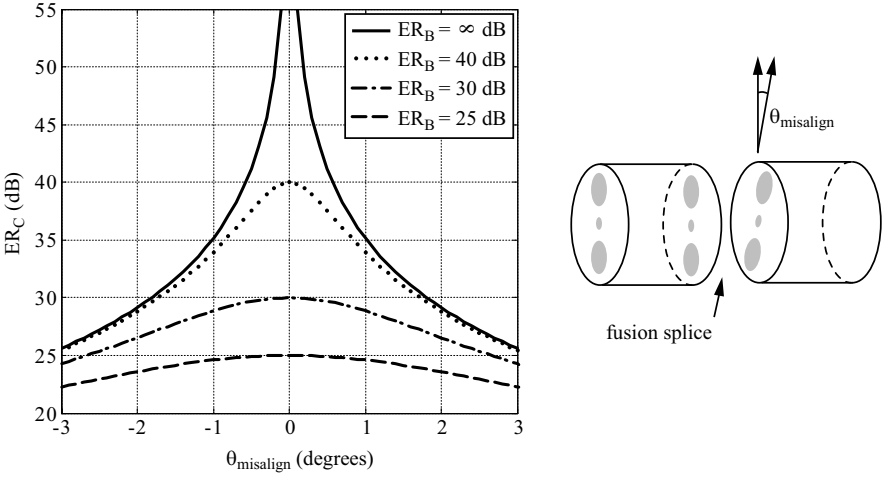

Fig. 9.5. ER_{C} as a function of the rotational misalignment between two PM fibers, θ_{misalign}, and the inherent polarization extinction ratio of the experimental setup, ER_{C}, in Fig. 9.4. Figure at left adapted from [9.8] and at right adapted from [9.12]

Because the guided mode in a PM fiber cannot ever be perfectly linearly polarized [9.13] ER_{B} cannot exceed about 45 dB. In high quality PM fusion splices, the polarization crosstalk induced by rotational misalignments and other imperfections typically results in a measured polarization extinction ratio (ER_{C}) on the order of 30 dB.

Any source of rotational misalignment is of great concern because the rotational alignment of PM fibers has a critical impact on the splice's polarization crosstalk. Poor quality cleaves, especially those with angles greater than about 1 degree, can cause the fiber tips to shear and rotate when they are pressed together during the hot push stage of the fusion splice process [9.8, 9.10].

9.2.4 PM Fiber Alignment

As is the case for conventional fiber alignment (Sect. 2.3), several different strategies for rotationally aligning PM fibers have been developed including sideview [9.8], (also known as either a profile alignment system (PAS) or

as polarization observation by lens-effect-tracing (POL)), endview, and active alignment [9.8, 9.14], in which the extinction ratio is actively monitored during fiber alignment. Most commercial fusion splicers employ the sideview approach, but the endview or active alignment approaches offer certain advantages.

Sideview PM fiber alignment takes advantage of the fact that the stress-applying members in a PM fiber typically have a different refractive index than the rest of the fiber's cladding. These index differences cause light traversing the fiber to be refracted. Thus, fine details apparent in the transverse image of most PM fibers will vary depending on the rotational orientation of the fibers. The relationship between the fiber's rotational orientation and the details of light and shadow near the fiber's core are quite complex, so it is sometimes difficult to properly interpret the image. It is essential that the fiber tips be stripped and cleaned properly to prevent coating residue or other contaminants from confounding the image processing algorithms responsible sideview PM alignment. A detailed description of one type of algorithm used to perform sideview alignment is available in [9.15].

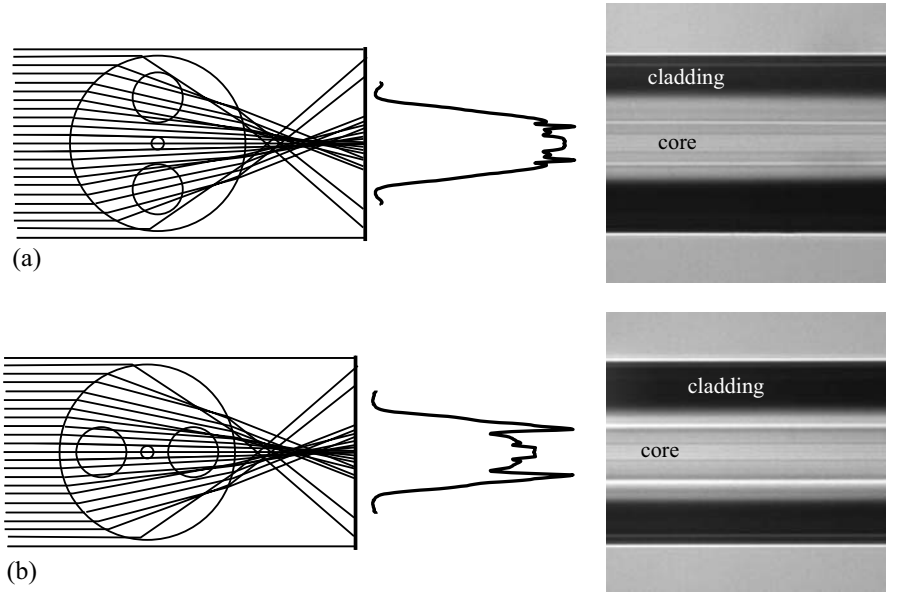

Fig. 9.6. Illustration of sideview, or PAS, alignment for PM fibers with stress-applying-members in (**a**) vertical and (**b**) horizontal rotational orientations. The ray traces (*left*) show how the internal structure of the PM fibers refracts the transverse illumination to result in characteristic intensity profiles (*middle*) and corresponding fiber images (*right*). See Sect. 5.1.3 and Fig. 5.5 for a more complete discussion of ray tracing during transverse fiber illumination. Figure adapted from [9.8, 9.10]

Most conventional fusion splicers already incorporate the basic elements required for sideview fiber imaging in order to perform lateral alignment (Sect. 2.3) as well as loss estimation (Chap. 5). Sideview alignment is less effective on elliptical core fibers, which do not include stress-applying members, because their sideview image has a relatively weak dependence upon rotational orientation.

The phenomena permitting sideview PM rotational alignment, namely the fact that the appearance of the fiber core depends upon the rotational orientation of the fiber, is actually an impediment to accurate loss estimation. As discussed in Chap. 5, accurate loss estimation depends on an accurate determination of the core position based on a transverse image of the completed splice. Stress-applying members add features to the transverse image of a fusion splice, making it harder for image processing algorithms to determine the core position. For this reason, PM fibers typically exhibit significantly inferior loss estimation accuracy compared with conventional fibers [9.10]. Optimized fusion splices between similar PM fibers usually exhibit less than 0.1 dB of loss.

Endview alignment utilizes a mirror system to show an end-on view of the cleaved PM fiber tips (Fig. 9.7). One advantage of this approach over sideview alignment systems is the ability to more easily identify the type of PM fiber and its rotational alignment. Furthermore, the endview approach is well suited to imaging the orientation and structure of microstructured fibers (Sect. 9.5), which is nearly impossible using a conventional sideview. Achieving sufficient endview contrast depends upon coupling different amounts light into the stress-applying-members compared with the remainder of the cladding. This can be accomplished by illuminating the region near the interface between the stripped and coated fiber with an LED. Sometimes a scattering agent is painted onto the coating near this strip interface in order to increase the amount of light coupled into the fiber.

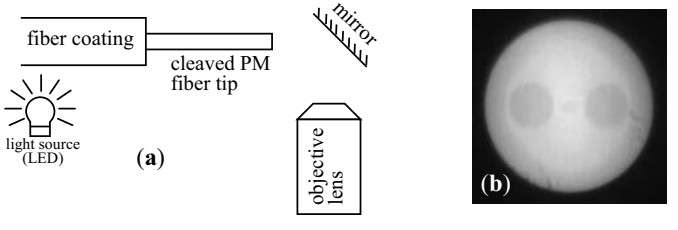

Fig. 9.7. (**a**) Schematic illustration of an endview imaging system for PM fiber alignment and (**b**) a typical endview of a PM fiber clearly showing the orientation of the stress-applying members. An LED light source is coupled into the fiber near the interface between the stripped and coated portion of the fiber tip. Note the small cracks near the periphery of the fiber, which are typical of PM fiber cleaves and result from residual stresses as well as differences in the mechanical properties of the glass comprising the cladding and the stress-applying members

In an active alignment system [9.8,9.14], the two PM fiber tips are laterally aligned to each other and separated by a small air gap. A polarized source launches light with a known polarization state into one of the fiber while a polarization analyzer monitors the polarization state of the light emerging from the other fiber, or reflected from the interface. The rotational alignment of the two fiber tips is adjusted to yield the best polarization and then the fibers are fusion spliced together. In principle, active alignment can achieve the best quality PM fiber splice. However, it requires access to the input and possibly the output fiber ends, as well as both a polarized source and polarization analyzer.

Many PM fiber fusion splicers now offer "polarization extinction ratio estimation" based on an assessment of the rotational misalignment of the completed splice. Fusion splicers employing sideview PM alignment are inherently capable of gauging the rotational alignment of the fiber on either side of a completed PM fiber splice (Fig. 9.8). Mathematical models such as (9.1-9.3) are employed to convert the misalignment detected by image processing into an estimate for the polarization extinction ratio that would be measured just after the splice.

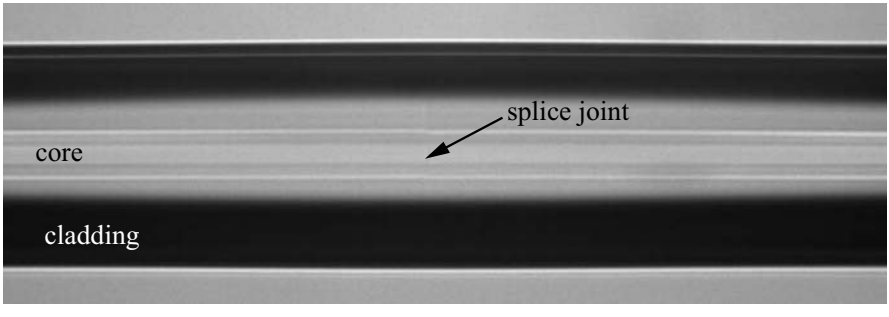

Fig. 9.8. Image of a typical PM fiber splice. The stress-applying members are misaligned by about 2 degrees in this splice, leading to a best case polarization extinction ratio measurement of about 29 dB, which is fairly typical of decent quality PM fusion splices. This misalignment leads to a barely perceptible difference in the appearance of the core region of the fibers that is nevertheless accurately detected by polarization extinction ratio estimation routines

9.3 Erbium-Doped Fibers

In the early 1990's the development of *erbium-doped fiber amplifiers* (EDFAs) utilizing *erbium-doped fiber* (EDF) revolutionized optical fiber telecommunications by enabling the simultaneous amplification of many distinct high bandwidth optical signals, each carried on a different wavelength using an

approach termed *wavelength division multiplexing* (WDM). EDFs enabled optical signals to travel remarkably long distances, in some cases longer than 1000 km, without having to convert the optical signal into an electrical signal for amplification and back into an optical signal for transmission, a costly and inefficient process. However, exploiting the potential of EDF required solving several important technical challenges, including fusion splicing EDF to other transmission fibers. EDFAs are complex devices incorporating large numbers of specialized optical fiber fusion splices, as depicted in Fig. 1.8b.

Amplifier fibers such as EDF can also be used to fabricate optical fiber lasers by attaching a reflective element to the beginning and end of the fiber thus forming a laser cavity. High-power optical fiber laser and amplifier technology has recently emerged as an important area of research. Special technologies originally developed for fusion splicing EDF are also applicable to other types of gain fibers, such as ytterbium-doped gain fibers. As a result, the specialized fusion splicing technologies discussed in this Section are also relevant for the rapidly advancing field of optical fiber lasers and amplifiers.

Excellent reviews of EDF, EDFAs, and fiber lasers and amplifiers are available in [9.16, 9.17]. In this section we review the challenges of fusion splicing EDF and similar fibers and discuss relevant fusion splicing technologies.

9.3.1 Introduction to Erbium-Doped Gain Fibers

Erbium-doped fiber is typically a single-mode silica fiber with a relatively small diameter core doped with erbium as well as germania, alumina, and other dopants. In order to achieve high amplification efficiency [9.18, 9.20], the difference in refractive index between the core and the cladding, known as Δn, is typically between 0.013 to 0.04 in EDF, which corresponds to an NA of 0.2 to 0.35, both of which are much higher than that of conventional SMF. EDF is typically spliced to either conventional SMF or a smaller core single-mode step-index fiber designed to serve as a pigtail.

According to (1.6), preventing the extremely high-Δ core of EDF from guiding higher-order modes necessitates a very small core diameter, sometimes as tiny as 3 μm. Such small core diameters result in small fundamental mode field diameters (MFD), whose size can be estimated using (4.43). The MFD of EDF at 1550 nm can be as small as 3.8 μm, which is much smaller than the 10.5 μm MFD of conventional SMF. According to (4.44), such a severe MFD mismatch will lead to a fusion splice loss of almost 4 dB!

The MFD mismatch between EDF and standard SMF is not the only important source of fusion splice loss. The mismatch in the shape of the mode field will also contribute to the total splice loss. Furthermore, the very small MFD of most EDF makes such fibers particularly sensitive to lateral core offsets resulting from eccentric core fiber or core deformations at the splice joint. For all of these reasons, EDF can be particularly challenging to fusion splice. As is the case when fusion splicing other specialty fibers, cleave

quality must be maximized to help ensure minimal core deformation and low splice loss.

EDF can only amplify an optical signal when it is accompanied by optical *pump energy*. The wavelength of the pump is shorter than that of the optical signal experiencing amplification, and is typically 915 or 1480 nm. The pump energy is combined with the optical signal by a wavelength combiner (multiplexer), which is often a fused taper coupler. Dopants in the core of the EDF convert the optical energy from the pump into the signal. In principle, the pump wavelength can also experience fusion splice loss between EDF and its pigtail fiber, but this loss usually can be ignored since the availability of pump energy is usually not the principal constraint on EDFA performance.

9.3.2 Strategies For Low-Loss EDF Fusion Splicing

As described in the preceding Section, EDF is difficult to fusion splice with low-loss because of MFD and mode field shape mismatch as well as increased sensitivity to both core eccentricity and geometric deformations. Two approaches have been applied to the problem of fusion splicing EDF: dopant diffusion (Sects. 3.3 and 8.2.3) and bridge fibers (Sect. 8.2.2). These distinct special splicing strategies can also be combined with each other.

Dopant diffusion is particularly effective for reducing EDF fusion splice loss. As we learned in Sect. 3.3, the rate of diffusion scales with the square of the core diameter, so the inherently small core diameter of EDF leads to rapid core dopant diffusion. Moreover, some of the key dopants comprising the core of EDF, such as erbium and alumina, diffuse more rapidly through silica compared to conventional optical fiber dopants such as germania.

EDF is frequently fusion spliced to conventional SMF, which has both a larger core diameter and MFD, as well as relatively slow-diffusing dopants (primarily germania). Heat treating a fusion splice between EDF and standard SMF causes the MFD of the EDF to quickly "catch up" to the much more slowly expanding MFD of the SMF [9.19]. For this reason, sufficiently low-loss (often less than 0.1 dB) fusion splices between EDF and SMF can often be achieved in a conventional fusion splicer by simply extending the splice heating time (known as the fusion time on some equipment) so that significant dopant diffusion can occur inside the EDF as a part of the fusion splice process [9.19, 9.21]. As discussed in Sect. 4.1.5, axial dopant diffusion across the splice joint itself can help to reduce the splice's reflectance to below -110 dB [9.22], which is too small to measure using most commercially available reflectometers. Fig. 5.4 shows how dopant diffusion changes the appearance of EDF during a fusion splice to SMF. Section 4.4.5 contains a beam propagation method (BPM) numerical simulation of a fusion splice between conventional SMF and EDF.

In addition to dopant diffusion, bridge fibers (Sect. 8.2.2), also known as intermediate fibers, can also be exploited to achieve low-loss EDF fusion

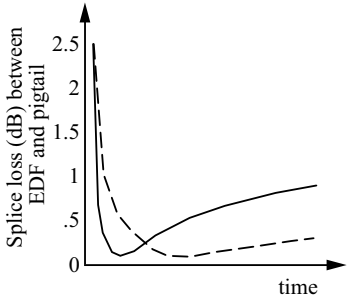

Fig. 9.9. Comparison of time dependence of fusion splice loss at a relatively high fusion splice temperature (*solid line*) and at a relatively low fusion splice temperature (*dashed line*). Adapted from [9.19]

splices [9.23]. Bridge fibers can reduce the total fusion splice loss between EDF and conventional SMF below 0.1 dB. Since EDF and its pigtail are both typically step-index fibers, designing an appropriate bridge fiber is not particularly challenging. When designing such bridge fibers, predictions based on the exact mode fields will be noticeably more accurate than those using the Gaussian approximation. As noted in Sect. 8.2.2, one disadvantage of the bridge fiber approach is the need to perform two separate fusion splices for each interconnection between EDF and its pigtail.

Active monitoring of the measured transmitted power can also be used to achieve low-loss EDF fusion splices [9.24, 9.25]. Figure 9.9 illustrates how fusion splice loss varies with time at two different fusion splice temperatures. At higher temperature, the diffusion proceeds more rapidly so that a minimum in the fusion splice loss is attained at an earlier time followed by a rapid escalation in loss. The minimum in the splice loss can be automatically obtained by terminating the heating when the splice loss begins to increase with time. As we discuss in the next Subsection, direct measurement of EDF splice loss is difficult to perform, so often the total transmitted optical power is monitored instead of the actual splice loss. Sometimes, the blackbody infrared emission of the heated fiber will contribute to the total transmitted signal, complicating detection of minimal splice loss. Instead of monitoring the transmitted power, an image of the cores in the heated fiber can be directly obtained (Sect. 5.1.3), and has been used to determine the optimal amount of heating [9.19].

Lin and Lin [9.26] as well as Takahara [9.27] have shown how the quantum efficiency of erbium-doped fiber lasers sensitively depends on fusion splice quality. They examined several techniques, including tapering and intermediate fibers, for improving the fusion splice loss between EDF and a standard SMF pigtail. Best results were obtained by pre-tapering the tip of the standard SMF pigtail prior to fusion splicing to the EDF. However, these investigators did not carefully explore the advantages of dopant diffusion.

9.3.3 Loss Measurement of Erbium-Doped Fiber Splices

EDF is designed to amplify optical signals in the near infrared between about 1530 and 1560 nm. Special types of EDF, or other types of gain fiber, are used to amplify signals in nearby wavelength bands. The gain band of EDF has helped to fix the location of contemporary WDM telecommunications to be in the vicinity of 1550 nm. However, the core dopants responsible for the amplification of the optical signal in the presence of pump energy will strongly absorb the optical signal in the absence of a pump. Moreover, unlike the relatively weak, linear optical fiber attenuation encountered in conventional transmission fiber, the absorption of an un-pumped EDF can be quite strong and also non-linear. Therefore, the amount of optical signal absorbed by only a few centimeters of EDF can be large and yet difficult to predict. As a result, it is difficult to accurately measure the fusion splice loss of EDF in its amplification band using the techniques discussed previously in Chap. 7 [9.21].

A common approach for overcoming the difficulties of measuring splice loss in EDF is to measure the splice loss at a wavelength outside the fiber's amplification band, for example near 1310 nm, since such wavelengths are not strongly absorbed [9.28]. Although fusion splices can, and in general, do exhibit wavelength dependent loss (Sects. 4.2.2 and 5.2.3), there is typically a strong correspondence between splice loss measured at similar wavelengths, so the splice loss of EDF measured at 1310 nm is a reasonable approximation to the splice loss at the operating wavelength of 1550 nm. Splice loss resulting from core deformation at 1310 nm is usually slightly higher than the loss measured at longer wavelengths, such as 1550 nm.

Although some investigators have reported that the fusion splice loss between single-mode EDF and other single-mode fibers is directionally dependent [9.21], this cannot be true for rigorously single-mode fibers, as we derived in Sect. 4.1.3. Recent experimental [9.28] and theoretical work [9.28, 9.29], support the view that the fusion splice loss between a purely single-mode EDF and other single-mode fibers is indeed independent of direction.

9.4 Dispersion-Compensating Fibers

Dispersion-compensating fibers (DCFs) are single-mode fibers designed to reverse the deleterious effects of chromatic dispersion, which distorts optical signals by causing different wavelengths to travel at different group velocities. The remarkable dispersion characteristics of DCF result from a carefully tailored refractive index profile. However, the special refractive index profile of DCF typically cause elevated fusion splice loss. DCF can be assembled into discrete optical components, termed dispersion-compensating modules (DCMs), or can be directly employed as transmission fiber, in which case the DCF is termed *inverse dispersion fiber* (IDF) or *reverse dispersion fiber*

(RDF). The material presented in this section is relevant to all of these types of DCF.

The role of DCF in optical fiber telecommunications systems is growing in importance since higher bit rates are more sensitive to chromatic dispersion and therefore require increasingly powerful and complex dispersion compensation. The fusion splice loss of DCF is important because the performance of a dispersion compensated optical fiber span depends on its loss budget, as well as its chromatic dispersion.

Excellent reviews of contemporary DCF technology are available in [9.1, 9.30]. In this Section we discuss how the special attributes of DCF make low-loss fusion splicing a challenge, and we review technologies for overcoming those challenges.

9.4.1 Introduction to Dispersion-Compensating Fibers

In order to compensate for the positive dispersion of conventional SMF, a DCF fiber must exhibit negative dispersion. A fiber with negative dispersion can be made by carefully tailoring its index profile so that a large negative waveguide dispersion overwhelms the smaller positive material dispersion. An optical fiber with a small core diameter and correspondingly large Δ will exhibit such desirable properties. Practical considerations, such as minimizing fiber attenuation and macrobend loss, as well as a desire to regulate the wavelength dependence of the dispersion (termed the *dispersion-slope*) can be satisfied by an index profile that incorporates a highly up-doped core, a deeply down-doped trench, and a slightly up-doped ring [9.30] as depicted in Fig. 9.10.

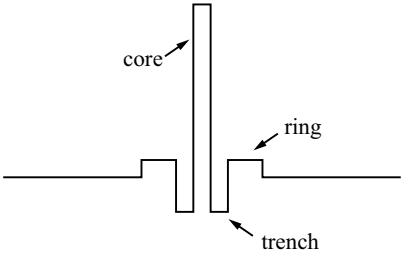

Fig. 9.10. Typical index profile for DCF showing the high-Δ core, a deeply down-doped trench, and an updoped ring. After [9.30]

The small core size of DCF results in a MFD diameter on the order of 5 μm at 1550 nm [9.30], which is about half the size of conventional SMF. Equation (4.44) predicts that such a discrepancy in MFD results in a splice loss on the order of 2 dB. Actually, this Gaussian approximation is not very accurate because the complex index profile of DCF results in a relatively

non-Gaussian mode field shape, as demonstrated in Fig. 4.8. The discrepancy between the mode field shape of DCF and the highly Gaussian mode field shape of standard SMF also contributes significantly to fusion splice loss [9.31]. Finally, the heavily down-doped ring found in most DCF is comprised of fluorine-doped silica [9.30], and as we learned in Sect. 3.3, fluorine diffuses very rapidly through silica at fusion splicing temperatures. As a result, the loss of a conventional fusion splice between most types of DCF and conventional SMF is unacceptably high, and special splicing strategies are required.

The relatively small MFD of DCF also makes fusion splices involving DCF much more sensitive to manufacturing imperfections, such as core eccentricity, as well as splice imperfections, such as core deformation. As is the case for other types of specialty fibers, low-loss DCF fusion splices require excellent cleave quality, with angles below 1 degree.

The large negative waveguide dispersion of dispersion-compensating fibers results from the fact that the MFD is very wavelength sensitive. This helps to explain why fusion splices between certain types of DCF have been shown to be wavelength dependent [9.4,9.32], which can be a problem in WDM systems incorporating numerous channels spread over a wide optical bandwidth.

DCF is not always fusion spliced to conventional SMF. Non-zero dispersion-shifted fiber (NZ-DSF) is increasingly used as a transmission fiber in place of conventional SMF. Since many types of NZ-DSF have a smaller MFD than conventional SMF, these types of NZ-DSF can exhibit lower splice loss to DCF than conventional SMF [9.32]. However, when a DCF is used as a transmission fiber, as in the case of IDF or RDF, a special large-effective-area fiber is usually employed as a positive dispersion transmission fiber in place of conventional SMF [9.1]. Such large-effective-area fibers have larger MFDs [9.4], making fusion splicing to DCF an even greater challenge [9.31].

9.4.2 Splicing Strategies for Dispersion-Compensating Fibers

As in the case of EDF, the elevated fusion splice loss when fusion splicing DCF to other types of SMF primarily results from a mismatch of MFD and mode field shape. Therefore, many of the same strategies effective for EDF fusion splicing, such as bridge fibers and dopant diffusion, are effective when applied to DCF fusion splicing. Dopant diffusion was described in Sect. 3.3 and 8.2.3 whereas bridge fibers were described in Sect. 8.2.2. In this Section we describe how these strategies have been applied to reduce splice loss between DCF and other fibers.

It is important to note that the fusion splicing behavior of DCF is very sensitive to its material composition and design. We have already described how there are many types of DCFs serving many applications. Early types of DCF were packaged on a spool and used to compensate transmission spans that are entirely composed of conventional SMF. Newer types of DCF compensate for both the dispersion and dispersion-slope of specific types of NZ-DSF. Yet

other types of DCF, such as IDF, are used as transmission fibers themselves and are designed to compensate for the dispersion of a dedicated type of large-effective-area NZ-DSF. A fiber manufacturer may tout the relative ease with which their particular DCF can be fusion spliced, but this advantage may be insignificant when considering the performance of a fiber span employing their fiber. Furthermore, the details of DCF fusion splicing strategies are often kept as trade secrets. For these reasons, the results reported in this section must be compared with care.

Optimizing the fusion splice parameters naturally leads to some amount of dopant diffusion since the fluorine dopant present in most types of DCF is known to diffuse rapidly at fusion splice temperatures [9.30]. Conventional arc-fusion splicers usually cannot achieve fusion splice losses below about 0.7 dB between conventional SMF and DCF [9.30]. Some investigations have claimed fusion splice losses as low as 0.1 dB between DCF and conventional SMF using dopant diffusion, but in these cases their equipment, methodology, or fiber characteristics were not detailed [9.33, 9.34].

Flame heating a completed fusion splice between an IDF and a large MFD NZ-DSF has been shown to yield splice losses on the order of 0.2 dB at 1550 nm with low wavelength dependence [9.4, 9.35]. One disadvantage of flame heating is that it is unsuitable for field splicing although it may be suitable for splicing in a manufacturing environment. A variant of the fire-polishing technology described in Sect. 8.2.1, called arc-scanning, has been used to obtain splice losses on the order of 0.5 dB between the same IDF and NZ-DSF using conventional fusion splicing equipment [9.4, 9.36]. This strategy can be readily implemented in commercial field splicing equipment.

Bridge fibers have been used to reduce fusion splice loss between DCF and conventional SMF from 0.7 dB to 0.4 dB [9.37]. The index profile of the bridge fiber was similar to the DCF except that it did not include a fluorine doped trench around the core. The fusion splice between the DCF and the bridge fiber exhibited about 0.15 dB loss and was a low-temperature splice (Sect. 8.2.4) in order to minimize fluorine diffusion. The splice between the bridge fiber and conventional SMF exhibited about 0.25 dB loss and was done at relatively high temperature with a long heating time to enable dopant diffusion to help match the index profile and MFD of the fibers [9.37].

In a separate investigation [9.4], a 9.5 μm MFD negative dispersion fiber was used as a bridge fiber between a large-effective-area NZ-DSF and an IDF. Depending on the splicing equipment, total losses as low as 0.37 dB were achieved [9.4]. There was some wavelength dependence in the total splice loss. Ohsono and coworkers reported total splice losses of about 0.3 dB between a DCF and a large-effective-area NZ-DSF using a NZ-DSF as a bridge fiber [9.32]. Some wavelength dependent splice loss was also apparent in their data.

Bridge fibers can be used in both field and factory fusion splicing environments. They can be accommodated into standard splice trays and splice

housings [9.4]. However, as noted earlier, two splices are required to complete a single interconnection and the length of bridge fiber must be long enough to minimize modal noise (Sect. 4.2.4) resulting from two splices in close proximity [9.4].

9.5 Microstructured Fibers

Microstructured fibers are optical fibers that contain voids running longitudinally along their length. Although they may be filled with any gas, liquid, or even a vacuum, these voids typically look like air holes when viewed in cross section (Fig. 9.11), so microstructured fibers are also termed *holey fibers*. Since the refractive index contrast between the glass and the voids is very large, and is in fact much larger than the refractive index contrast available in fibers fabricated from conventional doped silica, microstructured fibers can achieve waveguiding properties unattainable by conventional doped-silica fibers. Although the first microstructured fibers were fabricated over 25 years ago [9.38], there has been an explosion of microstructured fiber research over the past few years. Filling the voids with special gases or liquids can be exploited to yield a variety of unique functionalities.

In this section we describe the unique challenges associated with fusion splicing microstructured fiber as well as some recently developed approaches for overcoming those challenges. Readers interested in microstructured fiber are directed to several excellent reviews discussing their history, design, fabrication, and applications [9.39–9.41].

9.5.1 Types of Microstructured Fibers

When a large number of small air-filled voids completely surround a central core region of solid glass, a microstructured fiber can function as a waveguide analogous to a conventional doped-core optical fiber. The effective refractive index of the solid glass core region is higher than that of the surrounding void-filled glass, so an optical signal can be guided in the solid glass core. This class of microstructured fiber is termed *index-guiding* microstructured fiber and a typical example is depicted in Fig. 9.11a.

Photonic crystal fibers (PCFs) also known as photonic bandgap fibers (PBF) are another class of microstructured fiber whose voids exhibit a sufficiently periodic regularity that they can be described as a *photonic crystal* [9.42]. Like the bandgap in a crystalline material, the regular periodicity of the voids in a photonic crystal prohibits certain wavelengths of light from propagating in certain directions. A localized irregularity in the photonic crystal, for example at the center of the fiber, can serve as a waveguiding core, once again analogous to a doped-core in a conventional optical fiber. Since PCFs do not rely on effective-index waveguiding, their core can be comprised of an air-filled void instead of solid glass.

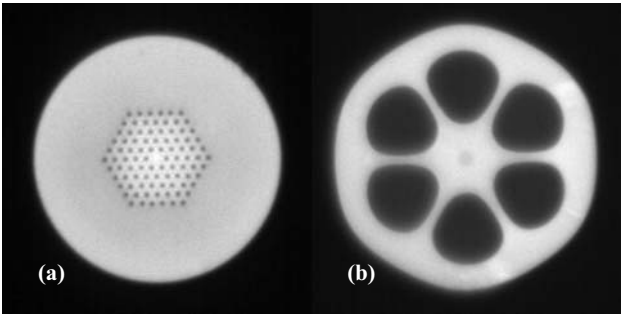

Fig. 9.11. Two different types of microstructured fiber: (**a**) solid-core index-guiding pure-silica microstructured fiber in which the air holes are responsible for waveguiding and (**b**) doped-core with large air holes that are not responsible for waveguiding. Both fibers are about 125 μm in diameter

Microstructured fibers can also incorporate features associated with conventional optical fibers, such as regions of doped glass [9.43–9.46], in which case they are sometimes referred to as *hybrid microstructured fibers*. The optical signal traveling in the doped core of these fibers typically interact weakly with the voids situated in the cladding. Fig. 9.11b depicts an example of such a doped-core microstructured fiber.

9.5.2 Fusion Splicing Microstructured Fibers

The development of microstructured fiber has been limited by the fact that these fibers are generally difficult, and in some cases even impossible, to fusion splice using conventional technologies [9.47]. For this reason, fusion splicing microstructured fiber is an important area of research that is likely to impact the future direction of optical fiber technology. In this Section we will review the challenges associated with fusion splicing microstructured fiber and some recently developed approaches to meet those challenges.

The unique characteristics of microstructured fibers can lead to differences in fiber preparation for fusion splicing. For example, liquid solvents are usually not used when stripping the polymer coating from microstructured fibers since such solvents will wick into the fine air holes. Furthermore, microstructured fibers can exhibit unique cleaving characteristics. As we learned in Sect. 2.2, the optimal cleave tension for a silica fiber is approximately proportional to the fiber diameter raised to the 3/2 power. When the cross sectional area of a microstructured fiber contains a large fill-fraction of voids, the optimal cleave tension may be somewhat lower than that predicted by the diameter of the fiber. Moreover, the cleave must propagate around the voids as it traverses across the fiber, which can lead to a somewhat inferior cleave surface compared to conventional fibers [9.63].

Fusion splicing microstructured fibers to conventional fibers is difficult because microstructured fibers are designed to have mode field sizes and

shapes that are radically different from conventional silica fibers [9.46, 9.60]. Microstructured fibers are attractive because they can have extraordinarily large or small MFDs (from <1 μm to >50 μm), in contrast to conventional single-mode fibers whose MFDs almost always lie between 2 and 15 μm.

Aside from MFD mismatch, the shapes of microstructured fiber mode fields can be very different than conventional fibers resulting in elevated mode field overlap losses when they are spliced to conventional fibers. The guided mode fields of most microstructured fiber are hexagonally symmetric, rather than radially symmetric like conventional single-mode fibers. Even if the mode field diameters of the two fibers are well matched, differences in rotational symmetry or the shape of the mode field can lead to splice loss [9.61]. The hexagonal symmetry of microstructured fiber can require fiber tips to be rotationally aligned to each other like PM fibers, discussed earlier in this Chapter. When the mode field shapes are known, the overlap integral, (4.36), can be used to estimate coupling losses due to mode field size, symmetry, and shape mismatch.

Ultimately, the mode field overlap loss depends on the fiber design, and as such, microstructured fiber design can be constrained by the mode field overlap losses associated with conventional fibers. Some recent investigations have probed the relationship between microstructured fiber design and overlap losses to conventional fibers [9.49–9.52]. Brute force numerical techniques such as finite element analysis can be used to compute the mode field shape of a microstructured fiber design. Estimating the mode field overlap loss requires simplified analytical equations to estimate the mode field shape and size based on the microstructure geometry in the fiber [9.49, 9.52]. Effective index approaches for modeling microstructured fibers have been used to predict the spectral characteristics of splice losses [9.50].

A second major challenge to fusion splicing microstructured fibers results from heat-induced damage to the microstructure occurring during fusion splicing. This problem can affect fusion splices between identical microstructured fibers as well as between dissimilar fibers such as a conventional fiber spliced to a microstructured fiber. As mentioned above, microstructured fibers usually derive their unique capabilities from voids that run axially along the length of the fiber. As we saw in Sect. 3.2, in order to form a conventional fusion splice joint between two silica optical fiber tips, the tips must be heated to the point that surface tension overcomes the viscosity of the glass. However, this not only forms a joint, but also collapses the fine voids of microstructured fiber as well [9.53, 9.54] (Fig. 9.12b). In Sect. 3.2.6 we learned that the velocity of void collapse is largely independent of hole size and is well described by (3.30), so smaller holes will inevitably collapse before larger ones. Consequently finer voids experience more severe damage than larger diameter voids. Maintaining a positive pressure in the voids can inhibit collapse, but it is difficult to maintain pressure inside the voids at a cleaved end during fusion splicing. Since the voids are usually responsible

for waveguiding, their destruction in the vicinity of a fusion splice can lead to high losses, well in excess of a dB. Moreover, refractive index matching oils cannot be used to fabricate mechanical splices from most microstructured fiber since such oils will wick into the voids [9.46] and induces loss in a manner similar to collapsed voids.

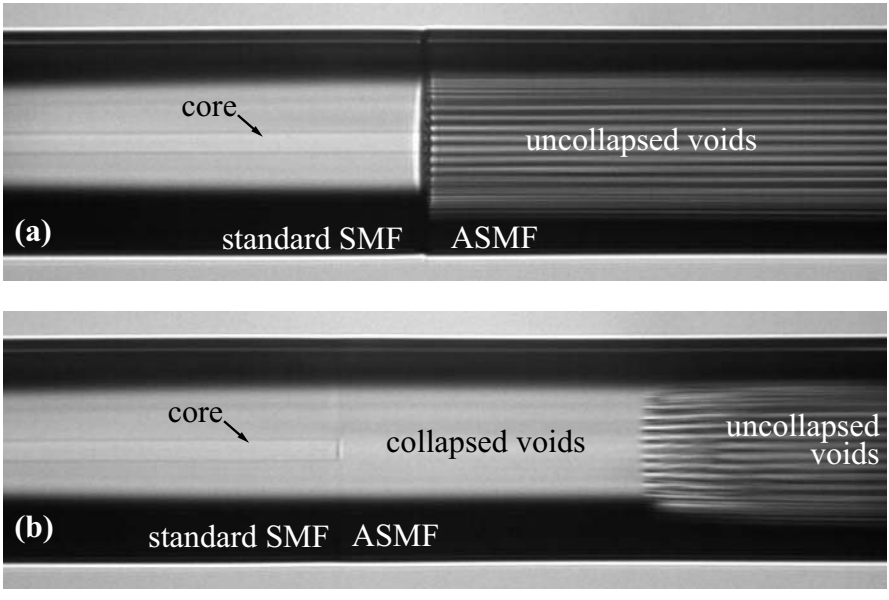

Fig. 9.12. (**a**) Solid-core index-guiding pure-silica microstructured fiber fusion spliced to standard SMF using short-duration low-temperature fusion splice parameters. Although the voids remain substantially unaffected by the fusion splice and the two fiber tips are physically attached, the joint is extremely weak and will exhibit very poor long term reliability. (**b**) Same fibers fusion spliced using conventional fusion splicing parameters results in total collapse of the air holes over a length of about 150 µm and a corresponding loss of waveguidance over this region. Although the fusion splice is very strong and will exhibit excellent long-term reliability, the splice loss is excessively high (>2 dB). Both fibers are about 125 µm in diameter

As a result, most microstructured fibers have been coupled to other fibers or to sources or detectors with *free-space coupling*, meaning bulk optics such as conventional lenses. Alternatively, microstructured fibers can be cleaved and directly *butt coupled* against other fibers as in a mechanical splice, without any heating or index matching oil. As we learned in earlier chapters, important advantages of fusion splicing include potentially lower reflectance, compactness, automatic and permanent alignment, and the absence of exposed optical surfaces that can be contaminated or damaged, especially by

high optical power densities. For all of these reasons, genuine fusion splices are preferred to either free space coupling or butt coupling.

By significantly reducing the duration and the temperature of the fusion splice process, a fragile joint can be formed while minimizing collapse of the air holes [9.54–9.56] as shown in Fig. 9.12a. This approach is a variant of the low-temperature fusion splices previously described in Sect. 8.2.4, and splice durations can be as short as 0.5 s [9.56]. Unfortunately, these joints rarely exhibit the high mechanical strength characteristic of true fusion splices (>100 kpsi). Moreover, they may exhibit elevated reflectance as detailed in Sect. 4.1.5. As we learned in Chap. 6, the long-term reliability of fusion splices has been linked to their mechanical strength, so relatively fragile low-temperature microstructured fiber splices are expected to exhibit relatively poor long-term reliability. Depending on the fiber combination, there can be a tradeoff between the higher mechanical strength but higher optical loss associated with a long-duration high-temperature fusion splice and the lower mechanical strength but lower optical loss of a short-duration low-temperature fusion splice [9.56].

Another approach for overcoming void collapse when fusion splicing microstructured fiber involves the use of a graded-index (GRIN) fiber lens [9.57–9.59]. A GRIN fiber lens is a short segment (typically <1 mm long) of graded-index multimode fiber, which can transform the MFD of an optical signal. The GRIN lens can enable an optical signal to traverse a region of fully collapsed voids in much the same way that a regular lens can collimate light to travel across a region of empty space. Using this approach, reasonably low-loss high-strength fusion splices were demonstrated between conventional SMF and an index-guiding microstructured fiber [9.58, 9.59].

One notable exception to the challenge posed by surface-driven hole collapse occurs in the case of hybrid microstructured fibers that include a doped core [9.43–9.46]. Since the guided optical signal typically interacts only weakly with the voids in the cladding, low-loss high strength fusion splices can be achieved in the presence of substantial hole collapse. Of course mode field mismatch loss can still contribute to elevated splice losses so the doped cores of hybrid fibers are usually designed to be well matched to that of other conventional fibers.

Another unusual challenge associated with fusion splicing microstructured fiber is contamination of the voids with cleaning solvents, water vapor, or ambient dust [9.54, 9.62]. This possibility may prohibit the use of solvents for stripping or cleaning microstructured fiber tips. A fusion splice joint will seal off the voids and can trap contaminants or gasses inside the voids. During a fusion splice, rapidly expanding gasses released by contaminants can induce bubbles and damage the fine structure of the voids, thus inducing high losses.

9.6 Summary

Unlike conventional single-mode (SMF) or multimode fibers (MMF), achieving low-loss when fusion splicing specialty fibers usually requires specially optimized splice parameters and excellent cleave quality.

Non-zero dispersion shifted fibers (NZ-DSF) are characterized by a more complex index profile than conventional SMF and usually, but not always, exhibit a smaller MFD. They can be fusion spliced to each other and to conventional SMF with acceptably low-loss after suitable splice parameter optimization.

The tips of polarization-maintaining (PM) optical fibers must be rotationally aligned to each other to preserve the polarization state of the guided optical signal. To meet this need, specialized commercial fusion splices incorporating various imaging strategies and algorithms for rotational alignment have been developed.

Erbium-doped fibers (EDF) are typically fusion spliced to conventional SMF. Their relatively high core Δ and small core diameter requires the use of dopant diffusion and/or bridge fibers in order to achieve acceptable fusion splice loss. The fusion splice loss of EDF can be difficult to measure because the erbium dopants strongly absorb the optical signal when there is no optical pump energy present.

Fusion splices involving dispersion-compensating fibers (DCF), like EDF, can also benefit greatly from dopant diffusion or bridge fibers. The splicing performance of DCF varies widely depending on the fiber's design and application.

Microstructured fibers are the newest type of specialty optical fiber and generally present the most vexing challenges. High temperature experienced during fusion splicing collapses the voids responsible for waveguiding in these fibers, leading to excessive splice loss. Strategies such as low-temperature splicing or GRIN fiber lenses have been used to overcome these difficulties.

10. Splicer Hardware: State of the Art

When optical fibers were first developed in the early 1970's, they were fusion spliced on custom laboratory equipment, often using an oxy-hydrogen flame or a laser as a heat source. By the 1980's, simple optical fiber fusion splicers utilizing the more rugged and practical electric arc heat source were developed. As this book goes to press, a wide assortment of sophisticated fusion splicing equipment is commercially available. This variety ranges from lightweight portable field fusion splicers to fully automated fusion splicing workstations designed for mass production to highly flexible fusion splicers specifically designed with research applications in mind.

The capital cost of optical fiber fusion splicing equipment is much higher than that of mechanical splicing or connectorization equipment, as it ranges from about US$10,000 to US$100,000. However, fusion splicing is often less labor intensive than connectorization and yields optical fiber joints with superior optical performance and reliability compared to mechanical splices or connectors. When amortized over thousands of individual splices, the real cost of fusion splices can actually be lower than that of mechanical splices or connectors.

The large number of fusion splices in worldwide optical communication networks is apparent from the large global market for optical fiber fusion splicers. The total commercial market for fusion splicers was US$233 million in 2002 [10.1] and is expected to grow robustly over the next decade. In 1999, about half of the worlds fusion splicers were sold in North America while about one quarter were sold in the European and Asian markets respectively. By 2007 this market is expected to grow to nearly half a billion US$. Much of this growth is expected to occur in Japan and the Pacific Rim regions [10.1].

In Sect. 1.2 we described the complete fusion splice process, which includes several preparatory and concluding steps, as well as joint formation. Depending on their specific purpose, commercial fusion splicers often only perform a subset of the total fusion splice process. For example, field splicers, used during the installation and deployment of optical fiber cable, typically require supplemental equipment to strip and cleave the fiber tips (Chap. 2), and sometimes even for packaging the completed splice (Chap. 6). However, all fusion splicers perform some kind of alignment and form the actual joint with a heat source. Fig. 1.2 is a schematic depiction of the elements common

to most fusion splicers including fiber chucks for gripping and aligning the fibers, an imaging system (including a lens and CCD camera), a microprocessor, and a heat source.

In this chapter we describe a few representative commercial fusion splicers and provide an overview of the technology currently available in the commercial fusion splicing market. This survey of equipment is by no means exhaustive and certain commercial fusion splicers may incorporate special features that are not covered in this discussion. The interested reader is encouraged to contact fusion splicer manufacturers for more details regarding specific commercial fusion splicers.

10.1 Introduction to Splicer Hardware

Fusion splicer hardware can be categorized into three general groups: *field splicers*, *factory splicers*, and *laboratory splicers*. Generally speaking, field splicers are the least flexible, most portable, and lowest cost pieces of equipment since they are intended primarily to fusion splice standard single-mode fiber during installation of optical fiber networks. Mass fusion, or ribbon fiber, splicers are often designed as field splicers. Factory splicers need not be portable, but often need to be more flexible to accommodate more complex fiber designs such as polarization-maintaining (PM) fiber or erbium-doped fiber (EDF). Factory splicers often exhibit a high degree of automation and fast cycle times to increase production rates and yields. Finally, laboratory splicing equipment is sometimes laboratory-built, and is usually designed to be particularly flexible in order to accommodate a wide variety of optical fiber types, including fibers that are only used in research such as microstructured fiber.

10.2 Field Splicers

Field splicers are designed to fusion splice standard transmission fibers at remote locations during optical fiber installation. As such, field splicers must be rugged and portable. Field splicers typically include features to protect the fiber tips, the imaging system, and the heat source from environmental effects such as wind and rain. A typical field splicer is depicted in Fig. 10.1. A compact handheld field fusion splicer designed for installing fiber-to-the-home (FTTH) is depicted in Fig. 10.2.

Nearly all field splicers utilize an electric arc as a heat source since it can be made more rugged and compact than alternatives such as lasers, chemical flames, and resistive filaments. Fig. 10.3 shows the two electrode tips of a conventional electric arc splicer. Such tips are made of a refractory conductive material, usually tungsten, and require periodic cleaning to ensure the best

Fig. 10.1. A typical field fusion splicer, the *Fitel* model *S176CR*, showing loss estimation following a fusion splice. This unit is compact, lightweight, and can use a battery to facilitate splicing in remote field locations. Like all field splicers, the *S176C* uses an electric arc as its heat source. The splice includes a profile alignment system (PAS) consisting of a microscope objective, a CCD camera, and a microprocessor. This same system also performs accurate loss estimation. The large LCD screen displays images of the fibers during alignment and following the splice. Simple menu driven software permits the unit to be programmed for a wide variety of fusion splices. A wind screen (deployed over the splice in the image) protects the arc discharge from the ambient environment. The sophisticated capabilities and ergonomic nature of this splicer make it suitable for a factory as well as field environment. Photo courtesy of *Furukawa America, Inc.*

possible splice results. Over time, the electrode tips experience wear and must be replaced and calibrated. Calibration can be accomplished by observing the surface tension drive flow of an optical fiber subject to a known discharge current (Sect. 3.2.2) [10.2–10.4].

Typical field splicers include an imaging system, which consists of a high numerical aperture microscope objective and a system of mirrors to provide two orthogonal high magnification views of the fiber. Two orthogonal views of the fiber are critical to both fiber alignment and loss estimation. Mod-

Fig. 10.2. The *Fitel S321A* is a mini handheld field fusion splicer designed to splice single strands of SMF or MMF. This compact arc-fusion splicer weighs only 1 kg and incorporates battery power, a CCD based alignment system, an LCD monitor, automatic fiber alignment and splicing, a proof-tester, and can even include an oven for curing heat-shrink splice protectors. The time require for alignment and splicing is only about 15 seconds and the splice loss averages about 0.1 dB for SMF and 0.05 dB for MMF. Photo courtesy of *Furukawa America, Inc.*

ern CCD cameras and LCD display screens permit high resolution alignment and viewing of the fiber as well as accurate loss estimation. Most contemporary single-fiber field splicers can align the fiber tips based on an image of the fiber's core as well as the fiber's cladding. This type of core alignment is often termed a *profile alignment system*, or PAS. The low cost of modern microprocessors has led to the availability of substantial amounts of computation power in contemporary fusion splicers, which in turn permits sophisticated image processing and loss estimation. Easy-to-use menu driven software makes it easy for the operator to modify splicing parameters or to log data.

Mass fusion splicers, also known as ribbon fiber splicers, are often designed as field splicers and can often fusion splice a variety of ribbons designs ranging from single fiber strands up to contemporary 24 fiber ribbon cables. Mass fusion splicers can greatly reduce the cost per splice by simultaneously fusion splicing all the fibers in a ribbon fiber cable. Specialized ribbon fiber strippers, cleavers, and splice protectors are used in conjunction with such ribbon fiber

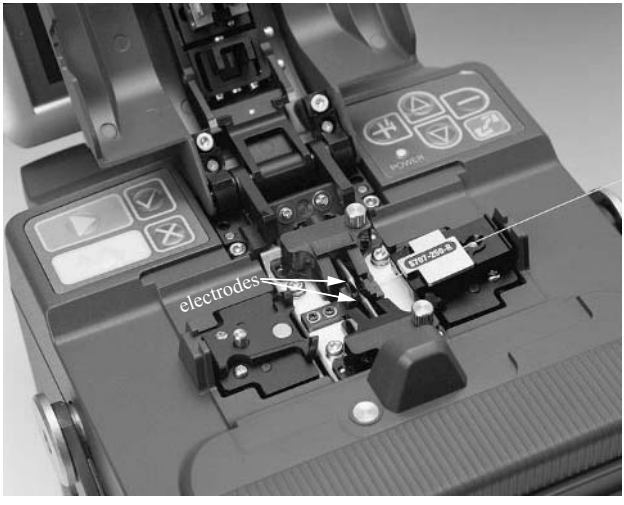

Fig. 10.3. Close up of the *Fitel S176CR*, clearly depicting the two opposing electrodes, labeled by white arrows in the center of the photo. The lower portion of the windscreen is visible in the top of the photo and is lifted up out of the way. The fiber chucks are removable in this type of fusion splicer. A standard 125 μm diameter optical fiber is loaded into the fiber chuck on the right side of the splicer. The left side fiber chuck is not loaded into the splicer. The operator uses the labeled buttons near the top of the photo to interact with the splicer's menu driven software. Photo courtesy of *Furukawa America, Inc.*

splicers. A typical contemporary mass fusion splicer is depicted in Fig. 10.4 and a close up of the fusion splice sequence is shown in Fig 10.5.

Mass fusion splicers do not align the individual fiber strands to each other, rather all the fibers in each cable are gripped by a special v-groove assembly and the two opposing v-groove assemblies are aligned to each other (Fig. 2.12). Needless to say, ribbon fibers are aligned based on their claddings, rather than their cores, and partly for this reason, the average fusion splice loss of ribbon fiber is somewhat higher than for standard single strand fusion splicers.

10.3 Factory Splicers

Unlike field splicers, factory fusion splicers need not portable, nor do they need to contend with environmental perturbations. However, factory splicers must be designed to maximize the yield and minimize the time required to complete the entire fusion splice process (including alignment and loss estimation), which is termed the *cycle time*. Moreover, factory equipment often must be flexible enough to effectively splice more challenging fiber designs such as polarization-maintaining (PM) fiber or dispersion-compensating fiber (DCF).

Fig. 10.4. The *Fitel S199M24* mass fusion splicer can simultaneously fusion splice all the strands of a 24 fiber ribbon cable. The LCD display on the front of the unit shows two orthogonal views of the 24 individual fiber strands with a small gap between the opposing fiber tips. Typical fusion splice losses are about 0.03 dB for standard single-mode fiber (SMF) and about 0.1 dB for non-zero dispersion-shifted fiber (NZ-DSF). This machine can be used in a field or factory environment. Photo courtesy of *Furukawa America, Inc.*

In some cases, high-quality field splicers, such as the *Fitel S176* depicted in Fig 10.1 can be effectively used in a factory environment. This fusion splicer has the added advantage of a remarkably short cycle time, only about 11 seconds [10.5].

A contemporary factory fusion splicer, the *Fitel S183* is depicted in Fig 10.6. This machine is designed to fusion splice PM fiber as well as other types of specialty fiber. PM fiber splicing, discussed in greater detail in Sect. 9.2, requires automatic identification of the stress-applying members and fiber chucks that can rotate the fiber tips relative to each other. The *Fitel S183* is flexible enough that it can also be used for fusion splicing novel fiber designs in a laboratory setting.

One of the most significant advances in factory fusion splicing hardware over the past decade has been the development of fully automated fusion splicing systems. By fully automated we mean that the entire splice process

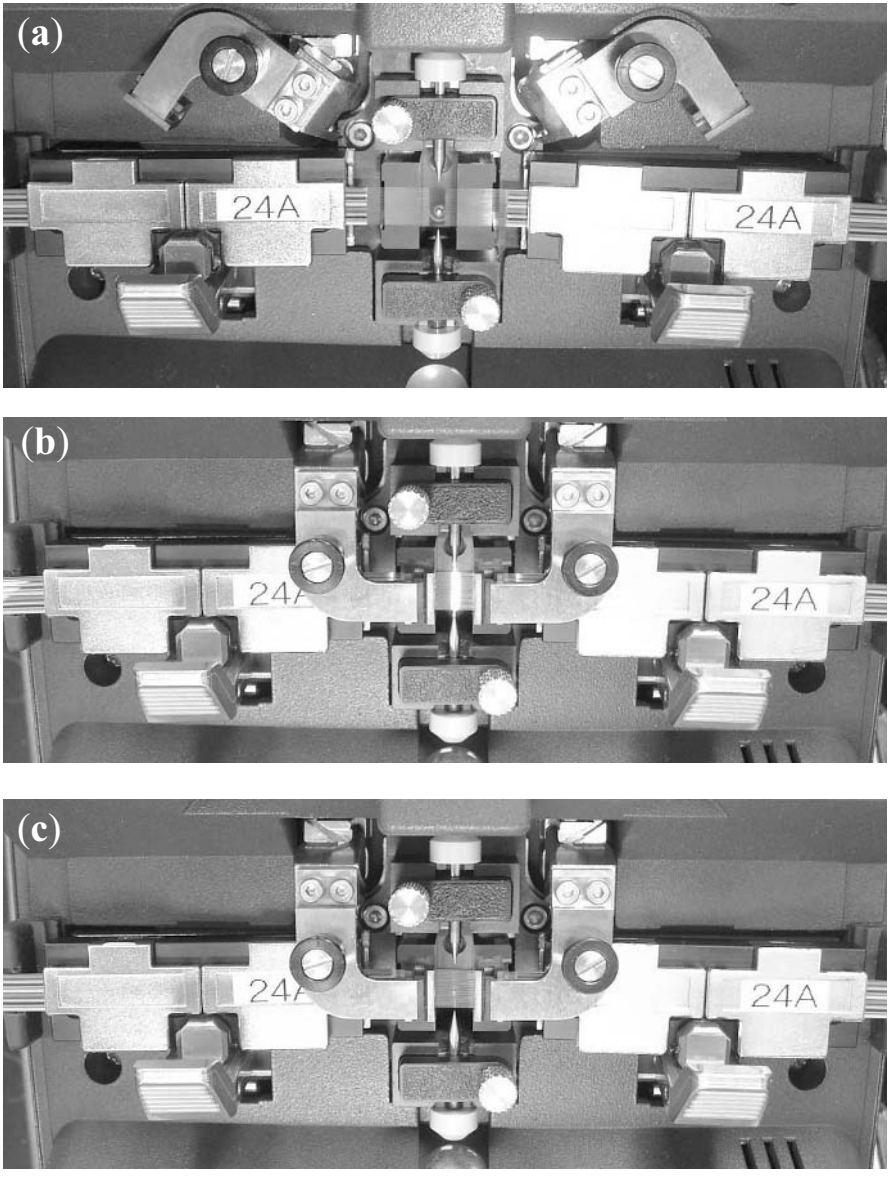

Fig. 10.5. Close up of the *Fitel S199M24* that can simultaneously fusion splice all the strands of a 24 fiber ribbon cable. The figure depicts the machine (**a**) just after loading the cleaved ends of two 24 strand ribbon fiber cables, (**b**) during joint formation, and (**c**) after the conclusion of joint formation. The two electrode tips are visible in the center of each photo while the fiber chucks are labeled with a number "24" to the left and right of the electrodes. A two mm air gap separates the opposing ribbon fiber tips in (**a**). The ribbon cable is about 6 mm wide and about 1 cm of coating is stripped from the cleaved ends. The white hot electric arc is visible spanning the gap between the electrode tips in (**b**) during joint formation. Photo courtesy of *Furukawa America, Inc.*

Fig. 10.6. The *Fitel S183* is a contemporary arc fusion splicer designed to incorporate a great deal of flexibility so that it can be applied to specialty fibers such as PM fiber in a factory setting as well as in a laboratory environment. The splice cover is in the down position obscuring the view of the fiber chucks and electrodes. A small heater for curing heat shrink splice protectors is visible on the front of the unit opposite the LCD screen mounted on the back. This machine includes a profile alignment system (PAS). Photo courtesy of *Furukawa America, Inc.*

including stripping, cleaving, testing, and packaging are automated so that the equipment operator need not ever touch the fiber during any point of the fusion splice process. Full automation can significantly improve the yield, quality, and cycle time of fusion splices. Much of the variation between nominally identical fusion splices is due to the human operator. As discussed in Chapters 2 and 6, even slight contact with the bare glass of a stripped fiber can reduce its mechanical strength and its long term reliability. Fully automated fusion splicers are designed to overcome such problems.

Fully automated splicing systems still require engineers to maintain the equipment and prepare the fibers in a pallet arrangement for splicing. However, the total labor cost per splice of a fully automated system is much lower than conventional bench top units with equivalent production capacity whereas the splicing yields are much higher. Furthermore, a fully automated system can better adjust to fluctuations in fusion splice demand since it can be deactivated during periods of slow demand.

A fully automated fusion splicers, the *Vytran Corp. FAS*, is depicted in Figs. 10.7 and 10.8. This system only requires the operator to setup a pallet containing a sequence of fibers to be spliced and automatically performs the entire fusion splice process. A complete fusion splice takes on the order of two minutes, including stripping, loss estimation, and recoating. The system is designed with an open architecture, comprised of several modules, each

Fig. 10.7. The *Vytran FAS* represents the automated future of factory fusion splicing since it is a fully automated fusion splicing workstation that can automatically strip, clean, cleave, fusion splice, proof test, package, and estimate splice loss. Fibers are laid up in a pallet arrangement by an operator and this pallet is then automatically processed by the machine. Only about 150 seconds are required to execute all the steps of the fusion splice process. This machine is also notable because it employs a tungsten filament (Fig. 10.10) as a heat source instead of the usual electric arc. Photo courtesy of *Vytran Corporation*

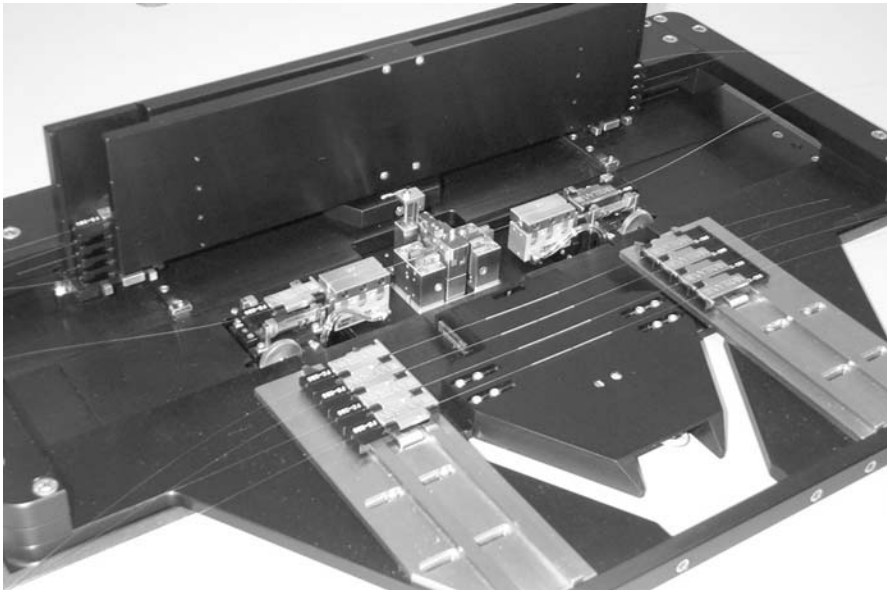

Fig. 10.8. Close up of the *Vytran FAS* in action showing the machine automatically fusion splicing a pallet of fibers. In the foreground, four completed and recoated splices are visible. Photo courtesy of *Vytran Corporation*

of which performs a single step of the fusion splice process. Data such as estimated splice loss or images of the completed splices can be logged for future reference.

10.4 Research and Laboratory Splicers

Research and laboratory fusion splicers are designed to have the maximum amount of flexibility so they can fusion splice specialty and research fibers. The *Vytran FFS-2000* is a particularly flexible fusion splicing system whose heat source and fiber chucks can be programmed to execute complex operations. This fusion splicer is unique in that it incorporates all the equipment required for the complete fusion splice process into a single workstation, including a fiber stripper, cleaner, cleaver, heat source, proof tester, and recoater. The operator must manually transfer the fiber from one station to another.

The *Vytran FFS-2000*, like the *Vytran FAS* mentioned earlier, is notable because instead of an electric arc, it uses a resistively heated filament of tungsten metal as a heat source. This heat source is continuously tunable over a wide range of temperatures unlike an electric arc, which grows unstable at low temperatures. The tungsten filament is a ribbon in the shape of an

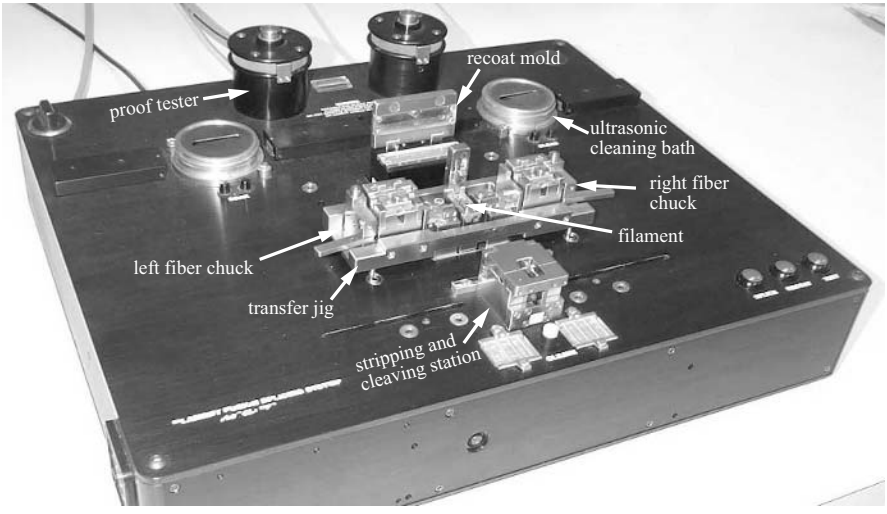

Fig. 10.9. The *Vytran FFS-2000* is a complete splicing workstation including an integrated stripper, cleaver, ultrasonic cleaner, recoater, and proof tester. All of the steps comprising the complete fusion splice process can be performed at various stations (labeled in white) on this desktop machine. The operator uses the transfer jig move the splice from one station to another. This workstation arrangement makes it faster and easier for the operator to properly perform all the steps of the fusion splice process. Like the *Vytran FAS*, this system uses a tungsten filament (Fig. 10.10), and includes a profile alignment system (PAS). The *Vytran FFS-2000* is suitable for either factory or laboratory use. Photo courtesy *Vytran Corporation*

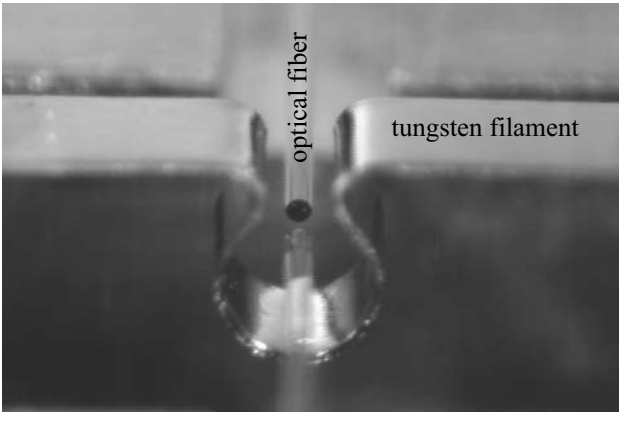

Fig. 10.10. Close up of the tungsten filament which serves as the heat source in the *Vytran FAS* and *Vytran FFS-2000* fusion splicers. The filament is a tungsten ribbon bent into the shape of an inverted omega. The filament is shown enveloping two 125 μm diameter fiber tips. Photo courtesy of *Vytran Corporation*

inverted "omega" which envelopes the fiber tips ensuring uniform heating (Fig. 10.10). The tungsten filament is shielded from reacting with atmospheric oxygen at high temperature by a high purity argon gas purge.

10.5 Summary

Optical fiber fusion splicing hardware has evolved over the past 30 years to the point that a wide variety of sophisticated equipment is now commercially available. Fusion splicing equipment can be loosely organized according to its application including field splicing, factory splicing, and laboratory splicing. Field splicers, which includes many types of mass fusion splicers, are distinguished by their rugged, compact design, relatively low cost, and portability. Factory splicers are noted for their ergonomics, automation, and flexibility. Laboratory splicers are designed to exhibit maximum flexibility so that they may be applied to the widest possible variety of optical fibers, including novel research fibers.

Future fusion splicers can be expected to incorporate added features to cope with the demands of future optical fibers, which may include microstructured fiber or optical fibers fabricated from novel materials such as non-silica glasses or polymers. Fusion splicing, especially in a factory environment, can be expected to become increasingly automated in order to reduce costs while improving quality.

Appendix A: List of Mathematical Symbols

Symbol	Meaning	Typical SI Units
a^+,a^-	element of BPM matrix $\boldsymbol{M}^k$	–
a_{critical}	critical crack size for fracture	m
a_i, b_j, c_i, d_j	modal power coefficients	$W^{0.5}$
a_ν, b_ν	loss estimation coefficients	–
A,A_0	surface area	m^2
A_c	power law crack growth material constant	depends on n_σ
A_{cs}	cross sectional area	m^2
a_n	Coefficient for Bessel series solution of diffusion equation	molecules/m
A_{shear}	amplitude of sheared cores	m
$\boldsymbol{a}$, $\boldsymbol{b}$, $\boldsymbol{c}$, $\boldsymbol{d}$	vectors of modal power coefficients	$W^{0.5}$
b	element of BPM matrix $\boldsymbol{M}^k$	–
Bi	Biot number	-
c_{light}	speed of light	$\text{m}s^{-1}$
c	modal amplitude coefficient for radiation modes	$\text{m}W^{0.5}$
C_{arc}	arc current constant	m^{-2}
C	molecular concentration	molecules m^{-3}
C_0	initial dopant concentration	molecules m^{-3}
c_p	specific heat at constant pressure	J kg^{-1} K^{-1}
c_{lm}	modal amplitude coefficient for LP_{lm} mode	$W^{0.5}$
c_ν, c_μ, c_{fund}	modal amplitude coefficient for mode ν, μ, fundamental	$W^{0.5}$
C_{si}	dopant concentration in step-index fiber	molecules m^{-3}
C_{total}	total amount of dopant	molecules or moles
$\boldsymbol{C_{\text{in}}}$	vector of incident modal power coefficients	$W^{0.5}$
$\boldsymbol{C_{\text{out}}}$	vector of exiting modal power coefficients	$W^{0.5}$

D	dopant diffusion coefficient	$\mathrm{m^2 s^{-1}}$
D_0	leading coefficient for dopant diffusivity equation	$\mathrm{m^2 s^{-1}}$
D_{core}	fiber core diameter	m
D_{mist}	distance between scribe and mist region in fiber cleave	m
D_{fiber}	fiber diameter	m
e_{rad}	radiative emissivity	–
E	scalar electric field	$\mathrm{V m^{-1}}$
$E_{\mathrm{L,in}}$	electric field incident from lefthand fiber	$W^{0.5} m^{-1}$
$E_{\mathrm{L,out}}$	electric field exiting to lefthand fiber	$W^{0.5} m^{-1}$
$E_{\mathrm{R,in}}$	electric field incident from righthand fiber	$W^{0.5} m^{-1}$
$E_{\mathrm{R,out}}$	electric field exiting to righthand fiber	$W^{0.5} m^{-1}$
E_{y}	Young's modulus of elasticity	$\mathrm{N\ m^{-2}}$
$\boldsymbol{E}$	electric field vector	$\mathrm{V m^{-1}}$
E_{act}	activation energy for dopant diffusion	$\mathrm{J\ mole^{-1}}$
ER, ER_{A},...	polarization extinction ratio	dB
ER_∞	ER assuming idealized fibers and launch conditions	dB
f	core deviation function	m
f_{x}, f_{y}	x, y component of core deviation function	m
$\mathcal{F}$	Fourier transform of a function	–
$F_{ai,bj}$	fraction of optical power transmitted	-
F_{bending}	concentrated bending force	N
F_{crit}	critical buckling force	N
F'_{dist}	distributed bending force	$\mathrm{N m^{-1}}$
F_m^k	fraction of BPM power in mode m at axial node k	–
F_γ	surface tension force	N
F_η	viscous force	N
h	convective heat transfer coefficient	$\mathrm{W m^{-2} K^{-1}}$
$\boldsymbol{H}$	magnetic field vector	$\mathrm{V s m^{-2}}$
i	current density	$\mathrm{A m^{-2}}$
i	radial node number for BPM	-
i	index	-
I	optical intensity	$\mathrm{W m^{-2}}$
I_{bend}	bending moment of inertia	$\mathrm{m^4}$
I_{tot}	total current flow between arc electrodes	A
j	index	-
$j_{0\mu}$, $j_{1\mu}$	eigenvalues of Bessel functions	–
$j_{\mathrm{x}}, j_{\mathrm{y}}, j_{\mathrm{z}}$	molecular flux in Cartesian directions	$\mathrm{molecules\ m^{-2} s^{-1}}$

k	index	–
k	axial node number for BPM	-
K_{fract}	material fracture constant	$\text{kg}^2\text{m}^{-1}\text{s}^{-4}$
k_0	vacuum wavenumber	m^{-1}
k_r	radial wavenumber for BPM transparent boundary condition	-
k_r'	radial wavenumber for BPM transparent boundary condition	-
k_s	fiber strength degradation during service life	depends on n_σ
K_I	stress intensity factor of a crack	$\text{Nm}^{-1.5}$
K_Ic	fracture toughness of a material	$\text{Nm}^{-1.5}$
l	azimuthal mode number	–
L	characteristic length of fiber	m
$\boldsymbol{L}$	modal loss matrix for multimode fiber splices	–
L_1, L_2, ...	loss coefficient for a mode in a multimode fiber	–
L_total	total loss at a multimode fusion splice	W
m	Weibull slope	–
$\boldsymbol{M}^k$	tridiagonal propagation matrix for BPM at axial node k	–
n, n_1, n_2	refractive index	–
N,M	number of modes	–
n_core	core refractive index	–
n_clad	cladding refractive index	–
N	number of radial nodes in BPM	–
N_weib	number splice samples in Weibull plot	–
N_exp	number of experiments comprising orthogonal array	–
N_modes	number of guided modes	–
N_p	fraction of splices failing prooftest	–
$N_{\text{P}_\text{j=k}}$	number of fusion splice experiments where P_j is set to k	–
n_r,n_z,n_ϕ	components of refractive index tensor in cylindrical coordinates	–
n_σ	stress corrosion susceptibility factor	–
NA	numerical aperture	–
p	stress-optic coefficient	m^2N^{-1}
P	operator used in Padé approximant	m^{-2}
P_1, P_2, ...	optical power carried in a mode	W
p_j, p_1, p_2, ...	splice parameters	–
P_cal, P_cal1, ...	optical power measurement for calibration	W
P_F	failure probability for prooftest	–

P_{inc}	incident optical power	W
$P_{\text{inc,local}}$	locally incident optical power	W
$P_{\text{L,in}}$, $P_{\text{L,out}}$, $P_{\text{R,in}}$, $P_{\text{R,out}}$	optical power from lefthand/righthand fiber entering/exiting splice	W
P_{major}	optical power traveling in major polarization axis	W
P_{meas}	optical power measurement	W
P_{minor}	optical power traveling in minor polarization axis	W
P_{refl}	reflected optical power	W
P_{S}	survival probability for prooftest	–
P_{initial}	initial power carried in a fiber upstream of splice	W
P_{lost}	power lost from fundamental mode of a splice	W
P_{lm}	optical power in LP_{lm} mode	W
P^k	total BPM power propagating at axial node k	W
P_m^k	total BPM power propagating in mode m at axial node k	W
P_{refl}	optical power reflected by a splice	W
P_{trans}	optical power transmitted across a splice	W
P_γ	effective pressure exerted by surface tension	Nm^{-2}
P_Ψ	total optical power carried in electric field envelope Ψ	W
q	stress-optic coefficient	m^2N^{-1}
$\bar{Q}$	overall mean splice quality	–
Q_i, Q_1, ...	quality of fusion splices	–
$Q_i \mid_{p_j=k}$	quality of splice experiment in which p_j is set to k	–
$Q_{\text{p}_\text{j}=\text{k}}$	effect of setting p_j to k	–
$q_{\text{conv,in}}$	input convective heat flux	Wm^{-2}
Q_{input}	input heat flow	W
Q_{output}	output heat flow	W
$Q_{\text{conv,in}}$	input convective heat flow	W
$Q_{\text{rad,in}}$	input radiative heat flow	W
$Q_{\text{cond,out}}$	output conduction heat flow	W
$Q_{\text{rad,out}}$	output radiative heat flow	W
r	radial coordinate	m
$\boldsymbol{r}$	position vector	m
$\hat{r}$	non-dimensional radial coordinate	–
$\mathcal{R}$	ideal gas constant	$\text{JK}^{-1}\text{mole}^{-1}$
R	radial portion of propagating electric field envelope	Vm^{-1}

R_i^k	discrete electric field envelope at radial node i, axial node k	Vm^{-1}
$\boldsymbol{R}^k$	vector of discrete electric field envelopes at node k	$W^{0.5}$
r'	dummy variable for diffusion integration	m
r_0	initial radius of Gaussian dopant concentration	m
R_{bend}	fiber bending radius	m
R_{bs}	fraction of backscattered optical power	dB
$R_{\mathrm{bs,1\,\mu s}}$	fraction of backscattered optical power for 1 µs pulsewidth	dB
R_{core}	fiber core radius	m
R_{cladding}	fiber cladding radius	m
R_{fiber}	fiber radius	m
$R_{\mathrm{planewave}}$	fraction of reflected power for a plane wave	–
R_{SMF}	reflectance of a single-mode fiber splice	dB
R_{splice}	splice reflectance	dB
R_{x}	radius of curvature in x-direction	m
R_{y}	radius of curvature in y-direction	m
RL	return loss	dB
$\boldsymbol{S}$	scattering matrix	–
$S_{ai,bj}$, $S_{dj,ci}$	elements of scattering matrix	–
$\boldsymbol{S_{\mathrm{sub}}}$	subset of scattering matrix	–
$SS_{\mathrm{P_j}}$	sum-of-squares resulting from P_j set to k	–
SS_{total}	total sum-of-squares	–
t	time	s
t_{l}	loading time of prooftest	s
t_{p}	duration of prooftest	s
t_{pe}	effective prooftest time	s
t_{s}	service lifetime of an optical fiber	s
t_{u}	unloading time of prooftest	s
T	temperature	K
t_{cond}	thermal conduction time constant	s
t_{diff}	diffusion time constant	s
T_{surround}	temperature of surrounding medium	K
T_{surface}	temperature of fiber surface	K
T_{fiber}	temperature of fiber	K
$\boldsymbol{T}$	fully assembled BPM transfer matrix	–
$\boldsymbol{T}_{\mathrm{eig}}$	eigenvectors of BPM matrix $\boldsymbol{T}$	–
V	normalized frequency of an optical fiber	–
V_{fiber}	volume of an optical fiber	m^3
V_{flow}	flow velocity	ms^{-1}
V_{collapse}	void collapse velocity	ms^{-1}
V_{crack}	crack propagation velocity	ms^{-1}
w, w_1, w_2	mode field radius	m
w_{g}	Gaussian mode field radius	m
w_{p}	Petermann II mode field radius	m

x,y,z	Cartesian coordinates	m
$\hat{x}$,$\hat{y}$,$\hat{z}$	Cartesian coordinate unit vectors	–
Y	crack geometry coefficient	–
α_n	eigenvalue of diffusion equation solution	m^{-1}
α_T	thermal diffusivity	$\mathrm{m}^2\mathrm{s}^{-1}$
β	axial propagation constant	m^{-1}
β_{lm}	axial propagation constant of LP_{lm} mode	m^{-1}
β_ν, β_μ, β_fund	axial propagation constant of mode ν, μ, fundamental	m^{-1}
γ	surface tension	Nm^{-1}
γ_shear	exponential decay constant of sheared cores	m^{-1}
$\mathit{\Gamma}_{ai,bj}$	splice loss of individual mode	dB
$\mathit{\Gamma}_\mathrm{cmt}$	splice loss computed by coupled mode theory	dB
$\mathit{\Gamma}_\mathrm{diam}$	multimode splice loss due to core diameter mismatch	dB
$\mathit{\Gamma}_\mathrm{Gaussian}$	splice loss of a Gaussian	dB
$\mathit{\Gamma}_\mathrm{index}$	multimode splice loss due to refractive index mismatch	dB
$\mathit{\Gamma}_\mathrm{offset}$	multimode splice loss due to core offset	dB
$\mathit{\Gamma}_\mathrm{splice}$	splice loss	dB
$\mathit{\Gamma}_\mathrm{SMF}$	splice loss of single-mode fiber	dB
δ_core	lateral offset of fiber cores	m
δ_clad	lateral offset of fiber claddings	m
δ_D	characteristic length scale for dopant diffusion	m
δ_bending	lateral deflection due to bending	m
δ_refl	apparent size of fusion splice reflection on OTDR	dB
$\mathit{\Delta}$	fractional difference between core and cladding refractive index	–
Δ_bs	change in fraction of backscattered energy across splice	dB
Δn	difference between core and cladding refractive index	–
Δr	BPM radial node spacing	m
Δz	BPM axial node spacing	m
ε	electric permittivity of material	Fm^{-1}
ε_0	electric permittivity of vacuum	Fm^{-1}
$\varepsilon_\mathrm{const}$	non-varying portion of electric permittivity	Fm^{-1}
ε'	perturbation to electric permittivity	Fm^{-1}
ζ	element of BPM $\boldsymbol{M}^k$	–
η	viscosity	$\mathrm{kg\ m}^{-1}\mathrm{s}^{-1}$

θ	angle between axes of two spliced fibers	radians
θ_1, θ_2	angle between surface normal and incident ray	radians
θ_{misalign}	angular misalignment between fiber polarization axes	radians
ι	element of BPM matrix $\boldsymbol{M}^k$	–
κ_{R}	effective radiative thermal conductivity	$\text{Jkg}^{-1}\text{K}^{-1}$
κ_{T}	thermal conductivity	$\text{Jkg}^{-1}\text{K}^{-1}$
$\kappa_{\nu\mu}$	coupling coefficient between modes ν and μ	m^{-1}
$\hat{\kappa}_{\text{fund}\mu}$	coupling coefficient between fundamental and mode μ	m^{-1}
λ	wavelength	m
λ_{c}	cutoff wavelength for single-mode operation	m
λ_{eig}	eigenvalues of BPM matrix $\boldsymbol{T}$ matrix	–
λ_{peak}	peak thermal emission wavelength	m
μ_0	magnetic permeability of a vacuum	Hm^{-1}
μ_{a}	optical absorption coefficient	m^{-1}
ξ	element of BPM matrix $\boldsymbol{M}^k$	–
ϱ	density	kgm^{-3}
ρ	coefficient for polarization extinction ratio measurement	–
σ_0	nominal tensile failure stress for Weibull distributions	Nm^{-2}
σ_{a}	tensile stress applied in vicinity of a crack	Nm^{-2}
σ_{arc}	radius of Gaussian electric discharge at z=0	m
$\sigma_{\text{bend,max}}$	maximum tensile stress experienced during bending	Nm^{-2}
σ_{f}	tensile failure stress	Nm^{-2}
$\sigma_{\text{f,initial}}$, $\sigma_{\text{f,final}}$	initial, final tensile failure stress	Nm^{-2}
σ_{p}	maximum tensile stress achieved during prooftest	Nm^{-2}
σ_{rr}, σ_{zz}, $\sigma_{\phi\phi}$	normal stresses in cylindrical coordinates	Nm^{-2}
σ_{s}	average tensile stress experienced during fiber lifetime	Nm^{-2}
σ_{SB}	Stefan-Boltzmann constant	$\text{Wm}^{-2}\text{K}^{-4}$
$\dot{\sigma}$	time rate of change of tensile stress	$\text{Nm}^{-2}\text{s}^{-1}$
τ	shear stress	Nm^{-2}
τ_{D}	non-dimensional diffusion parameter	–
τ_{pw}	OTDR pulsewidth	s
υ	constant for scaling fiber surface area	–
χ	element of BPM matrix $\boldsymbol{M}^k$	–
ϕ	azimuthal coordinate	radians
$\boldsymbol{\Phi}$	azimuthal portion of propagating electric field envelope	–

ψ	spatial envelope of propagating electric field	Vm^{-1}
Ψ	spatial envelope of propagating electric field	$W^{0.5}\mathrm{m}^{-1}$
ψ_β	spatial envelope for orthonormal radiation modes	m^{-1}
ψ_g	spatial envelope of normalized Gaussian mode field	m^{-1}
ψ_{lm}	spatial envelope of orthonormal mode field	m^{-1}
ψ_ν,ψ_μ	spatial envelope of orthonormal mode ν, μ	m^{-1}
$\psi_1^{(R)}$, $\Psi_2^{(R)}$, ...	spatial envelopes of orthonormal modes in righthand fiber	m^{-1}
$\psi_1^{(L)}$, $\Psi_2^{(L)}$, ...	spatial envelopes of orthonormal modes in lefthand fiber	m^{-1}
ω	angular frequency of optical signal	radians s^{-1}

Appendix B: List of Abbreviations

Abbreviation	Meaning
ANOVA	analysis-of-variance
BER	bit-error rate
BPM	beam-propagation method
CCD	charge-coupled-device
CEI	International Electrotechnical Commission
CMT	coupled-mode theory
DCF	dispersion-compensating fiber
DCM	dispersion compensating module
DOE	design of experiments
DSF	dispersion-shifted fiber
DEMUX	demultiplexer
DWDM	dense wavelength-division-multiplexing
EDF	erbium-doped fiber
EDFA	erbium-doped fiber amplifier
ETSI	European Telecommunications Standards Institute
FD-BPM	finite-difference beam-propagation-method
FDTM	finite-difference time-domain
FT-BPM	Fourier-transform beam-propagation-method
FTTH	fiber-to-the-home
FTTP	fiber-to-the-premises
GIF	graded-index fiber
GRIN	graded-index
HCS^{TM}	hard-clad silica
IDF	inverse-dispersion fiber
IEC	International Electrotechnical Commission
ITU	International Telecommunications Union
LAN	local area network
LD	laser diode
LED	light-emitting diode
LID	light-injection and detection
LP	linearly polarized

MFD	mode field diameter
MMF	multimode fiber
MPI	multipath interference
MUX	multiplexer
NA	numerical aperture
NZ-DSF	non-zero dispersion-shifted fiber
OCWR	optical continuous-wave reflectometer
OEM	original equipment manufacturing
OFDR	optical frequency-domain reflectometer
OLCR	optical low-coherence reflecometry
OSA	optical spectrum analyzer
OTDR	optical time-domain reflectometer
PAS	profile alignment system
PBF	photonic bandgap fiber
PCF	photonic crystal fiber
PEEK	poly-ether-ether-keytone
PM	polarization maintaining
PMMA	polymethylmethacrylate
POL	polarization observation by lens-effect-tracing
PZ	polarizing
RDF	reverse-dispersion fiber
RNF	refracted near-field
RSM	response surface methodology
SAM	stress-applying member
SMF	single-mode fiber
S/N	signal-to-noise ratio
TBC	transparent boundary condition
TIA	Telecommunications Industry Association
TIM	transverse interferometric method
TNF	transmitted near field
TVV	thermo-vacuum vaporization
UV	ultraviolet

Appendix C: List of Relevant Published Standards and Requirements

Issuing Agency	Standard Number	Year	Title
Telcordia[a]	GR-1095-CORE	1995	Generic Requirements for Multi-Fiber Single-Mode Optical Splices and Splicing Systems
Telcordia	GR-771-CORE	1994	Generic Requirements for Fiber Optic Splice Closures
Telcordia	GR-765-CORE	1997	Generic Requirements for Single Fiber Single-Mode Optical Splices and Splicing Systems
Telcordia	GR-1380-CORE	1994	Generic Requirements for Fusion Splice Protectors
ETSI[b]	I-ETS 300 783	1998	Transmission and Multiplexing (TM); Passive optical components; Fibre optic fusion splices for single-mode optical fibre transmission systems; Common requirements and conformance testing
ITU[c]	L.12	2000	Optical fibre joints
IEC[d]	61073-1	1999	Mechanical splices and fusion splice protectors for optical fibres and cables Part 1: Generic Specification
IEC	1073-3	1993	Splices for optical fibres and cables Part 3: Sectional specification – Fusion splices for optical fibres and cables
TIA[e]	TIA-6090000	2000	Generic Specification for Optical Fiber Splices
TIA	TIA-5150000	2002	Generic Specification for Optical Fiber and Cable Splices

TIA	TIA/EIA-455-8 (FOTP-8)	2000	Measurement of Splice or Connector Loss and Reflectance Using an OTDR
TIA	TIA-455-179 (FOTP-179)	1988	Inspection of Cleaved Fiber End Faces by Interferometry

[a] Telcordia and Bellcore standards are available from http://www.telcordia.com
[b] ETSI standards are available from http://www.etsi.org
[c] ITU standards are available from http://www.itu.int
[d] IEC standards are available from http://www.iec.ch
[e] TIA standards are available from http://www.tiaonline.org

References

Chapter 1

1.1 T. Liang, T. Hoffman, J. Greene, D. Gaudry, A. Bhat, T. Goddard, H. Watanabe, H. Yonenaga, T. Uchida, T. Shibata: '24-Fiber Mass Fusion Splicing Based on Two-Step Arc Power Process'. In: *Proceedings of the National Fiber Optic Engineers (NFOEC) Conference at Orlando, FL, Sept. 7–11 2003* (Telcordia, Piscataway, NJ 2003) pp. 36–44

1.2 C. R. Kurkjian, J. T. Krause: 'An Overview of Unsolved Problems'. In: *Optical Fiber and Fiber Component Mechanical Reliability and Testing, at Boston, MA, November 5–8, 2000*, ed. by M. J. Matthewson, (SPIE Vol 4215, Bellingham, WA 2001) pp. 1–15

1.3 K. Takahashi, S. Yaguchi, N. Kawanishi, T. Ohtani: 'Development of a New Factory Fusion Splicer.' In: *Proceedings of the 50th International Wire and Cable Symposium (IWCS) at Lake Buena Vista, FL, November 12–15, 2001* (IWCS, Eatontown, NJ 2001) pp. 68–76

1.4 A. W. Snyder, J. D. Love: *Optical Waveguide Theory*, (Chapman and Hall, London 1983)

1.5 E.-G. Neumann: *Single-Mode Fibers: Fundamentals*, (Springer-Verlag, Berlin 1988)

1.6 L. B. Jeunhomme: *Single Mode Fiber Optics: Principles and Applications* 2nd edn. (Dekker, New York 1990)

1.7 A. Ghatak, K. Thyagarajan: *Introduction to Fiber Optics*, (Cambridge University Press, Cambridge 1998)

1.8 R. H. Doremus: *Glass Science*, (John Wiley & Sons, New York 1973)

1.9 N. P. Bansal, R. H. Doremus: *Handbook of Glass Properties*, (Academic Press, New York, 1986)

1.10 J. T. Krause, C. R. Kurkjian: Electron. Lett. **21**, 533 (1985).

1.11 W. W. Wood: 'Reliability of Optical Connectors and Splices'. In: *Fiber Optics Reliability and Testing: Benign and Adverse Environments IV at Boston, MA, September 8–10, 1993*, (SPIE Vol 2074, Bellingham, WA 1994) pp. 276–287

1.12 D. D. Davis, S. C. Mettler, D. J. DiGiovanni: 'A comparative evaluation of fiber fuse models'. In: *Laser Induced Damage in Optical Materials*, ed. by H. E. Bennet, (SPIE Vol 2966, Bellingham, WA 1997) pp. 592–606.

1.13 C. M. Miller: IEEE J. Lightwave Technol. **LT-4**, 1228 (1986)

1.14 G. Wiegand, D. M. Wright, D. R. Peterson: 'A Study of Field and Application Performance of Optical Fiber Splices'. In: *Proceedings of the National Fiber Optic Engineers Conference (NFOEC) at Boston MA, June 18–22, 1995* (Telcordia, Piscataway, NJ 1995) pp. 1086–1097

1.15 T. Katagiri, M. Tachikura, Y. Murakami: IEEE J. Lightwave Technol. **17**, 2297 (1999)

1.16 T. Katagiri, M. Tachikura, Y. Murakami: IEEE J. Lightwave Technol. **19**, 195 (2001)
1.17 J. J. Refi: *Fiber Optic Cable - A Lightguide*, 2nd edn. (AVO Training Institute, 2001)
1.18 J. Hecht: *Understanding Fiber Optics*, (Prentice Hall, Upper Saddle River, NJ 2002)
1.19 P. P. Mitra, J. B. Stark: Nature **411**, 1027 (2001)
1.20 ElectroniCast Corp. cited in Lightwave Magazine Web Exclusive, http://lw.pennnet.com, June 27, 2003
1.21 B. Chomycz: *Fiber Optic Installer's Manual*, (McGraw-Hill, New York, 2000)
1.22 C. DeCusatis, G. Li: 'Chapter 6: Fiber-optic Communication Links (Telecom, Datacom, and Analog)'. In: *Handbook of Optics Vol. IV Fiber Optics and Nonlinear Optics*. ed. by M. Bass (McGraw-Hill, New York 2001) pp. 6.1–6.20
1.23 C. M. Miller, S. C. Mettler, I. A. White: *Optical Fiber Splices and Connectors*, (Marcel Dekker, New York 1986)
1.24 P. Lindskog, B. Sundström, J. Tyrcha, R. Sundberg: 'Minimize Network Installation Costs by Setting Appropriate Maximum Splice Loss Values'. In: *Proceedings of The International Wire and Cable Symposium, 1998* (IWCS, Eatontown, NJ 1998) pp. 522–526
1.25 D. Gibb, R. Grigsby, A. Berney, M. Adcox: 'Setting Splice Specifications for Single-Mode Fiber Cables'. In: *Proceedings of the National Fiber Optic Engineers Conference (NFOEC) at Baltimore, MD, July 8–12 2001.* (Telcordia Technologies, Piscataway, NJ 2001) pp. 379–390
1.26 B. Zamzow, K. Takasu: 'Splicing Loss Control and Assembly Yield Management'. In: *Proceedings of the Telecom Hardware Solutions Conference & Exhibition at Dallas, TX, May 15–16, 2002* (International Microelectronics And Packaging Society in conjunction with Surface Mount Technology Association, 2002)
1.27 B. Zamzow, K. Takasu: 'Fusion Splicing of Fiber Optic Components - How to Minimize Rework'. In: *Proceedings of APEX at San Diego, CA January 20-24, 2002* (IPC, Northbrook, IL 2002) pp. S09 1-1 – S09 1-9
1.28 D. L. Bisbee: Bell Syst. Tech. J. **50**, 3153 (1971)
1.29 F. P. Kapon, D. B. Keck, R. D. Maurer: Appl. Phys. Lett. **17**, 423 (1970)
1.30 R. B. Dyott, J. R. Stern, J. H. Stewart: Electron. Lett. **8**, 290 (1972)
1.31 D. Gloge, P. W. Smith, D. L. Bisbee, E. L. Chinook: Bell Syst. Tech. J. **52**, 1579 (1973)
1.32 U.-C. Paek, A. L. Weaver: Appl. Opt. **14**, 294 (1975)
1.33 H. Fujita, Y. Suzaki, A. Tachibana: Appl. Opt. **15**, 320 (1976)
1.34 D. L. Bisbee: Appl. Opt. **15**, 796 (1976)
1.35 Y. Kohanzadeh: Appl. Opt. **15**, 793 (1976)
1.36 I. Hatakeyama, H. Tsuchiya: Trans. IECE **OQE 75**, 25 (1975) (in Japanese)
1.37 R. Jocteur, A. Tarday: "Optical Fibers Splicing with Plasma Torch and Oxhydric Microburner". In: *European Conference on Optical Fibre Communication 1976*, (Comit du Colloque International sur les Transmissions par Fibres Optiques, Paris 1976) p. 261
1.38 D. Marcuse: Bell Syst. Tech. J. **56**, 703 (1977)
1.39 I. A. White, J. F. Kuhl: 'Microbending theory of single-mode fiber splices – butt joint and fusion'. In: *Proceedings of Fourth IOOC at Tokyo, Japan, 1983*, (1983) p. 402
1.40 K. Kinoshita, M. Kobayashi: Appl. Opt. **18**, 3256 (1979)
1.41 M. Tachikura: Electron. Lett. **17**, 695 (1981)
1.42 A. Berg, and M. Johansen: Electron. Lett. **31**, 308 (1995)

1.43 C. Good, D. Gross, T. Watanabe: 'Fiber Connection Considerations for FTTP'. In: *Proceedings of the 19th Annual National Fiber Optic Engineers Conference (NFOEC) at Orlando, FL, September 7–11, 2003*, (Telcordia Technologies, Piscataway, NJ 2003) pp. 173–179
1.44 A. Weinert: *Plastic Optical Fibers : Principles, Components, Installation*, (Publicis MCD, Erlangen, 1999)
1.45 W. R. White, L. L. Blyler, Jr., R. Ratnagiri, M. Park: 'Manufacture of Perfluorinated Plastic Optical Fibers.' In: *Proceedings of the Optical Fiber Communication Conference (OFC) 2004 at Los Angeles, CA, February 22-27, 2004*, (Optical Society of America, Washington, DC 2004) paper ThI1
1.46 G. Appollinari, D. Scepanovic, S. White: Nucl. Instr. and Meth. A **311**, 520 (1992)
1.47 K. Hara, K. Horiuchi, S. Kim, I. Nakano, T. Takebayashi, K. Takikawa, K. Yasuoka, M. Koyano, S. Matsui, H. Takeuchi: Nucl. Instr. and Meth. A **348**, 139 (1994)
1.48 S. D. Carson, R. A. Salazar: 'Splicing Plastic Optical Fibers'. In: *Plastic Optical Fibers at Boston, MA, September 6, 1991*, ed. by M. Kitazawa, J. F. Kreidl, R. E. Steele, (SPIE Vol 1592, Bellingham, WA 1991) pp. 134–138

Chapter 2

2.1 J. T. Krause, D. Stroumbakis: 'Factors affecting arc fusion splice strengths.' In: *Optical Network Engineering and Integrity at Philadelphia, PA, October 24–25, 1995*, ed. by H. H. Yuce, D. K. Paul, R. A. Greenwell (SPIE, Bellingham, WA 1996) pp. 98–109
2.2 W. W. Wood: 'Reliability of Optical Connectors and Splices'. In: *Fiber Optics Reliability and Testing: Benign and Adverse Environments, SPIE Vol. 2074, at Boston, MA September 8–10, 1993*, ed. by D. K. Paul, H. H. Yuce (SPIE, Bellingham, WA, 1994) pp. 276–286
2.3 J. J. Refi: *Fiber Optic Cable - A Lightguide*, 2nd edn. (AVO Training Institute, 2001)
2.4 O. S. Gebizlioglu, J. D. Mann, C. R. Kurkjian: 'An Overview of Optical Fiber Strippability'. In *15th National Fiber Optic Engineers Conference (NFOEC), September 1999* (Telcordia, Piscataway, NJ 1999)
2.5 S. Siddiqui, L. R. Pritchett, J. R. Szwec, C. R. Taylor, R. J. Brown, Jr., H. C. Chandan: 'A New Chemical Stripping Method for Obtaining High Strength Splices of UV Colored Optical Fibers'. In: *Proceedings of the 47th International Wire and Cable Symposium at Philadelphia, PA November 16–19, 1998*, (IWCS, Eatontown, NJ 1998) pp. 864–873
2.6 B. Chomycz: *Fiber Optic Installer's Manual*, (McGraw-Hill, New York, 2000)
2.7 J. Hecht: *Understanding Fiber Optics*, (Prentice Hall, Upper Saddle River, NJ 2002)
2.8 N. Yoshizawa, H. Tada, Y. Katsuyama: IEEE J. Lightwave Technol. **9**, 417 (1991)
2.9 T. Mizushima, S. Morita, H. Sugawara, T. Sato, S. Yaguchi: 'Development of a Mass Fusion Splicing System for up to 24-Fiber Ribbon'. In: *Proceedings of the 51st International Wire and Cable Symposium (IWCS) at Lake Buena Vista, FL, November 18–21, 2002* (IWCS, Eatontown, NJ, 2002) pp. 708–714
2.10 M. J. Matthewson, C. R. Kurkjian, J. R. Hamblin: IEEE J. Lightwave Technol. **15**, 490 (1997)

2.11 C. E. Walraven, R. G. Wiley: 'Method for Heat Stripping Optical Fibers'. *US Patent 5968283* (1999)
2.12 J. T. Krause, C. R. Kurkjian: Electron. Lett. **21**, 533 (1985)
2.13 H.-S. Park, S. Lee, C. S. Kim, J. H. Kim, U.-C. Paek, Y. Chung: 'A novel method of removing optical fiber coating with hot air stream.' In: *Optical Fiber Communication Conference (OFC) and International Conference on Integrated Optics and Optical Fiber Communications (IOOC) at San Diego, CA, February 21–26, 1999*, (Optical Society of America, Washington, DC, 1999) pp. 371–373
2.14 Datasheet for 'Autoprep'. 3SAE Corporation (2002) available from http://www.3sae.com
2.15 C. J. Vetrano: 'Method and Apparatus for Stripping an Optical Fiber', *US Patent 6402856* (2002)
2.16 H.-S. Park, S. Lee, U.-C. Paek, Y. Chung: IEICE Trans. Commun. **E85-B**, 206 (2002)
2.17 Datasheet for 'TVV-50 Decoater'. Vytran Corporation (Morganville NJ, 2002) available from http://www.vytran.com
2.18 R. F. Swain, A. D. Yablon: 'Method and apparatus for removing polymeric coatings from optical fiber', *US Patent 6436198* (2002)
2.19 B. F. Johnston, A. J. Lee, M. J. Withford, J. A. Piper: Opt. Express **10**, 818 (2002)
2.20 F. Barnier, P. E. Dyer, P. Monk, H. V. Snelling, H. Rourke: J. Phys. D: Appl. Phys. **33**, 757 (2000)
2.21 G. Ogura: Laser Focus World **37**, No. 6, 169 (2001)
2.22 D. Gloge, P. W. Smith, D. L. Bisbee, E. L. Chinnock: Bell Syst. Tech. J. **52**, 1579 (1973)
2.23 J. G. Woods: 'Cleaving of Optical Fibers'. In: *Components for Fiber Optic Applications at Cambridge, MA, September 22–24, 1986*, (SPIE vol 722, Bellingham, WA, 1986) pp. 147–152
2.24 J. E. Field, B. Samuels, D. Townsend, J. T. Hagan: Phil. Mag. A **57**, 151 (1988)
2.25 S. T. Gulati: 'Mechanical Properties of SiO_2 vs. SiO_2-TiO_2 Bulk Glasses and Fibers'. In: *Optical Waveguide Materials: Symposium at Boston, MA, December 2–4, 1991*, ed. by M. M. Broer (Materials Research Society, Pittsburgh, PA 1992) pp. 67–84
2.26 J. C. Meyer: 'Cleavability of Titania-Clad Optical Fiber'. In: *Proceedings of the 48th International Wire and Cable Symposium (IWCS) at Atlantic City, NJ November 15–18, 1999*, (IWCS, Eatontown, NJ, 1999) pp. 636–643
2.27 Y. Ohuchi, A. Wada, R. Yamauchi, N. Sato, K. Inada: 'Abrasion resistant optical fibers with mechanically induced compressive surface stress'. In: *Optical Fiber Communications Conference at San Francisco, CA, January 22–26, 1990*, ed. by R. A. Linke, A. J. Morrow, D. M. Fye, R. E. Wagner (Optical Society of America, Washington, DC 1990) p. 172
2.28 'Inspection of Cleaved Fiber End Faces by Interferometry'. EIA-455-179, also known as FOTP-179, (EIA, Washington, DC 1988) available from http://www.tiaonline.com
2.29 S. H. Crandall, N. C. Dahl, T. J. Lardner: *An Introduction to the Mechanics of Solids*, 2nd edn. (McGraw-Hill, New York 1978)
2.30 M. J. Saunders: Appl. Opt. **18**, 1480 (1979)
2.31 V. Shah, G. Kiss, W. C. Young: 'Sensitivity of Insertion Loss on Fiber Endface Angles in Single-Mode Fiber Splices'. In: *10th National Fiber Optic Engineers Conference (NFOEC) Vol. 3, at San Diego, June 13–16, 1994*, (Telcordia, Piscataway NJ, 1994) pp. 407-417

2.32 International Telecommunication Union (ITU) 'Series L: Construction, Installation and Protection of Cables and Other Elements of Outside Plant: Optical fibre joints'. Recommendation L.12 (ITU, 2000) available from http://www.itu.int
2.33 T. Haibara, M. Matsumoto, T. Tanifuji, M. Tokuda: Opt. Lett. **8**, 235 (1983)
2.34 O. Kawata, K. Hoshino, K. Ishihara: Electron. Lett. **19**, 1049 (1983)
2.35 O. Kawata, K. Hoshino, Y. Miyajima, M. Ohnishi, K. Ishihara: IEEE J. Lightwave Technol. **LT-2**, 185 (1984)
2.36 T. Katagiri, M. Tachikura, I. Sankawa: IEEE J. Lightwave Technol. **LT-3**, 277 (1984)
2.37 J. T. Krause, W. A. Reed, K. L. Walker: IEEE J. Lightwave Technol. **LT-4**, 837 (1986)
2.38 H. Y. Tam: Electron. Lett. **27**, 1957 (1991)
2.39 C. M. De Blok, P. Matthijsse: Electron. Lett. **20**, 109 (1984)
2.40 E.-G. Neumann: *Single-Mode Fibers: Fundamentals* (Springer-Verlag, Berlin, 1988)
2.41 G.-D. Khoe, J. A. Luijendijk, L. J. C. Vroomen: IEEE J. Lightwave Technol. **LT-4**, 1219 (1986)
2.42 V. C. Y. So, R. P. Hughes, J. B. Lamont, P. J. Vella: IEEE J. Lightwave Technol. **LT-5**, 1663 (1987)
2.43 R. Watson: 'Characterization of splice loss estimation accuracy using local injection/detection and profile alignment methods.' In: *13th National Fiber Optic Engineers Conference (NFOEC) at San Dieo, CA, September 22–23, 1997*, (Telcordia, Piscataway NJ, 1997) pp. 149-155

Chapter 3

3.1 A. F. Mills: *Heat and Mass Transfer* (Irwin, Boston, MA 1995)
3.2 J. H. Lienhard: *A Heat Transfer Textbook*, 2nd edn. (Prentice-Hall, Englewood Cliffs, NJ 1987)
3.3 I. Hatakeyama, H. Tsuchiya: IEEE J. of Quant. Electron. **QE-14**, 614 (1978)
3.4 W. Frost, P. Ruffin, W. Long: 'Computational Model of Fiber Optic, Arc Fusion Splicing; Analysis'. In: *Fiber Optics Reliability: Benign and Adverse Environments II at Boston, MA, September 6–8, 1988*, ed. by D. K. Paul, R. A. Greenwell, S. G. Wadekar, (SPIE Vol 992, Bellingham, WA 1988) pp. 296–311
3.5 P. Ruffin, W. Frost, W. Long: 'Computational Model of Fiber Optic, Arc Fusion Splicing; Experimental Comparison'. In: *Components for Fiber Optic Applications and Coherent Lightwave Communications III at Boston, MA, September 7–9, 1988*, ed. by P. M. Kopera, H. R. D. Sunak, (SPIE Vol 988, Bellingham, WA 1988) pp. 163–173
3.6 C. W. Long: Modeling of Glass Flow During Arc Fusion Splicing of Fiber Optic Filaments, Ph.D. Thesis, University of Tennessee, Knoxville, TN (1988)
3.7 R. Jocteur, A. Tarday: 'Optical Fibers Splicing with Plasma Torch and Oxhydric Microburner'. In: *European Conference on Optical Fibre Communication 1976*, (Comit du Colloque International sur les Transmissions par Fibres Optiques, Paris 1976) p. 261
3.8 J. T. Krause, C. R. Kurkjian: Electron. Lett. **21**, 533 (1985).
3.9 H. Fujita, Y. Suzaki, A. Tachibana: Appl. Opt. **15**, 320 (1976)
3.10 U.-C. Paek, A. L. Weaver: Appl. Opt. **14**, 294 (1975)
3.11 M. Tachikura: Appl. Opt. **23**, 492 (1984)

3.12 F. Llewellyn-Jones: *The Glow Discharge and an Introduction to Plasma Physics* (John Wiley & Sons. New York 1966)
3.13 K. Ohzawa, S. Yaguchi, J.-I. Suzuki, N. Kawanishi, S. Saito: 'Development of a New Optical Fusion Splicer for Factory Use'. In *Proceedings of the 48th International Wire and Cable Symposium (IWCS) at Atlantic City, NJ, November 15–18, 1999* (IWCS, Eatontown, NJ 1999) pp. 644–649
3.14 B. Zamzow, K. Takasu: 'Splicing Loss Control and Assembly Yield Management'. In: *Proceedings of the Telecom Hardware Solutions Conference & Exhibition at Dallas, TX, May 15–16, 2002* (International Microelectronics And Packaging Society in conjunction with Surface Mount Technology Association, 2002)
3.15 G. Mackie, G. Karl, R. E. Dorian, D. Duke: 'Evolution of Mass Fusion Splicing Technology For Utility in Outdoor/Adverse Environments.' In *14th National Fiber Optic Engineers Conference (NFOEC), September 14–17, 1998* (Telcordia, 1998)
3.16 T. Mizushima, S. Morita, H. Sugawara, T. Sato, S. Yaguchi: 'Development of a Mass Fusion Splicing System for up to 24-Fiber Ribbon'. In: *Proceedings of the 51st International Wire and Cable Symposium (IWCS) at Lake Buena Vista, FL, November 18–21, 2002* (IWCS, Eatontown, NJ, 2002) pp. 708–714
3.17 M. Ratuszek, Z. Zakrzewski, J. Majewski, S. Strozecki, J. Zalewski, T. Konefal, W. Kula: 'Influence of weather conditions on splicing process and parameters of splicing single mode telecommunication fibers of different types'. In: *Optical Fibers and Their Applications VI at Bialowieza, Poland January 22–24, 1999* ed. by J. Wojcik, W. Wojcik (SPIE, Bellingham, Washington, 1999) pp. 128–132
3.18 M. Ratuszek, Z. Zakrzewski, J. Majewski, S. Strozecki, J. Zalewski: 'Arc fusion splicing of telecommunication optical fibers in exterme climatic circumstances'. In: *Lightguides and Their Applications at Krasnobrod, Poland October 14–16, 1999* ed. by J. Dorosz, R. S. Romaniuk (SPIE, Bellingham, Washington, 1999) pp. 150–154
3.19 S. Saito, N. Kawanishi, S. Yaguchi: 'Discharge power control for fusion splice of optical fiber'. In: *Proceedings of the Optical Fiber Communication Conference and Exhibit at Los Angeles, CA February 22-27, 2004* (Optical Society of American, Washington, DC 2004) p. MF4
3.20 N. P. Bansal, R. H. Doremus: *Handbook of Glass Properties*, (Academic Press, New York, 1986)
3.21 E. Serafini: 'Mechanical Strength of Optical Fiber Arc Fusion Splices'. In: *5th International Conference on Integrated Optics and Optical Fiber Communication and 11th European Conference on Optical Communication at Venice, Italy, October 1-4, 1985* (Istituto Internazionale delle Communicazioni, Compagnia dei Librai Editrice, Genevo, 1985) pp. 445–448.
3.22 S. M. Oh: Ceramic Bulletin, **55**, 1108 (1979)
3.23 U.-C. Paek, R. B. Runk: J. Appl. Phys. **49**, 4417 (1978)
3.24 E. C. Beder, C. D. Bass, W. L. Shackleford: Appl. Opt. **10**, 2263 (1971)
3.25 A. V. Dvurechenskii, V. A. Petrov, V. Yu Reznick: High Temp. **17**, 51 (1979)
3.26 R. Gardon: J. Am. Ceram. Soc. **44**, 305 (1961)
3.27 A. V. Dvurechensky, V. A. Petrov, V. Yu Reznick: Infrared Phys. **19**, 465 (1979)
3.28 V. A. Petrov, S. V. Stepanov: High Temp. **13**, 308 (1975)
3.29 E. M. Sparrow, R. D. Cess: *Radiation Heat Transfer*, (Hemisphere Publishing, London 1978)
3.30 S. H. Crandall, N. C. Dahl, T. J. Lardner: *An Introduction to the Mechanics of Solids*, 2nd edn. (McGraw-Hill, New York 1978)

3.31 E. M. O'Brien, C. D. Hussey: Electron. Lett. **35**, 168 (1999)
3.32 K. Furuya, T. C. Chong, Y. Suematsu: Trans. of the IECE of Japan, **E61**, 957 (1978)
3.33 A. Ishikura, Y. Kato, M. Miyauchi: Appl. Opt. **25**, 3460 (1986)
3.34 W. Stieb, J. Shulte, A. M. Oehler, T. M. Hauff, W. E. Heinlein: 'Fusion splices with low loss between SM-Fibers of different types'. In: *Proceedings of the 37th International Wire & Cable Symposium, Reno, NV, November 15–17, 1988* (US Army Commun.-Electron. Command, Fort Monmouth, NJ 1988) pp. 569–575
3.35 A. M. Oehler, T. Hauff, W. E. Heinlein, W. Stieb, J. Shulte: 'New field-matching technique for low-loss splices between conventional and dispersion-flattened single-mode fibers'. In *Fourteenth European Conference on Optical Communication Vol. 1, London, September 11–15, 1988*, (IEE, London, 1988) pp. 603–606
3.36 D. B. Mortimore, J. W. Wright: Electon. Lett. **22**, 319 (1986)
3.37 P. M. Gerhart, R. J. Gross: *Fundamentals of Fluid Mechanics*, (Addison-Wesley, Reading, MA 1985)
3.38 W. D. Kingery: J. Am. Ceram. Soc. **42**, 6 (1959).
3.39 R. H. Doremus: *Glass Science*, (John Wiley & Sons, New York 1973)
3.40 K. Tajima, M. Tateda, M. Ohashi: IEEE J. Lightwave Technol. **12**, 411 (1994)
3.41 S. Sakaguchi, S. Todoroki: J. Non-Cryst. Solids **244**, 232 (1999)
3.42 G. Kiss, E. Vogel: 'High Yield Fusion Splicing in the Outside Plant: Using Fiber Meltback to Monitor Electrode Condition'. In: *Proceedings of the National Fiber Optic Engineers Conference (NFOEC) September 9–12, 1996* (Telcordia, Piscataway, NJ 1996) pp. 819–835
3.43 O. Kawata, K. Hoshino, K. Ishihara: Opt. Lett. **9**, 255 (1984)
3.44 W. Zheng: IEEE J. Lightwave Technol. **11**, 548 (1993)
3.45 Y. Kato, S. Seikai, M. Tateda: Appl. Opt. **21**, 1332 (1982)
3.46 J. M. Haynes: J. Colloid. Interface Sci., **32**, 652 (1970)
3.47 J. Meseguer: J. Fluid Mech. **130**, 123 (1983)
3.48 S.-J. Kim, J.-M. Kim: 'Thermally expanded core fiber fabrication method and optical fiber coupling method'. *United States Patent no. 6,244,757* (2001)
3.49 J. K. Mackenzie, R. Shuttleworth: Proc. Phys. Soc. London **62**, 833 (1949)
3.50 J. T. Krause, W. A. Reed, K. L. Walker: IEEE J. Lightwave Technol. **LT-4**, 837 (1986)
3.51 H. Y. Tam: Electron. Lett. **27**, 1597 (1991)
3.52 Y. Koyano, M. Onishi, K. Tamano, M. Nishimura: 'Compactly-Packaged High Performance Fiber-Based Dispersion Compensation Modules'. In: *22nd European Conference on Optical Communications at Oslo, Norway, September 15–19, 1996*, (IEEE, Piscataway NJ 1996) pp. 321–324
3.53 L. Grüner-Nielsen, S. N. Knudsen, B. Edvold, T. Veng, D. Magnussen, C. C. Larsen, H. Damsgaard: Opt. Fiber Technol. **6**, 164 (2000)
3.54 K. Shiraishi: Appl. Opt. **29**, 3469 (1990)
3.55 M. Kihara, M. Matsumoto, T. Haibara, S. Tomita: IEEE J. Lightwave Technol. **14**, 2209 (1996)
3.56 H. S. Carslaw, J. C. Jaeger: *Conduction of Heat in Solids*, 2nd edn. (Oxford, New York 1959)
3.57 Y. L. Luke: *Integrals of Bessel Functions*, (McGraw-Hill, New York 1962)
3.58 H. Rau, W. Hermann: Ber. Bunsenges. Phys. Chem. **91**, 833 (1987)
3.59 K. Shiraishi, Y. Aizawa, and S. Kawakami: IEEE J. Lightwave Technol. **8**, 1151 (1990)
3.60 H. Yamada, H. Hanafusa: IEEE J. Lightwave Technol. **6**, 531 (1994)

3.61 J. Kirchhof, S. Unger, K.-F. Klein, B. Knappe: J. Non-Cryst. Solids **181**, 266 (1995)
3.62 W. Hermann, A. Raith, H. Rau: Ber. Bunsenges. Phys. Chem. **91**, 56 (1987)
3.63 C. P. Botham: Electron. Lett. **24**, 243 (1988)
3.64 G. Kweon, I. Park, J. Shim: Appl. Opt. **37**, 4789 (1998)
3.65 A. D. Yablon: IEEE J. Select. Topics Quantum Electron. **10**, 300 (2004)
3.66 G. W. Scherer: Appl. Opt. **19**, 2000 (1980)
3.67 W. Hermann, M. Hutjiens, D. U. Weichert: Appl. Opt. **28**, 1980 (1989)
3.68 S. Gulati: 'Mechanical Properties of SiO_2 vs. SiO_2-TiO_2 Bulk Glasses and Fibers'. In: *Optical Waveguide Materials at Boston, MA, December 2-4, 1991*, ed. by M. M. Broer, H. Kawazoe, G. H. Sigel, and R. Th. Kersten (Materials Research Society, Pittsburgh, PA 1992) pp. 67–84
3.69 Y. Park, K. Oh, U. C. Paek, D. Y. Kim, C. R. Kurkjian: IEEE J. Lightwave Technol. **17**, 1823 (1999)
3.70 M. Akiyama, K. Nishide, K. Shima, A. Wada, R. Yamauchi: 'A novel long-period fiber grating using periodically released residual stress of pure-silica core fiber'. In: *Optical Fiber Communication Conference, San Jose, CA, February, 1998*, (Optical Society of America, Washington, DC, 1998) pp. 276–277
3.71 T. Enomoto, M. Shigehara, S. Ishikawa, T. Danzuka, H. Kanamori: 'Long-period fiber grating in a pure-silica-core fiber written by residual stress relaxation'. In: *Optical Fiber Communication Conference, San Jose, CA, February, 1998*, (Optical Society of America, Washington, DC, 1998) pp. 277–278
3.72 P. L. Chu, T. Whitbread: Electron. Lett. **20**, 599 (1984)
3.73 Y. Mohanna: IEE Proc. Optoelecton., **142**, 313 (1995)
3.74 T. Volotinen, M. Zimnol, M. Tomozawa, Y.-K. Lee, K. Raine: 'Effect of Mechanical Stripping and Arc-Fusion on the Strength and Aging of a Spliced Recoated Optical Fiber'. In: *Reliability of Photonics Materials and Structures at San Francisco, USA, April 13–16, 1998*, ed. by E. Suhir, M. Fukuda, C. R. Kurkjian (Materials Research Society, Warrendale, PA 1998) pp. 163–179
3.75 K. Brugger: Appl. Opt. **10**, 437 (1971)
3.76 U. C. Paek, C. R. Kurkjian: J. Am. Ceram. Soc. **58**, 330 (1975)
3.77 G. W. Scherer: J. Non-Crystal. Sol. **34**, 223 (1979)
3.78 F. Tosco: *Fiber Optic Communications Handbook*, (Tab Books, Summit, PA, 1990)
3.79 P. K. Bachmann, W. Hermann, H. Wehr, D. U. Weichert: Appl. Opt. **26**, 1175 (1987)
3.80 L. Rongved, C. R. Kurkjian, F. T. Geyling: J. Non-Cryst. Sol. **42**, 579 (1980)
3.81 A. K. Varshneya, D. Varshneya, V. Jain, J. Non-Crystal. Sol. **93**, 215 (1987)
3.82 C.-S. Kim, Y. Han, B. H. Lee, W.-T. Han, U.-C. Paek, Y. Chung: Opt. Commun. **185**, 337 (2000)
3.83 B. H. Kim, Y. Park, T.-J. Ahn, D. Y. Kim, B. H. Lee, Y. Chung, U. C. Paek, W.-T. Han: Opt. Lett. **26**, 1657 (2001)
3.84 K. W. Raine, R. Feced, S. E. Kanellopoulos, V. A. Handerek: Appl. Opt. **38**, 1086 (1999)
3.85 W. Primak, D. Post: J. Appl. Phys. **30**, 779 (1959)
3.86 P. L. Chu, T. Whitbread: Appl. Opt. **21**, 4241 (1982)
3.87 D. D. Davis, T. K. Gaylord, E. N. Glytsis, S. G. Kosinski, S. C. Mettler, A. M. Vengsarkar: Electron. Lett. **34**, 302 (1998)
3.88 D. A. Krohn, A. R. Cooper: J. Am. Ceram. Soc. **52**, 661 (1969)
3.89 S. M. Oh, P. H. Predieux, X. G. Glavas: Opt. Lett. **7**, 241 (1982)
3.90 P. L. Chu, T. Whitbread: Electron. Lett. **20**, 449 (1984)

3.91 Y. Ohuchi, A. Wada, R. Yamauchi, N. Sato, K. Inada: 'Abrasion resistant optical fibers with mechanically induced compressive surface stress'. In *Optical Fiber Communication Conference at San Francisco, CA, January 22–26, 1990, 1990*, (Optical Society of America, Washington, DC 1990) p. 172
3.92 L. Rivoallan, J. Y .Guilloux: Electron. Lett. **24** 756 (1988)
3.93 B. B. Harbison, W. I. Roberts, I. D. Aggarwal: Electron. Lett. **25** 1214 (1989)
3.94 B. Srinivasan, M. Erlandsson, G. S. Feller, E. W. Mies, R. K. Jain: 'Reproducible fusion splicing of low melting point (fluoride) optical fibers with the use of a stable heat source'. In: *Technical Digest of the Optical Fiber Communication Conference (OFC) at Dallas TX, February 16–21, 1997*, (Optical Society of America, Washington, DC) pp. 1–2
3.95 Y. Kuriowa, N. Sugimoto, K. Ochiai, S. Ohara, Y. Fukusawa, S. Ito: 'Fusion Spliceable and High Efficient Bi_2O_3-based EDF for Short-Length and Broadband Application Pumped at 1480 nm'. In: *Proceedings of the Optical Fiber Communication Conference (OFC) at Anaheim, CA, March 17-22, 2001* (Optical Society of America, Washington, DC) p. TuI5
3.96 K. Kikuchi, K. Taira, N. Sugimoto: 'Highly-nonlinear Bismuth Oxide-based glass fibers for all-optical signal processing'. In: *Proceedings of the Optical Fiber Communication Conference (OFC) at Anaheim, CA, March 17-22, 2002* (Optical Society of America, Washington, DC) pp. 567–568
3.97 K. Kikuchi, K. Taira, N. Sugimoto: Electron. Lett. **38**, 166 (2002)
3.98 M. R. Lange, E. Bryant, M. J. Myers, J. D. Myers: 'High gain coefficient phosphate glass fiber amplifier'. In: *Technical Proceedings of the National Fiber Optic Engineers Conference (NFOEC) at Orlando, FL USA, Sept., 2003*, (Telcordia, Piscataway, NJ) pp. 960–967

Chapter 4

4.1 F. P. Kapron, B. P. Adams, E. A. Thomas, J. W. Peters: IEEE J. Lightwave Technol. **7**, 1234 (1989)
4.2 V. Poudyal, L. A. Reith, E. M. Vogel: 'Accuracy of optical component reflectance measurements using an OTDR'. In: *Optical Network Engineering and Integrity, SPIE Vol. 2611*, ed. by H. H. Yuce, D. K. Paul, R. A. Greenwell, (SPIE, Bellingham, WA 1996) pp. 180–188
4.3 J. P. von der Weid, R. Passy, G. Mussi, N. Gisin: IEEE J. Lightwave Technol. **15**, 1131 (1997)
4.4 A. Ghatak, K. Thyagarajan: *Introduction to Fiber Optics*, (Cambridge University Press, Cambridge 1998)
4.5 A. W. Snyder, J. D. Love: *Optical Waveguide Theory*, (Chapman and Hall, London 1983)
4.6 D. Marcuse: *Theory of Dielectric Optical Waveguides*, 2nd edn. (Academic Press, New York 1991)
4.7 H. A. Haus: *Waves and Fields in Optoelectronics*, (Prentice Hall, Englewood Cliffs, NJ 1984)
4.8 A. Yariv: *Optical Electronics*, 4th edn. (Saunders, London, 1991)
4.9 D. Gloge: Appl. Opt. **10**, 2252 (1971)
4.10 E.-G. Neumann: *Single-Mode Fibers: Fundamentals* (Springer-Verlag, Berlin, 1988)
4.11 M. Born, E. Wolf: *Principles of Optics*, 6th Edn. (Cambridge University Press, Cambridge, 1980)
4.12 G. R. Fowles: *Modern Optics*, 2nd Edn. (Dover Publications, New York 1975)

4.13 R. P. Feynman, R. B. Leighton, M. Sands, *The Feynman Lectures on Physics, Vol. 3: Quantum Mechanics*, (Addison-Wesley, Reading, MA 1965)
4.14 A. Siegman: *Lasers* (University Science Books, Mill Valley 1986 CA)
4.15 R. B. Kummer, S. R. Fleming: 'Monomode optical fiber splice loss - combined effects of misalignment and spot size mismatch.' In: *Fifth Topical Meeting on Optical Fiber Communication at Phoenix, AZ, April 13–15, 1982*, (Optical Society of America: Washington, DC 1982) paper THAA1, as cited in C. M. Miller, S. C. Mettler, I. A. White: *Optical Fiber Splices and Connectors*, (Marcel Dekker, New York 1986)
4.16 C. M. Miller, S. C. Mettler, I. A. White: *Optical Fiber Splices and Connectors*, (Marcel Dekker, New York 1986)
4.17 H. Y. Tam: Electron. Lett. **27**, 1597 (1991)
4.18 W. Zheng, O. Hulten, R. Rylander: IEEE J. Lightwave Technol. **12**, 430 (1994)
4.19 P. Leproux, P. Roy, D. Pagnoux, B. Kerrinckx, J. Marcou: Opt. Commun. **174**, 419 (2000)
4.20 G. Kweon, I. Park: IEEE J. Lightwave Technol. **17**, 690 (1999)
4.21 T. Erdogan: J. Opt. Soc. Am. A **14**, 1760 (1997)
4.22 N. Kashima, I. Sankawa: Appl. Opt. **22**, 3820 (1983)
4.23 E. Hecht: *Optics*, 2nd Edn. (Addison-Wesley Publishing, Reading, MA 1987)
4.24 V. A. Burdin, A. V. Bourdine: 'Estimation of probability distribution of reflection attenuation at optical fiber fusion splices'. In: *Optical Fiber and Planar Wave Technology, at Beijing, China, November 13–15, 2001* ed. by S. Jian, Y. Liu (SPIE, Bellingham, WA, 2001) pp. 6–15
4.25 W. V. Sorin, D. M. Baney: IEEE Photon. Technol. Lett. **4**, 374 (1992)
4.26 J. A. Kong: *Electromagnetic Wave Theory*, (EMW Publishing, Cambridge, MA 2000)
4.27 K. Petermann: Electron. Lett. **19**, 712 (1983)
4.28 C. Pask: Electron. Lett. **20**, 144 (1984)
4.29 D. Marcuse: Bell Syst. Tech. J. **56**, 703 (1977)
4.30 D. Marcuse: J. Opt. Soc. Am. **68**, 103 (1978)
4.31 S. Nemoto, T. Makimoto: Opt. and Quant. Elect. **11**, 447 (1979)
4.32 H. R. .D. Sunak, S. P.Bastien: IEEE Photon. Technol. Lett. **1**, 146 (1989)
4.33 Q. Cao, S. Chi: IEEE J. Lightwave Technol. **18**, 54 (2001)
4.34 J. J. Refi: *Fiber Optic Cable - A Lightguide*, 2nd edn. (AVO Training Institute, 2001)
4.35 F. M. Sears, I. A. White, R. B. Kummer, F. T. Stone: 'Probability of modal noise in single-mode lightguide systems'. In: *IOOC-ECOC at Venice, Italy October 1–4, 1985*, pp. 823–826
4.36 C. DeCusatis, G. Li: 'Chapter 6: Fiber-optic Communication Links (Telecom, Datacom, and Analog)'. In: *Handbook of Optics Vol. IV Fiber Optics and Nonlinear Optics*. ed. by M. Bass (McGraw-Hill, New York 2001) pp. 6.1-6.20
4.37 J. C. Goodwin, P. J. Vella: IEEE J. Lightwave Technol. **9**, 954 (1991)
4.38 K. Abe, Y. Lacroix, L. Bonnell, Z. Jakubczyk: IEEE J. Lightwave Technol. **10**, 401 (1992)
4.39 D. Kalish: Commun. Eng. Design **15**, 44 (1989)
4.40 D. G. Duff, D. A. Fishman, J. A. Nagel: 'Measurements and simulation of multipath interference for 1.7 Gbit/s lightwave systems utilizing single and multifrequency lasers'. In: *Optical Fiber Communication Conference at Houston, TX February 6–9 1989*, p. 128
4.41 N. Kashima: *Passive Optical Components for Optical Fiber Transmission*, (Artech, Boston 1995)

4.42 R. B. Kummer: 'Observation of a Cascade Effect for Optical Fiber Splices'. In: *3rd Topical Meeting On Optical Fiber Communication Conference*, (Optical Society of America: Washington, DC 1979) paper ThE2 as cited in C. M. Miller, S. C. Mettler, I. A. White: *Optical Fiber Splices and Connectors*, (Marcel Dekker, New York 1986)
4.43 I. A. White, S. C. Mettler: Bell Syst. Tech. J. **62**, 1189 (1983)
4.44 S. Sekai, N. Uchida: Trans. IECE of Japan **E-65**, 485 (1982)
4.45 P. W. Shumate, J. L. Gimmlett, M. Stren, M. B.Romeiser, N. K. Cheung: Electron. Lett. **21**, 522 (1985).
4.46 Y. Chung, N. Dagli: IEEE J. Quantum Electron. **26**, 1335 (1990)
4.47 R. Scarmozzino, R. M. Osgood, Jr.: J. Opt. Soc. Am. A **8**, 724 (1991)
4.48 D. Yevick: Opt. Quantum Electron. **26**, S185 (1994)
4.49 D. Yevick: SPIE Vol. 2693 (1996)
4.50 R. Scarmozzimo, A. Gopinath, R. Pregla, S. Helfert: IEEE J. Select. Topics Quantum Electron. **6**, 150 (2000)
4.51 M. D. Feit, J. A. Fleck, Jr.: Appl. Opt. **17**, 3990 (1978)
4.52 M. D. Feit, J. A. Fleck, Jr.: Appl. Opt. **18**, 2843 (1979)
4.53 M. D. Feit, J. A. Fleck, Jr.: Appl. Opt. **19**, 1154 (1980)
4.54 M. D. Feit, J. A. Fleck, Jr.: Appl. Opt. **19**, 2240 (1980)
4.55 B. Zamzow, G. Ruegenberg, M. Anderson, H. Krupp: 'Numerical Simulation of High Quality Fiber Optic Splices For High Precision Loss Evaluation'. In: *Proceedings of the 48th International Wire and Cable Symposium at Atlantic City, NJ, November 15–18, 1999* (IWCS, Eatontown, NJ 1999), pp 621-628
4.56 W. P. Huang, S. T. Chu, A. Goss, S. K. Chaudhuri: IEEE Photon. Technol. Lett. **3**, 524 (1991)
4.57 J. Yamauchi, K. Nishio, H. Nakano: IEEE J. Lightwave Technol. **16**, 465 (1998)
4.58 A. Taflov: *Computational Electrodynamics: The Finite Difference Time Domain Method*, (Artech, Norwood, MA, 1995)
4.59 J. Yamauchi, M. Ikegaya, T. Ando, H. Nakano: IEICE Trans. Electron. **E75-C**, 1093 (1992).
4.60 J. Yamauchi, Y. Akimoto, M. Nibe, H. Nakano: IEEE Photon. Technol. Lett. **8**, 236 (1996)
4.61 J. Shibayama, K. Matsubara, M. Sekiguchi, J. Yamauchi, H. Nakano: IEEE J. Lightwave Technol. **17**, 677 (1999)
4.62 W. H. Press, B. P. Flannery, S. A. Teukolsky, W. T. Vetterling: *Numerical Recipes in C*, 2nd edn. (Cambridge, New York 1992)
4.63 G. R. Hadley: Opt. Lett. **16**, 624 (1991)
4.64 G. R. Hadley: IEEE J. Quantum Electron. **28**, 363 (1992)
4.65 C. D. Hussey, K. P. Oakley: 'Low-loss splices between different fibres'. In: *Opto-Ireland 2002: Optics and Photonics Technologies and Applications at Galway Ireland, September 5–6, 2002* ed. T. J. Glynn (SPIE, Bellingham, WA, 2003) pp. 266-272

Chapter 5

5.1 A. Ishikura, Y. Kato, T. Ooyanagi: J. Opt. Commun. **10**, 56 (1989)
5.2 T. Onodera, H. Taya, T. Yamada, M. Yoshinuma: Opt. Lett. **15**, 1406 (1990)
5.3 W. Zheng, O. Hulten, S. Esmaeli: IEEE J. Lightwave Techol. **17**, 1366 (1999)
5.4 W. Zheng, O. Hulten, R. Rylander: IEEE J. Lightwave Technol. **12**, 430 (1994)

5.5 Telcordia Corp.: *Generic Requirements for Multi-Fiber Single-Mode Optical Splices and Splicing Systems GR-1095-CORE* (Bellcore, Piscataway, NJ November 1996) available from http:\\www.telcordia.com
5.6 K. Osaka, M. Hamada, T. Yanagi, Y. Asano, K. Watanabe, T. Seike: Sumitomo Electric Tech. Rev. **29**, 85 (1990)
5.7 G. Mackie, G. Karl, R. E. Dorian, D. Duke: 'Evolution of Mass Fusion Splicing Technology For Utility in Outdoor/Adverse Environments.' In *14th National Fiber Optic Engineers Conference (NFOEC) at Orlando, FL, September 14–17, 1998* (Telcordia, Piscataway, NJ 1998)
5.8 T. Nakamichi, K. Ohzawa, S. Yaguchi: 'Improvement of Estimated Splice Loss Accuracy by Measuring MFD of Spliced Fiber'. In: *Vol. 1 of the Proceedings of the Optical Fiber Communications Conference at Atlanta, GA, March 22–28, 2003* (Optical Society of America, Washington, DC 2003) pp. 10–11
5.9 D. L. Myers: 'Producing Low Loss Singlemode Fusion Splices Using Video Alignment Techniques.' In *The Seventh Annual European Fibre Optic Communications & Local Area Networks Exposition (E-FOC/LAN 1989) at Amsterdam, Holland, 1989* (1989), pp. 77–82
5.10 G. Mackie, D. Duke, G. Karl, R. Menard: 'Evolution of Fusion Splicing Technology and Application Based on Fiber Geometry'. In: *Proceedings of the National Fiber Optic Engineers Conference (NFOEC) at Boston, MA June 18-22, 1995* (NFOEC, Telcordia, Piscataway, NJ 1995) pp. 93–95
5.11 T. Katagiri, M. Tachikura, I. Sankawa: IEEE J. Lightwave Technol. **LT-2**, 277 (1984)
5.12 T. Katagiri, M. Tachikura, K. Ishiharar: Electron. Commun. Japan, Part 2 **71**, 77 (1988)
5.13 M. Mansuripur, L. Li, W.-H. Yeh: 'Scanning Optical Microscopy, Part I'. Opt. Photonics News **9**, No. 5, 56 (1998)
5.14 M. Mansuripur, L. Li, W.-H. Yeh: 'Scanning Optical Microscopy: Part II'. Opt. Photonics News **9**, No. 6, 42 (1998)
5.15 W. Zheng: IEEE J. Lightwave Technol. **11**, 548 (1993)
5.16 J. C. Russ: *The Image Processing Handbook*, 3rd Edn. (CRC Press, Boca Raton, FL 1998)
5.17 B. Zamzow, G. Ruegenberg, M. Anderson, H. Krupp: 'Numerical Simulation of High Quality Fiber Optic Splices For High Precision Loss Evaluation'. In: *Proceedings of the 48th International Wire and Cable Symposium at Atlantic City, NJ, November 15–18, 1999* (IWCS, Eatontown, NJ 1999), pp 621-628
5.18 T. Erdogan: J. Opt. Soc. Am. A **14**, 1760 (1997)
5.19 D. Marcuse: *Theory of Dielectric Optical Waveguides*, 2nd edn. (Academic Press, New York, 1991)
5.20 I. A. White, J. F. Kuhl: 'Microbending theory of single mode fiber splices - butt-joint and fusion'. In: *Fourth International Conference on Integrated Optics (IOOC) and Optical Fiber Communications (OFC) at Tokyo, Japan, June 27–30, 1983*, (Denshi Tshushin Gakkai, Tokyo, Japan 1983) pp. 402-403.
5.21 C. M. Miller, S. C. Mettler, I. A. White: *Optical Fiber Splices and Connectors*, (Marcel Dekker, New York 1986)
5.22 W. Zheng: 'Loss Estimation for Fusion Splices of Single-mode Fibers'. In: *Fiber Optic Components and Reliability at Boston, MA, Sept. 3–6, 1991*, ed. by P. M. Kopera, D. K. Paul, (SPIE, Bellingham, WA 1992), pp. 380-390
5.23 H. A. Haus: *Waves and Fields in Optoelectronics*, (Prentice Hall, Englewood Cliffs, NJ 1984)
5.24 J. J. Refi: *Fiber Optic Cable - A Lightguide*, 2nd edn. (AVO Training Institute, 2001)

Chapter 6

6.1 J. J. Refi: *Fiber Optic Cable - A Lightguide*, 2nd edn. (AVO Training Institute, 2001)
6.2 T. Kuwabara, H. Koga, Y. Mitsunaga, S. Isobe: Electron. Lett. **27** 1774
6.3 B. G. LeFevre: 'Failure Mechanisms and Reliability of Fiber Optic Connectors and Splices'. In: *Passive fiber optic components and their reliability at Berlin, April 6–8 1993*, ed. by V. J. Tekippe, J. V. Varachi (SPIE Vol 1973, Bellingham, WA 1993) pp. 264–278
6.4 S. C. Mettler: 'Reliability considerations for fiber optic connections'. In: *Fiber optics reliability : benign and adverse environments, at San Diego, CA, August 17-18 1987*, ed. by D. K. Paul, (SPIE Vol 842, Bellingham, WA 1987) pp. 132–134
6.5 C. R. Kurkjian, J. T. Krause, M. J. Mathewson: IEEE J. Lightwave Technol. **7**, 1360 (1989)
6.6 C. R. Kurkjian, D. Inniss: Opt. Engineering **30**, 681 (1991)
6.7 F. P. Kapron: 'Standards Issues in Fiber Environmental Performance and Reliability'. In: *Fiber Optics Reliability: Benign and Adverse Environments, at San Diego, CA, August 17–18 1987*, ed. by D. K. Paul, (SPIE Vol 842, Bellingham, WA 1987) pp. 14–21
6.8 S. R. Nagel: 'Reliability Issues in Optical Fibers'. In: *Reliability Considerations in Fiber Optic Applications at Cambridge, MA, Sept. 25–26, 1986*, ed. by D. K. Paul (SPIE Vol 717, Bellingham, WA 1987), pp. 8–20.
6.9 I. Hatakeyama, M. Tachikura, H. Tsuchiya: Electron Lett. **14**, 613 (1978)
6.10 Y. Miyajima, K. Ishihara, T. Kakii, Y. Toda, S. Tanaka: Electron. Lett. **17**, 670 (1981)
6.11 Y. Miyajima, S. Furukawa, O. Kawata: IEEE J. Lightwave Technol. **LT-1**, 184 (1983)
6.12 T. A. Michalske, B. C. Walker: Sci. Am. **257**, 122 (1987).
6.13 L. A. Reith, H. H. Yuce, P. B. Grimado: 'Mechanical reliability of fiber optic splices'. In: *Passive fiber optic components and their reliability at Berlin, April 6–8 1993*, ed. by V. J. Tekippe, J. V. Varachi (SPIE Vol 1973, Bellingham, WA 1993) pp. 315–330
6.14 C. R. Kurkjian, J. T. Krause: 'An Overview of Unsolved Problems'. In: *Optical Fiber and Fiber Component Mechanical Reliability and Testing, Boston, MA, November 5–8, 2000*, ed. by M. J. Matthewson, (SPIE Vol 4215, Bellingham, WA 2001) pp. 1–15
6.15 K. Takahashi, S. Yaguchi, N. Kawanishi, T. Ohtani: 'Development of a New Factory Fusion Splicer.' In: Proceedings of the 50th International Wire and Cable Symposium (IWCS) at Lake Buena Vista, FL, November 12–15, 2001 (IWCS, Eatontown NJ, 2001) pp. 68-76
6.16 M. Tachukura, T. Haibara: IEEE J. Lightwave Technol. **LT-3**, 662 (1985)
6.17 J. T. Krause, C. R. Kurkjian: Electron. Lett. **21**, 533 (1985)
6.18 J. T. Krause, C. R. Kurkjian: Electron. Lett. **22**, 1075 (1985)
6.19 A. Berg, M. Johansen: Electron. Lett. **31**, 308 (1995)
6.20 J. T. Krause, G. W. Kammlott, S. G. Kosinski: 'Improved Strengths (3.7 GPa) of Arc Fusion Splices for High Yield-High Reliability.' In: *Proceedings of the 19th European Conference on Optical Communication Volume 2 at Montreux, Switzerland, September 12–16, 1993* pp.449–452
6.21 G. W. Kammlott, S. G. Kosinski, J. T. Krause, R. S. Riggs: 'Method and apparatus for fusion splicing optical fibers,' *United States Patent 5414788*, (1995)

6.22 J. T. Krause, D. Stroumbakis: 'Factors affecting arc fusion splice strengths.' In: *Optical Network Engineering and Integrity at Philadelphia, PA, October 24–25, 1995*, ed. by H. H. Yuce, D. K. Paul, R. A. Greenwell (SPIE, Bellingham, WA 1996) pp. 98–109
6.23 J. T. Krause, S. N. Kher, D. Stroumbakis: 'Arc fusion splices with near pristine strengths and improved optical loss.' In: *Proceedings of the 22nd European Conference on Optical Communication Volume 2 (ECOC 1996) at Oslo, Sweden, September 15–19, 1996* (Telenor R&D, Piscataway, NJ 1996) pp. 2.237-2.240
6.24 M. F. Ashby, D. R. H. Jones: *Engineering Materials 1, An Introduction to their Properties and Applications* (Pergamon Press, New York 1980)
6.25 M. F. Ashby, D. R. H. Jones: *Engineering Materials 2, An Introduction to Microstructures, Processing, and Design* (Pergamon Press, New York 1986)
6.26 D. Kalish, P. L. Key, C. R. Kurkjian, B. K. Tariyal, T. T. Wang: 'Fiber Characterization- Mechanical'. In: *Optical Fiber Telecommunications*, ed. by S. E. Miller and A. K. Chynoweth (Academic Press, New York 1979) pp. 401–433
6.27 T. C. Chu, H. C. Chandan: AT&T Technical J. **64**, 971 (1985)
6.28 D. Kalish, B. K. Tariyal: J. Am. Ceram. Soc. **61**, 518 (1978)
6.29 Y. Mitsunaga, Y. Katsuyama, H. Kobayashu, Y. Ishida: J. Appl. Phys. **53**, 4847 (1982)
6.30 I. Scanlan: 'A physical interpretation of the slope of Weibull plots'. In: *Physics of Fiber Optics, Proceedings of the Special Conference on Physics of Fiber Optics at Chicago, IL, April 27–30, 1980*, ed. by B. Bendow, S. S. Mitra (American Ceramics Society, Columbus, OH 1981) pp. 166-175
6.31 A. G. Evans, E. R. Fuller: Mat. Sci. Eng. **19**, 69 (1975)
6.32 Y. Miyajima: IEEE J. Lightwave Technol. **LT-1**, 340 (1983)
6.33 Y. Miyajima, M. Ohnishi, O. Kawata, K. Ishihara, Y. Negishi: IEEE J. Lightwave Technol. **LT-3**, 248 (1985)
6.34 Y. Miyajima, M. Ohnishi, O. Kawata, K. Ishihara, Y. Negishi: IEEE J. Lightwave Technol. **LT-3**, 332 (1985)
6.35 Y. Negishi, Y. Miyajima, M. Ohnishi, O. Kawata, K. Ishihara: J. Optical Comm. **6** 122 (1985)
6.36 H. Damsgaard, O. Hansen: 'Factory Spliced Fibers: Technology, Performance and Field Experience'. In: *Proceedings of the 39th International Wire and Cable Symposium, 1990* (IWCS, Eatontown, NJ, 1990) 284–287
6.37 M. Matsumoto, T. Haibara, M. Miyauchi: IEEE J. Lightwave Technol. **LT-3**, 322 (1985)
6.38 M. Komachiya, R. Minamitani, T. Fumino, T. Sakaguchi, S. Watanabe: Appl. Opt. **38**, 2767 (1999)
6.39 M. Zimnol, B. Sundström, T. Svensson: 'Lifetime of Splices Under Tension'. In: *Proceedings of the European Conference on Optical Communicaiton at Madrid, Sept. 20–24, 1998*, (Telefnica de Espaa, Madrid, 1998) pp. 361–362
6.40 S. H. Crandall, N. C. Dahl, T. J. Lardner: *An Introduction to the Mechanics of Solids*, 2nd edn. (McGraw-Hill, New York 1978)
6.41 P. D. Patel, H. C. Chandan, D. Kalish: 'Failure Probability of Optical Fibers in Bending'. In: *Proceedings of the 30th International Wire and Cable Symposium at Cherry Hill, NJ, Nov. 17–19, 1981*, (US Army CECOM, Fort Monmouth, NJ 1981), pp. 37-43
6.42 'Generic Requirements for Single-mode Fiber Splicing Systems'. Technical Reference TR-NWT-000765 (Current edition published as General Requirement GR-765-CORE) (Telcordia, Piscataway, NJ 1992) available from http://www.telcordia.com

6.43 'Transmission and Multiplexing (TM); Passive optical components; Fibre optic fusion splices for single-mode optical fibre transmission systems; Common requirements and conformance testing'. ETSI Standard I-ETS 300 783 (European Telecommunications Standards Institute, Valbonne, France 1998) available from http://www.etsi.fr
6.44 'Series L: Construction, installation and protection of cables and other elements of outside plant: Optical fibre joints'. ITU Standard L.12 (International Telecommunications Union, 2000) available from http://www.itu.int
6.45 'Generic Requirements for Fusion Splice Protectors'. Generic Requirement GR-1380-CORE (Telcordia, Piscataway, NJ 1994) available from http://www.telcordia.com
6.46 K. Osaka, M. Hamada, T. Yanagi, Y. Asano, K. Watanabe, T. Seike: Sumitomo Tech. Rev. **29**, 85 (1990)
6.47 T. Mizushima, S. Morita, H. Sugawara, T. Sato, S. Yaguchi: 'Development of a Mass Fusion Splicing System for up to 24-Fiber Ribbon'. In: *Proceedings of the 51st International Wire and Cable Symposium (IWCS) at Lake Buena Vista, FL, November 18–21, 2002* (IWCS, Eatontown, NJ, 2002) pp. 708–714

Chapter 7

7.1 T. G. Beckwith, R. D.Maragoni: *Mechanical Measurements* 4th ed. (Addison-Wesley, New York 1989)
7.2 D. Marcuse: *Prinicples of Optical Fiber Measurements* (Academic Press, New York 1981)
7.3 J. J. Refi: *Fiber Optic Cable - A Lightguide*, 2nd edn. (AVO Training Institute, 2001)
7.4 D. Derickson, editor: *Fiber Optic Test and Measurement*, (Prentice Hall, Upper Saddle River, NJ 1998)
7.5 V. C. Y. So, R. P. Hughes, J. B. Lamont, P. J. Vella: IEEE J. Lightwave Technol. **LT-5**, 1663 (1987)
7.6 C. Hentschel, D. Derickson: 'Insertion Loss Measurements'. In: *Fiber Optic Test and Measurement*, ed. by D. Derickson (Prentice Hall, Upper Saddle River, NJ 1998) pp. 339–382.
7.7 Y. Kato, S. Sekai, T. Tanifuji: IEEE J Lightwave Technol. **LT-2** 442 (1984)
7.8 C. Ming, J. Desheng: 'Loss measuring and process monitoring in splicing two different fibers'. In: *International Conference on Sensors and Control Techniques (ICSC) at Wuhan, China June 19–21, 2000* ed. by D. Jiang A. Wang, (SPIE Bellingham, WA 2000) pp. 97–100
7.9 E.-G. Neumann: *Single-Mode Fibers: Fundamentals* (Springer-Verlag, Berlin, 1988)
7.10 J. Beller: 'OTDRs and Backscatter Measurements'. In: *Fiber Optic Test and Measurement*, ed. by D. Derickson (Prentice Hall, Upper Saddle River, NJ 1998) pp. 434-474
7.11 L. Bjerkan: IEEE J. Lightwave Technol. **7**, 490 (1989)
7.12 D. Anderson: 'Making True Splice Loss Measurements with OTDRs from One End of the Fiber'. In: *Proceedings of the National Fiber Optic Engineers Conference at Boston, MA, June 18-22, 1995* pp. 1127-1138 (Telcordia, Piscataway, NJ 1995)
7.13 D. Suino, F. Montalti: 'Fibre Optic Splice Loss Assessment by Means of Unidirectional OTDR Measurement'. In: *Proceedings of the International Wire and Cable Symposium 1999* pp. 629–635 (IWCS, Eatontown, NJ 1999)

7.14 L. Faltin: J. Optical. Comm. **9**, 24 (1988)
7.15 Agilent Corporation Application Note: 'Single-ended Bi-directional OTDR Measurements'. available at www.agilent.com (2003)
7.16 A. Ghatak, K. Thyagarajan: *Introduction to Fiber Optics*, (Cambridge University Press, London, 1998)
7.17 W. Sorin: 'Optical Reflectometry for Component Characterization'. In: *Fiber Optic Test and Measurement*, ed. by D. Derickson (Prentice Hall, Upper Saddle River, NJ 1998) pp. 383–433
7.18 G. P. Agrawal: *Nonlinear Fiber Optics* 3rd edn. (Academic, New York 2001)
7.19 W. V. Sorin, D. M. Baney: IEEE Photon. Technol. Lett. **4**, 374 (1992)
7.20 V. A. Burdin, A. V. Bourdine: 'Estimation of probability distribution of reflection attenuation at optical fiber fusion splices'. In: *Optical Fiber and Planar Wave Technology, at Beijing, China November 13–15, 2001*, ed. by S. Jian, Y. Liu (SPIE, Bellingham, WA, 2001) pp. 6–15. M. Baney: IEEE Photon. Technol. Lett. **4**, 374 (1992)
7.21 F. P. Kapron, B. P. Adams, E. A. Thomas, J. W. Peters: IEEE J. Lightwave Technol. **7**, 1234 (1989)
7.22 J. P. von der Weid, R. Passy, G. Mussi, N. Gisin: IEEE J. Lightwave Technol. **15**, 1131 (1997)
7.23 S. A. Newton: 'Fundamentals of Optical Reflectometry Techniques'. In: *Proceedings of the Tutorial Sessions of the Optical Fiber Communication Conference, at San Diego, CA, February 25 – March 1, 1996* (Optical Society of America, Washington, DC) pp. 97–130

Chapter 8

8.1 S. R. Schmidt, R. G. Launsby: *Understanding Industrial Designed Experiments* 4th edn. (Air Academy Press, Colorado Springs, CO 1997)
8.2 P. J. Ross: *Taguchi Techniques for Quality Engineering* 2nd edn. (McGraw-Hill, New York, 1996)
8.3 R. D. Moen, T. W. Nolan, L. P. Provost: *Quality Improvement Through Planned Experimentation* (McGraw-Hill, New York, 1999)
8.4 A. Mitra: *Fundamentals of Quality Control and Improvement* 2nd edn. (Prentice Hall, Upper Saddle River, NJ, 1998)
8.5 M. S. Phadke: *Quality Engineering Using Robust Design* (Prentice hall, Englewood Cliffs, NJ 1989)
8.6 Y. Ando: IEEE Photon. Technol. Lett. **4**, 1028 (1992)
8.7 T. A. Birks, Y. W. Li: IEEE J. Lightwave Technol. **10**, 432 (1992)
8.8 R. J. Black, S. Lacroix, F. Gonthier, J. D. Love: IEE Proceedings-J **138**, 355 (1991)
8.9 M. Cheng: 'Optimized Process to Splice Dispersion Compensation Fibres with Standard Single-Mode Fibres'. In: *Proceedings of the 49th International Wire and Cable Symposium (IWCS) at Atlantic City, NJ, November, 2000* (IWCS, Eatontown, NJ 2000) pp. 385–388
8.10 B. Edvold, L. Grüner-Nielsen: 'New technique for reducing the splice loss to dispersion compensating fiber.' In: *Proceedings of the 22nd European Conference on Optical Communication Volume 2 (ECOC 1996) at Oslo, Sweden, September 15–19, 1996* (Telenor R&D, Piscataway, NJ 1996) pp. 2.245-2.248
8.11 A. J. Fielding, K. Edinger, C. C. Davis: IEEE J. Lightwave Technol. **17**, 1649 (1999)

8.12 K. Furuya, T. C. Chong, Y. Suematsu: Transactions of the IECE of Japan **E61**, 957 (1978)
8.13 C. Gomez-Reino, M. V. Perez, C. Bao: *Gradient-Index Optics* (Springer, New York 2000)
8.14 L. Grüner-Nielsen, S. N. Knudsen, B. Edvold, T. Veng, D. Magnussen, C. C. Larsen, H. Damsgaard: Opt. Fiber Technol. **6**, 164 (2000)
8.15 H. Hanafusa, M. Horiguchi: Electron. Lett. **27**, 1968 (1991)
8.16 M. Ratuszek, Z. Zakrzewski, J. Majewski, M. Ratuszek: 'Diffusion processes and emerging intermediate area during arc fusion splicing of single mode optical telecommunication fibers'. In: *Lightguides and Their Applications at Krasnobrod, Poland October 14-16, 1999* ed. by J. Kojcik, W. Wojcik (SPIE Bellingham, WA 2000) pp. 155–167
8.17 K. Shiraishi, Y. Aizawa, S. Kawakami: IEEE J. Lightwave Technol. **8**, 1151 (1990)
8.18 K. Himeno, S. Kumayasu, K. Aikawa, A. Wada, R. Yamauchi: 'Splice loss of large effective area fiber and its reduction by mode field conversion.' In: *Proceedings of the 23nd European Conference on Optical Communication (ECOC 1997) at Edinburgh, Scotland, September 22–25, 1997* (Institution of Electrical Engineers, London, 1997), pp. 131–134
8.19 A. W. Snyder, J. D. Love: *Optical Waveguide Theory*, (Chapman and Hall, London 1983)
8.20 C. D. Hussey, K. P. Oakley: 'Low-loss splices between different fibres'. In: *Opto-Ireland 2002: Optics and Photonics Technologies and Applications at Galway Ireland, September 5–6, 2002* ed. T. J. Glynn (SPIE, Bellingham, WA, 2003) pp. 266-272
8.21 M. J. Holmes, F. P. Payne: Electron. Lett. **26**, 2102 (1990)
8.22 E.-G. Neumann: *Single-Mode Fibers: Fundamentals* (Springer-Verlag, Berlin, 1988)
8.23 E. M. O'Brien, C. D. Hussey: Electron. Lett. **35**, 168 (1999)
8.24 A. Ishikura, Y. Kato, M. Miyauchi: Appl. Opt. **25**, 3460 (1986)
8.25 M. Kihara, S. Tomita, M. Matsumoto: IEEE Photon. Technol. Lett. **4**, 1390 (1992)
8.26 C. R. Kurkjian, J. T. Krause: 'An Overview of Unsolved Problems'. In: *Optical Fiber and Fiber Component Mechanical Reliability and Testing, Boston, MA, November 5–8, 2000*, ed. by M. J. Matthewson, (SPIE Vol 4215, Bellingham, WA 2001) pp. 1–15
8.27 Y. Koyano, M. Onishi, K. Tamano, M. Nishimura: 'Compactly-packaged high performance fiber-based dispersion compensation modules.' In: *Proceedings of the 22nd European Conference on Optical Communication Volume 3 (ECOC 1996) at Oslo, Sweden, September 15–19, 1996* (Telenor R&D, Piscataway, NJ 1996) pp. 3.221–3.224
8.28 J. T. Krause, W. A. Reed, K. L. Walker: IEEE J. Lightwave Technol. **LT-4**, 837 (1986)
8.29 J. D. Love, W. M. Henry, W. J. Stewart, R. J. Black, S. Lacroix, F. Gonthier: IEE Proceedings-J **138**, 343 (1991)
8.30 D. Marcuse: IEEE J. Lightwave Technol. **LT-5**, 125 (1987)
8.31 D. B. Mortimore, J. V. Wright: Electron. Lett. **22**, 318 (1986)
8.32 M. Nakano, H. C. Chandan, J. Luo, L. R. Pritchett, T. Ellithi, T. Veng, A. D. Yablon and J. F. Ryan: 'Improvements in Splicing Dissimilar Fibers for Dispersion-Managed Ultra Long Haul Network'. In: *Proceedings of the 51st International Wire and Cable Symposium (IWCS) at Lake Buena Vista, FL, November 18–21, 2002* (IWCS, Eatontown, NJ 2002) pp. 687–695

8.33 A. M. Oehler, T. M. Hauff, W. E. Heinlein, W. Stieb, J. Schulte: 'New field-matching technique for low-loss splices between conventional and dispersion-flattened single-mode fibres'. In: *14th European Conference on Optical Communication, Volume 1, at London, UK September 11–15, 1988* (IEE, London, England 1988) pp. 603–606
8.34 K. Ohsono, K. Kotani, K. Murakami, Y. Bing, T. Yamazaki, H. Shimane: 'The Study of Large Effective Area Fiber & Mating Dispersion Slope Compensating Fiber for Dispersion Flattened Hybrid Optical Fiber DWDM Link'. In: *Proceedings of the 50th International Wire and Cable Symposium (IWCS) at Lake Buena Vista, FL, November 12–15, 2001* (IWCS, Eatontown, NJ 2001) pp. 483–486
8.35 J. J. Refi: *Fiber Optic Cable - A Lightguide*, 2nd edn. (AVO Training Institute, 2001)
8.36 T. Sato, J. Sun, R. Kasahara, S. Kawakami: Opt. Lett. **24**, 1337 (199)
8.37 K. Shiraishi, A. Ogura, K. Matsumuura: IEEE Photon. Technol. Lett. **10**, 1757 (1998)
8.38 W. Stieb, J. Schulte, A. M. Oehler, T. M. Hauff, W. E. Heinlein: 'Fusion splices with low loss between SM-fibers of different types'. In: *Proceedings of the 37th International Wire & Cable Symposium, at Reno, NV, November 15–17, 1988* (US Army Commun.-Electron. Command, Fort Monmouth, NJ 1988) pp. 569–575
8.39 K. Takahashi, S. Yaguchi, N. Kawanishi, T. Ohtani: 'Development of a New Factory Fusion Splicer.' In: *Proceedings of the 50th International Wire and Cable Symposium (IWCS) at Lake Buena Vista, FL, November 12–15, 2001* (IWCS, Eatontown, NJ 2001) pp. 68–76
8.40 H. Y. Tam: Electron. Lett. **27**, 1597 (1991)
8.41 Q. Wu: *US Patent 6,321,006* (2001)
8.42 W. Zell, J. A. Becker, P. K. Bachmann, W. G. Hermann: IEEE J. Lightwave Technol. **LT-5**, 1192 (1987)

Chapter 9

9.1 J. J. Refi: *Fiber Optic Cable - A Lightguide*, 2nd edn. (AVO Training Institute, 2001)
9.2 M. E. White, S. A. Cooper: 'Splice Loss in Non-Zero Dispersion-Shifted Fibers'. In: *Proceedings of the International Wire and Cable Symposium (IWCS), November 16–19, 1998*, (International Wire and Cable Symposium, Eatontown, NJ 1998) pp. 891–896.
9.3 M. Adcox: 'Splicing and Fiber Assembly Compatibility for Non-Zero Dispersion-Shifted Fiber and Standard Single-Mode Fiber'. In: *Proceedings of the National Fiber Optic Engineers Conference (NFOEC) at Denver, CO, August 27-31, 2000* (Telcordia, Piscataway, NJ, 2000)
9.4 M. Nakano, H. C. Chandan, J. Luo, L. R. Pritchett, T. Ellithi, T. Veng, A. D. Yablon and J. F. Ryan: 'Improvements in Splicing Dissimilar Fibers for Dispersion-Managed Ultra Long Haul Network'. In: *Proceedings of the 51st International Wire and Cable Symposium (IWCS) at Lake Buena Vista, FL, November 18–21, 2002* (IWCS, Eatontown, NJ 2002) pp. 687–695
9.5 M. Ratuszek, J. Majewski, Z. Zakrzewski, J. Zlewski, Z. Drzycimski: 'Examination of connections of splice fibers NZDF of TrueWave Type'. In *Optical Fibers and Their Applications VI, SPIE Vol. 3731, at Bialowieza, Poland, January 22-24, 1999*, ed. by J. Dorosz, R. S. Romaniuk (SPIE, Bellingham, WA, 1999)

9.6 S. C. Mettler, L. R. Dunn, A. L. Ingles, H. C. Chandan: 'Splicing Considerations for Non-Zero Dispersion Fiber'. In: *Proceedings of the National Fiber Optic Engineers Conference (NFOEC), 1999* (Telcordia, Piscataway, NJ 1999)
9.7 J. Noda, K. Okamoto, Y. Sasaki: IEEE J. Lightwave Technol. **LT-4**, 1071 (1986)
9.8 W. Zheng: IEEE J. Lightwave Technol. **15**, 125 (1997)
9.9 C. Good, D. Gross, J. Paulsen, T. Watanabe, K. Ito: 'Improvements in Splicing Polarization Maintaining Fiber'. In *Proceedings of the 17th National Fiber Optic Engineers Conference (NFOEC) at Baltimore, MD, July 8-12, 2001*, (Telcordia, Piscataway, NJ 2001) pp. 362-369
9.10 J. E. Johnson: 'Challenges Associated With Splicing Polarization Maintaining Fiber (PMF)'. In: *Proceedings of the National Fiber Optic Engineers Conference (NFOEC) at Orlando, FL, Sept. 7–11, 2003*, (Telcordia, Piscataway, NJ 2003) pp. 1465–1472
9.11 A. Ishikura, Y. Kato, T. Abe, M. Miyauchi: Appl. Opt. **25**, 3455 (1986)
9.12 Y. Kikuchi, N. Kawakami, K. Himeno, F. Suzuki, O. Fukuda, K. Inada: Fujikura Technical Review, **16** 1 (1987)
9.13 M. P. Varnham, D. N. Payne, J. D. Love: Electron. Lett., **20**, 55 (1983)
9.14 Y. Kato: Appl. Opt. **24**, 2346 (1985)
9.15 W. Zheng: 'Auto-aligning and Splicing PM-Fibers of Different Types with a Passive Method'. In: *Fiber Optic Gyros: 20th Anniversary Conference at Denver CO, August 5–6, 1996*, ed. by E. Udd, H. C. Lefevre, K. Hotate (SPIE, Bellingham, WA, 1996) pp. 356–367
9.16 E. Desurvire: *Erbium-Doped Fiber Amplifiers: Principles and Applications*, (Wiley-Interscience, Hoboken, NJ 2002)
9.17 M. J. F. Digonnet: *Rare-Earth-Doped Fiber Lasers and Amplifiers*, 2nd ed., (Marcel Dekker, New York 1993)
9.18 B. Pederson, A. Bjarklev, J. H. Poulson: Electron. Lett. **27** 255 (1991)
9.19 W. Zheng, O. Hulten, and R. Rylander: IEEE J. Lightwave Technol. **12**, 430 (1994)
9.20 M. J. Holmes, D. M. Spirit, F. P. Payne: Electron. Lett. **26**, 1873 (1990)
9.21 H. Y. Tam: Electron. Lett. **27**, 1597 (1991)
9.22 W. V. Sorin, D. B. Baney: IEEE Photon. Technol. Lett. **4**, 374 (1992)
9.23 M. J. Holmes, F. P. Payne: Electron. Lett. **26**, 2102 (1990)
9.24 M. P. Singh, J. O. Reese, T. Wei: 'Low-Loss Fusion Splicing of Erbium-Doped Optical Fibers for high Performance Fiber Amplifiers'. In: *Proceedings of the 40th Electronic Components and Technology Conference May 20-23, 1990* (IEEE, Piscataway NJ, 1990) pp. 873–876
9.25 M. P. Singh, J. O. Reese, T. Wei, D. G. Storch: IEEE Trans. Components Hybrids Mfg. Technol. **13**, 811 (1990)
9.26 G.-R. Lin, G.-C. Lin: IEEE Photon. Technol. Lett. **15**, 1201 (2003)
9.27 M. Takahara, T. Yokoo, H. Gomi: 'Splice effects of Er-Doped Fiber in Er-Doped Fiber Amplifiers'. In: *Proceedings of the International Conference on Communication Systems at Singapore November 14–18, 1995* (IEEE Piscataway, NJ 1994) pp. 73–77
9.28 P. Leproux, P. Roy, D. Pagnoux, B. Kerrinckx, J. Marcou: Opt. Commun. **174**, 419 (2000)
9.29 G. Kweon, I. Park: IEEE J. Lightwave Technol. **17**, 690 (1999)
9.30 L. Grüner-Nielsen, S. N. Knudsen, B. Edvold, T. Veng, D. Magnussen, C. C. Larsen, H. Damsgaard: Opt. Fiber Technol. **6**, 164 (2000)

9.31 R. J. Brown, H. C. Chandan, H. P. Debban, R. H. Jackson, A. F. Judy, S. N. Knudsen, D. W. Peckham, M. O. Pedersen, P. L. Tabaddor, C. Wu, B. Zhu: 'Disperion Managed Cables: Advantages and Practical Considerations for Terrestrial Use'. In *Proceedings of the National Fiber Optic Engineers Conference (NFOEC) at Dallas, TX, September 15–19 2002*, (Telcordia, Piscataway NJ, 2002) pp. 1537–1547
9.32 K. Ohsono, K. Kotani, K. Murakami, Y. Bing, T. Yamazaki, H. Shimane: 'The Study of Large Effective Area Fiber & Mating Dispersion Slope Compensating Fiber for Dispersion Flattened Hybrid Optical Fiber DWDM Link'. In: *Proceedings of the 50th International Wire and Cable Symposium (IWCS) at Lake Buena Vista, FL, November 12–15, 2001* (IWCS, Eatontown, NJ 2001) pp. 483–486
9.33 Y. Koyano, M. Onishi, K. Tamano, M. Nishimura: 'Compactly-packaged high performance fiber-based dispersion compensation modules.' In: *Proceedings of the 22nd European Conference on Optical Communication Volume 3 (ECOC 1996) at Oslo, Sweden, September 15–19, 1996* (Telenor R&D, Piscataway, NJ 1996) pp. 3.221–3.224
9.34 M. Cheng: 'Optimized Process to Splice Dispersion Compensation Fibres with Standard Single-Mode Fibres'. In: *Proceedings of the 49th International Wire and Cable Symposium (IWCS) at Atlantic City, NJ, November, 2000* (IWCS, Eatontown, NJ 2000) pp. 385–388
9.35 C. D. Hussey, K. P. Oakley: 'Low-loss splices between different fibres'. In: *Opto-Ireland 2002: Optics and Photonics Technologies and Applications at Galway Ireland, September 5–6, 2002* ed. T. J. Glynn (SPIE, Bellingham, WA, 2003) pp. 266-272
9.36 K. Takahashi, S. Yaguchi, N. Kawanishi, T. Ohtani: 'Development of a New Factory Fusion Splicer.' In: *Proceedings of the 50th International Wire and Cable Symposium (IWCS) at Lake Buena Vista, FL, November 12–15, 2001* (IWCS, Eatontown, NJ 2001) pp. 68–76
9.37 B. Edvold, L. Grüner-Nielsen: 'New technique for reducing the splice loss to dispersion compensating fiber.' In: *Proceedings of the 22nd European Conference on Optical Communication Volume 2 (ECOC 1996) at Oslo, Sweden, September 15–19, 1996* (Telenor R&D, Piscataway, NJ 1996) pp. 2.245-2.248
9.38 P. Kaiser, W. H. Astle: Bell Syst. Tech. J. **53**, 1021 (1974)
9.39 J. C. Knight, T. A. Birks, P. St. J. Russell: ' "Holey" Silica Fibers'. In: *Optics of Nanostructured Materials*. ed. by V. A. Markel and T. F. George (John Wiley, New York, 2001) pp. 39–71
9.40 P. S. J. Russell: Science **299**, 358 (2003)
9.41 J. C. Knight: Nature **424**, 847 (2003)
9.42 R. F. Cregan, B. J. Mangan, J. C. Knight, T. A. Birks, P. St. J. Russell, P. J. Roberts, D. C. Allan: Science **285**, 1537 (1999)
9.43 C. Kerbage, A. Hale, A. D. Yablon: Appl. Phys. Lett. **79**, 3191 (2001)
9.44 J. K. Chandalia, B. J. Eggleton, R. S. Windeler, S. G. Kosinski, X. Liu, C. Xu: IEEE Photon. Technol. Lett. **13**, 52 (2001)
9.45 D. Nishioka, T. Hasegawa, T. Saito, E. Sasaoka, T. Hosoya: 'A Holey Fiber With SMF-Compatible MFD and Ultra-Low Bending Loss for Dense Optical Wiring Applications'. In: *Proceedings of the National Fiber Optic Engineers Conference (NFOEC), Orlando, FL, Sept. 8-11, 2003*, (Telcordia, Piscataway, NJ 2003), p. 398.
9.46 K. Nakajima, K. Hogari, J. Zhou, K. Tajima, I. Sankawa: IEEE Photon. Technol. Lett. **15**, 1737 (2003)
9.47 P. J. Bennett, T. M. Munro, D. J. Richardson: Opt. Lett. **24**, 1203 (1999)

9.48 K. Borzycki: 'Holey Fibers – Applications Issues'. In: *Proceedings of the 3rd International Conference on Transparent Optical Networks at Cracow, Poland June 18-21 2001*, ed. by M. Marciniak (IEEE, Piscataway, NJ 2001) pp. 92–95
9.49 R. K. Sinha, S. K. Varshney: 'Estimation of Splice Loss in Photonic Crystal Fiber'. In: *Photonic Bandgap Materials and Devices at San Jose, CA January 23-25, 2002*, ed. by A. Adibi, A. Scherer, S.-Y. Lin (SPIE, Bellingham WA, 2002) pp. 296–302
9.50 S. K. Varshney, R. K. Sinha, T. Iwai: 'Spectral Response of Splice Loss in Photonic Crystal Fibers'. In: *Proceedings of the 5th Pacific Rim Conference on Lasers and Electro-Optics (CLEO/Pacific Rim) December 15-19, 2003* (IEEE, Piscataway, NJ 2003) p. 404
9.51 Y. L. Hoo, W. Jin, J. Ju, H. L. Ho: Microwave Opt. Technol. Lett. **40**, 378 (2004)
9.52 J. Ju, W. Jin, Y. L. Hoo, M. S. Demokan: Microwave Opt. Technol. Lett. **42**, 171 (2004)
9.53 J. H. Chong, M. K. Rao, Y. Zhu, P. Shum: 'Investigations of Photonic Crystal Fiber Splicing'. In: *Proceedings of the 2003 Joint Conference of the Fourth International Conference on Information, Communications and Signal Processing at Singapore December 15-18, 2003* (IEEE Piscataway, NJ 2003) pp. 164-166
9.54 J. H. Chong, M. K. Rao: Opt. Express **11**, 1365 (2003)
9.55 T. P. Hansen, J. Broeng, C. Jakobsen, G. Vienne, H. R. Simonsen, M. D. Nielsen, P. M. W. Skovgaard, J. R. Folkenberg: 'Air-guidance over 345m large-core photonic bandgap fiber'. In: *Proceedings of the Optical Fiber Communications Conference, Atlanta, GA, March 17-22, 2003*, (Optical Society of America, Washington, D.C., 2003), Postdeadline paper PD4
9.56 B. Bourliaguet, C. Pare, F. Emond, A. Croteau: Opt. Express **11**, 3412 (2003)
9.57 C. Gomez-Reino, M. V. Perez, C. Bao: *Gradient-Index Optics* (Springer, New York 2000)
9.58 A. D. Yablon, R. T. Bise: 'Low-Loss High-Strength Microstructured Fiber Fusion Splices Using GRIN Fiber Lenses'. In: *Proceedings of the Optical Fiber Communications (OFC) Conference at Los Angeles, CA, Feb. 22–27, 2004*, (Optical Society of America, Washington DC 2004) paper MF14
9.59 A. D. Yablon, R. T. Bise: 'Low-Loss High-Strength Microstructured Fiber Fusion Splices Using GRIN Fiber Lenses'. Accepted for publication in IEEE Photon. Technol. Lett.
9.60 K. G. Hougaard, A. Bjarklev, E. Knudsen, S. B. Libori, J. Riishede, P. M. W.Skovgaard, J. Broeng: 'Coupling to Photonic Crystal Fibers'. In: *Proceedings of the Optical Fiber Communications Conference, Anaheim, CA, March 17-22, 2002*, (Optical Society of America, Washington, DC, 2003), paper ThGG11, 627
9.61 J. T. Lizier, G. T. Town: IEEE Photon. Technol. Lett. **13**, 794 (2001)
9.62 J. H. Chong, M. K. Rao, Y. Zhu, P. Shum: IEEE Photon. Technol. Lett. **15**, 942 (2003)
9.63 S. T. Huntington, K. Lyytikainen, J. Canning: Opt. Express **11**, 535 (2003)

Chapter 10

10.1 ElectroniCast Corp. cited in Lightwave Magazine Web Exclusive, http://lw.pennnet.com, June 27, 2003

10.2 G. Kiss, E. Vogel: 'High Yield Fusion Splicing in the Outside Plant: Using Fiber Meltback to Monitor Electrode Condition.' In *12th National Fiber Optic Engineers Conference (NFOEC) Volume 2 September 9–12, 1996*, (OmniPress, 2000) pp. 819-835.
10.3 D. Duke, C. Henderson, G. Karl, G. Mackie: 'Migration of Core-Alignment Fusion Splicing from the Splicing Van to Outdoor/FTTH Applications.' In *16th National Fiber Optic Engineers Conference (NFOEC) at Denver, Colorado, August 27–31, 2000*, (Omnipress, 2000)
10.4 T. Mizushima, S. Morita, H. Sugawara, T. Sato, S. Yaguchi: 'Development of a Mass Fusion Splicing System for up to 24-Fiber Ribbon'. In: *Proceedings of the 51st International Wire and Cable Symposium (IWCS) at Lake Buena Vista, FL, November 18–21, 2002* (IWCS, Eatontown, NJ, 2002) pp. 708–714
10.5 K. Yamamoto, A. Tanabe, S. Yokomizo, J. Kazama, S. Harada, H. Watanabe, T. Hino: Furukawa Review **21**, 32 (2002)
10.6 J. J. Refi: *Fiber Optic Cable - A Lightguide*, 2nd edn. (AVO Training Institute, 2001)

Index

Springer Series in

OPTICAL SCIENCES

Volume 1

1 **Solid-State Laser Engineering**
By W. Koechner, 5th revised and updated ed. 1999, 472 figs., 55 tabs., XII, 746 pages

Published titles since volume 80

80 **Optical Properties of Photonic Crystals**
By K. Sakoda, 2nd ed., 2004, 107 figs., 29 tabs., XIV, 255 pages

81 **Photonic Analog-to-Digital Conversion**
By B.L. Shoop, 2001, 259 figs., 11 tabs., XIV, 330 pages

82 **Spatial Solitons**
By S. Trillo, W.E. Torruellas (Eds), 2001, 194 figs., 7 tabs., XX, 454 pages

83 **Nonimaging Fresnel Lenses**
Design and Performance of Solar Concentrators
By R. Leutz, A. Suzuki, 2001, 139 figs., 44 tabs., XII, 272 pages

84 **Nano-Optics**
By S. Kawata, M. Ohtsu, M. Irie (Eds.), 2002, 258 figs., 2 tabs., XVI, 321 pages

85 **Sensing with Terahertz Radiation**
By D. Mittleman (Ed.), 2003, 207 figs., 14 tabs., XVI, 337 pages

86 **Progress in Nano-Electro-Optics I**
Basics and Theory of Near-Field Optics
By M. Ohtsu (Ed.), 2003, 118 figs., XIV, 161 pages

87 **Optical Imaging and Microscopy**
Techniques and Advanced Systems
By P. Török, F.-J. Kao (Eds.), 2003, 260 figs., XVII, 395 pages

88 **Optical Interference Coatings**
By N. Kaiser, H.K. Pulker (Eds.), 2003, 203 figs., 50 tabs., XVI, 504 pages

89 **Progress in Nano-Electro-Optics II**
Novel Devices and Atom Manipulation
By M. Ohtsu (Ed.), 2003, 115 figs., XIII, 188 pages

90/1 **Raman Amplifiers for Telecommunications 1**
Physical Principles
By M.N. Islam (Ed.), 2004, 488 figs., XXVIII, 328 pages

90/2 **Raman Amplifiers for Telecommunications 2**
Sub-Systems and Systems
By M.N. Islam (Ed.), 2004, 278 figs., XXVIII, 420 pages

91 **Optical Super Resolution**
By Z. Zalevsky, D. Mendlovic, 2004, 164 figs., XVIII, 232 pages

92 **UV-Visible Reflection Spectroscopy of Liquids**
By J.A. Räty, K.-E. Peiponen, T. Asakura, 2004, 131 figs., XII, 219 pages

93 **Fundamentals of Semiconductor Lasers**
By T. Numai, 2004, 166 figs., XII, 264 pages

Springer Series in

OPTICAL SCIENCES

94 **Photonic Crystals**
Physics, Fabrication and Applications
By K. Inoue, K. Ohtaka (Eds.), 2004, 209 figs., XV, 320 pages

95 **Ultrafast Optics IV**
Selected Contributions to the 4th International Conference on Ultrafast Optics, Vienna, Austria
By F. Krausz, G. Korn, P. Corkum, I.A. Walmsley (Eds.), 2004, 281 figs., XIV, 506 pages

96 **Progress in Nano-Electro Optics III**
Industrial Applications and Dynamics of the Nano-Optical System
By M. Ohtsu (Ed.), 2004, 186 figs., 8 tabs., XIV, 224 pages

97 **Microoptics**
From Technology to Applications
By J. Jahns, K.-H. Brenner, 2004, 303 figs., XI, 335 pages

98 **X-Ray Optics**
High-Energy-Resolution Applications
By Y. Shvyd'ko, 2004, 181 figs., XIV, 404 pages

99 **Few-Cycle Photonics and Optical Scanning Tunneling Microscopy**
Route to Femtosecond Ångstrom Technology
By M. Yamashita, H. Shigekawa, R. Morita (Eds.) 2005, 241 figs., XX, 393 pages

100 **Quantum Interference and Coherence**
Theory and Experiments
By Z. Ficek and S. Swain, 2005, 178 figs., approx. 432 pages

101 **Polarization Optics in Telecommunications**
By J. Damask, 2005, 110 figs, XVI, 528 pages

102 **Lidar**
Range-Resolved Optical Remote Sensing of the Atmosphere
By C. Weitkamp (Ed.), 161 figs., approx. 416 pages

103 **Optical Fiber Fusion Splicing**
By A. D. Yablon, 2005, 137 figs., XIV, 306 pages

104 **Optoelectronics of Molecules and Polymers**
By A. Moliton, 2005, 200 figs., approx. 460 pages

105 **Solid-State Random Lasers**
By M. Noginov, 2005, 149 figs., approx. 380 pages

106 **Coherent Sources of XUV Radiation**
Soft X-Ray Lasers and High-Order Harmonic Generation
By P. Jaeglé, 2005, 150 figs., approx. 264 pages

107 **Optical Frequency-Modulated Continuous-Wave (FMCW) Interferometry**
By J. Zheng, 2005, 137 figs., approx. 250 pages

108 **Laser Resonators and Beam Propagation**
Fundamentals, Advanced Concepts and Applications
By N. Hodgson and H. Weber, 2005, 497 figs., approx. 790 pages

109 **Progress in Nano-Electro Optics IV**
Characterization of Nano-Optical Materials and Optical Near-Field Interactions
By M. Ohtsu (Ed.), 2005, 127 figs., approx. 225 pages